
Site U1368¹

Expedition 329 Scientists²

Chapter contents

Background and objectives	1
Operations	2
Lithostratigraphy	3
Igneous lithostratigraphy, petrology, alteration, and structural geology	8
Paleontology and biostratigraphy	19
Physical properties	20
Downhole logging	22
Paleomagnetism	24
Biogeochemistry	25
Microbiology	28
References	31
Figures	33
Tables	104
Appendix	120

Background and objectives

Integrated Ocean Drilling Program (IODP) Site U1368 (proposed Site SPG-6A) was selected as a drilling target because

- Its microbial activities and cell counts were expected to be characteristic of the gyre center and
- Its basement age renders it a reasonable location for testing the extent of sediment-basement interaction, basalt alteration, and openness to flow in a thinly sedimented region of ~13.5 Ma basaltic basement.

The principal objectives at Site U1368 were

- To document the habitats, metabolic activities, genetic composition, and biomass of microbial communities in subseafloor sediment with very low total activity;
- To test how oceanographic factors (such as surface ocean productivity, sedimentation rate, and distance from shore) control variation in sedimentary habitats, activities, and communities from gyre center to gyre margin;
- To quantify the extent to which these sedimentary microbial communities may be supplied with electron donors by water radiolysis; and
- To determine how basement habitats, potential activities, and, if measurable, communities vary with basement age and hydrologic regime (from ridge crest to abyssal plain).

Site U1368 (~3740 meters below sea level) is in the South Pacific Gyre within a region of primarily seamount topography with possible evidence of original abyssal hill seafloor fabric oriented nearly north–south (Fig. F1). The site is bordered to the east and west with what appear to be large (500 m high; 6 km wide) seamounts preferentially perched on top of abyssal hills. The closest previous drilling site is Deep Sea Drilling Project Leg 92 Site 598, 550 nmi away.

Site U1368 is within magnetic polarity Chron 5ABn, so the original crustal age ranges from 13.4 to 13.6 Ma (Gradstein et al., 2004). Based on the age of the crust and regional tectonic history (Tebbens and Cande, 1997), the crust was accreted along the Pacific-Farallon spreading center at ~13.5 Ma. The calculated spreading rate from the KNOX-02RR magnetic survey suggests the crust was accreted at an ultrafast spreading ridge with spreading half-rates of ~80–85 km/m.y. (D'Hondt et al., 2010; D'Hondt et al., 2011).

¹Expedition 329 Scientists, 2011. Site U1368. In D'Hondt, S., Inagaki, F., Alvarez Zarikian, C.A., and the Expedition 329 Scientists, *Proc. IODP*, 329: Tokyo (Integrated Ocean Drilling Program Management International, Inc.).
doi:10.2204/iodp.proc.329.106.2011

²Expedition 329 Scientists' addresses.



Many geological and geophysical characteristics of the target site were characterized by the 2006/2007 KNOX-02RR survey expedition (D'Hondt et al., 2011) (Figs. F1, F2, F3, F4, F5, F6). The cored sediment grades from dark yellowish brown clay to yellowish brown foraminifer-bearing clayey nannofossil ooze. The core is mottled (D'Hondt et al., 2009).

D'Hondt et al. (2009) documented the presence of microbial cells and oxic respiration throughout the uppermost 2.6 m of sediment at Site U1368. Cell concentrations were approximately three orders of magnitude lower than at similar depths in previously drilled marine sediment of other regions. Net respiration was similarly much lower than at previously drilled sites. From extrapolation of dissolved oxygen content in the uppermost 2.6 m of sediment, Fischer et al. (2009) predicted that dissolved oxygen penetrates the entire sediment column, from seafloor to basement.

Operations

Transit to Site U1368

After an 80.75 h transit from Site U1367, covering 793 nmi and averaging 9.8 kt, a sonar survey was initiated over Site U1368. The survey essentially replicated the lines of the original site survey in order to confirm depths of bottom and hard returns under the seafloor. After the survey was completed at 1515 h, the speed was reduced and thrusters were lowered. Speed was less than expected because one of the propulsion motors was offline and the vessel sailed most of the voyage into headwinds and seas. Dynamic positioning was initiated over Site U1368 at 1545 h on 12 November 2010. The reference position was a combination of GPS signals. No acoustic beacon was deployed, but a beacon remained on standby in the event of a loss of GPS satellite coverage. Whereas automatic input into the dynamic positioning system was not possible because of a system malfunction, it was possible to manually hold the vessel in position to clear the seafloor with the bottom-hole assembly (BHA) if necessary.

All times in this section are given in local ship time unless otherwise noted. For most of the expedition, local time was Universal Time Coordinated – 10 h.

Site U1368

Six holes were drilled or cored at this site (Table T1). The first hole was a washdown hole drilled with the center bit to establish the sediment depth of 13.6 meters below seafloor (mbsf). The next four holes were cored with the advanced piston corer (APC) system. The last hole was drilled and cored with the ro-

tary core barrel (RCB) system to 115.1 mbsf through sediment and into basement. The advanced piston corer temperature tool was not deployed because of the shallow sediment depth. Perfluorocarbon tracer (PFT) was pumped for the entire drilling/coring interval until the last core was on deck. APC system recovery for Site U1368 was 99.8%. RCB system recovery was 27.6%. A total of 23 cores were attempted while coring 173 m. The total length of core recovered at this site was 89.52 m (51.7% recovery).

Hole U1368A

Rig floor operations commenced at 1545 h on 12 November 2010. The trip to the seafloor was uneventful. The top drive was picked up and the drill string was spaced out, and Hole U1368A was spudded at 0130 h on 13 November. The PFT pump was turned on to displace the drill string with the contamination testing fluid. The washdown hole was drilled to determine depth of basement. Mudline was established as 4302.0 meters below rig floor (mbrf) by tagging with the bit. After drilling down, basement was established at 13.6 mbsf. The bit was pulled back above the seafloor, clearing the seafloor at 0200 h and ending Hole U1368A.

Hole U1368B

After clearing the seafloor, the center bit was pulled by wireline, the vessel was offset 20 m west, and the drill string was spaced out to spud Hole U1368B. After making up the first APC core barrel, the core barrel was run to bottom on the wireline and Hole U1368B was spudded at 0330 h on 13 November. Seafloor depth was established at 3750 mbrf with a mudline core. APC coring continued to 16.0 mbsf. Three cores were taken with a total recovery of 15.84 m for an overall recovery in Hole U1368B of 99.0%. After Core 329-U1368B-3H, the bit was tripped back to just above the seafloor, ending Hole U1368B at 0655 h on 13 November. PFT was mixed with the drilling fluid (seawater) and pumped on all cores for contamination testing.

Hole U1368C

Hole U1368C began at 0655 h when the APC assembly cleared the seafloor after completing Hole U1368B. After offsetting the vessel 20 m north, Hole U1368C was spudded at 0730 h on 13 November and advanced with the APC system to 16.3 mbsf before encountering basement. Seafloor was established at 3749.5 mbrf. PFT was mixed with the drilling fluid (seawater) and pumped on all cores for contamination testing. Two cores were taken with a total recovery of 16.34 m for an overall recovery in Hole U1368C of 100.2%. The drill string was tripped

to just above the mudline, clearing the seafloor at 0915 h and ending Hole U1368C.

Hole U1368D

Hole U1368D began at 0915 h on 13 November when the APC assembly cleared the seafloor after completing Hole U1368C. After offsetting the vessel 20 m east, Hole U1368D was spudded at 1000 h and advanced with the APC system for two cores to 15.0 mbsf with a 15.04 m recovery (100.3%). Seafloor was established at 3750 mbrf. PFT was mixed with the drilling fluid (seawater) and pumped on all cores for contamination testing. The drill string was tripped to just above the mudline, clearing the seafloor at 1135 h and ending Hole U1368D.

Hole U1368E

Hole U1368E began at 1135 h on 13 November when the APC assembly cleared the seafloor after completing Hole U1368D. The vessel was offset 20 m east of Hole U1368D. After making up the first APC core barrel, the core barrel was run to bottom on the wireline and Hole U1368E was spudded at 1210 h. Seafloor depth was established with a mudline core at 3751.9 mbrf. The APC system was used to take two cores to 10.6 mbsf with 10.58 m recovery (99.8%). PFT was mixed with the drilling fluid (seawater) and pumped on all cores for contamination testing. The drill string was tripped to the surface, clearing the rotary table at 2000 h on 13 November and ending Hole U1368E.

Hole U1368F

After a 20 m offset to the south, Hole U1368F began on 13 November at 2000 h when the bit cleared the rotary table after tripping out of Hole U1368E. The BHA was set back, the APC bit was removed, and the rotary core bit and rotary coring system were assembled in preparation for running the new RCB BHA. The BHA was run into the hole, followed by the drill pipe. After reaching 3741 mbrf, the top drive was picked up and the drill string was spaced out to spud Hole U1368F. Water depth was recorded at 3751.9 mbrf using an offset depth from Hole U1368E. Rotary coring began at the seafloor when Hole U1368F was spudded at 0520 h on 14 November. Core 329-U1368F-2R crossed the sediment/basalt interface at 11.8 mbsf. RCB coring continued from 11.8 to 115.1 mbsf with average recovery. A total of 14 cores were taken, and a total of 115.1 m was cored with a recovery of 31.74 m of core. RCB system recovery for Hole U1368F was 27.6%. PFT was mixed with the drilling fluid (seawater) and pumped on all cores for contamination testing. Microspheres were also deployed on all RCB cores after Core 2R. After reaching a total

depth of 115.1 mbsf, the center bit was deployed and the hole was conditioned for logging. The mechanical bit release was activated, dropping the RCB bit at the bottom of the hole. The drill string, minus the bottom half of the mechanical bit release and RCB bit, was tripped to ~30 mbsf and the logging tools were rigged up and deployed. Four logging runs, two with the triple combination (triple combo) and two with the Formation MicroScanner (FMS) tool string (no sonic) were performed successfully. At the end of logging activities, the tools were rigged down and the drill string was tripped back to the rig floor and secured for the 1073 nmi transit to the next site, ending Hole U1368F and Site U1368 at 1233 h on 18 November.

Lithostratigraphy

The sediment at Site U1368 is 15–16 m thick and consists of calcareous ooze, pelagic clay, and lithic sand. An additional 1 m of volcanoclastic breccia was recovered from an interval between basalt flows, 80 m below the upper sediment/basalt interface. The principal components of the ooze are calcareous nannofossils, accompanied by red-brown to yellow-brown semiopaque oxide (RSO) and foraminifers (see Site U1368 smear slides in “[Core descriptions](#)”; Fig. F7). Clay minerals are in relatively low abundance throughout the sediment. Clay-rich and sandy intervals contain a wide variety of minerals, including albite-anorthite, ankerite, augite, calcite, chlorite, hematite, and titanomagnetite. The volcanoclastic breccia contains altered basaltic, lithic and vitric grains.

Based on compositional and textural attributes, the sediment at Site U1368 is divided into three lithologic units (Fig. F7). Unit I is nannofossil ooze, clay-bearing nannofossil ooze, and nannofossil marl. Unit I is separated into Subunits IA and IB based on the vertical distribution of nannofossils and RSO. Subunit IA contains abundant nannofossils and thus qualifies as nannofossil ooze and clay-bearing nannofossil ooze. Nannofossil abundance decreases in Subunit IB as RSO increases proportionately. Unit II is nannofossil-bearing clay that can be distinguished easily from the other units by its uniform, very dark brown color. Unit III includes three sand intervals separated by a thick (20 cm) bed of hematitic nannofossil-bearing clay. The sandy intervals contain a distinctive mineral suite that includes indicators of basaltic origins (plagioclase and augite) and hydrothermal alteration (ankerite, chlorite, and titanomagnetite).

Lithostratigraphic correlation among Site U1368 holes shows that sediment composition remains

fairly uniform; however, unit thickness varies over the 20–40 m distances that separate holes (Fig. F8). The thickness of Unit I, for example, thins by ~2 m across the 40 m lateral distance that separates Holes U1368B and U1368E. Nonetheless, each hole contains similar ooze, marl, and sand intervals.

Description of units

Unit I

Subunit IA

Intervals: 329-U1368B-1H-1, 0 cm, to 2H-2, 143 cm; 329-U1368C-1H-1, 0 cm, to 2H-1, 20 cm; 329-U1368D-1H-1, 0 cm, to 1H-4, 113 cm; 329-U1368E-1H-1, 0 cm, to 1H-4, 34 cm; 329-U1368F-1R-1, 0 cm, to 1R-2, 22 cm

Depths: Hole U1368B = 0–7.43 mbsf, Hole U1368C = 0–8.2 mbsf, Hole U1368D = 0–5.63 mbsf, Hole U1368E = 0–5.2 mbsf, Hole U1368F = 0–1.72 mbsf

Lithology: clay-bearing nannofossil ooze

The overall color of Subunit IA is dark yellowish brown (10YR 4/6, 3/6) (Figs. F9A, F9B). Specific intervals of nannofossil ooze with lower RSO abundance are yellowish brown (10YR 5/6). The top 25 cm of this interval is brown (10YR 5/3) and overlies dark grayish brown (10YR 4/2) clay-bearing intervals (Fig. F10A). Several widely dispersed silty layers (as thick as 10 cm) are very pale brown (10YR 7/4).

Subunit IA contains too many laminations and beds to allow examination of each layer petrographically. Therefore, we prepared 5–7 samples from each of the light-, intermediate-, and dark-colored intervals and used the results to form a characterization of average lithology and compositional trends. Smear slide analyses indicate that Subunit IA consists primarily of calcareous nannofossil ooze (Fig. F7). The uppermost 25 cm of the subunit contains a higher abundance of RSO (10%–15%) and clay (5%–8%) than the lower interval (5%–10% and 2%–3%, respectively) and is the only portion of the sediment that contains phillipsite. X-ray diffraction (XRD) analysis of the ooze (Sample 329-U1368B-1H-1, 146–148 cm) indicates that the clay mineral in Subunit IA is smectite (Fig. F11A). The mass concentration of foraminifers >63 µm in the ooze varies from <1% in the upper clay-rich interval (Sample 329-U1368B-1H-3, 0–2 cm; ~3 mbsf) to >7% near the base of Subunit IA (Sample 329-U1368-2H-1, 25–27 cm; 5.75 mbsf). In addition to low abundance, most of the foraminifers in the upper clay-rich interval are broken and partially dissolved (see “Paleontology and biostratigraphy”). The lower subunit contact consists of pebbles of indurated pelagic clay overlying a clay-rich matrix that contains abundant RSO (Fig. F12A).

Although the sediment is poorly consolidated, it is highly cohesive. The sediment also clings persistently to physical properties and sampling instruments inserted into the split core sections.

The dark color of the upper 25 cm of sediment is distinct from the underlying pale brown sediment and contains traces of horizontal burrowers of transition-layer (5–8 cm) organisms (Ekdale et al., 1984). Although the sediment is mottled, individual *Planolites* and *Zoophycos* burrows are evident (see core photographs from Site U1368 in “Core descriptions”). Several meters of the middle of Subunit IA contain very faint, short (2–3 cm), vertical burrows (*Trichichnus* and *Teichichnus*). Very pale brown, very thin to thick (1–10 cm) beds of foraminiferal ooze occur occasionally. Laminations within the beds exhibit two distinct sedimentary structures: (1) undeformed horizontal bedding and (2) soft-sediment deformation. The lower contact of Subunit IA observed in Hole U1368B is inclined 30° from horizontal. In Hole U1368E, the contact is irregular, showing 8 mm of vertical relief.

Subunit IB

Intervals: 329-U1368B-2H-2, 143 cm, to 2H-5, 52 cm; 329-U1368C-2H-1, 20 cm, to 2H-4, 140 cm; 329-U1368D-1H-4, 113 cm, to 2H-3, 150 cm; 329-U1368E-1H-4, 34 cm, to 2H-2, 150 cm; 329-U1368F-1R-2, 22 cm (lower contact not cored)

Depths: Hole U1368B = 7.43–12.02 mbsf, Hole U1368C = 8.2–13.9 mbsf, Hole U1368D = 5.63–12.0 mbsf, Hole U1368E = 5.2–8.6 mbsf, Hole U1368F = 1.72 mbsf (lower contact not cored)

Lithology: nannofossil marl

Sediment in Subunit IB is dark yellowish brown (10YR 3/4, 3/6) to dark brown (10YR 3/3) (Fig. F9C).

The uniformity of Subunit IB lends itself to a simple description of its lithology. Smear slide analyses indicate an overall abundance of nannofossils and RSO (Fig. F10B). RSO increases from ~10% in the upper 10–50 cm of the subunit to 60%–80% in the dark brown clay at the bottom of the subunit (Fig. F7). Sample 329-U1368B-2H-4, 60–61 cm, was selected to represent an average Subunit IB lithology and analyzed by X-ray diffraction (XRD). An analysis of the sample’s XRD pattern resolves calcite and smectite but fails to contain any diagnostic indicators of the RSO. Foraminifers >63 µm constitute slightly more than 6% (by mass) of the sediment in the upper 10–50 cm of the interval but <1% (by visual estimation) in the lower 30–100 cm. Overall preservation of planktonic foraminifers in Subunit IB is moderate to good (see “Paleontology and biostratigraphy”).

Firmness of the sediment increases with depth and varies with color, not bulk density. Dark, RSO-rich sediment in the lower half of Subunit IB is firm. Layers of very pale brown nannofossil marl are poorly consolidated.

The upper half of Subunit IB is massive. The lower half exhibits light and dark layering suggestive of bedding, although all sediment is affected by bioturbation. In Section 329-U1368B-2H-4, *Zoophycos* burrows as wide as 5 mm stand out as evidence of the bioturbation. Contrasting very dark brown and dusky red sediment form a steeply (~45°) inclined interval of metalliferous clay in interval 329-U1368E-2H-3, 48–55 cm. The texture of the clay on either side of the line separating these colors is similar and thus the origin of this structure is unclear.

Unit II

Intervals: 329-U1368B-2H-5, 52 cm, to 2H-6, 99 cm; 329-U1368C-2H-4, 140 cm, to 2H-5, 135 cm through 2H-6, 10 cm; 329-U1368D-2H-4, 0 cm, through 2H-4, 100–125 cm; 329-U1368E-2H-3, 0 cm, to 2H-4, 34 cm

Depths: Hole U1368B = 12.02–13.5 mbsf, Hole U1368C = 13.9 to 15.50–15.13 mbsf, Hole U1368D = 12.0 to 13.0–13.25 mbsf, Hole U1368E = 8.6–10.16 mbsf

Lithostratigraphy: nannofossil-bearing clay

Unit II sediment is black to very dark brown (7.5YR 2.5/1, 2.5/3, 3/4) (Fig. F9D).

Color differences define three zones in Unit II that range in thickness from 15 to 50 cm. Smear slide analyses indicate that all three intervals are predominantly RSO, accompanied by nannofossils (Fig. F10C). RSO abundance increases slightly with depth from 60% to 80% in the uppermost interval and from 70% to 90% in the lowermost interval (Fig. F7). XRD analysis of Sample 329-U1368B-2H-6, 60–61 cm, from the middle interval clearly confirms the presence of calcite and suggests the presence of hematite and montmorillonite (Fig. F11B). In Sample 329-U1368B-2H-7, 10–11 cm, XRD confirms the presence of calcite and hematite in the lowermost interval and contains several peaks that cannot be easily explained. Specifically, the very strong peak at $7.12^{\circ}2\theta$ (5.23\AA) defies easy recognition. The automated search/match function available through the R/V *JOIDES Resolution's* X-ray pattern evaluation software couples this peak with other unmatched peaks at $24.33^{\circ}2\theta$ (1.82\AA) and $15.84^{\circ}2\theta$ (2.82\AA) and indicates that the mineral calcihelairite is the most likely match; however, the common association of this mineral with perialkalic igneous intrusions casts suspicion on the likelihood of this mineral's presence in clay obtained at Site U1368.

The uniform dark brown clay is firm. During description, the clay shrunk quickly and developed transverse and longitudinal desiccation cracks.

This relatively thin unit (120 cm maximum thickness in Hole U1368E) is massive. The boundary between the uppermost and intermediate intervals is sharp but contains small-scale irregularities indicative of horizontal burrowing organisms. The boundary between the intermediate and lower layer contains short (<21 cm) *Chondrites* burrows. The lower contact of Unit II is highly irregular and exhibits 5 cm of vertical relief (Fig. F12B). Similar to the overlying sediment, the dusky red clay immediately overlying the irregular contact is massive.

Unit III

Intervals: 329-U1368B-2H-6, 99 cm, to 3H-1, 10 cm; 329-U1368C-2H-5, 135 cm, through 2H-6, 10 cm, to 2H-CC, 15 cm (end of core); 329-U1368D-2H-4, 100–125 cm, to 2H-5, 139 cm (end of core); 329-U1368E-2H-4, 34 cm, to 2H-CC, 2 cm (end of core)

Depths: Hole U1368B = 13.5–15.1 mbsf, Hole U1368C = 15.50–15.13 to 16.1 mbsf (end of core), Hole U1368D = 13.0–13.25 to 14.9 mbsf (end of core), Hole U1368E = 10.16–10.50 m (end of core)

Lithology: lithic sand interbedded with nannofossil-bearing clay

Unit III contains between one and three sandy intervals and one clay-rich interval (Fig. F8). All three sandy intervals are found in the lowermost core section of Hole U1368B. The upper sand is very dark gray (N3) with white (2.5Y 8/1) and dark reddish brown (5YR 3/3) highlights on the edges of numerous pebble-sized nodules. The middle sand is multicolored, including dark greenish gray (5GY 3/1), bluish black (10B 2.5/1), and very dark brown (7.5YR 2.5/1) (Fig. F9E). Part of the well-indurated dark greenish gray sand contains reddish yellow (5YR 6/6) grains. The lower sand is mostly black (2.5Y 2.5/1) with dark gray and white grains. The clay interval, between the upper and medial sands, is very dark brown (7.5YR 2.5/3) at its core and grades into gray/dark gray (7.5R N5/N3) and white (GLEYS 1 N8) in the few centimeters adjacent to its lower contact.

The apparent continuity of the three sandy intervals from hole to hole varies from one layer to another. The upper layer was observed only in material recovered from Hole U1368B. The middle layer was observed in cores from Holes U1368B–U1368D. The lower layer was observed in cores from Holes U1368B and U1368C. The sandy layer found in Hole U1368E has textural similarity to the upper sand in Hole U1368B, but has magnetic susceptibility similar

to the lower sand of Hole U1368B. Consequently, this sandy layer's relationship to the three sand layers of Hole U1368B is not clear. The absence of the upper layer from Hole U1368C and U1368D cores may be due to either whole-round sampling for biogeochemistry and microbiology or to limited spatial continuity of the layer. The absence of the lower layer in Hole U1368D (and possibly Hole U1368E) may be due to poor recovery of the lowermost few centimeters of sediment.

All three sands are lithic, but each possesses a distinct assemblage of minerals. The upper (dark gray) sand contains numerous plagioclase minerals confirmed by thin section observation and XRD patterns of albite-anorthite (Fig. F11C). The upper sand's other abundant primary mineral component is more difficult to identify because cross-sectional views of its crystal habit were not diagnostic. However, XRD intensity peaks suggest that it is augite. A thin section created from the sand's lower contact shows that most minerals are weathered to clay (Fig. F13A). The middle (green) sand also contains albite-anorthite and augite, as well as petrographic and very strong XRD indications of abundant chlorite (Fig. F11C). The lowermost (black) sand contains abundant calcareous nannofossils and is strongly magnetic. Sieved samples of the black sand yield granular carbonate pieces with bulbous outer surfaces. Planktonic foraminifers with recrystallized tests are also evident in the sieved samples (Fig. F14). Confirmed visually and by XRD analyses, the magnetic mineral is titanomagnetite (Fig. F11C). A major uncertainty about the composition of this sand involves our visual observation of numerous acicular crystals (Fig. F10D). Visual observations and XRD analyses could not positively identify this mineral, although our studies did rule out several suspected minerals including antigorite, aragonite, and natrolite.

The very dark brown clay is calcareous. Smear slide analyses of sediment drawn from the middle of the clay showed numerous nannofossils and RSO (Fig. F7). In Hole U1368B, the upper part of the clay contains four small nodules with composition similar to the overlying lithic sand. A thin section prepared from the sediment at the upper (clay/sand) contact contains minute titanomagnetite (octahedral) and apatite (hexagonal and botryoidal) crystals and many microfossil (foraminifer and radiolarian) molds, some containing secondary calcite crystals (Figs. F13B, F13C).

The upper sand of this unit is well consolidated. Nodules within the sand are either well indurated (rock) or brittle and crumbly. The green sand contains two thin (2–3 cm), firm layers but is otherwise easily disaggregated into loose sand-sized particles.

The lower black sand is very poorly consolidated (soupy). The clay interval between the upper (dark gray) sand and middle (green) sand is mostly firm but tends to become crumbly in the short (1–5 cm) intervals adjacent to the lithic sands.

The lower two sands (green and black) are merged into one contiguous interval in Holes U1368B and U1368C.

Contacts between neighboring lithotypes are abrupt. In Hole U1368B, the uppermost sand's contact with overlying clay is very irregular (see "Unit II"). The lower contact of the upper sand is very sharp and concave against an underlying clay interval. The lower contact of the clay, against the middle (green) sand, is concave and gradational at the top. Based on observations of core from Hole U1368C, the contact between the middle (green) sand and underlying (black) sand is sharp and slightly convex. The black sand is highly disturbed (soupy) and devoid of internal structures. The lower contact of the sand was not observed.

Sediment texture is variable within the upper and middle sand layers. Within the uppermost sand, particles are arranged in nodules that are separated by wide, irregular gaps. The nodules are generally small (2 cm in diameter). When they possess visibly long and short axes, the long axis is usually oriented horizontally. In the green sand, particle size increases from silty to sand in the lower 12 cm. The black sand is soupy; textures and structures were unobservable.

The nannofossil-bearing clay is massive and featureless except for several isolated locations that are associated with indurated nodules. The unit possesses burrowed laminations. Burrows are filled with nannofossil and microfossil debris. The edges of the burrows and space between laminations host consecutive layers of botryoidal apatite, secondary calcite, and pore/vein-filling radiating acicular crystals (Fig. F13C).

Sediment/Basalt contact

We attempted to sample the sediment/basalt interface in each hole. Mixed sediment and basalt fragments were recovered in Holes U1368B, U1368C, and U1368D. Lithologic types associated with the basalt included green and black lithic sand (see "Unit III"). Textural and structural properties of the sediment were not recorded because the sediment was very highly disturbed. In general, the basalt at the sediment/basalt interface is highly altered. Of the ~10 fragments recovered at Site U1368, most were friable and grainy and contained abundant zeolite. More information regarding the altered and relatively unaltered basalt fragments recovered in APC

cores in **“Igneous lithostratigraphy, petrology, alteration, and structural geology.”**

The lowermost core (2H) in Hole U1368E did not contain basalt. However, we believe the sediment/basalt interface was penetrated in the hole because (1) the sediment recovered in Section 329-U1368E-2H-CC contained pebble-sized clasts of friable, highly altered basalt and (2) the core barrel's cutting shoe was irreparably damaged by impact with a very hard substrate during the Core 329-U1368E-3H coring attempt (the cutting shoe was gouged to a depth of ~2 cm, the stroke was incomplete, and the core barrel was recovered empty).

We attempted to recover the sediment/basalt contact in Hole U1368F using RCB coring. The core that spanned the interface (Core 329-U1368F-2R) recovered 4.01 m of the advanced interval (11.6 m). No sediment was recovered in the core and the basalt appeared only mildly altered. See **“Igneous lithostratigraphy, petrology, alteration, and structural geology”** for more details regarding the basalt recovered in Hole U1368F.

Volcaniclastic breccia

Volcaniclastic breccia was recovered during RCB coring of basaltic rocks ~80 m below the upper sediment/basalt contact. Sedimentologists and igneous petrologists worked cooperatively to describe the core, and results are presented in **“Igneous lithostratigraphy, petrology, alteration, and structural geology.”**

Discussion

The foregoing results support preliminary interpretations of depositional and diagenetic environments. The interpretations that pertain to sediment accumulation and alteration in Units I–III warrant discussion and are listed below.

Sediment accumulation

By thickness and duration of sediment accumulation, the majority of sediment at Site U1368 is in Unit I. The lithologically similar calcareous oozes and marls of Unit I comprise >80% of the 12–15 m of sediment thickness and ~80% of the ~14 m.y. depositional history (see **“Paleontology and biostratigraphy”**). To the level of specificity afforded by our smear slide and X-ray analyses, the minerals that make up Subunits IA and IB are identical. The lithologic differences found in Unit I are caused by variations in the abundances of calcite, clay, and RSO. The RSO is particularly important because it is responsible for the dark reddish brown colors that

mark bedding features and because it is associated with slow rates of sediment accumulation (Heath and Dymond, 1977).

Although the abundance of RSO generally increases with depth, the trend has several notable deviations. First, RSO abundance does not increase at a constant rate; it experiences highs and lows that exist in layers ranging from 10 to 30 cm thick. Second, several beds (3–10 cm thick) of laminated foraminiferal silt are nearly devoid of RSO and have very low clay content. Third, the unit boundary between Subunits IA and IB is very thin (2–6 cm) but sharp and contains abundant RSO and indurated clay clasts (0.5–1 cm in diameter). Because seafloors are evolving environments responsive to internal and external processes, variations in RSO abundance are expected. However, the very low abundance of clay and RSO in the foraminiferal silt and dramatic abundance at the Subunit IA/IB boundary carries sedimentary and oceanographic implications briefly outlined in the following paragraphs.

The foraminiferal silt layers are devoid of clay and RSO. Options for limiting the clay content in mid-Pacific seafloor sediments include

1. Reducing the influx of atmospheric dust,
2. Prohibiting clay deposition by increasing the velocity of bottom currents, and
3. Outpacing clay accumulation by increasing surface productivity or combining two or more of these effects.

Option 1 is unlikely because reducing the influx of terrigenous clay should reduce overall sediment accumulation and thus promote greater RSO abundance in the foraminiferal silt layers. Option 2 follows similar logic and is therefore unsupported by the observed paucity of RSO in the silt layers. Therefore, we speculate that the foraminiferal silts correspond to episodes of increase biogenic flux and thus higher sediment accumulation rates, option 3.

The Subunit IA/IB boundary represents an event in which reduced sediment accumulation is inferred. The irregularity of this surface and abundance of indurated clay clasts may have resulted from prolonged bioturbation and not subsequent removal of previously deposited sediment (Stow and Lovell, 1979; Ekdale et al., 1984; Ujiie, 1984; Uchman, 2007). The great abundance of RSO in the sediment is consistent with very slow sediment accumulation rates (~0.001 m/m.y.). Preliminary shipboard biostratigraphy places this event between Miocene and Pliocene foraminiferal Zones M11/M10 (~12 Ma) and PL2/PL1 (5.8–4.3 Ma) (see **“Paleontology and biostratigraphy”**).

Lithologic alteration and diagenesis

Each stratigraphic unit at Site U1368 contains compositional and textural evidence of alteration and/or diagenesis. Alteration found in carbonate minerals and basalt is the most evident and is discussed below.

The most common biogenic constituents of the sediment at Site U1368 are calcareous nannofossils and microfossils. Spot checks of foraminiferal preservation found dissolution effects in the uppermost part of Unit I and extensive recrystallization in Unit III (see “[Paleontology and biostratigraphy](#)”). Alteration of fossils in Unit III included infilling of shell pores and entire shells with secondary calcite, zeolite, RSO, and hematite. Nannofossils in the lowermost sand appear only as outlines in carbonate masses that include the tests of dozens of organisms.

The lithic sand intervals in Unit III may have resulted from alteration of basaltic debris. Evidence supporting this interpretation includes (1) mineral constituency, (2) sharp contacts with the overlying and underlying clay layers, and (3) proximity (<2 m) to underlying basaltic basement. Each of these intervals possesses unique compositional and textural attributes. For example, the uppermost sand of Unit III consists of a series of indurated nodules with strong partings that correspond to weak zones of elevated clay content. Zeolite crystals are also common among its veins and pores. In contrast to the uppermost sand, the medial (green) sand is more uniform in texture and possesses a uniquely high abundance of chlorite. The lowermost (black) sand consists almost entirely of titanomagnetite, zeolite, and altered microfossils. Given that these three sand layers lie within approximately one vertical meter of each other, these compositional and textural differences are remarkable. Accurately identifying the origin of these lithologic differences requires detailed petrographic and geochemical analyses beyond the scope of our shipboard studies.

Interhole correlation

Lithologic units are correlated among holes at Site U1368 to facilitate the integration of physical properties, geochemical, and microbiological data. The stratigraphic correlation panel for Site U1368 is presented in Figure [F8](#). Correlations shown in this figure are based on a number of horizons with characteristic features, including

- High-amplitude natural gamma ray (NGR) responses from sediment between 0.1 and 0.25 mbsf (Fig. [F7](#)),
- The presence of phillipsite above 2 mbsf,

- Distinctive indurated clay clasts and abundant RSO at the Subunit IA/IB boundary,
- A dramatic color and textural change associated with the Unit I/II contact, and
- Unique sand lithologies in Unit III that permit each sand to be distinguished from one another.

Assuming subsea depths and coring intervals were recorded accurately and/or consistently, interhole correlation shows lithologic units at Site U1368 to generally thin to the south and east (Fig. [F8](#)). Comparison of the continuously cored intervals in Holes U1368B and U1368E illustrates this point. The total thickness of Unit I, for example, thins from 12.5 m in Hole U1368B to 10.4 m in Hole U1368E. Despite this change in thickness, the composition of Unit I changes very little; the two sites each possess the surficial NGR response, the phillipsite constituency near the top of the unit, the clay clast and RSO sequence in the middle of the unit, and the distinctive lower contact with Unit II. The difference in thickness is therefore associated with slight changes in sediment accumulation and not deposition of unique sedimentary units (i.e., mass wasting deposit) or postdepositional phenomena such as erosion or faulting.

Igneous lithostratigraphy, petrology, alteration, and structural geology

In Hole U1368F, basement was cored from 11.8 to 115.1 mbsf, of which 31.74 m was recovered (27.6% recovery).

The recovered basement at Site U1368 is predominantly composed of very fine grained (cryptocrystalline to microcrystalline) aphyric to phyric basaltic fragments that contain large quench structures and glassy margins. Several intervals contain larger in situ fragments that texturally exhibit similar features to the basaltic fragments. In addition, more massive microcrystalline aphyric to sparsely phyric intervals that resemble sheet flows were also recovered. One interval includes a hyaloclastite breccia composed of variably altered glass shards and basaltic fragments cemented in quartz. These lithologies were divided into 13 basement units based on changes in lava morphology, flow boundaries, the presence of pillow basalt textures, and phenocryst occurrence. The distribution of lithologic units is summarized in Figure [F15](#). Further detail regarding the definition of igneous units is reported in “[Lithostratigraphy, igneous petrology, alteration, and structural geology](#)” in

the “Methods” chapter (Expedition 329 Scientists, 2011a).

Basement Units 1, 3, 5, 7, 9, and 11 were interpreted to represent flowlike units. Units 2, 4, 6, 8, 10, and 12 are interpreted to represent variably fractured pillow lavas. No subunits were defined at Site U1368. The presence of pillow lavas at Site U1368 is discussed in “**Lithologic units.**” One volcanoclastic hyaloclastic breccia (Unit 13) was recovered at the base of the hole in interval 329-U1368F-14R-1, 43–150 cm, and is interpreted to represent a collapse event, in which partially altered glassy rinds and pillow basalt fragments were deposited into a topographic low. Samples of basement were also recovered in Holes U1368B and U1368D; however, their relationship with the units defined from the basement recovered in Hole U1368F is not known, and therefore we did not assign units to these samples. These samples include a glassy margin recovered in interval 329-U1368D-2H-CC, 0–8 cm, in which the glass is moderately altered with a few fresh glassy interiors exposed. In addition, basaltic samples within the core catcher are cryptocrystalline and aphyric, with pervasive alteration and a ropy pahoehoe texture, suggesting surface contact with cold seawater. In Holes U1368B–U1368D, basalt at the sediment/basement interface has been 100% altered to form dark green sand (see “**Lithostratigraphy**” for more details).

Lithologic units

Units 2, 4, 6, 8, 10, and 12 (fractured pillow lavas)

Fractured pillow lavas occupy 20.2 m (58.8% by volume) of the recovered core, making fractured pillow lavas the most abundant lava morphology at Site U1368. Classification of fractured pillow lavas was based on the presence of curved chilled margins and glassy rinds, conchoidal fracturing, abundant vesicles near the chilled margins, quenching structures that flank cooling fractures, and concentric cooling zones within some fragments (Figs. F16, F17). The basaltic groundmass is composed of plagioclase, clinopyroxene ± olivine, and Fe-Ti oxides. We observed subophitic, spinifex, and spherulitic textures. Phenocrysts of plagioclase and rare clinopyroxene are present in Units 2 and 4, with abundances from 0.1% to 3% by volume of the recovered core. Glassy margins are present throughout the fractured pillow lava units, most of which are either devitrified or slightly to moderately altered with saponite and iron oxyhydroxides. The distribution of fresh and altered glassy margins is shown in Figure F15. Alteration within Units 2, 4, 6, 8, 10, and 12 varies from very slight to slight. Many vesicles within the central portions of

the fragments are only partially filled by secondary minerals. Alteration is most pervasive within the spinifex and interstitial textures within the quench structures and glassy margins.

Units 1, 3, 5, 7, 9, and 11 (sheet and massive flows)

Sheet flows occupy 38 m (~38% by volume) of the recovered core and are the second most abundant lava morphology at Site U1368. Recovery of complete or near-complete flows occurred in Cores 329-U1365E-5R, 6R, 8R, and 12R. Classification was based on the presence of continuous sections of the same lithology, very slight coarsening of grain size away from the top of the flow, and vesicle variation within the lava flow. In terms of flow thickness, Units 1 and 3 are larger than Units 5, 7, 9, and 11, and they are tentatively classified as massive sheet flows. Units 1 and 3 share the same characteristics as Units 5, 7, 9, and 11; therefore, we group Units 1, 3, 5, 7, 9, and 11 as sheet flows. The sheet and massive flows are also noted for their low abundance of chilled margins.

The sheet and massive flows are aphyric, with groundmass composed of plagioclase, clinopyroxene ± olivine, and Fe-Ti oxides. Unit 3 contains rare (<0.2%) plagioclase phenocrysts that range from 0.1 to 0.4 mm in size. Major textural features within the lava flows vary from intergranular, subophitic, hyalophitic, and glomeroporphyritic. However, textural observations of thin sections include spinifex, spherulitic, ophitic, subophitic, hyalophitic, intersertal, and glomeroporphyritic textures. Grain sizes range from cryptocrystalline toward the flow margins to fine grained in the central portions of some flows. Vesicle abundance in the flow basalt units varies from none (Unit 3) to 10%; however, modal abundance is ~1%. Vesicle abundance within an individual flow unit varies from 0% to 10%, with most vesicles typically near the unit boundaries. Almost all vesicles are partially to completely filled with secondary minerals (see “**Basement alteration**”). Rare flow margins are usually altered and exhibit cryptocrystalline and sometimes glassy textures.

Alteration within the sheet and massive flows is generally slight but ranges from very slight to moderate. Alteration may include groundmass replacement, vesicle fill, veins, halos, and alteration patches (see “**Basement alteration**”). Unit 1 is the most pervasively altered, with a gray-brown background that shares some similarity to the obliterated basaltic sediment in Core 329-U1368B-2R (Fig. F18). Although no real changes in alteration were observed near the top or base of the flow units, the actual contacts were not recovered, implying that alteration may be

under-represented. The flows within Units 7, 9, and 11 contain large brown alteration halos that relate to steeply dipping curved fractures. The more massive flow within Units 1, 3, 5, 7, 9, and 11 are better recovered than the fractured pillow lava units, with many more oriented individual pieces than the fractured pillow lavas (Units 2, 4, 6, 8, 10, and 12).

Unit 13 (volcaniclastic breccia)

The lowermost 1.07 m (3.1%) of Hole U1368F is volcaniclastic breccia that consists of partially to completely altered glassy clasts and altered basaltic clasts with quartz cement. Alteration of the glassy clasts gives this breccia a characteristic pale orange-brown color. The breccia is described in greater detail in “[Basement alteration](#).”

Igneous petrology

As described above, the basaltic rocks recovered from Hole U1368F are divided into massive sheet flows and thin basalt flows. A total of 18 samples were selected for petrographic analyses by thin section (see Site U1368 thin sections in “[Core descriptions](#)”).

Sheet and massive flow basalt

The mineralogy of the sheet and massive flow units at Site U1368 (Units 1, 3, 5, 7, 9, and 11) is typical of seafloor basalt. The groundmass is composed of plagioclase (58%–75%), clinopyroxene (26%–35%), Fe-Ti oxides (2%–5%), and rare olivine (approximately <1%). The plagioclase typically forms bladed crystals that are intergrown with anhedral to subhedral clinopyroxene and Fe-Ti oxides (titanomagnetite). Overall grain size of the groundmass ranges from cryptocrystalline to microcrystalline, and the most common textures are intergranular and subophitic to hyalophitic. The sheet flows identified at Site U1368 show no variation in grain size from the top to the center to the bottom of the units. Only Unit 3 contains some minor plagioclase phenocrysts (0%–0.2% modal abundance) only plagioclase and rare clinopyroxene phenocrysts are present. Plagioclase is blocky to prismatic and ranges in size from 0.2 to 0.8 mm. Clinopyroxene crystals are lathlike to prismatic and range in size from 0.2 to 0.6 mm. Olivine is rare and only observable as saponite/iddingsite pseudomorphs recognized by a rough, six-sided outline. Some pseudomorphs of olivine are identified by the presence of sphene intergrown contemporaneously with olivine prior to replacement of the olivine by saponite/iddingsite.

Vesicle abundance within the flow units varies from 0% to ~11%. Vesicle morphology is rounded, sub-

rounded, angular, and interconnected. In Units 1, 5, and 11, vesicles are concentrated near the top of the units, whereas vesicles in Unit 7 are concentrated in the middle portion. Unit 9 contains no vesicles. Vesicles vary from 0.1 to 3 mm in diameter; most are ~0.4 mm wide. Vesicles are predominantly filled with silicates, zeolite, celadonite, and iron oxyhydroxides. Less common vesicle fillings include saponite, calcite, and pyrite. The secondary mineral fills of vesicles are discussed in “[Basement alteration](#).”

Fractured pillow basalt

The fractured pillow basalt of Units 2, 4, 6, 8, 10, and 12 has groundmass compositions that are typical of seafloor basalts. Plagioclase and clinopyroxene are the most abundant primary mineral phases. Minor phases include Fe-Ti oxides (titanomagnetite), rare olivine, and sphene. Primary igneous textures and mineralogical differences within the lava are defined by the rapid nature of cooling, including glassy margins, quench structures, and changes in crystal size. Grain size ranges from microcrystalline to glassy; most of the fractured pillow basalt, especially within the chill margins, is cryptocrystalline to glassy. The most common textures observed include intergranular, spinifex, and porphyritic. Other textures observed include glomeroporphyritic and spherulitic. Within chilled margins, grain size is irregular, with patches of glassy and spinifex textures surrounded by cryptocrystalline to microcrystalline intergranular and glomeroporphyritic groundmass.

Units 6, 8, 10, and 12 are aphyric, whereas phenocryst abundance in Units 2 and 4 ranges from 0.1% to 3%. Phenocrysts in Unit 2 are composed of plagioclase (75% of phenocrysts) and clinopyroxene (25% of phenocrysts), with crystal sizes ranging from 0.2 to 2 mm (mode = 0.8 mm) and 0.2 to 0.8 mm (mode = 0.4 mm), respectively. Plagioclase is relatively fresh with crystal shapes that range from prismatic to blocky and having endured only minor corrosion around the edges and partial replacement by saponite. Clinopyroxene is subhedral to blocky and has endured slightly greater alteration to saponite than plagioclase. Phenocrysts in Unit 4 are very similar to those in Unit 2 but range in crystal size from 0.2 to 1 mm (mode = 0.4 mm) for plagioclase and 0.3 to 0.5 mm (mode = 0.4 mm) for clinopyroxene. Rare altered olivine phenocrysts are also present. Glassy margins range from fresh to slightly altered, whereas overall alteration within Unit 1 is slight. Small portions of each fragment contain brown and dark gray complex halos that propagate inward from the fracture and chill margins. These alteration halos are not to be confused with the large chilling margins,

which are dark and have a sharp front when viewed in hand specimen. Alteration is discussed in more detail in “**Basement alteration.**”

Phenocryst phases

Plagioclase

Although plagioclase phenocrysts at Site U1368 are present only in Units 2, 3, and 4, they remain the most abundant phenocryst phase. Plagioclase phenocrysts make up <0.1% of the sheet and massive flows and 0.2% of the fractured pillow lavas. Their shape ranges from subhedral to euhedral and is commonly blocky to prismatic. Bladed and acicular plagioclase phenocrysts are also observed. Plagioclase phenocrysts range from 0.1 to 2 mm in length, with most between 0.1 and 0.8 mm long. Rarely, plagioclase forms skeletal or quench plagioclase crystals within the pillow lava units (Figs. F19A, F19B) and zoning of plagioclase occasionally occurs in the larger phenocrysts (Fig. F19B). Although plagioclase phenocrysts are typically fresh or very slightly altered, replacement by secondary minerals can vary from 0% to 50%. Replacement minerals that include clays, saponite, and iron oxyhydroxides occur along cracks, cleavage planes, or crystal edges. In addition, secondary Fe-Ti oxides occasionally form around the edges of some plagioclase phenocrysts.

Pyroxene

Clinopyroxene phenocrysts are present throughout the Site U1368 basalt but make up <0.1% of the recovered core. These phenocrysts range from 0.2 to 1 mm in length, although most are 0.2 to 0.4 mm long. They are typically anhedral to subhedral and either irregular, prismatic, or lathlike, with simple basal twinning present throughout. Clinopyroxene is typically intergrown with plagioclase in glomerophyritic clots or as subophitic to ophitic crystals around plagioclase (Figs. F19C, F19D). Alteration of clinopyroxene varies from 0% to 80% and manifests as replacement by secondary clays, saponite, iron oxyhydroxides, and oxides along cracks, cleavage planes, or crystal edges.

Olivine

Fresh olivine is extremely rare, and olivine pseudomorphs make up <0.01% of the recovered material. Olivine phenocrysts are, on average, 0.4 mm wide and blocky to prismatic in shape. They are almost always completely replaced by secondary minerals (Fig. F20), including saponite, celadonite, iddingsite, and opaques (sphene and Fe-Ti oxides). Olivine's identification, therefore, relied on crystal morphology (subhedral to euhedral) and textural relationships with surrounding minerals. Additionally, the

presence of sphene next to phenocryst pseudomorph is used as an indicator of olivine.

Groundmass

The basaltic groundmass at Site U1368 varies from hypocrystalline to holocrystalline and is composed primarily of plagioclase and clinopyroxene with minor accessory Fe-Ti oxides. Olivine in the groundmass is extremely rare. Plagioclase is the most abundant groundmass crystalline phase, comprising between 58% and 70% of the groundmass; it occurs as microlaths, microlites, acicular crystals in a spinifex texture or microcrysts in chill margins. Within chilled margins and alteration halos, plagioclase may be partially corroded by secondary mineral phases.

Clinopyroxene comprises between 25% and 30% of the pillow lavas and 30% and 35% of the flow units. It occurs as interstitial growths between plagioclase, microlaths, microlites, and aggregates of fibrous or plumose crystals. Anhedral to subhedral microcrysts of pseudomorphed olivine are very rare within the massive lavas and thin basalt flows. The lack of fresh olivine and the difficulty in identifying olivine pseudomorphs (based on relict crystal structure) hampers efforts to estimate its abundance; however, our observations imply that it occupies <0.1% of the recovered core.

Mesostasis in Hole U1368F ranges from 0.5% to 20% by volume. Mesostasis textures include hyalophitic and intersertal. These textures are present throughout the recovered basement but are most common within quenching structures and chilled margins. Spherulitic and variolitic textures are most common in the thin basalt flows and close to chill margins. Mesostasis is typically subject to patchy alteration, in which it is preferentially altered relative to the plagioclase and clinopyroxene groundmass. Almost all patchy alteration observed at Site U1368 is the result of altered mesostasis. Replacement minerals in the groundmass include clay (saponite and celadonite), iron oxyhydroxides, and, rarely, carbonate. Primary magmatic opaques (<1%–4%) are present in all units. These form small (<0.2 mm), granular, subhedral crystals of sphene and secondary hematite and titanomagnetite.

Hard rock geochemistry

Twenty-three representative samples of the basaltic basement and one whole breccia sample were analyzed for major and trace elements using a Teledyne-Leeman (Prodigy) inductively coupled plasma-atomic emission spectrometer (ICP-AES). Analyses were carried out in the same way as for samples from Sites U1365 and U1367. Samples analyzed from Site U1368 include relatively unaltered basalt ground-

mass (gray to green) and variably altered halos (red to brown). The least altered samples were chosen based on (1) the lowest abundance of secondary mineral phases present in thin section and (2) the least number of veins, halos, and filled vesicles. Altered samples were chosen so that each alteration phase is represented. Details of the methods for preparation and analyses are given in “[Lithostratigraphy, igneous petrology, alteration, and structural geology](#)” in the “Methods” chapter (Expedition 329 Scientists, 2011a). International Standard BCR-2 was analyzed 24 times over 3 runs. Analytical precision and accuracy is reported in Table T2 in the “Methods” chapter (Expedition 329 Scientists, 2011a).

Results

Major and trace element data and loss on ignition (LOI) for the selected samples are shown in Table T2. For all basaltic samples, the ranges of major element oxides include

SiO₂ = 45.6–52.6 wt%,
 Al₂O₃ = 13.1–17.2 wt%,
 Fe₂O₃^(T) = 8.9–15.4 wt%,
 MgO = 4.9–14.8 wt%,
 Na₂O = 2.4–3.2 wt%,
 TiO₂ = 1.47–2.26 wt%, and
 K₂O = 0.14–0.76 wt%.

Trace element ranges and averages include

Sr = 117–376 ppm (average = 172 ppm),
 V = 208–479 ppm (average = 379 ppm), and
 Zr = 113–172 ppm (average = 149).

Trends in least altered basalt

Twelve least altered samples that ranged in color from gray to gray/green were selected, based on their low abundance of secondary minerals, for primary whole-rock chemical analyses. Total alkaline (K₂O + Na₂O) concentration ranges from 2.94 to 3.56 wt%, and SiO₂ concentration ranges from 49.6 to 52.6 wt%. Al₂O₃ ranges from 13.1 to 14.9 wt%, and CaO ranges from 9.9 to 11.9 wt%.

Vertical distribution of major and trace elements for all samples, including alteration halos and breccia, is shown in Figure F21. Tie lines are included to indicate halo/background pairs. The altered rocks on this plot are discussed in “[Lithostratigraphy, igneous petrology, alteration, and structural geology](#)” in the “Methods” chapter (Expedition 329 Scientists, 2011a). Only the background and least altered rocks are described below. Overall geochemical trends for Site U1368 basement indicate increasing MgO and possibly increased Fe₂O₃^(T) with depth and decreased K₂O with depth. The basalt samples from the upper-

most 10 m of basement appear to show markedly different chemistry relative to the rest of the basalt, with notably lower Fe₂O₃^(T) and TiO₂ and higher Sr and LOI than the rest of the basalt. In addition, in these samples from the uppermost 10 m both one of the least altered samples and two altered samples are strongly enriched in MgO compared to the rest of the basement. Although the basaltic clast sample (329-U1368F-14R-1, 141–142 cm) compositionally behaves similarly to the other whole-rock samples, the presence of halos indicates that this sample was subject to alteration.

On plots of MgO versus Na₂O, Fe₂O₃^(T), TiO₂, and K₂O for the least altered samples (Fig. F22), increasing Na₂O, TiO₂, and K₂O may indicate primary magmatic evolution. However, Fe₂O₃^(T) exhibits no distinctive trends. K₂O/TiO₂ for the least altered basalts at Site U1368 ranges from 0.063 to 0.179 and falls within the accepted range for depleted basaltic compositions. All trends observed in Figures F21 and F22 provide limited insight into the primary magmatic evolution of the basement at Site U1368. Because all rocks at Site U1368 are altered (especially the uppermost 10 m of basement), the deviation from the primary igneous chemistry remains uncertain. The extent to which downhole variation in chemical composition of these least altered samples is due to magma evolution or basalt alteration will be addressed by postexpedition research.

Basement alteration

All basement rocks at Site U1368 have been subjected to alteration by interaction with seawater. Alteration varies from slight to high. However, the majority of recovered basement material at Site U1368 is only slightly altered. Basement alteration at Site U1368 consists of

- Replacement of phenocrysts by secondary mineral assemblages,
- Replacement of mesostasis in the groundmass by secondary minerals,
- Filling of veins and the formation of halos by emplacement of secondary minerals, and
- Lining and filling of vesicles.

Visible alteration in macroscopic view or thin section constitutes between 2% and ~60% of individual samples, with most alteration concentrated around veins and vesicles. The most intense alteration is present within chilled margins and the volcanoclastic breccias, where alteration can be nearly complete. Alteration products include saponite, celadonite, iron oxyhydroxides, quartz, carbonate, and accessory zeolite (laumontite by XRD) and sulfides (chalcopyrite and pyrite).

Secondary minerals were identified by macroscopic observation and thin section observation. XRD analyses were carried out on two samples at this site, the results of which are shown in Figure F22. Clay minerals are predominantly in the saponite group or celadonite group and were distinguished by color variations.

Saponite is present throughout the recovered core. In macroscopic observation, it is black, dark green, greenish brown, or pale blue. In thin section, it is characterized by pale brown color and it may be mottled, fibrous, or botryoidal in form. Replacement of the groundmass is usually even and slight, only replacing olivine mesostasis and some of the groundmass. In areas of moderate alteration, saponite replaces mesostasis and a varying proportion of groundmass crystals. High to completely altered basalt exhibits continuous mottled replacement, destroying most or all original textures. Saponite also frequently fills vesicles, forms monomineralic or polymineralic veins, and variably alters glass within the volcanoclastic breccia.

Celadonite is present throughout the recovered basement and is the next most common secondary mineral at Site U1368 after saponite. In hand specimen and thin section, celadonite is bright green/blue. It fills veins and vesicles and replaces primary interstitial zones in basaltic groundmass to form a pervasive dark gray to dark green background.

Iron oxyhydroxides are present throughout the recovered core. However, they are less abundant than celadonite. They occur alone or, more commonly, intermixed with saponite, imparting red, brown, and orange-brown staining. They are identifiable by a bright red-orange color and they often stain other secondary mineral phases (e.g., saponite stained by iron oxyhydroxide becomes brown/red-brown). In addition, iron oxyhydroxide typically replaces phenocrysts as a mixture with saponite (iddingsite) to form a hyalophitic texture. Iron oxyhydroxides may also fill or partially fill veins and they commonly form iron oxyhydroxide-dominated halos.

Less dominant secondary minerals at Site U1368 identified by XRD (Fig. F23) include stevensite, zeolite (laumontite and phillipsite), and clay (montmorillonite and sepiolite). Carbonate at Site U1368 is relatively uncommon with only a few veins present in Cores 329-U1368F-2R, 3R, 9R, and 10R. Pyrite was observed only in one vein in interval 329-U1368F-5R-2, 26–31 cm. Pyrite was identified by macroscopic and microscopic observation (gold in hand specimen and bright yellow in reflected light) and partially fills vesicles, veins, and patches. The crystal structure of pyrite at Site U1368 ranges from blocky to irregular.

Alteration features within the basement at Site U1368 are described below in order of alteration intensity. At Site U1368, breccia exhibits the greatest degree of alteration, albeit at only one very concentrated zone at the bottom of Hole U1368F (see below). The most pervasive forms of alteration at Site U1368 are halos and veins. Like the alteration at Sites U1365 and U1367, halos and veins represent the evolution of low-temperature secondary mineral emplacement within the basalt. Although vesicle fill is the least pervasive form of alteration at Site U1368, it provides a clear indication of the relative timing of secondary mineral emplacement; as such, it is described separately.

Breccias

One breccia unit (Unit 13) was recovered at the very bottom of Hole U1368F at interval 329-U1368F-14R-1, 43–150 cm. The breccia is a volcanoclastic hyaloclastite that comprises 3.1% of the total recovered rock at Site U1368. Given that core recovery is 26.3% and rheologically stronger units (sheet flows and massive flows) are preferentially recovered, it is likely that the recovered breccia percentage underestimates the true proportion of brecciated basement at Hole U1368F.

The hyaloclastite at interval 329-U1368F-14R-1, 43–150 cm, consists of variably altered glassy and basaltic clasts encased in quartz cement. Variably altered glass makes up 90% of the clasts, which range in size from 0.1 to 8 mm with most clasts between 1 and 3 mm in size. Basaltic fragments make up 10% of the clasts and range from 0.1 to 39 mm in size, although the typical size range is 1 to 15 mm. Clasts make up 80% of the total volume of the breccia, whereas quartz and void space between the clasts each contribute 10% to the total breccia volume. All clasts within the breccia are angular and poorly sorted. Steeply dipping grading of some clasts is present, in which the clasts vary from coarse to fine (Fig. F24).

Alteration of the breccia is dominated by variable alteration within the glassy clasts and quartz cement. Glassy clasts exhibit zoned alteration with highly altered brown to orange saponitic zones on the outside edge and a less altered zone in the center (Fig. F24). Many of the larger glass clasts contain a fresh, unaltered glass interior (fresh glass makes up ~15% of the total breccia). The basaltic clasts resemble the fractured pillow lavas, such as Units 4 and 12, in that they are cryptocrystalline and aphyric and contain chilled margins and quench structures. Alteration of the basaltic clasts ranges from slight to moderate. They are characterized by brown to dark gray altera-

tion halos within the quench structures and flanking microveins of celadonite, saponite, and iron oxyhydroxide. Halos appear to terminate abruptly at the edge of some larger clasts. In addition, relatively fresh portions of basaltic clasts are adjacent to the cement. These observations suggest that alteration within the larger basaltic clasts took place prior to brecciation. Smaller (<10 mm) clasts are all highly altered to saponite, secondary silicates, and iron oxyhydroxides; however, the timing of alteration relative to brecciation within the smaller clasts is not known (Fig. F24).

The highly angular nature of the clasts combined with steeply dipping particle gradients and the lack of alteration within the larger basaltic and glassy clasts suggests that the breccia represents infill from collapse from higher ground. The presence of nearby seamounds and the variable depth at which basement was tagged in Holes U1368A–U1368E (see “[Lithostratigraphy](#)”) imply that the bottom surface topography is irregular, further increasing the likelihood of breccias forming by collapse of nearby pillow lavas. In addition, two thin (1 mm) lamellae of sediment are present at intervals 329-U1368F-14R-1, 125–125 cm, and 14R-1, 133–133 cm, and imply that brecciation was not a single event and that there was elapsed time between successive lava collapses.

Vein- and halo-related alteration

Vein- and halo-related alteration at Site U1368 is similar in style to that of Site U1365, albeit with notably less abundant carbonate veins. Similarities include the presence of dark gray/brown saponitic and celadonitic background alteration throughout recovered basement and the presence of monomineralic and polymineralic veins flanked by variably colored alteration halos. Veins may contain any combination of the secondary minerals saponite, celadonite, iron oxyhydroxides, and silicates (quartz and chalcidony). Less common vein-filling phases include carbonate (calcite and aragonite), zeolite (possibly laumontite or phillipsite), and secondary sulfides (pyrite). Alteration halos at Site U1368 share the same nomenclature and styles as those from Site U1365. Alteration halos along the vein margins at Site U1368 include dark green/black halos, green/brown halos, and mixed halos. The most abundant halo type is dark gray/green halos, followed by red-brown to orange-brown halos. Red halos and complex (mixed) halos are the least common and primarily occur near chilled margins within the fractured pillow lava units and occasionally near veins. Halos and veins are discussed in detail below.

Halos

Dark green/black halos are present throughout the basaltic basement of Site U1368, flanking veins and fractures as individual halos and as part of mixed halos (Fig. F25). Dark halos range in width from 1 to 20 mm but are most commonly 1 to 10 mm wide. Secondary mineral abundance in the dark green/black halos is slightly greater than in the gray background basalt, with celadonite replacing olivine and interstitial material and filling vesicles. Like at Sites U1365 and U1367, celadonite is identified by its green color in thin section or its blue-green color and brittle texture in hand specimen; it typically replaces between 2% and 5% of the rock within the halo. As with celadonite observed at Sites U1365 and U1367, this phase may either be celadonite, nontronite, or a mixed-layer celadonite-nontronite. Therefore, detailed postcruise XRD analyses will be required to further refine our mineral definitions. Within these halos, saponite is occasionally observed replacing olivine, interstitial material, and vesicles, as well as overprinting celadonite. Vein- and vesicle-filling sequences (discussed later) indicate that the saponite phase arrived after celadonite. Iron oxyhydroxides may also be present in small amounts.

Green/brown halos occur throughout the recovered basalt at Site U1368. However, the greatest intensity of these halos occurs at the top of the basaltic basement, in Cores 329-U1368F-2R and 3R. Although green/brown halos range in width from 1 to 20 mm, the majority range from 1 to 13 mm. These halos are typically associated with saponite veins, but they also flank polymineralic veins and veins of celadonite, iron oxyhydroxides, and/or carbonate (Fig. F24). Thin section observation indicates that the dominant secondary mineral is saponite, which is green to brown in plane-polarized light and dark green/brown in hand specimen. Saponite fills vesicles and replaces olivine phenocrysts and interstitial material. Overall, saponite replaces between 3% and 80% of the rock within the halo. Most halos, however, exhibit only slight to moderate replacement (3%–20% replacement by saponite). Iron oxyhydroxides that stain the saponite to an orange-brown color are frequently present within these halos. Iron oxyhydroxide covers between 0.5% and 2% of the rock within the halo. One example of a brown saponitic halo sequence exhibits multiple banding in which the iron-rich saponite has formed concentric halos within coarser grained bands (Fig. F17) of the groundmass. Red halos represent any halo in which iron oxyhydroxides are the dominant mineral.

Other mineral phases that are sometimes present include saponite and celadonite. At Site U1368, iron

oxyhydroxide-dominated halos are not common and most “red” halos actually contain iron-rich saponite. Iron oxyhydroxide halos occur in greatest concentrations at the top of the basalt in Hole U1368F; in the rest of the core, only discrete iron oxyhydroxide patches and individual crystals are present. Approximately 1% of the rock within the halo is composed of iron oxyhydroxides, which fill vesicles, replace olivine, and fill interstitial areas. An example of an iron oxyhydroxide halo is shown in Figure F25. In a style similar to the oxidation halos at Site U1365, iron oxyhydroxide occurs as narrow strands that propagate between individual grain boundaries, staining the background rock to form the halo. Red halos range in thickness from 0.5 to 5 mm. Halo margins are typically irregular and diffuse, with iron oxyhydroxide forming concentrated zones within the halo. Red halos are typically associated with veins of iron oxyhydroxide or iron oxyhydroxide and celadonite, but they can also flank saponite and carbonate veins.

Mixed halos are uncommon at Site U1368, but they are evenly distributed throughout the recovered core. Mixed halos are typically found flanking multi-mineralic veins. However, they are also found flanking veins observed to contain only carbonate and quartz. Careful observation of core samples and thin sections reveals that mixed halos are the result of overprinting by green/brown halos over dark green/black halos (Fig. F25). Mixed halos range in width from 3 to 20 mm but are usually between 5 and 10 mm wide, and the mineralogy of each individual halo within each mixed halo essentially falls into any one of the dark green/black, red, or green/brown halo categories. However, because of overprinting, typically the innermost halo contains mineralogy that relates to two or more alteration phases; therefore, the coloration is mixed. As with the simple “single alteration phase” halos, the intensity of coloration reflects the level of alteration. In mixed halos, the dark green/black celadonitic halos are partially to completely overprinted by iron-rich saponite and often have indistinct or diffuse boundaries. In most mixed halos, only discrete patches of celadonite remain. In a number of mixed halos, earlier sequences are overprinted by later alteration halos that extend well beyond the boundary of the previous halo.

Veins

A total of 308 veins were identified in the basement core recovered from Hole U1368F with an average density of 10 veins/m of recovered core. Vein fill makes up 0.16% by volume of recovered core. Vein thickness varies from <0.1 to 4 mm, although the

thickness of most veins is in the 0.1–1 mm range. Vein morphology observed in basement at Site U1368 exhibits planar, straight, curved, branching, anastomosing, kinked, sinusoidal, and irregular forms. Secondary minerals that fill veins include saponite, celadonite, iron oxyhydroxides, carbonate, and accessory phases (other unidentified clays, quartz, chalcedony, zeolite, and secondary sulfides). Veins may be monomineralic or polymineralic with any combination of the major secondary minerals. Veins may be flanked by alteration halos or may simply penetrate the groundmass with no alteration halo. Crosscutting relationships and vein-filling orders, relative to each vein mineral, are described below.

Iron oxyhydroxide is by far the most abundant secondary mineral at Site U1368. By volume, it makes up 56% of the vein fill and 0.09% of the recovered rock. Iron oxyhydroxide veins range from <0.1 to 4 mm thick (0.3 mm thick on average). Although a number of veins are exclusively iron oxyhydroxide (e.g., in Fig. F26), most iron oxyhydroxide is present with saponite and celadonite. Iron oxyhydroxide is typically overprinted or crosscut by saponite and, rarely, calcite; however, it is often overprinted or intergrown with celadonite. Iron oxyhydroxide is present throughout Hole U1368E. Although iron oxyhydroxide is most abundant in Core 329-U1368F-2R, the overall trend is toward increasing iron oxyhydroxide abundance downhole.

Celadonite is the next most abundant vein-filling mineral, filling 16% of the total veins and forming 0.03% by volume of the recovered core. Celadonite-filled vein thicknesses vary from <0.1 to 2 mm. However, most celadonite veins are between <0.1 and 0.4 mm thick. Pure (100%) celadonite veins tend to be narrow (<0.1–0.3 mm thick). Most celadonite veins are either intergrown with or overprinted by iron oxyhydroxides. In addition, celadonite is overprinted by saponite and carbonate. In many veins, only discrete patches of celadonite remain. Celadonite was identified in thin section by its green color and in hand specimen by its blue-green color and brittle texture. XRD analyses of celadonite indicate intergrowths of saponite.

Saponite is present throughout the basalt of Site U1368, albeit at much lower abundance than iron oxyhydroxide and celadonite (just 0.003% by volume of the core). Saponite-bearing veins range from <0.1 to 0.8 mm thick and their thickness averages ~0.21 mm. Although saponite is observed to occur with every other secondary mineral, it is most commonly associated with iron oxyhydroxides. Saponite typically crosscuts celadonite and iron oxyhydroxide and is itself crosscut by rare carbonate and zeolite.

XRD analyses of a saponite vein indicate a trioctahedral smectite structure. The brown-red color of saponite at Site U1368 indicates that it is iron rich.

Carbonate veins make up 5.5% of all veins and 0.01% of the total volume of recovered core. Carbonate is present in its own veins; crosscutting celadonite, iron oxyhydroxide, and saponite; or, more frequently, as a late-stage infill in polymineralic veins (Fig. F26). The proportion of carbonate in a given polymineralic vein ranges from trace to almost 100%. In almost all situations where overprinting/replacement relationships can be discerned, carbonate replaces all other major secondary phases. Veins bearing carbonate can be as thin as <0.1–2 mm. Most 100% carbonate veins are not flanked by halos. A number of vertical to subvertical veins with only carbonate infilling occur with no halos. These veins usually have no halos flanking them and they appear to crosscut all other subhorizontal veins, including carbonate. The majority of the carbonate veins are present near the top of Hole U1368F (Core 329-U1368F-2R).

Quartz, zeolite, and pyrite make up the remainder of the vein-filling minerals, with each comprising 3.6%, 0.27%, and 0.1% of the total vein-filling mineral percentage, respectively. Although a number of quartz-only veins are present, these minerals typically make up discrete portions of polymineralic veins. Quartz appears to crosscut celadonite and iron oxyhydroxides, making it one of the last phases to precipitate. The timing of emplacement for zeolite and pyrite was not ascertained because of a dearth of crosscutting features. Examples of these secondary minerals are shown in Figure F26.

Vesicles

All units from Hole U1368F contain vesicles, which vary in abundance from <0.1% to 10%. Most vesicles at Site U1368 are partially filled, with secondary minerals lining the inside edge of the vesicle; these vesicles are typically found in the central portion of recovered pieces. Totally filled or near-totally filled vesicles typically occur within alteration halos and chilled margins near fractures. Secondary mineral fill consists of celadonite, iron oxyhydroxides, saponite, zeolite, silicates, and calcite, in order of occurrence. On both a unit scale and a piece scale, the variability of vesicle-filling minerals is high, with the typical assemblage of each unit containing several different secondary minerals. Zeolite-filled vesicles are exclusively present near the top of the hole. Vesicles within alteration halos are usually filled with the dominant phase of that halo (e.g., iron oxyhydroxides in a red halo). However, earlier fill (lining at the edge of a vesicle) may also be present (Fig. F27). In

order of filling, common mineralogical relationships within polymineralic vesicles observed at Site U1368 are

1. Celadonite, saponite, and calcite;
2. Iron oxyhydroxide, celadonite, and calcite;
3. Saponite and iron oxyhydroxide;
4. Iron oxyhydroxide and calcite;
5. Iron oxyhydroxide and saponite; and
6. Iron oxyhydroxide, zeolite, celadonite, and calcite.

The high variability of vesicle fill history and vesicle fill distribution indicates that continuous, localized fluid evolution and secondary mineral emplacement has taken place. The lack of vesicle fill in the central portions of much of the recovered core indicates relatively limited alteration extent. This limited extent of alteration is in contrast to vesicles observed at Sites U1365 and U1367, where vesicles are almost always filled. Within a number of examples, for example in interval 329-U1368F-12R-1, 2–3 cm (Fig. F27C), saponite appears to precipitate before iron oxyhydroxides.

Compositional comparison of alteration features to least altered material

A suite of 12 samples, including one whole-rock breccia and one basaltic clast, was selected for shipboard study of compositional alteration at Site U1368. The ICP-AES results are presented in Table T2. The altered samples were selected based on visual observation of secondary minerals within the groundmass, either as alteration halos or as alteration present within the groundmass. Samples were also selected adjacent to samples of least altered background; comparisons of these “pairings” are discussed in this section.

Ranges and averages of some key elements for altered samples include

Fe₂O₃^(T) = 10.37–14.38 wt% (average = 13.65 wt%),
 MgO = 4.94–14.83 wt% (average = 6.70 wt%),
 CaO = 8.14–11.98 wt% (average = 10.49 wt%),
 K₂O = 0.33–0.76 wt% (average = 0.55 wt%),
 TiO₂ = 1.51–2.21 wt% (average = 1.99 wt%), and
 Sr = 117–376 wt% (average = 164 wt%).

Overall differences between the ranges and averages of the altered and the least altered basalt are relatively small. On average, there is an overall increase from least altered basalt to altered basalts in Fe₂O₃^(T), MnO, K₂O, and LOI. Overall, on average, decreases occur in SiO₂, Al₂O₃, MgO, Ca, Co, and Sr. These average differences between least altered and altered basalt may reflect variable replacement of groundmass by secondary minerals and scavenging of metals (including Fe, Al, and Mg) to form secondary

minerals within veins. Examples of possible mechanisms include corrosion and/or replacement of titanomagnetite to supply iron oxyhydroxides and alteration of plagioclase and clinopyroxene to release SiO₂, Al, and Mg to form saponite in veins.

The decrease in Mg in the more altered samples and lack of observed change in Ca suggest that Ca/Mg exchange between seawater and wall rock has been either modest but pervasive in the recovered basalt.

For basic assessment of elemental mobility within the whole rock, 10 of the alteration halo samples were selected to have direct contact with a measured least altered background. Changes of all the sample pairs are shown as ratios of altered versus unaltered (Fig. F28). Values that are greater or less than 1 (outside of error) indicate chemical change. All altered samples exhibit increased K₂O and Fe₂O₃^(T) and most exhibit variable increases in MnO₂ and LOI compared to the least altered portion of the whole rock. Observed decreases include variably decreased Ba (despite large error), Cu, Ni, and SiO₂. The increases in Fe₂O₃^(T), MnO₂, K₂O, and LOI may reflect the incorporation of secondary minerals (saponite, celadonite, and iron oxyhydroxides) that contain Fe, Mn, K, and LOI into the groundmass.

The reduction in MnO₂ in Samples 329-U1368F-9R-1, 54–65 cm, versus 9R-1, 42–53 cm, and 11R-1, 65–67 cm, may have resulted from either Mn scavenging from primary oxides within the groundmass followed by subsequent precipitation within veins and fractures or variation in primary composition on a scale larger than that of the sample. The changes observed in the chilled margin sample (329-U1368F-7R-1, 31–36 cm) are similar to those observed within the alteration halos, which suggests that chilled margins are more susceptible to alteration effects than the interiors. The relatively altered sample pairs are plotted as concentrations versus depth in Figure F21. Vertical variation of chemical change is variable, with overall decreasing Fe₂O₃^(T) and K₂O enrichment. MgO and TiO₂ exhibit relatively similar changes. In all plots on Figure F21, breccia exhibits the greatest alteration with very high concentrations of Fe₂O₃^(T) (17.21 wt%), K₂O (3.65 wt%), TiO₂ (2.42 wt%), and LOI (10.9 wt%). These values reflect the high to intense replacement of the glassy clasts to saponite and other clay minerals. Although these high values are in contrast to the least altered samples and the basaltic clast sampled at Site U1368, the origin of the basaltic clasts and, therefore, the chemical relationship between the breccia and the rest of the basement remains uncertain.

Overall, the relative changes observed between altered samples and least altered samples are consis-

tent with (1) incorporation of the secondary minerals saponite, celadonite, and iron oxyhydroxides and (2) partial chemical exchange with the basement. The high variability of trends associated with alteration suggests that alteration varies on a localized scale. The level of uncertainty of LOI means that only the largest changes are detected. It is possible that all rock at Site U1368, including the least altered rock, has undergone some degree of alteration; however, detailed postexpedition work will be required to fully compositionally characterize rock alteration at Site U1368.

Alteration summary

Alteration extent was recorded by visual observation from core descriptions and by NGR logging (using NGR-based potassium concentration as a proxy for alteration extent). The style of low-temperature hydrothermal alteration at Site U1368 is similar to that of Site U1365, albeit at a lower intensity (lower volumes of halos and veins), but higher than that of Site U1367. Given that basement at Sites U1368 and U1367 is poorly recovered (26.3% and 11.2%, respectively) when compared to Site U1365 (74.6%), any comparisons of overall alteration intensity must be treated with caution. Alteration intensity at Site U1368, as measured by visual observation and NGR potassium content, is greatest in the top (Core 329-U1368F-2R) and bottom (Cores 12R and 13R) cores.

Similar to alteration observed at Sites U1365 and U1367, alteration at Site U1368 can be divided into two components: (1) open circulation of seawater causing oxidative alteration and (2) restricted fluid circulation giving rise to oxygen-starved alteration (Laverne et al., 1996; Teagle et al., 1996; Teagle, Alt, Umino, Miyashita, Banerjee, Wilson, and the Expedition 309/312 Scientists, 2006). Secondary minerals iron oxyhydroxide and celadonite are typical of oxidative alteration, whereas the presence of saponite and minor secondary sulfides suggest oxygen-poor alteration. It is not yet clear how these stages are distributed within the basement. However, observations of individual veins and halos indicate that, at least on a local level, fluid flow becomes restricted as voids are filled by secondary phases. Complex alteration at Site U1368 is relatively uncommon. Halos usually represent a single alteration phase or sometimes two phases.

Polymineralic veins indicate that some areas underwent more than one phase of secondary mineral emplacement. The extent to which renewed oxidative alteration has taken place in zones with more than one phase of secondary mineral emplacement remains unclear. The occurrence of late-stage carbonate, however, indicates that reopening must have

taken place. Saponite followed by iron oxyhydroxide precipitation in vesicles in interval 329-U1368F-12R-1, 2–3 cm, suggests that at least some renewed oxidation took place. In a similar situation to Site U1365, the presence in the lowermost sediment of dissolved Mg at below-deepwater concentrations and dissolved Ca at above-deepwater concentrations indicates that basalt-water interaction in the form of Mg exchange for Ca persists today (see **“Biogeochemistry”** in the **“Site U1365”** chapter (Expedition 329 Scientists, 2011b)). This exchange may continue to drive late-stage calcite precipitation. In addition, the overall lower abundance of carbonate precipitate at the younger site (0.01% calcite at Site U1368; 13.5 Ma) than that of the older site (1.05% calcite at Site U1365; 84–120 Ma) supports the hypothesis that seafloor weathering continues (intermittently or continuously) for tens of millions of years after crustal formation. Our shipboard studies of hand specimens and thin sections provide no evidence that late-stage fills are oxidative (i.e., we observed no late-stage alteration halos, celadonite, or iron oxyhydroxide). However, in similar style to Site U1365, the presence of dissolved oxygen in the lowermost sediment at below-deepwater concentrations indicates that oxidation or loss to overlying sediment along the flow path continues to take place, albeit perhaps at a very low rate (see **“Biogeochemistry”** in the **“Site U1365”** chapter (Expedition 329 Scientists, 2011b)).

Structural geology

Basalt recovered from Site U1368 has been subject to a small variety of synmagmatic and postmagmatic structural changes, with structural features that include flow laminations, planar flow margins, jointing, volcanoclastic breccia, and veins. Nongeological structural features include joints induced by the coring and core-handling process. Structural features were described and entered into the Laboratory Information Management System (LIMS) database using DESClogik software (see **“Lithostratigraphy, igneous petrology, alteration, and structural geology”** in the **“Methods”** chapter [Expedition 329 Scientists, 2011a]). In addition, breccia units were described in terms of their textural features and composition.

As with Sites U1365 and U1367, only geological features were recorded in the structural log and only planar features were entered. This practice restricted the number of records to only a few measurements.

Veins

Veins constitute the most pervasive and numerous structural features observed in basement recovered at Site U1368. Structurally, veins are extensional frac-

tures that have been filled with secondary minerals (see **“Basement alteration”**). Measurements were made on planar veins that were present on oriented pieces. In addition, to minimize unreliable data, veins with geometries that appeared to represent thermal contraction were excluded from measurement; these included veins with Y-shaped intersections and sinuous, steeply dipping veins that are intersected by radiating veins. This restricted useful measurements to <1% of all veins at Site U1368.

Most veins at Site U1368 represent fracture fills within the fractured pillow lava units. As such, these veins form curves around the chilled margins and quench structures. A number of narrow irregular branching veins that postdate the cooling features are present; these veins occasionally have splayed ends or kinks where the vein has propagated along weaker portions of the rock (e.g., along quench margins, glassy zones, or changes in grain size). Planar veins are present in the massive and thin flow units and are typically inclined to vertical. Horizontal veins are not common at Site U1368; however, they are the most common within the more massive units. These veins tend to be irregular or ribbonlike and crosscut by vertical veins. Most veins do not have known orientation; therefore we cannot be certain of the overall orientation trends.

Structural orientation

A lack of orientation of the recovered core means that only dip can be determined, with dip direction being defined relative to an arbitrary north (see **“Lithostratigraphy, igneous petrology, alteration, and structural geology”** in the **“Methods”** chapter [Expedition 329 Scientists, 2011a]). Shore-based analyses utilizing paleomagnetic data and wireline logging results will need to be carried out to reorient some of the veins. A summary of the dips and apparent strikes of veins and joints for basement at Site U1368 is shown in Figure F29. Most structures are vertical features.

Structural summary

Hand-specimen observations support the following sequence of structure formation in rocks from Hole U1368F:

1. Formation of radial cooling cracks perpendicular to pillow margins and fracturing of pillow basalts;
2. Formation of horizontal cracks that were possibly formed at or near lava-flow boundaries from which fluid flow was focused; and
3. Development of younger vertical fractures without halos, which was possibly related to tectonic stresses caused by rotational movement of the

basement within a fault block as the crust moved away from the spreading axis.

Paleontology and biostratigraphy

At Site U1368, we recovered a ~16 m section of pelagic clay, clay-bearing nannofossil ooze with foraminifers, and lithic sand deposited over basaltic basement 13.4–13.6 Ma in age (Gradstein et al., 2004). Four samples covering the different lithologic units (Figure F30; see also “[Lithostratigraphy](#)”) were examined for paleontological and biostratigraphic purposes using the coarse (>63 µm) sediment size fraction. The coarse sediment size fraction of the samples taken from the calcareous ooze interval is dominated by planktonic foraminifers, with lesser amounts of benthic foraminifers and ostracods. The silt and clay size fractions (<63 µm) were examined by smear slide samples taken at a higher resolution to characterize the lithologic units (see “[Lithostratigraphy](#)”). The biogenic component of the fine fraction (<63 µm) is dominated by calcareous nannofossils.

The preservation and abundance of calcareous microfossils varies with depth. They are well-preserved and abundant in samples from the middle part of the stratigraphic section (329-U1368D-1H-CC [7.47 mbsf] and 329-U1368B-2H-4, 25–27 cm [10.25 mbsf]) (Fig. F14A) and poorly preserved and scarce in the uppermost sample at 3 mbsf (Sample 329-U1368B-1H-3, 0–2 cm) and in the lowermost sample at 16.08 mbsf (Sample 329-U1368C-2H-CC). The lowermost sample comes from a lithic black sand layer composed of strongly magnetic altered basaltic grains (see “[Lithostratigraphy](#)”). In this layer, most foraminifers are very recrystallized and altered (Fig. F14B). The decrease in preservation near the top is probably due to sinking of the aging seafloor relative to the lysocline. The decrease in carbonate preservation is also reflected in the deepwater environment by the near absence of benthic foraminifers and ostracods (Tables T3, T4). Only one specimen of the benthic foraminifer genus *Epistominella* was found in Sample 329-U1368B-1H-3, 0–2 cm. See the “[Appendix](#)” for a list of foraminifer taxa.

Planktonic foraminifers

Biostratigraphic assignments for Site U1368 are derived from planktonic foraminifers. The planktonic foraminiferal assemblage near the sediment/basalt interface (at the base of Core 329-U1368C-2H; ~16.1 mbsf) is characterized by *Sphaeroidinellopsis disjuncta*, *Globigerinita naparimaensis*, *Praeorbulina glomerosa*,

Praeorbulina sicana, *Praeorbulina transitoria*, *Sphaeroidinellopsis kochi*, and *Sphaeroidinellopsis subdehiscens*. Other taxa such as *Catapsydrax dissimilis*, *Globigerina woodi*, *Globigerinita uvula*, *Globigerinella praesiphonifera*, *Globigerinoides trilobus*, *Globoquadrina binaiensis*, *Globoquadrina dehiscens*, *Orbulina universa*, and *Paragloborotalia mayeri* occur in lesser abundances (Table T5). The assemblage composition allows us to assign the base of the sedimentary record at Site U1368 to planktonic foraminiferal Zone M9/M8 (~13–14 Ma) based on the last occurrence (LO) datums of *C. dissimilis*, *G. naparimaensis*, *G. binaiensis*, *Globorotalia archeomenardii*, *P. mayeri*, and *P. sicana* and the first occurrence (FO) datums of *S. subdehiscens* and *P. glomerosa* (Pearson and Chaisson, 1997; Shackleton et al., 1999; Wade et al., 2011). The biostratigraphic age assignment agrees with Gradstein et al.’s (2004) tectonic and paleomagnetic age for the oceanic crust at this location.

Sample 329-U1368B-2H-4, 25–27 cm (10.25 mbsf), contains the FO and LO of *Fohsella fohsi* and the FO of *Globoturborotalita nepenthes* in the record. The FO of *F. fohsi* is placed between 12.7 and 13.74 Ma by Berggren et al. (1995) and Wade et al. (2011), respectively, and the LO is placed between ~11.7 Ma (Chaisson and Pearson, 1997; Wade et al., 2011) and 11.9 Ma (Berggren et al., 1995). The FO of *G. nepenthes* has been set between 11.55 and 11.8 Ma (Berggren et al., 1995; Wade et al., 2011). Based on these datums, we can assign Sample 329-U1368B-2H-4, 25–27 cm, to planktonic foraminiferal Zones M11–M10.

Sample 329-U1368D-1H-CC (7.47 mbsf) yielded the FO of *Globorotalia crassaformis*, *Globoconella inflata*, *Globorotalia pseudomiocenica*, and *Globorotalia tosaensis*, which allows us to assign this sample to Zones PL2–PL1 (Pearson and Chaisson, 1997; Wade et al., 2011). The common occurrence of *G. nepenthes* and *Dentoglobigerina altispira* in the uppermost sample (329-U1368B-1H-3, 0–2 cm) indicates that Zone PL2 extends to at least 3 mbsf. This interpretation is supported by the lack of typical late Pliocene–Pleistocene taxa in this part of the record. Shore-based examination at a higher resolution will be carried out on samples from Site U1368 to refine the foraminifer biostratigraphy at this site.

Benthic foraminifers

More than 17 species of benthic foraminifers were observed in the four samples examined from Site U1368 (Table T3). Overall, the assemblage was of relatively high diversity in the samples from ~7.5 and 10.25 mbsf. The uppermost sample was affected by dissolution, and only one specimen of the genus *Epistominella* was found. Overall, the benthic foraminiferal

fer taxa resemble those found at Site U1367 and include *Anomalinoidea globosus*, *Buliminella parvula*, *Cassidulina subglobosa*, *Cibicidoides mundulus*, *Cibicidoides wuellerstorfi*, *Epistominella* sp., *Gyroidina* sp., *Gyroidinoidea lamarckiana*, *Gyroidinoidea soldanii*, *Karrerella chapapotensis*, *Lagena* spp., *Nodosaria* sp. A, *Nodosaria* sp. B, *Nuttallides umbonifer*, *Oridorsalis umbonatus*, *Polymorphina* spp., and *Siphonodosaria spinata* (Table T3).

Ostracods

Seven ostracod genera were observed at Site U1368 (Table T4). As with the benthic foraminifers, maximum diversity was observed in Samples 329-U1368D-1H-CC (7.47 mbsf) and 329-U1368B-2H-4, 25–27 cm (10.25 mbsf). No ostracods were found in the upper- or lowermost samples. Ostracods were identified to the generic level and consist of genera that have worldwide distribution and are common in Cenozoic deep-sea sediment (Whatley and Ayress, 1988; Ayress et al., 1997; Dingle and Lord, 1990; Cronin et al. 2002; Alvarez Zarikian, 2009; Alvarez Zarikian et al., 2009). The assemblage is dominated by *Krithe*, followed by *Poseidonamicus*, *Henryhowella*, *Bradleya*, *Eucythere*, and *Pelecocythere*.

Physical properties

Physical properties at Site U1368 were measured on whole cores, split cores, and discrete samples. After sediment cores reached thermal equilibrium with ambient temperature at $\sim 20^{\circ}\text{C}$, gamma ray attenuation (GRA) density, magnetic susceptibility, and *P*-wave velocity were measured with the Whole-Round Multisensor Logger (WRMSL). After WRMSL scanning, the whole-round sections were logged for NGR. Thermal conductivity measurements were made on sedimentary whole rounds using the full-space method and on basement split cores using the half-space technique. Compressional wave velocity measurements on sedimentary split cores were made once per core and moisture and density (MAD) analyses on discrete core samples were made at a nominal frequency of every other section. On basaltic basement cores, these measurements were made twice per core. The Section Half Multisensor Logger (SHMSL) was used to measure spectral reflectance on archive-half sections and take point measurements of magnetic susceptibility. Additionally, discrete measurements of electrical resistivity were made on the split sediment sections at approximately every 10 cm. These measurements were used to calculate formation factor. The Section Half Imaging Logger and a color spectrophotometer were used to collect images of the split surfaces of the archive-half cores.

Four holes targeted the sedimentary cover, Holes U1368B–U1368E. The most complete sedimentary sequence for logging physical properties comes from Holes U1368B and U1368E. In Hole U1368F, we targeted basement but also recovered a few meters of sediment above basement. Cores from the different holes through the sediment have not been correlated and offsets exist.

Density and porosity

Sedimentary values of bulk density at Site U1368 were determined from both GRA measurements on whole cores and mass/volume measurements on discrete samples from the working halves of split cores (see “Physical properties” in the “Methods” chapter [Expedition 329 Scientists, 2011a]). A total of 29 discrete sedimentary samples were analyzed for MAD, 7 samples from Hole U1368B, 9 samples from Hole U1368C, 4 samples from Hole U1368D, 7 samples from Hole U1368E, and 2 samples from Hole U1368F.

Wet bulk density values determined from whole-round GRA measurements from Hole U1368B display conspicuous density inversions correlated with section breaks that indicate core disturbance (Fig. F31A). Discrete bulk density values plotted on these disturbed trends suggest that fluids drained from the sediment during core handling, possibly because of the longer than normal time before WRMSL measurements. Prior to WRMSL measurements, these cores were measured for dissolved oxygen, accounting for the time delay. The departures in density have magnitudes of up to 0.3 g/cm^3 or almost 20%. Because the perturbing trends are well delineated, we detrended segments and adjusted the density data (Fig. F31B). One sign that these corrections may be appropriate is that the magnitudes of discontinuities across section breaks are substantially decreased. The adjusted data show greater continuity across section breaks (Fig. F31C).

Similar perturbations caused by core handling also likely affected data from Holes U1368C and U1368D (Fig. F32), but because whole rounds were removed prior to GRA measurements, trends are less clear. Density inversions in the uppermost sections of Hole U1368E also suggest disturbance. In detail, it appears that the measurements in the uppermost part of each section are fairly constant but then oscillate in the lower part. We have not attempted to remove these density inversions. In both Holes U1368B and U1368E, the perturbations suggest that fluids preferentially drained from the lower part of each section. It remains puzzling why the perturbations preferentially affected the bottoms of sections in all cases rather than the tops. However, this observation im-

plies that MAD samples taken from the tops of sections, as they were in Hole U1368E, may be more representative of in situ values than samples taken from the lower portions of sections, as exhibited in Hole U1368B. Neglecting the low values between 1.8 and 3.0 mbsf because of a collapsed core liner, the adjusted density in lithologic Unit I is 1.6 g/cm^3 in both Holes U1368B and U1368E. Bulk density values in Unit III are generally much more variable than in the upper two units.

Relationships between discrete measurements of bulk density, grain density, and porosity in Holes U1368B–U1368E are shown in Figure F33. Given the likely core disturbance discussed above, the most robust MAD measurements may be those of grain density based on dry weights and volumes. Within lithologic Unit I, the mean and standard deviation grain density is 2.78 and 0.05 g/cm^3 , respectively. Porosity reduction may have also occurred, but the MAD measurements are too sparse to make a quantitative assessment.

Density values and MAD samples from Hole U1368F are shown in Figure F34. The WRMSL density calculation assumes that the core liner is entirely filled with rock. This assumption is appropriate for sediment cores, but basement cores have a smaller maximum diameter of 58.5 mm , narrower than the 66 mm internal diameter of the plastic core liner. WRMSL density values are adjusted by a factor of $66/58.5 = 1.18$. Peak values of WRMSL density are slightly greater than 3 g/cm^3 . MAD density values are somewhat lower than maximum WRMSL values with an average density of 2.85 g/cm^3 . Porosity values of basement have an average value of 4.5% .

Magnetic susceptibility

Volumetric magnetic susceptibilities were measured using the WRMSL, and point measurements were made using the SHMSL on all recovered cores from Site U1368. Uncorrected values of magnetic susceptibility are presented for Holes U1368B–U1368E (Fig. F35). Values collected on the WRMSL and SHMSL are in general agreement. The spatial resolution of the WRMSL magnetic susceptibility loop is $\sim 5 \text{ cm}$, and the observed ringing in Holes U1368C–U1368E is caused by edge effects.

Magnetic susceptibility values in Holes U1368B and U1368E show high wave number variations in the upper portion of lithologic Unit I. In the lower portions of Unit I, values slowly increase with depth to Unit II. Values in Unit II are generally lower than in Unit I. Magnetic susceptibility in Unit III is more variable and generally higher than the upper units. At $\sim 14.5 \text{ mbsf}$ in Hole U1368B, magnetic susceptibil-

ity attains an extremely high value of $8.222 \times 10^{-5} \text{ SI}$. These high values have a spatial association with titanomagnetite (see “Lithostratigraphy”).

Magnetic susceptibility in Hole U1368F is shown in Figure F36. Values in the basalt are generally higher than in the sediment and attain a maximum at $\sim 40 \text{ mbsf}$.

Natural gamma radiation

NGR results are reported in counts per second (cps) (Fig. F37). NGR counting intervals were $\sim 1 \text{ h}$ per whole-core interval for Hole U1368B but decreased to 0.5 h per whole-core interval for Holes U1368C–U1368F. NGR counts are considered reliable. NGR at the tops of all holes is high, with the exception of Hole U1368D, where a whole round was sampled. These high counts indicate that the sediment/water interface was sampled.

Below the sediment/seawater high, NGR counts are uniformly low but tend to increase with depth and are somewhat higher in lithologic Unit III. Ringing is more prevalent in cores from Holes U1368C and U1368D because only short core pieces remained of them after whole-round sampling prior to NGR measurements.

NGR counts in Hole U1368F basalt are low but increase slightly with depth (Fig. F38). Between 100 and 110 mbsf , counts associated with breccia are higher, with values $>10 \text{ cps}$.

P-wave velocity

Compressional wave velocity was measured by the P-wave logger (PWL) on all whole cores and by the insertion and contact probe systems on sedimentary split cores in Hole U1368B. The contact probe system allows determination of velocities in the y -, z -, and x -directions. In general, compressional wave velocities on split cores are somewhat higher than on whole cores, with a mean offset of $\sim 40 \text{ m/s}$ (Fig. F39). This offset may have resulted from excessive wetting of sediment to ensure good contact between the sensor and the split core sediment, a water-rich rind inside the core liner, and possible variations in pressure/probe contact between the PWL and discrete x -direction transducers. The mean value of the PWL measurements is $\sim 1497 \text{ m/s}$ (close to the compressional velocity of water) (Fig. F39B). Below ~ 8 – 10 mbsf in all holes, P-wave velocities decrease perceptibly through lithologic Unit II. Values of P-wave velocity in Unit III are more variable than in either Unit I or II. Cores from Holes U1368C and U1368D exhibit greater apparent scatter than cores from Holes U1368B and U1368E; this increased scatter is an artifact caused edge effects, as these measure-

ments were made after whole-round sampling for chemistry and microbiology.

Point measurements of compressional wave velocity for Hole U1368F are shown in Figure F40. The mean *P*-wave velocity through the basalt has a mean value of 5480 m/s.

Formation factor

Electrical conductivity was measured on working halves of the split sediment cores from Hole U1368B, and the formation factor was calculated. For each measurement, the temperature of the section was also noted. Surface seawater was used as a standard and measured at least twice per section (Table T6), normally prior to making measurements for that section and then around the 75 cm offset of each section. These measurements were used to compute the drift (Fig. F41), which was very low at this site. The temperature dependence of electrical conductivity was corrected and all reported measurements correspond to a temperature of 20°C. Electrical conductivity measurements were transformed to a dimensionless formation factor by dividing the measurements for the drift (Table T7).

Within lithologic Unit I, the formation factor is relatively uniform (Fig. F42). Formation factor values in lithologic Unit II increase slightly with depth, and values in Unit III are more scattered (Fig. F36).

Thermal conductivity

Thermal conductivity measurements were conducted on sediment whole-round cores using the full-space method. Measurements were made at a frequency of once per section. The mean and standard deviation of the sediment thermal conductivity measurements are 0.80 and 0.16 W/(m·K), respectively (Fig. F43A). These values are compared with thermal conductivity values measured on returned material from a piston core collected during the KNOX-02RR site survey cruise. The mean and standard deviation of these values are 0.96 and 0.14 W/(m·K), respectively (R. Harris, unpubl. data).

Thermal conductivity measurements were collected on recovered basalt using the half-space method (see “Physical properties” in the “Methods” chapter [Expedition 329 Scientists, 2011a]). Measurements were made at an approximate frequency of once per section if suitable pieces were present. Thermal conductivity values are relatively uniform with depth in the basalt and have a mean and standard deviation of 1.66 and 0.11 W/(m·K), respectively (Fig. F43B).

Color spectrometry

Spectral reflectance was measured on split archive-section halves from Holes U1368A–U1368F using the SHMSL. The parameters *L** (luminescence) (Fig. F44) and *a** (green–red) (Fig. F45) have limited relationships with lithologic variation downhole. The parameter *b** (blue–yellow) (Fig. F46) decreases through lithologic Units II and III with increasing clay and sand content as the units become increasingly darker.

Spectral reflectance parameters *a** and *b** in Hole U1368F (Fig. F47) have lower values in the basalt than in the sediment (0–10 mbsf). *L** shows greater variability in the basalt than in the sediment. In general, spectral reflectance values are relatively uniform for parameters *L** and *a**. Maximum values of *b** increase slightly with depth within the basalt.

Downhole logging

Downhole logging data obtained from Hole U1368F included NGR, spectral gamma radiation, density, photoelectric factor, electrical resistivity measurements, and FMS images of the borehole wall. Interpretations of NGR downhole logs were used to identify two logging units in Hole U1368F, with one in the sediment sequence and one in the basaltic basement.

Wireline operations

A wiper trip was completed throughout the open hole before the start of the wireline logging operations. The drill pipe was set at 34 m wireline matched depth below seafloor (WMSF; 3592.5 mbrf), which is ~17 m below the sediment/basement interface. The hole was circulated with seawater. Downhole logging operations lasted 18 h, beginning at 1330 h on 17 November 2010. The wireline logging operations consisted of two tool string deployments and testing of the wireline heave compensator (WHC). Logging operations in Hole U1368F took place in good sea conditions with ship heave between 0.4 and 2 m, peak-to-peak.

Tool string deployment

HNGS-HLDS-GPIT-DIT

The wireline tool string deployment consisted of a 23.22 m long triple combo tool string that included a logging equipment cable head (LEH-QT), digital telemetry cartridge (DTC-H), Hostile Environment Natural Gamma Ray Sonde (HNGS), Hostile Environ-

ment Natural Gamma Ray Cartridge (HNGC), Litho-Density Sonde Cartridge (LDSC), Hostile Environment Litho-Density Sonde (HLDS), digital telemetry adapter (DTA-A), General Purpose Inclinometry Tool (GPIT), and the Digital Dual Induction Tool model E (DIT-E). Downhole logs were recorded in three passes:

1. A downlog from seafloor to 104.5 m WMSF,
2. An uplog from 104.5 to 53 m WMSF, and
3. An uplog from 104.5 m WMSF to seafloor.

After the downlog was stopped and prior to starting Pass 1, ~1 h was spent assessing downhole tool motion and optimizing the efficiency of the WHC for the water depth at Hole U1368F and heave conditions at the time of the logging operations. Once the best possible WHC parameters were chosen for the prevailing heave conditions, the tool string was lowered to 104.5 m WMSF to begin the first uplog.

HNGS-GPIT-FMS

The second wireline tool string deployment consisted of a 14.27 m long FMS-HNGS that included a LEH-QT, DTC-H, HNGS, DTA-A, GPIT, and FMS. Downhole logs were recorded in three passes:

1. A downlog from seafloor to 104.5 m WMSF,
2. An uplog from 104.5 to ~53 m WMSF, and
3. A second uplog from 104.5 m WMSF to seafloor.

Data processing

Logging data were recorded onboard the *JOIDES Resolution* by Schlumberger and archived in digital log information standard (DLIS) format. Data were sent by satellite transfer to the Borehole Research Group of the Lamont-Doherty Earth Observatory, processed there, and transferred back to the ship for archiving in the shipboard database. Processing and data quality notes are given below.

Depth shifting

In general, depth shifts that are applied to logging data by selecting a reference (base) log (usually the total gamma ray log from the run with the greatest vertical extent and no sudden changes in cable speed) and features in equivalent logs from other passes are aligned by eye. The logging data seafloor depth could not be determined by the step in gamma ray values because the signal was affected by the presence of the drill collars. As a result, the seafloor depth given by the drillers (3752 m drilling depth below rig floor) was used for depth shift.

Data quality

The quality of wireline logging data was assessed by evaluating whether logged values are reasonable for

the lithologies encountered and by checking consistency between different passes of the same tool. Gamma ray logs recorded through the BHA should be used only qualitatively because of the attenuation of the incoming signal. The thick-walled BHA attenuates the signal more than the thinner walled drill pipe.

A wide (>30.5 cm) and/or irregular borehole affects most recordings, particularly those like the HLDS that require eccentricization and a good contact with the borehole wall. The density log roughly correlates with the resistivity logs but is largely affected by hole conditions. Hole diameter was recorded by the hydraulic caliper on the HLDS tool (LCAL), which shows a very irregular borehole with intervals exceeding the maximum caliper aperture. Good repeatability was observed between Passes 1 and 2, particularly for measurements of electrical resistivity, gamma radiation, and density.

The FMS images are generally of good quality because of the relatively good hole conditions (hole size <35.6 cm). The irregular and possibly elliptical shape of the borehole occasionally prevented some FMS pads from being in direct contact with the formation, resulting in poor resolution or dark images.

Preliminary results

Electrical resistivity measurements

A total of three electrical resistivity curves were obtained with the DIT-E. The spherically focused resistivity (SFLU), medium induction phasor-processed resistivity (IMPH), and deep induction phasor-processed resistivity (IDPH) profiles represent different depths of investigation into the formation (64, 76, and 152 cm, respectively) and different vertical resolutions (76, 152, and 213 cm, respectively). Downhole open-hole electrical resistivity measurements covered 74 m of the basement lithologic units (Fig. F48). The DIT-E was the only tool that reached the bottom of the logged interval in Hole U1368F because it was the lowermost tool in the logging tool string (see Fig. F12 in the “Methods” chapter [Expedition 329 Scientists, 2011a]). IDPH measurements in the basaltic basement range from 3.0 to 84 Ωm , IMPH measurements range from 1.4 to 3.16 Ωm , and SFLU values range from 1.9 to 202.7 Ωm (Fig. F48).

Gamma ray measurements

Standard, computed, and individual spectral contributions from ^{40}K , ^{238}U , and ^{232}Th were part of the gamma ray measurements obtained in Hole U1368F with the HNGS. Downhole gamma ray measurements covered 95 m of the lithostratigraphic sequence in Hole U1368F. NGR measurements in the

sediment sequence are attenuated by the BHA but show consistently lower values for total gamma, K, Th, and U than the underlying basement. The sediment/basement interface is clearly identifiable in total gamma ray and potassium measurements at 17 m WMSF.

Total gamma ray measurements in the basaltic basement are low, with basement values ranging between 3.5 and 14.1 gAPI (Fig. F49).

Potassium concentrations in the basaltic basement range between 0.08 and 0.65 wt%. Uranium concentrations range between 0.0 and 0.68 ppm. Thorium concentration ranges from 0.0 to 0.92 ppm).

Comparison between NGR measurements made on whole-round core sections and downhole logs shows good agreement between the two (Fig. F50). Total gamma ray data from the downhole logs have been corrected by a factor of 3.5 for the attenuation caused by the BHA between seafloor and 34 m WMSF. The measurements made on whole cores were used to provide a check on this correction.

Density

Density values range from 1.1 and 3.4 g/cm³ in the basement section. Comparison with caliper data indicate that the data are affected by hole size, particularly where the hole is washed out (Fig. F51). Caliper data indicate the hole diameter varies between 33 cm and the maximum extension of the caliper arm, 50.8 cm.

Formation MicroScanner images

FMS images were obtained for the open-hole interval between 39 and 103 m WMSF. The diameter of hole from the FMS calipers varied between 18.8 and 35.1 cm. High-quality FMS images were obtained in much of the borehole; only intervals that were washed out show poor-quality images. FMS images from the basement section show well-defined pillow structures, some of which are between 50 and 100 cm in size (Fig. F52). The most massive pillows show good recovery in core samples, and core photographs from Core 329-U1368F-5R are compared to FMS images from the same interval in Figure F53.

Lithostratigraphic correlations

Preliminary interpretation of the downhole log data divides Hole U1368F into two logging units (Figs. F48, F49). Unit I covers the sediment sequences logged through the BHA. Unit II covers the basaltic basement sequence.

Logging Unit I was identified in the section covered by the BHA between 0 and 17 m WMSF (Figs. F48,

F49) and corresponds to the carbonate oozes and metalliferous clays described in the sediment sequence (see “[Lithostratigraphy](#)”).

Logging Unit II extends from the sediment/basement interface at 17 m WMSF to the logging total depth of 104.5 m WMSF. This unit covers a sequence of basaltic pillow lavas.

Paleomagnetism

At Site U1368, we measured natural remanent magnetization (NRM) of all archive-half sections from Holes U1368B–U1368E using the three-axis cryogenic magnetometer at 2.5 cm intervals before and after alternating-field (AF) demagnetization. The archive-half sections were demagnetized by alternating fields of 10 and 20 mT. The present-day normal field in this region, as expected from the geocentric axial dipole model at Site U1368, has a negative inclination (approximately -46.7°), so positive remanence inclinations indicate reversed polarity. Data from Holes U1368C and U1368D provide only a partial record because whole-round core samples were taken from these holes for geochemical and microbiological analyses. From Hole U1368B, 13 discrete sediment samples (7 cm³ cubes) were taken at an interval of one per section from the working halves, and compatibility of magnetization between archive half and working half was analyzed. Of these discrete samples, eight were measured for NRM after demagnetization at peak fields of 10 and 20 mT using the pass-through magnetometer. The primary objective of the shipboard measurements for Site U1368 was to provide chronostratigraphic constraint by determining magnetic polarity stratigraphy. A discrete rock sample was also taken and measured for NRM from each of the RCB basement cores from Hole U1368F. With the basement samples, NRM was measured after AF demagnetization at peak fields of 10, 20, 30, 40, 50, and 60 mT using the pass-through magnetometer and the Agico spinner magnetometer. During coring operations at Site U1368, neither non-magnetic core barrels nor the Flexit core orientation tool were used because of the shallow drilling depth of the sediment column (see “[Operations](#)”).

Results

Paleomagnetic data for Holes U1368B–U1368F are presented in Figures F54, F55, F56, F57, and F58, together with the whole-core susceptibility data measured on the WRMSL (see “[Physical properties](#)”). The lithology at Site U1368 changes from clay-bearing nannofossil ooze (lithologic Unit I) at the top to nannofossil-bearing clay (Unit II) to metalliferous lithic sand and clay (Unit III) at the bottom (see

“**Lithostratigraphy**”). The nannofossil ooze unit extends from 0 to ~12 mbsf in Hole U1368B. Using magnetic susceptibility data, it was possible to correlate between Holes U1368B and U1368E (Fig. F59). This correlation was applied to the magnetic intensity data and to the inclination and declination data (Fig. F60).

Magnetic directions at Site U1368 show both reversed and normal polarity. However, the records are not consistent between holes, possibly because of a magnetic overprint acquired during coring (high negative inclination), viscous remanent magnetization, or diagenetic changes in the sediment.

According to the shipboard interpretation of planktonic foraminiferal assemblages, the sedimentary record at Site U1368 spans from the late Miocene (~13 Ma) near the sediment/basement interface (~16 mbsf in Hole U1368C) to ~3.5 Ma at 3 mbsf in Hole U1368B (see “**Paleontology and biostratigraphy**”).

The AF demagnetization record from eight discrete samples from Hole U1368B deviates significantly from the half-core record (Fig. F54). It is likely that the influence of the magnetic overprint is not completely removed from the half-core record.

Given the difficulty in determining sediment age by shipboard paleomagnetic studies, chronostratigraphy for Site U1368 must be determined by postexpedition studies, including further magnetic cleaning by increased AF demagnetization and use of other chronostratigraphic tools.

Biogeochemistry

Site U1368 presented the thinnest sedimentary sequence targeted by Expedition 329. The sequence is dominated by carbonate-bearing sediment (see “**Lithostratigraphy**”) and is ~15 m thick. As at previous sites, onboard measurements and sample processing continued to focus on

- Understanding microbially mediated chemical processes,
- Chemical fluxes between the sediment and the underlying basalt, and
- The potential of radiolysis to support microbial activities.

To achieve these objectives, a broad range of chemical species was measured. High spatial-resolution profiles of dissolved oxygen were acquired using optodes and electrodes, headspace samples were used for hydrogen analyses, and interstitial waters were obtained for analysis using Ti Manheim squeezers and Rhizon pore fluid samplers. Additional sediment samples were taken for solid-phase nitrogen and car-

bon determination, and separate whole-round intervals were sectioned and squeezed for postexpedition ¹⁴C studies.

Dissolved oxygen

Measurements of dissolved oxygen (O₂) were performed on intact 1.5 m core sections with electrodes (Table T8) on Cores 329-U1368B-1H and 2H, 329-U1368E-1H and 2H, and on the mudline core from Core 329-U1368F-1R. Measurements were typically performed at 15–20 cm intervals. Oxygen electrode measurements were also carried out on 20–50 cm long whole-round sections from Cores 329-U1368C-1H and 2H in 30–50 cm intervals after sampling in the core refrigerator on the Hold Deck of the *JOIDES Resolution*. Oxygen was measured by optode in intact 1.5 m core sections from Core 329-U1368B-1H (Table T9). Below 5.2 mbsf, optode measurements were difficult because of optode breakage, and no further measurements with optodes were attempted.

The dissolved oxygen profiles from the different Site U1368 holes are very similar to each other. Although optode measurements are limited to the uppermost 5 m of sediment from Hole U1368B, they are in good agreement with the electrode profiles. The oxygen profile from Hole U1368E exhibits slightly more scatter than profiles of cores from the other holes but otherwise exhibits a similar pattern of decrease with depth.

Dissolved oxygen penetrates from the seafloor to the sediment/basalt interface (Fig. F61A). Near-seafloor oxygen concentrations are between 156 and 159 μM for all holes (U1368B–U1368D and U1368F), approximating the regional bottom water oxygen concentration (Talley, 2007). The largest decline over depth in oxygen concentration was in the uppermost 2.5 mbsf, with a decrease from ~158 to ~145 μM at 2.5 mbsf (Fig. F61B). The high-resolution optode measurements from Hole U1368B and the electrode readings from Hole U1368F suggest that the only discernible curvature in oxygen concentration takes place in the uppermost 50 cm below seafloor. Below this depth, oxygen concentration declines linearly (Fig. F61A) with depth to ~140 μM at 12 mbsf.

The oxygen profiles at Site U1368 generally match the profiles from Sites U1365–U1367, except for slightly lower values caused by slightly lower bottom water oxygen concentration (Talley, 2007). Evidence of in situ oxygen consumption is limited to the topmost 50 cm below seafloor at Site U1368. The gradual decrease in oxygen concentration with depth indicates an oxygen flux towards the basaltic basement.

Dissolved hydrogen and methane

Dissolved hydrogen (H_2) concentrations were quantified in 33 samples collected from Hole U1368C (Fig. F62; Table T10). Ten samples were taken on the catwalk and 23 were taken in the core refrigerator on the Hold Deck. Analyzed depths ranged from 0.2 to 15.6 mbsf. Based on the average of 13 blanks, the detection limit at this site was calculated to be 3.6 nM. The concentration of H_2 remains below the detection limit in the uppermost 9.4 m of the sediment column (Fig. F62). Below this depth, 6 of the 13 samples were above the detection limit, with H_2 concentrations ranging from 5 to 36 nM. One of the six samples containing a detectable H_2 concentration (7 nM) was collected on the catwalk.

Methane concentrations are below the detection limit (<1.3 mM) in all samples from Holes U1368B (IODP standard safety protocol) and U1366C (refined protocol). The detection limit is defined here as three times the standard deviation of the blank (ambient air).

Interstitial water samples

Interstitial water was taken from 33 whole-round samples from Hole U1368C (Table T11). The samples were obtained at the high resolution of three per section (approximately one sample every 50 cm). Eleven of the interstitial water whole-round samples were cut and taken on the catwalk and delivered immediately to the Geochemistry Laboratory for squeezing. These samples are referred to as “catwalk” samples, and aliquots for ^{14}C analysis were taken from them. Furthermore, 32 Rhizon samples (Table T12) for dissolved nitrate analyses were obtained from a combination of the whole-round samples taken before squeezing as well as additional samples taken from other depths in the core. The Rhizon extractions were performed in the Hold Deck refrigerated core storage area (see “Biogeochemistry” in the “Methods” chapter [Expedition 329 Scientists, 2011a]). All profiles are presented in Figure F63.

Nitrate concentration near the sediment surface (Sample 329-U1368C-1H-1, 10–20 cm) was 35.84 μM (Fig. F63A). This concentration is slightly higher than that found at Sites U1365–U1367. The nitrate concentration profile subsequently shows virtually no change with increasing depth. In comparison with the previous sites that exhibit increasing nitrate concentrations to greater depths, this lack of change with depth at Site U1368 suggests that the organic matter flux to the sediment is extremely low at the center of the oligotrophic gyre.

Like the pattern exhibited at the previous Expedition 329 sites, the distribution of phosphate exhibits a de-

cline in concentration from near-seawater values with increasing depth (Fig. F63B). The concentration in the surface sediment at 0.05 mbsf (Sample 329-U1368C-1H-1, 0–10 cm) is 2.29 μM , which is very close to the deepwater concentration for the South Pacific Ocean for this region of the Pacific Ocean (Talley, 2007). Phosphate concentrations decrease to <1.0 μM at 5.5 mbsf. With the exception of two values that depart from a smoothly decreasing profile (Samples 329-U1368C-1H-4, 50–60 cm, and 100–110 cm), the concentration of phosphate remains below or close to 1.0 μM to 15.44 mbsf. This value is slightly greater than the lowest values observed in the previous sites (typically close to 0.5 μM). Below 13 mbsf (in Sections 329-U1368C-2H-5 and 2H-6), phosphate begins to increase with increasing depth and attains a concentration of 1.60 μM at 15.48 mbsf (329-U1368C-2H-6, 0–15 cm). Whether this increase at the bottom of Hole U1365C is related to flow in the basalt aquifer remains to be tested. The pooled standard deviation (1σ), based on 2 runs of 3 replicate measurements of each interstitial water sample ($n = 6$), is 0.13 μM (see “Biogeochemistry” in the “Methods” chapter [Expedition 329 Scientists, 2011a]). Measured phosphate concentrations in immediately squeezed catwalk samples were indistinguishable from samples processed in the normal fashion.

Dissolved silicate concentrations exhibit no clearly discernible trend with depth, have an average value of 245 μM , and vary ~ 23 μM (1σ) around this mean value (Fig. F63C). No difference is apparent in dissolved silicate concentration between those samples squeezed immediately (catwalk) and the normally processed samples.

Alkalinity and dissolved inorganic carbon (DIC) behave similarly with depth in the interstitial water of Site U1368. Alkalinity starts between 2.6 and 2.8 mM in surface sediment and then monotonously decreases with depth. At the bottom of the sequence (15.5 mbsf), the values are between 2.4 and 2.6 mM. Alkalinities of interstitial water samples stored in the core refrigerator on the Hold Deck were consistently lower than those of the rapidly squeezed catwalk samples, which indicates carbonate precipitation in sediment before interstitial water squeezing. Standard deviation and error of alkalinity measurements on standard seawater (CRM94) are 0.018 and 0.005 mM ($N = 11$), respectively. DIC increases from 2.62 mM at the sediment surface to a broad peak of ~ 2.7 mM from 4.45 to 9.45 mbsf. The values then decrease to 2.4 mM to at 15 mbsf. The range in DIC values is 0.3 mM, whereas the average standard deviation of triplicate injection of the samples is 0.015 mM. Catwalk samples that were squeezed right away

show higher values than samples that spent time in the cold room before being squeezed (see “**Biogeochemistry**” in the “Methods” chapter [Expedition 329 Scientists, 2011a]). The average difference between those two set of samples is ~0.15 mM. This shift could be caused by at least two different (but coupled) processes, calcium carbonate precipitation or CO₂ degassing.

Chloride concentrations were determined by ion chromatography. All samples were analyzed in duplicate. Based on the pooled standard deviation of duplicate analyses, the 66% (1 σ) confidence limit is 0.08%. Concentrations in Hole U1368C are indistinguishable from present-day bottom water in this region (554.4 mM). The average measured value is 544.3 mM with a standard deviation of 0.7 mM. The homogeneity reflects the relative stability of seawater salinity over the past few thousand years and the relatively short diffusion timescale for a sequence that is 15 m thick, as well as the limited influence of hydration/dehydration reactions.

Sulfate concentrations were also determined by ion chromatography. All samples were analyzed in duplicate. Based on the pooled standard deviation of duplicate analyses, the 66% confidence limit is 0.09%, whereas the sulfate anomaly 66% (1 σ) confidence limit is 0.05%. There is no difference in the sulfate anomaly between samples squeezed immediately (catwalk) and normally processed samples. Measured sulfate concentrations are <28.6 mM in the entire section (the concentration in local bottom water). The range in the sulfate anomaly (see “**Biogeochemistry**” in the “Methods” chapter [Expedition 329 Scientists, 2011a]) is -1.3% to -4.5% (Fig. F63G). The depletion relative to seawater may be due to adsorption onto sediment during sample recovery and extraction. The sulfate anomaly increases back to -0.7% within the bottommost depths of Site U1368 (14.55–15.48 mbsf; 329-U1368C-2H-5, 50–60 cm, to 2H-6, 0–10 cm). This increase in sulfate concentration (both absolute and relative to chloride) mirrors the increase of phosphate concentration at these depths, but the underlying cause is not clear.

As at previous sites, cations were measured by both ICP-AES and ion chromatography. Samples were analyzed in duplicate (same solution twice in two separate analytical batches). The precision of the measurements of cations by ICP-AES was, as quantified by multiple triplicate and quadruplicate analyses of International Association for the Physical Sciences of the Oceans (IAPSO) standard seawater and internal matrix matched standards,

Ca = 0.6% of the measured value,
Mg = 0.7% of the measured value,
Na = 0.5% of the measured value, and

K = 0.6% of the measured value.

Analyzing the samples in duplicate did not appreciably change the precision of the measurements for Ca or Mg but significantly improved the precision of the measurement of Na and K. Accuracy of the ICP-AES results, as quantified by comparison to multiple replicate analyses of IAPSO not included in the calibration, was within precision of the measurement. For the ion chromatography analyses, precision (pooled standard deviation, 1 σ) was

Ca = 0.7%,
Mg = 0.3%,
Na = 0.3%, and
K = 0.7%.

The shape of the concentration profiles determined by ICP-AES and ion chromatography agree well, although the absolute values of the concentrations differ, with the ion chromatography data being higher than the ICP-AES data (Figs. F63I, F63J, F63K, F63L; Table T11). This contrast is most pronounced for Ca and less so for Na, Mg, and K. Despite the ICP-AES and ion chromatography protocols both being rigorously calibrated against multiple replicate analyses of IAPSO, with identical items being analyzed by both instruments and detailed determinations of analytical precision, the cause of this discrepancy remains unclear. Postcruise shore-based analyses will aim to resolve the ambiguity.

The profile of dissolved Ca (Fig. F63I) shows a slight decrease with depth, from near-surface values approximating that of typical seawater (10.5 mM) to values closer to ~10 mM at depth. Ca concentrations increase through the deepest four samples closest to the basalt. Overall, Mg shows no significant change in concentration with depth. The profiles of Na and K also show no significant change with depth. Over such a short sequence, the lack of significant concentration changes is not surprising.

Comparison of the catwalk samples (squeezed immediately upon core recovery) to those samples stored in the cold room on the Hold Deck (see “**Microbiology**” in the “Methods” chapter [Expedition 329 Scientists, 2011a]) shows no offset between the data sets for any cation (Figs. F63I, F63J, F63K, F63L).

Solid-phase carbon and nitrogen

Contents of total carbon, total organic carbon (TOC), total inorganic carbon (TIC), and total nitrogen were determined for 15 samples from Hole U1368B (Fig. F64; Table T13). Weight percent CaCO₃ was calculated from TIC.

Total nitrogen content is 0.014 wt% at the seafloor but below the detection limit at greater depths (below 0.1 mbsf; Fig. F64A). TOC rapidly decreases from

0.085 wt% at the seafloor to 0.03 wt% at 0.46 mbsf and remains low thereafter (Fig. F64B). Total carbon content obtained with the CHNS analyzer shows a curved profile with a maximum of 10.51 wt% at 4.36 mbsf. At the seafloor, total carbon content is 9.31 wt%; just above basement it is 7.33 wt%.

The TIC and CaCO₃ values obtained by coulometry show the same pattern as total carbon content obtained from the CHNS elemental analyzer. CaCO₃ content varies between 70.8 and 87.4 wt% in the uppermost 4.36 mbsf and gradually decreases to 61.3 wt% at 13.98 mbsf (Fig. F64C). TIC content varies between 8.5 and 10.5 wt% in the uppermost 4.36 mbsf and gradually decreases to 7.4 wt% at 13.98 mbsf.

Microbiology

Sediment samples for microbiological studies were obtained by APC, primarily from Holes U1368C and U1368D. Basalt samples from the sediment/basalt interface were collected from Holes U1368B and U1368D using APC. The RCBS system was used to obtain basalt samples from Hole U1368F. During APC coring, sample contamination was monitored by PFT injection into the drilling fluid. Samples for cell and virus-like particle (VLP) abundance were taken from the cut cores facing interstitial water whole-round samples. After core recovery on the catwalk, core sections were immediately transferred to the core refrigerator on the Hold Deck, where whole-round cores were collected for microbiological analyses. The temperature of the core refrigerator during subsampling was ~7°–10°C. Microbiological whole-round cores were generally taken at a high depth resolution from the first cores (1H), as well as from the core above the sediment/basalt interface (2H).

Cell abundance

Microbial cells were enumerated by direct counting using epifluorescence microscopy (see “Microbiology” in the “Methods” chapter [Expedition 329 Scientists, 2011a]). Sediment subcores (2 cm³) were taken by tip-cut syringes from Hole U1368C for shipboard analysis. For shore-based analysis, 10 cm whole-round cores were taken from Hole U1368D and frozen at –80°C. Thirty-three 2 cm³ syringe samples (Table T14) and 7 whole-round cores (Sections 329-U1368D-1H-1, 1H-2, 1H-4, 2H-1, 2H-2, 2H-3 and 2H-4) were taken from Site U1368.

Four blanks were prepared and counted during processing of the samples from Site U1368, resulting in a mean blank of 6.7×10^2 cells/cm³ with a standard deviation of 4.8×10^2 cells/cm³. The minimum detec-

tion limit (MDL; blank plus three times standard deviation) was calculated to be 2.1×10^3 cells/cm³. As the blanks did not vary much between sites, all data were pooled. At the end of the expedition, a single MDL for all sites (1.4×10^3 cells/cm³) was calculated based on the extended database.

As the sediment at Site U1368 contained calcium carbonate, a carbonate extraction step was employed prior to the actual cell extraction. Samples from Core 329-U1368C-1H were very stiff and did not suspend in the carbonate dissolution; therefore, an initial treatment with detergent mix (see “Microbiology” in “Methods” chapter [Expedition 329 Scientists, 2011a]) was used to disperse the particles before the carbonate dissolution. The order of sample processing therefore changed to

1. Detergent mix/methanol,
2. Carbonate dissolution, and
3. Detergent mix/methanol.

Samples from Core 329-U1368C-2H downhole were treated in the conventional order. No obvious difference is seen in the data from either order of treatment.

Cell abundance in the uppermost sample (329-U1368C-1H-1, 10–15 cm) was $\sim 6 \times 10^4$ cells/cm³. Numbers decreased sharply to $\sim 10^3$ cells/cm³ at 1.4 mbsf (Sample 1H-1, 135–140 cm) and remained near 10^3 cells/cm³ to the basalt with a few samples below MDL (Fig. F65).

A subset of the sediment samples was recounted by two additional shipboard microbiologists for cross-comparison. These counts were indistinguishable from the initial counts. Also, several samples from the upper part of the core were counted without cell extraction. In the uppermost sample (329-U1368C-1H-1, 10–15 cm), the nonextracted cell counts were almost one order of magnitude higher, suggesting that either the cell extraction did not retrieve all cells or the nonextracted cell numbers were overestimated because of mineral autofluorescence. Counting of nonextracted samples from deeper horizons exhibited cell abundances that were all below the detection limit with large standard deviations.

Virus abundance

As at Site U1367, most of the sediment samples from Site U1368 contain abundant carbonate. Because autofluorescence of carbonate minerals significantly hampers recognition of VLPs in sediment, we treated the samples with sodium acetate buffer (0.47 M; pH 4.7) instead of water during the extraction process and the carbonates were dissolved by gently shaking the buffered slurries for a few minutes. Further extraction of VLPs followed the protocol described in

“**Microbiology**” in the “Methods” chapter (Expedition 329 Scientists, 2011a). Samples from Hole U1368C were taken at a high depth resolution (Table T15). A subset of these samples was used for shipboard counting of VLPs. Additional samples were preserved at -80°C for shore-based analysis.

For the uppermost sample (329-U1368C-1H-1, 10–20 cm), 1.4×10^6 VLP/cm³ were observed. VLP abundance decreases rapidly within the upper meter of the sediment column (Fig. F65). VLP abundance in Sample 1H-2, 110–120 cm, is $\sim 10^5$ VLP/cm³, and VLP abundance decreases slightly with depth. Samples from deeper horizons (Sections 329-U136C-2H-1, 2H-3, and 2H-5) were not counted because the ship movement during transit prevented additional shipboard VLP abundance estimates from Site U1367.

Cultivation

Sediment samples

Multiple cultivations were initiated onboard using a variety of media for heterotrophic (both aerobic and anaerobic) and autotrophic microorganisms. The core samples were subsampled aseptically with sterilized tip-cut syringes to make slurries for inoculation in liquid or on solid media (Table T16). Additional samples were stored in N₂-flushed serum bottles or in syringes packed in sterile foil packs and stored at 4°C (referred to as SLURRY in Table T16) for future shore-based cultivation experiments. For use in future cultivation experiments, the filtered bottom seawater was transferred to sterile 50 mL serum bottles, sparged for 5 min with N₂, and capped with rubber stoppers and aluminum crimp caps. The bottles were stored at 4°C for preparing liquid media on shore.

Surface seawater control sample

A surface seawater sample was collected from Site U1368 with a sterile 500 mL glass bottle immediately after the *JOIDES Resolution* arrived at the site. Cultivation of aerobic heterotrophic bacteria in the seawater sample was performed on marine agar and marine R2A plates and in liquid medium SPG-9 (see Table T8 in the “Methods” chapter [Expedition 329 Scientists, 2011a]) at 25°C . No visible colonies were observed on either the marine agar or R2A plates after 1 week of incubation, whereas very good growth was observed in the SPG-9 medium after 1 day of incubation. Highly motile, curved rods were observed under the phase-contrast microscope.

Bottom seawater samples were collected from the uppermost cores (1H) in Holes U1368A–U1368D in a sterilized plastic bag and immediately stored at 4°C . Aerobic heterotrophic bacteria were cultured at 25°C

for 3 days. The abundance of cultivable aerobic heterotrophic bacteria on marine agar and R2A plates were ~ 200 and ~ 150 colony-forming units/mL, respectively, which is in marked contrast to numbers obtained from surface seawater as described above.

Molecular analyses

Sediment samples

Whole-round cores were taken throughout the entire sediment column and transferred to -80°C freezers for storage. These samples will be used to determine microbial community composition and the presence or absence of several functional genes. Four 10 cm whole-round core samples were taken as routine microbiology samples (curatorial code MBIO) and stored at -80°C . These samples will be stored at -80°C at the core repositories for future biological sample requests.

Deep seawater control sample

As a control sample for shore-based molecular analysis, ~ 300 mL of bottom seawater was collected from the mudline cores (1H) of Holes U1368A–U1368D in a sterile plastic bag and immediately stored at 4°C in the Microbiology Laboratory. The bottom seawater sample was then filtered through $0.2 \mu\text{m}$ polycarbonate membrane filters under aseptic conditions and stored at -80°C for shore-based microbiological analyses.

Basalt samples

Samples of basement basalt (Sections 329-U1368F-2R-1, 2R-4, 4R-2, 5R-3, 7R-3, 9R-1, 13R-3, and 14R-1), as well as sediment, basalt, and alteration material from the sediment/basalt interface (Sections 329-U1368B-2H-1 and 3H-1 and 329-U1368D-2H-CC) were processed for microbiological and (bio-)mineralogical analyses. Before being frozen at -80°C , each basalt piece was washed at least twice with 3% NaCl solution, briefly flamed, and crushed into powder (see “**Microbiology**” in the “Methods” chapter [Expedition 329 Scientists, 2011a]). Some portions of these powdered samples were incubated at 4°C in RNAlater solution overnight and then frozen at -80°C for shore-based DNA and RNA analyses.

Fluorescence in situ hybridization analysis

Duplicate 10 cm³ subcores of sediment from Sections 329-U1368F-1H-1, 1H-2, 1H-5, 2H-4, and 2H-5 were fixed as described in “**Microbiology**” in the “Methods” chapter (Expedition 329 Scientists, 2011a) for shore-based fluorescence in situ hybridization analyses.

Radioactive and stable isotope tracer incubation experiments

Stable isotope (^{13}C and ^{15}N) experiments to measure carbon and nitrogen uptake activities were initiated on board in the Isotope Isolation Van. Sediment subcores (15 cm^3) were taken from the inner part of 20 cm whole-round cores, placed in a sterile glass vials, flushed with N_2 , sealed with a rubber stopper, and stored until processing in the core refrigerator on the Hold Deck (see “**Microbiology**” in the “Methods” chapter [Expedition 329 Scientists, 2011a]). From Site U1368, four whole-round cores (Sections 329-U1368D-1H-2, 1H-5, 2H-4, and 2H-5) were processed for stable isotope tracer incubation experiments, as described in “**Microbiology**” in the “Site U1365” chapter (Expedition 329 Scientists, 2011b).

Slurries were prepared from the following whole-round intervals from Site U1368 for experiments investigating potential metabolic activities (i.e., assimilation and dissimilative respiration) using radio and stable isotopes: Samples 329-U1368C-1H-3, 90–100 cm; 2H-1, 80–90 cm; and 2H-5, 80–90 cm (see “**Microbiology**” in the “Methods” chapter [Expedition 329 Scientists, 2011a]). In addition, ~40 mL of 1/5 diluted (v/v) slurries from two samples (1H-3, 90–100 cm, and 2H-5, 80–90 cm) were used for cell viability studies with ^{14}C -labeled compounds (ATP, leucine, and thymidine). Potential metabolic activity was also tested by adding 2.5 mL of ^{18}O -labeled water (H_2^{18}O) to aliquots (5 mL) of the same slurries and incubated at 4°C . These slurries from Site U1368 were processed together with other samples from Sites U1365, U1366, and U1367 in the Isotope Isolation Van.

For sulfate reduction rate measurements, four whole-round cores were collected from Hole U1368C (Samples 329-U1368C-1H-1, 85–90 cm; 1H-5, 85–90 cm; 2H-3, 85–90 cm; and 2H-5, 35–40 cm). Five to seven subsamples (~2.5 cm^3) were collected directly from each whole-round core for shore-based distillation analysis of ^{35}S -labeled reduced sulfur (see “**Microbiology**” in the “Methods” chapter [Expedition 329 Scientists, 2011a]).

Samples of basement basalt (Sections 329-U1368F-2R-1, 2R-4, 4R-2, 5R-3, 7R-3, 9R-1, 13R-3, and 14R-1) as well as sediment, basalt, and alteration material from the sediment/basalt interface (Sections 329-U1368B-2H-1 and 3H-1 and 329-U1368D-2H-CC) were stored at 4°C . Incubations of samples from the sediment/basalt interface with ^{15}N -labeled NO_3^- as a nitrogen source and ^{13}C -labeled HCO_3^- or acetate as a carbon source were initiated onboard.

Contamination assessment

Perfluorocarbon tracer

We used perfluoromethylcyclohexane as a PFT to monitor the level of drilling fluid contamination in sediment cores. PFT was constantly injected into drilling fluids during APC coring in Holes U1368C and U1368D. Sediment subcore samples (3 cm^3) were taken on the catwalk and from whole-round cores in the Hold Deck refrigerator and stored in vials with 2 mL of water for postexpedition gas chromatography measurement (see “**Microbiology**” in the “Methods” chapter [Expedition 329 Scientists, 2011a]).

Particulate tracer

Fluorescent microspheres (0.5 μm diameter) were used for contamination testing during basaltic basement coring (see “**Microbiology**” in the “Methods” chapter [Expedition 329 Scientists, 2011a]). This approach is not quantitative but provides evidence for the occurrence of contamination, even in interior structures of basaltic samples (e.g., microfractures and veins). For detection of microspheres, small rock pieces and/or surface wash solutions were stored in 3% NaCl solution for microscopic observation.

Contamination was first examined on the untreated exterior by removing small pieces of rock using a flame-sterilized hammer and chisel. The rock surface was washed twice with 25 mL 3% NaCl solution in a sterile plastic bag. Small pieces of the washed exterior were removed using a flame-sterilized hammer and chisel, and the wash solutions were pooled in a 50 mL centrifuge tube. After the washing step, the rock surface was briefly flamed. After flaming, the rock was cracked open using a flame-sterilized hammer and chisel, and small pieces from the interior and exterior were separately inspected for the presence of microspheres using epifluorescence microscopy.

Microscopic counts of microspheres in subsamples at each cleaning step are shown in Figure F66 and Table T17. The unit in the figure is either per cubic centimeter of rock for crushed basalt pieces or per cubic centimeter of post-surface-wash solution. Eight basalt cores (Sections 329-U1368F-2R-1, 2R-4, 4R-2, 5R-3, 7R-3, 9R-1, 13R-3, and 14R-1) contained high abundances of microspheres, whereas no microspheres were detected from one untreated core (Section 5R-3) and two cores after washing and flaming (Sections 2R-1 and 2R-4). Even after the cleaning steps, microspheres were detected from the interior in the four lower cores (Sections 5R-3, 7R-3, 13R-3, and 14R-1). These results indicate that unlike the cores from Hole U1365E, many of the cores from

Hole U1368F were susceptible to drilling fluid contamination.

References

- Alvarez Zarikian, C.A., 2009. Data report: late Quaternary ostracodes at IODP Site U1314 (North Atlantic Ocean). In Channell, J.E.T., Kanamatsu, T., Sato, T., Stein, R., Alvarez Zarikian, C.A., Malone, M.J., and the Expedition 303/306 Scientists, *Proc. IODP*, 303/306: College Station, TX (Integrated Ocean Drilling Program Management International, Inc.). doi:10.2204/iodp.proc.303306.213.2009
- Alvarez Zarikian, C.A., Stepanova, A.Y., and Grütznert, J., 2009. Glacial–interglacial variability in deep sea ostracod assemblage composition at IODP Site U1314 in the subpolar North Atlantic. *Mar. Geol.*, 258(1–4):69–87. doi:10.1016/j.margeo.2008.11.009
- Ayress, M., Neil, H., Passlow, V., and Swanson, K., 1997. Benthonic ostracods and deep water masses: a qualitative comparison of southwest Pacific, Southern and Atlantic Oceans. *Palaeogeogr., Palaeoclimatol., Palaeoecol.*, 131(3–4):287–302. doi:10.1016/S0031-0182(97)00007-2
- Berggren, W.A., Kent, D.V., Swisher, C.C., III, and Aubry, M.-P., 1995. A revised Cenozoic geochronology and chronostratigraphy. In Berggren, W.A., Kent, D.V., Aubry, M.-P., and Hardenbol, J. (Eds.), *Geochronology, Time Scales and Global Stratigraphic Correlation*. Spec. Publ.—SEPM (Soc. Sediment. Geol.), 54:129–212.
- Chaisson, W.P., and Pearson, P.N., 1997. Planktonic foraminifer biostratigraphy at Site 925: middle Miocene–Pleistocene. In Shackleton, N.J., Curry, W.B., Richter, C., and Bralower, T.J. (Eds.), *Proc. ODP, Sci. Results*, 154: College Station, TX (Ocean Drilling Program), 3–31. doi:10.2973/odp.proc.sr.154.104.1997
- Cronin, T.M., Boomer, I., Dwyer, G.S., and Rodriguez Lázaro, J., 2002. Ostracoda and paleoceanography. In Holmes, J.A., and Chivas, A.R. (Eds.), *The Ostracoda: Applications in Quaternary Research*. Geophys. Monogr., 131:99–119.
- Dingle, R.V., and Lord, A.R., 1990. Benthic ostracods and deep water masses in the Atlantic Ocean. *Palaeogeogr., Palaeoclimatol., Palaeoecol.*, 80(3–4):213–235. doi:10.1016/0031-0182(90)90133-R
- D’Hondt, S., Abrams, L.J., Anderson, R., Dorrance, J., Durbin, A., Ellett, L., Ferdelman, T., Fischer, J., Forschner, S., Fuldauer, R., Goldstein, H., Graham, D., Griffith, W., Halm, H., Harris, R., Harrison, B., Hasiuk, F., Horn, G., Kallmeyer, J., Lever, M., Meyer, J., Morse, L., Moser, C., Murphy, B., Nordhausen, A., Parry, L., Pockalny, R., Puschell, A., Rogers, J., Schrum, H., Smith, D.C., Soffientino, B., Spivack, A.J., Stancin, A., Steinman, M., and Walczak, P., 2011. KNOX-02RR: drilling site survey—life in seafloor sediments of the South Pacific Gyre. In D’Hondt, S., Inagaki, F., Alvarez Zarikian, C.A., and the Expedition 329 Scientists, *Proc. IODP*, 329: Tokyo (Integrated Ocean Drilling Program Management International, Inc.). doi:10.2204/iodp.proc.329.112.2011
- D’Hondt, S., Spivack, A.J., Pockalny, R., Ferdelman, T.G., Fischer, J.P., Kallmeyer, J., Abrams, L.J., Smith, D.C., Graham, D., Hasiuk, F., Schrum, H., and Stancine, A.M., 2009. Subseafloor sedimentary life in the South Pacific Gyre. *Proc. Natl. Acad. Sci. U. S. A.*, 106(28):11651–11656. doi:10.1073/pnas.0811793106
- Ekdale, A.A., Bromley, R.G., and Pemberton, S.G. (Eds.), 1984. *Ichnology: The Use of Trace Fossils in Sedimentology and Stratigraphy*. SEPM Short Course, 15.
- Expedition 329 Scientists, 2011a. Methods. In D’Hondt, S., Inagaki, F., Alvarez Zarikian, C.A., and the Expedition 329 Scientists, *Proc. IODP*, 329: Tokyo (Integrated Ocean Drilling Program Management International, Inc.). doi:10.2204/iodp.proc.329.102.2011
- Expedition 329 Scientists, 2011b. Site U1365. In D’Hondt, S., Inagaki, F., Alvarez Zarikian, C.A., and the Expedition 329 Scientists, *Proc. IODP*, 329: Tokyo (Integrated Ocean Drilling Program Management International, Inc.). doi:10.2204/iodp.proc.329.103.2011
- Fischer, J.P., Ferdelman, T.G., D’Hondt, S., Røy, H., and Wenzhöfer, F., 2009. Oxygen penetration deep into the sediment of the South Pacific gyre. *Biogeosciences*, 6:1467–1478. http://www.biogeosciences.net/6/1467/2009/bg-6-1467-2009.pdf
- Gradstein, F.M., Ogg, J.G., and Smith, A. (Eds.), 2004. *A Geologic Time Scale 2004*: Cambridge (Cambridge Univ. Press). http://cambridge.org/uk/catalogue/catalogue.asp?isbn=9780521781428
- Heath, G.R., and Dymond, J., 1977. Genesis and transformation of metalliferous sediments from the East Pacific Rise, Bauer Deep, and Central Basin, Northwest Nazca Plate. *Geol. Soc. Am. Bull.*, 88(5):723–733. doi:10.1130/0016-7606(1977)88<723:GATOMS>2.0.CO;2
- Laverne, C., Belarouchi, A., and Honnorez, J., 1996. Alteration mineralogy and chemistry of the upper oceanic crust from Hole 896A, Costa Rica rift. In Alt, J.C., Kinoshita, H., Stokking, L.B., and Michael, P.J. (Eds.), *Proc. ODP, Sci. Results*, 148: College Station, TX (Ocean Drilling Program), 151–170. doi:10.2973/odp.proc.sr.148.127.1996
- Pearson, P.N., and Chaisson, W.P., 1997. Late Paleocene to middle Miocene planktonic foraminifer biostratigraphy of the Ceara Rise. In Shackleton, N.J., Curry, W.B., Richter, C., and Bralower, T.J. (Eds.), *Proc. ODP, Sci. Results*, 154: College Station, TX (Ocean Drilling Program), 33–68. doi:10.2973/odp.proc.sr.154.106.1997
- Shackleton, N.J., Crowhurst, S.J., Weedon, G.P., and Laskar, J., 1999. Astronomical calibration of Oligocene–Miocene time. In Shackleton N.J., McCave, I.N., and Graham, P.W. (Eds.), *Astronomical (Milankovitch) Calibration of the Geological Time-Scale*. Philos. Trans. R. Soc., Ser. A., 357(1757):1907–1929. doi:10.1098/rsta.1999.0407
- Stow, D.A.V., and Lovell, J.P.B., 1979. Contourites: their recognition in modern and ancient sediments. *Earth Sci. Rev.*, 14(3):251–291. doi:10.1016/0012-8252(79)90002-3
- Talley, L.D., 2007. *Hydrographic Atlas of the World Ocean Circulation Experiment (WOCE) (Vol. 2): Pacific Ocean*. Spar-

- row, M., Chapman, P., and Gould, J. (Eds.): Southampton, U.K. (International WOCE Project Office). http://www-pord.ucsd.edu/whp_atlas/pacific_index.html
- Teagle, D.A.H., Alt, J.C., Bach, W., Halliday, A.N., and Erzinger, J., 1996. Alteration of upper ocean crust in a ridge-flank hydrothermal upflow zone: mineral, chemical, and isotopic constraints from Hole 896A. In Alt, J.C., Kinoshita, H., Stokking, L.B., and Michael, P.J. (Eds.), *Proc. ODP, Sci. Results*, 148: College Station, TX (Ocean Drilling Program), 119–150. doi:10.2973/odp.proc.sr.148.113.1996
- Teagle, D.A.H., Alt, J.C., Umino, S., Miyashita, S., Banerjee, N.R., Wilson, D.S., and Expedition 309/312 Scientists, 2006. *Proc. IODP*, 309/312: Washington, DC (Integrated Ocean Drilling Program Management International, Inc.). doi:10.2204/iodp.proc.309312.2006
- Tebbens, S.F., and Cande, S.C., 1997. Southeast Pacific tectonic evolution from early Oligocene to Present. *J. Geophys. Res., [Solid Earth]*, 102(B6):12061–12084. doi:10.1029/96JB02582
- Uchman, A., 2007. Deep-sea ichnology: development of major concepts. In Miller, W., III (Ed.), *Trace Fossils: Concepts, Problems, Prospects*: Amsterdam (Elsevier), 248–267. doi:10.1016/B978-044452949-7/50141-8
- Ujiié, H., 1984. A middle Miocene hiatus in the Pacific region: its stratigraphic and paleoceanographic significance. *Palaeogeogr., Palaeoclimatol., Palaeoecol.*, 46(1–3):143–164. doi:10.1016/0031-0182(84)90031-2
- Wade, B.S., Pearson, P.N., Berggren, W.A., and Pälike, H., 2011. Review and revision of Cenozoic tropical planktonic foraminiferal biostratigraphy and calibration to the geomagnetic polarity and astronomical time scale. *Earth-Sci. Rev.*, 104(1–3):111–142. doi:10.1016/j.earsci-rev.2010.09.003
- Whatley, R.C., and Ayress, M., 1988. Pandemic and endemic distribution patterns in Quaternary deep-sea Ostracoda. In Hanai, T., Ikeya, N., and Ishizaki, K. (Eds.), *Evolutionary Biology of Ostracoda: Its Fundamentals and Applications—Proc. Ninth Int. Symp. Ostracoda*. Dev. Palaeontol. Stratigr., 11:739–755. doi:10.1016/S0920-5446(08)70219-X

Publication: 13 December 2011
MS 329-106

Figure F1. Multibeam bathymetry of the Site U1368 survey area with the KNOX-02RR survey track overlain.

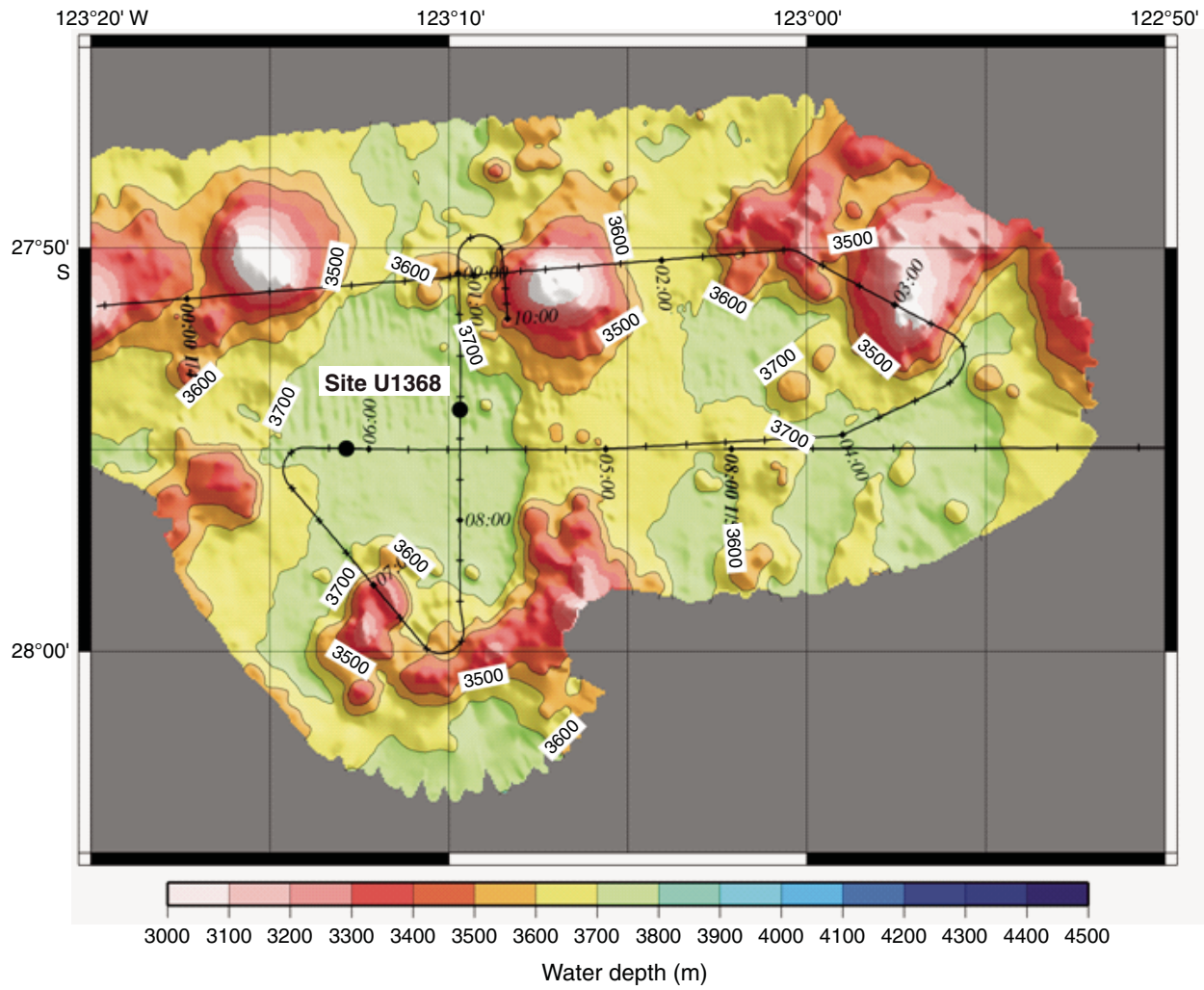


Figure F2. KNOX-02RR seismic survey track, Site U1368. sol = start of seismic line, eol = end of seismic line, z = time (Greenwich Mean Time), sp = shotpoint.

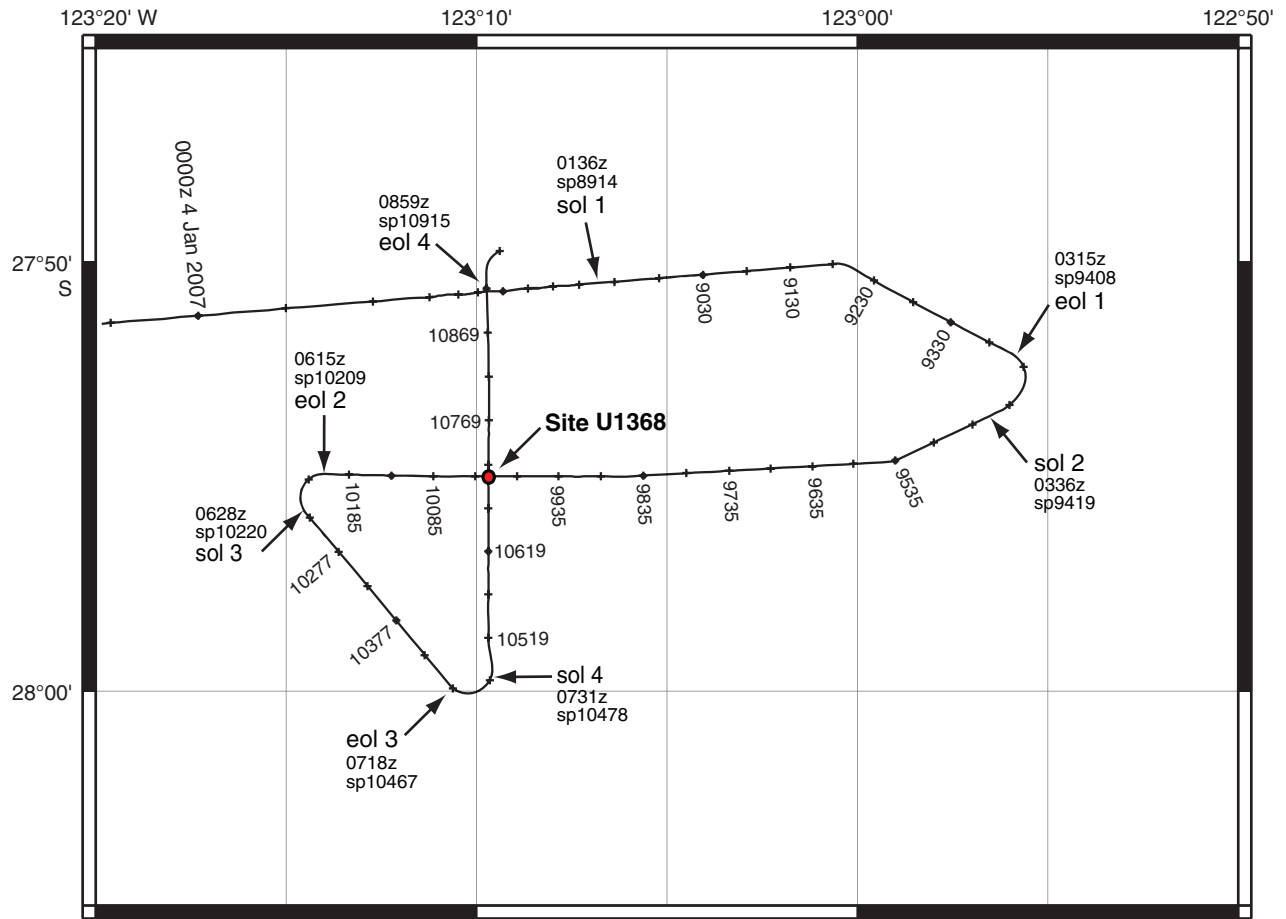


Figure F3. Portion of KNOX-02RR Channel 48 of MCS Line 4 across Site U1368. z = time (Greenwich Mean Time), SP = shotpoint, VE = vertical exaggeration.

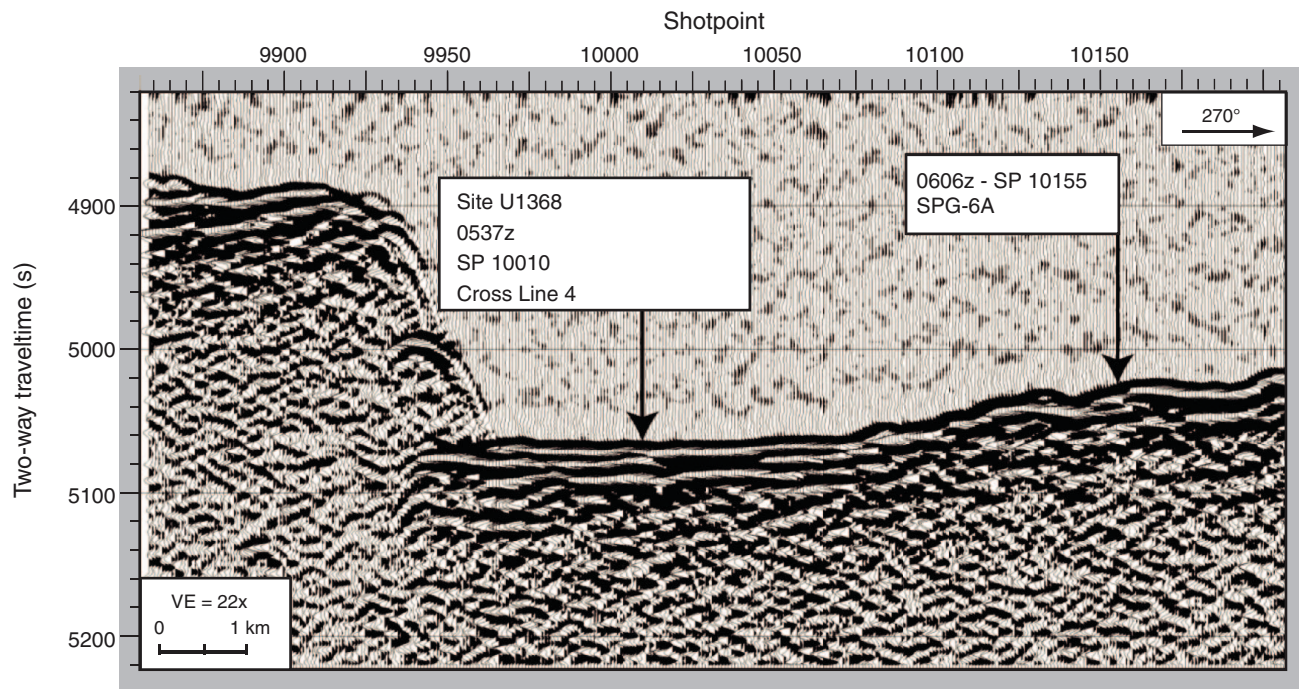




Figure F4. Portion of KNOX-02RR Channel 48 of MCS Line 4 crossing MCS Line 2, northeast of Site U1368. z = time (Greenwich Mean Time), SP = shotpoint, MORB = mid-ocean-ridge basalt, WD = water depth, SCS = single-channel seismic, BP = band-pass, AGC = automatic gain control, VE = vertical exaggeration.

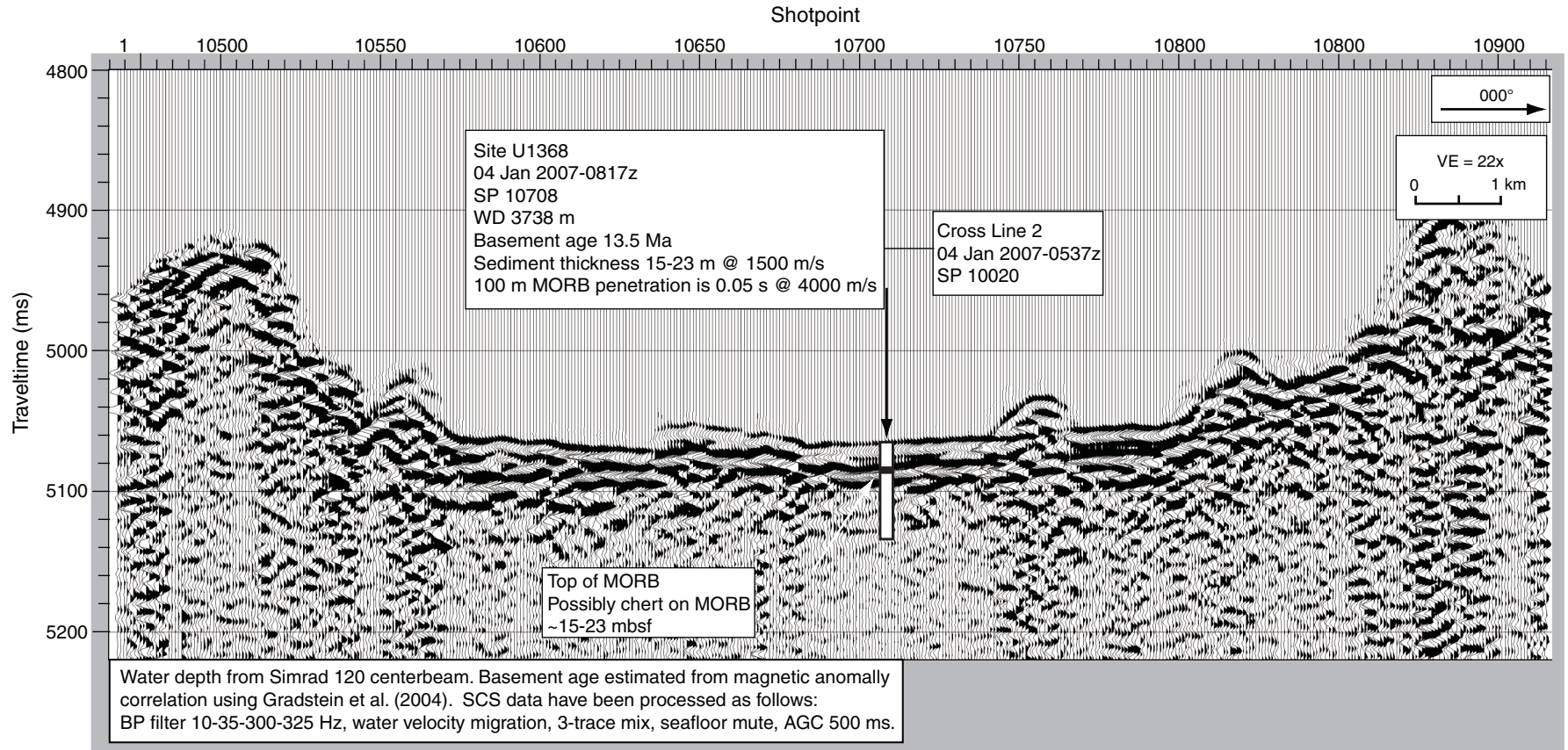


Figure F5. Portion of KNOX-02RR 3.5 kHz seismic Line 2 across Site U1368.

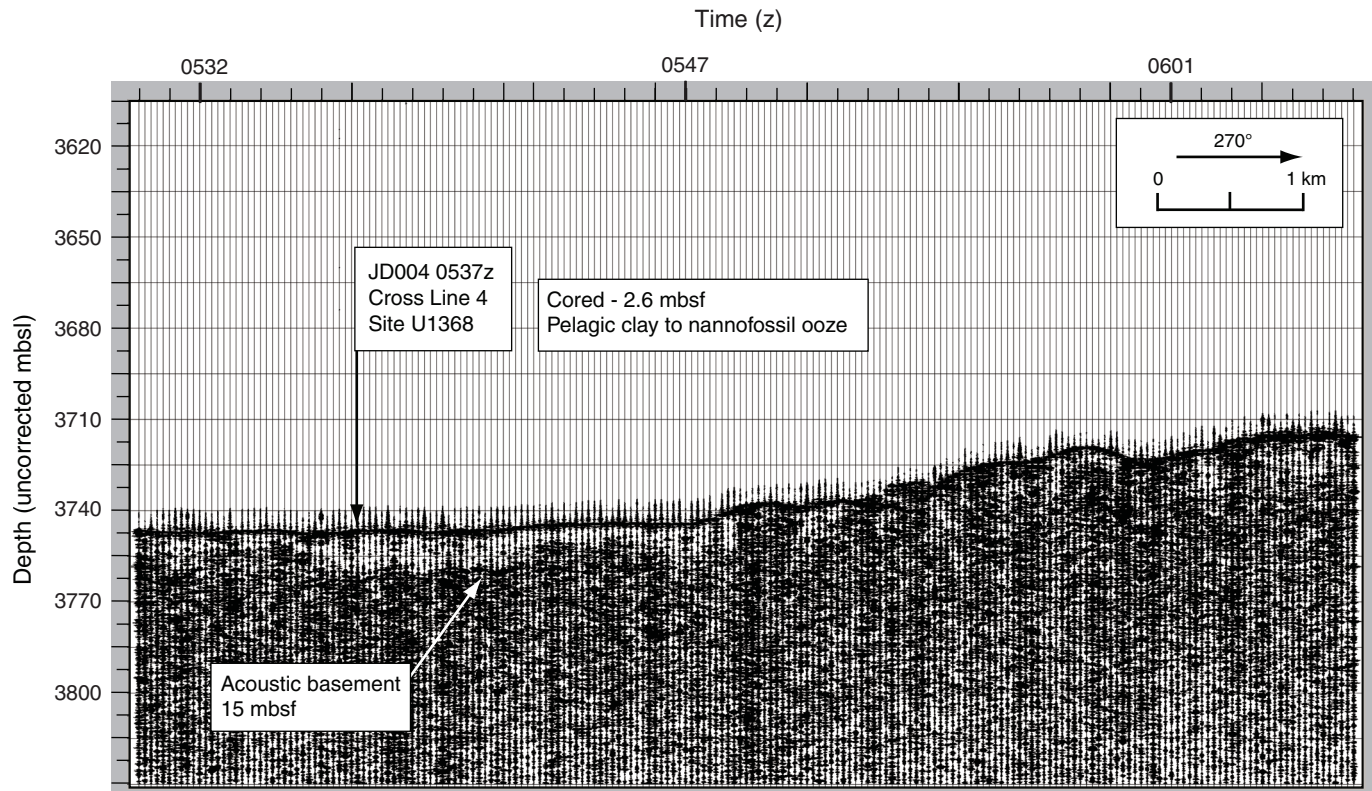


Figure F6. Portion of KNOX-02RR 3.5 kHz seismic Line 4 crossing 3.5 kHz seismic Line 2, northeast of Site U1368.

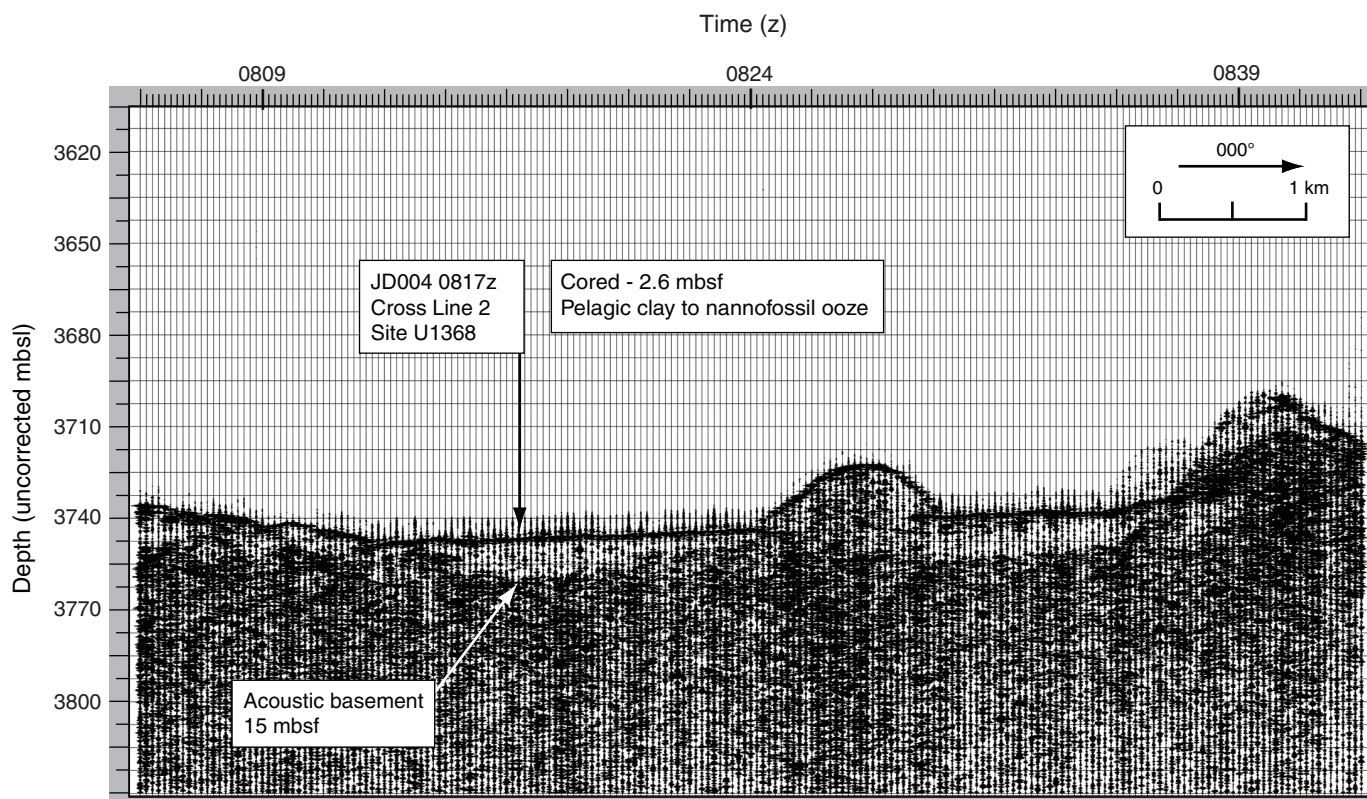


Figure F7. Lithology summary and physical property data. MS = magnetic susceptibility, GRA = gamma ray attenuation, K = absolute potassium concentration, based on analysis of spectral gamma ray responses, NGR = natural gamma radiation, RSO = red-brown to yellow-brown semiopaque oxide. A. Hole U1368B. (Continued on next page.)

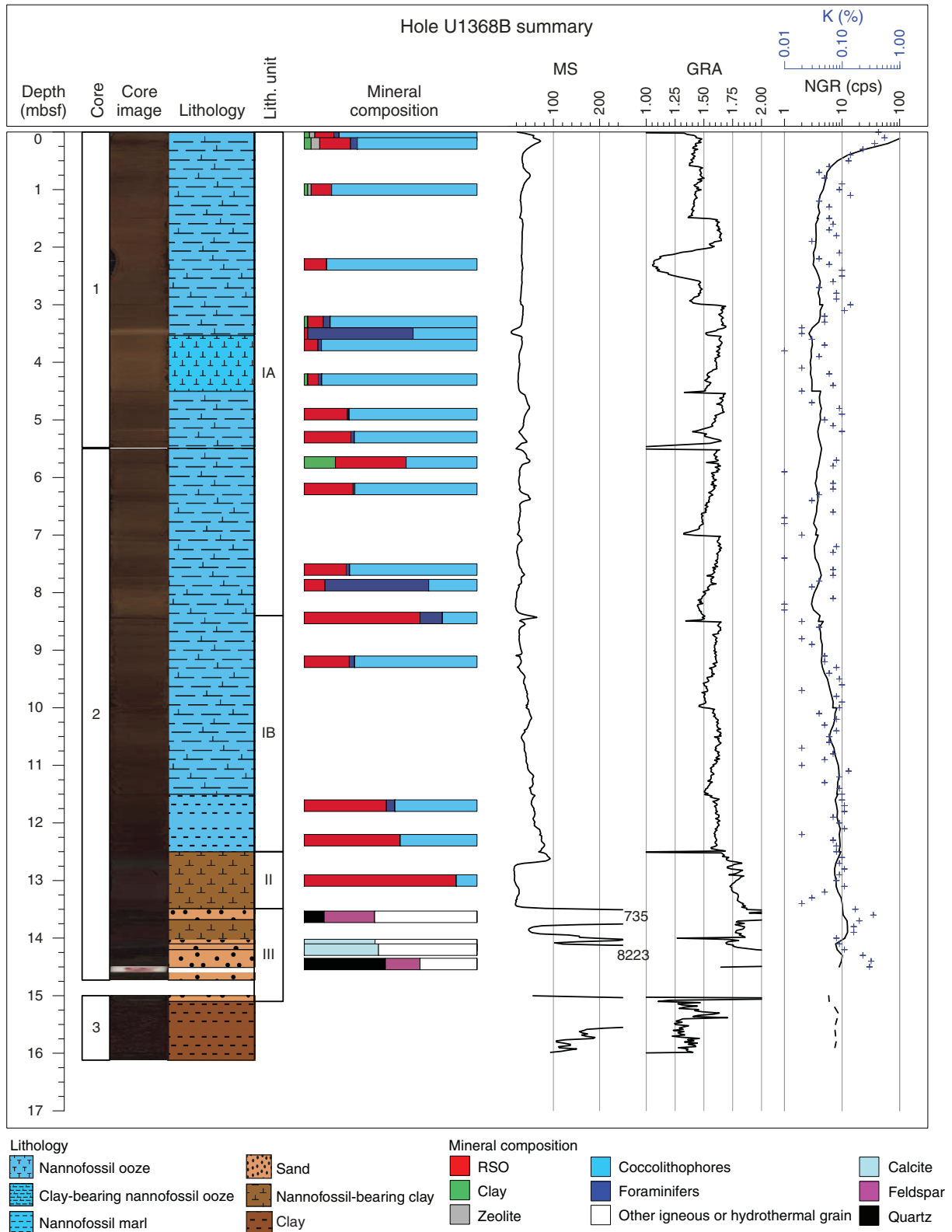


Figure F7(continued). B. Hole U1368E.

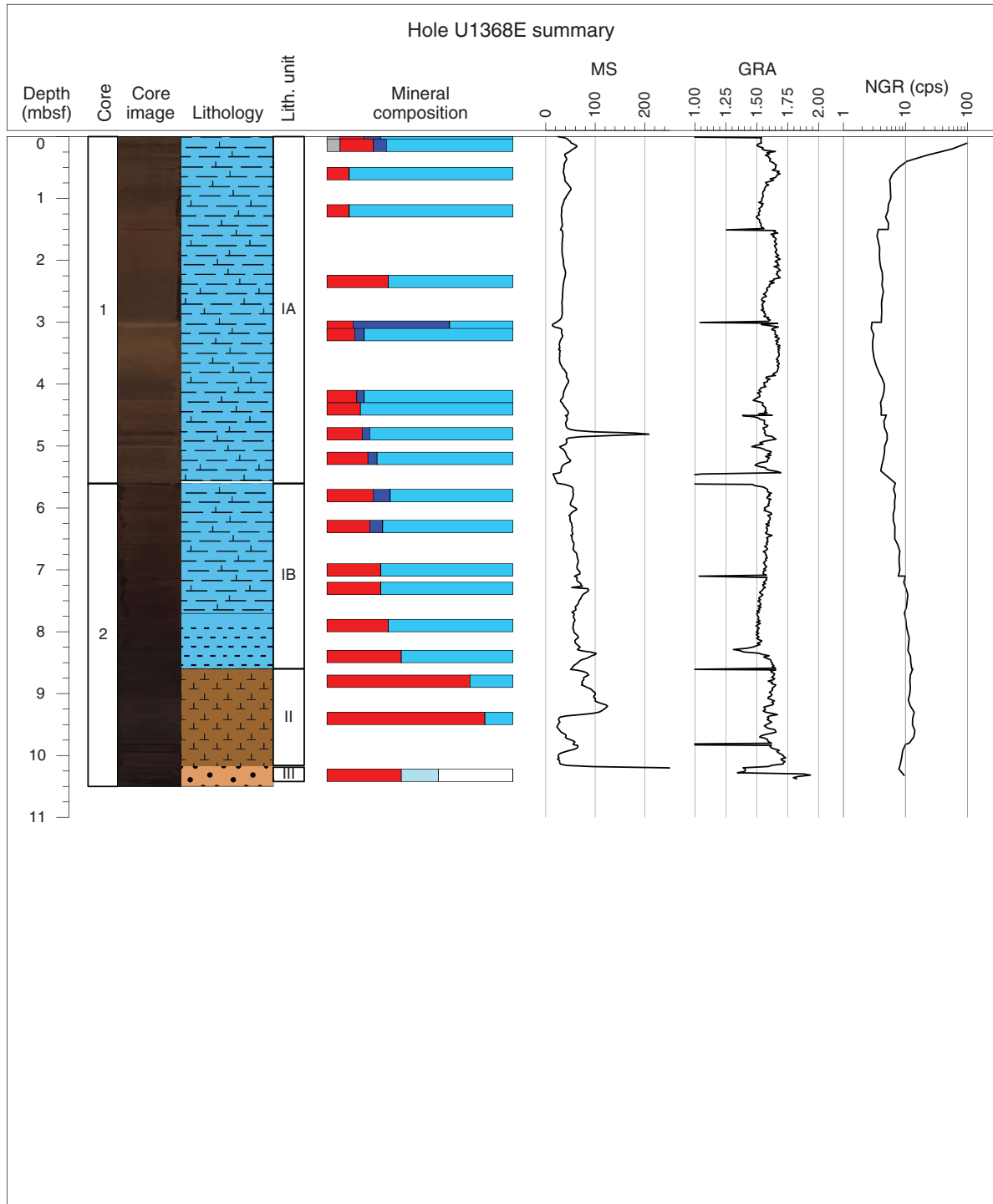


Figure F8. Lithostratigraphic correlations among holes at Site U1368. H1 = thin foraminiferal ooze layer, H2 = yellowish brown nannofossil ooze or clay-bearing nannofossil ooze, H3 = very thin interval (<1 cm) of slightly indurated clay pebbles, H4 = very dark brown nannofossil marl.

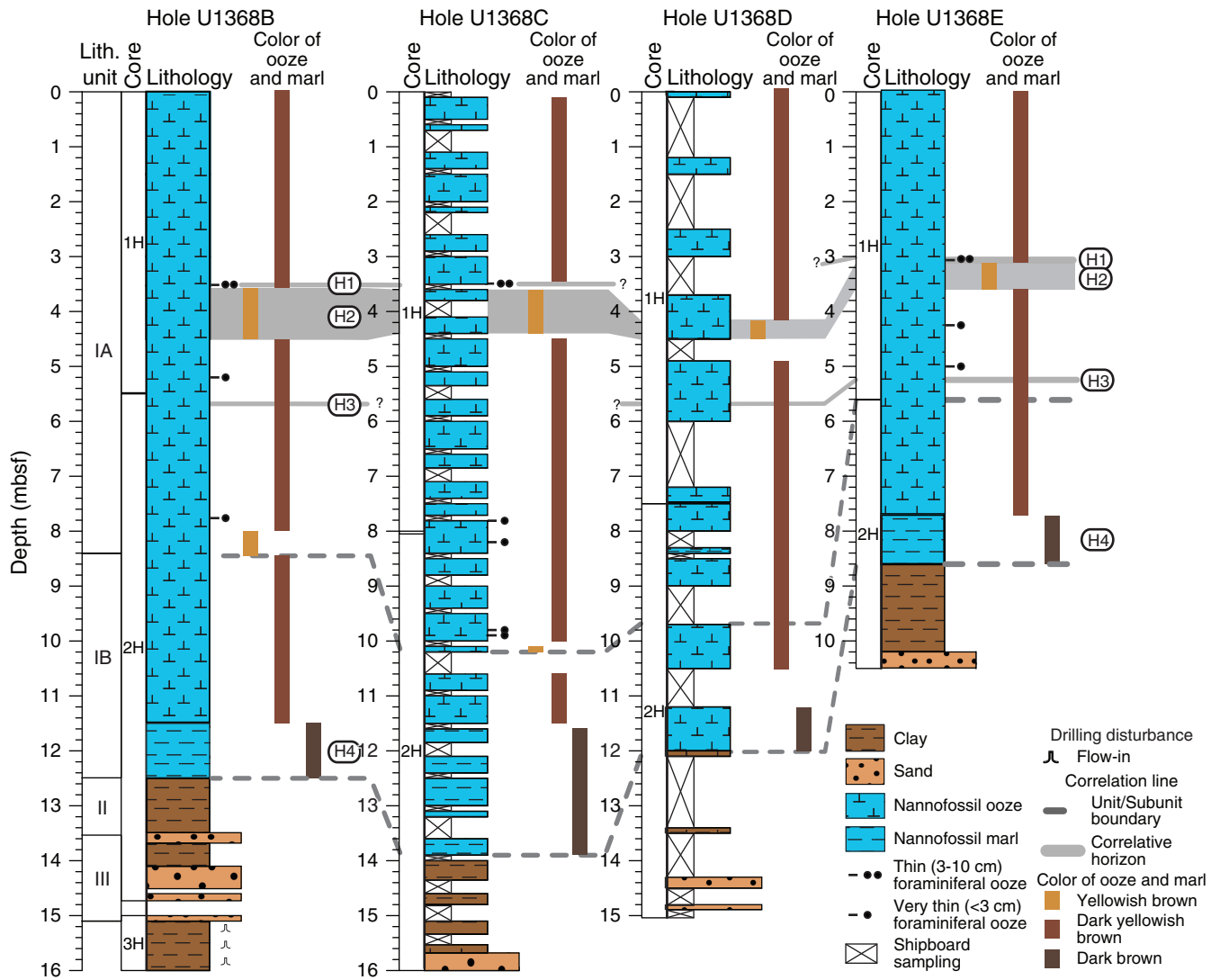




Figure F9. Representative core photographs, Site U1368. **A.** Dark yellowish brown clay-bearing nannofossil ooze in Subunit IA (interval 329-U1368E-1H-2, 5–45 cm). **B.** Yellowish brown clay-bearing nannofossil ooze in Subunit IA. Very pale brown foraminifer sand layer is recognizable at 42–53 cm (interval 329-U1368B-1H-3, 30–70 cm). **C.** Dark yellowish brown nannofossil marl in Subunit IB (interval 329-U1368B-2H-5, 10–50 cm). **D.** Very dark brown nannofossil-bearing clay in Unit II (interval 329-U1368B-2H-6, 50–90 cm). **E.** Gray to dark greenish gray sand in Unit III (interval 329-U1368E-2H-7, 5–45 cm).

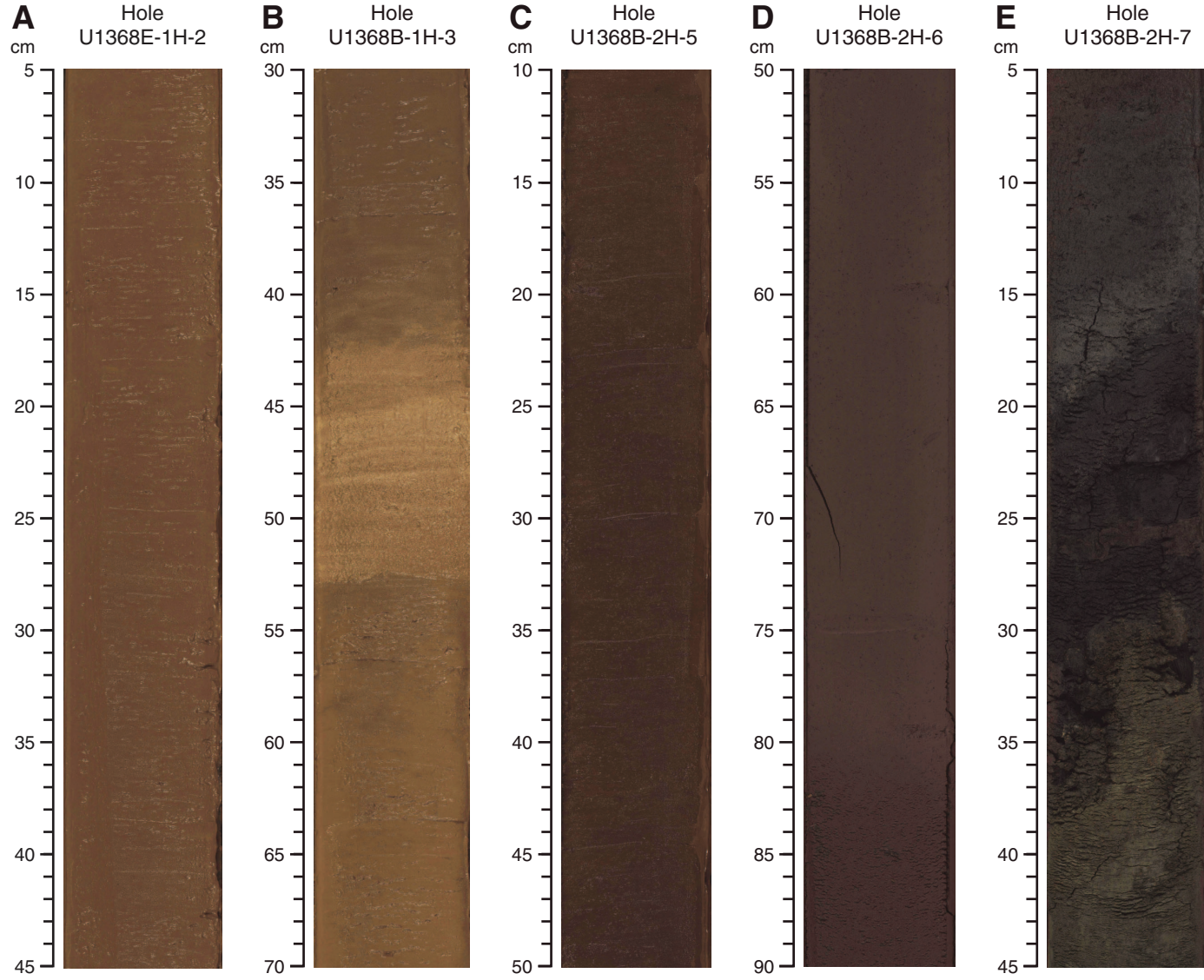


Figure F10. Smear slide photomicrographs of clay-rich sediment, Site U1368. **A.** Clay-bearing nannofossil clay in Subunit IA (Sample 329-U1368B-1H-1, 5 cm). **B.** Nannofossil marl in Subunit IB (Sample 329-U1368B-2H-5, 20 cm). **C.** Nannofossil-bearing clay in Unit II (Sample 329-U1368B-2H-6, 50 cm). **D.** Gray silty sand with numerous unidentified acicular crystals in Unit III (Sample 329-U1368B-2H-7, 12 cm). **E.** Very dark gray silty sand in Unit III (Sample 329-U1368B-2H-7, 20 cm). **F.** Dark greenish gray silty sand in Unit III (Sample 329-U1368B-2H-7, 45 cm).

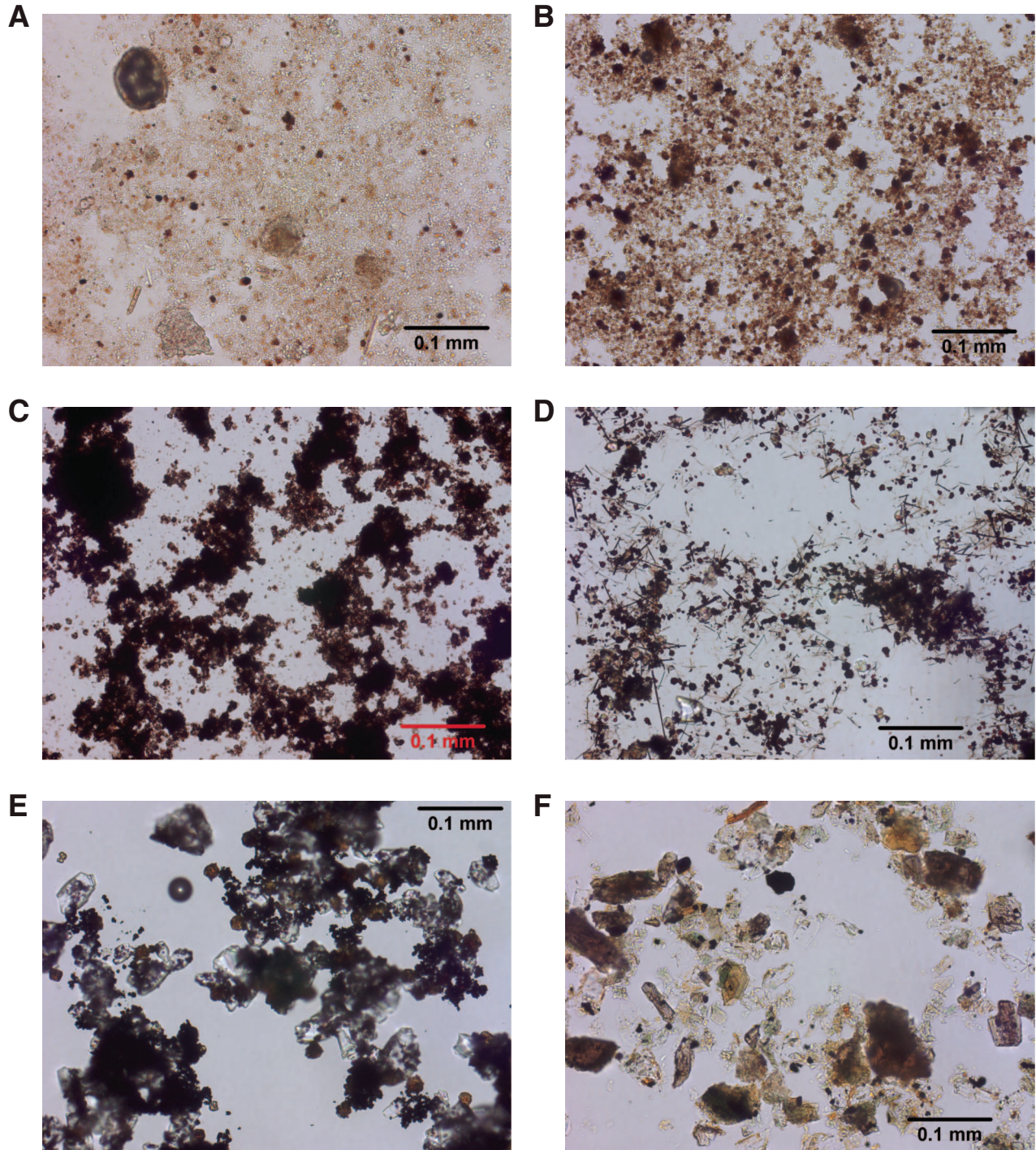


Figure F11. X-ray diffractograms from selected Site U1368 sediment. **A.** Sample from Subunit IA, pretreated with acetic acid but still dominated by the XRD pattern representative of calcite. Smectite clay forms peaks between 5° and $7^\circ 2\theta$. (Continued on next two pages.)

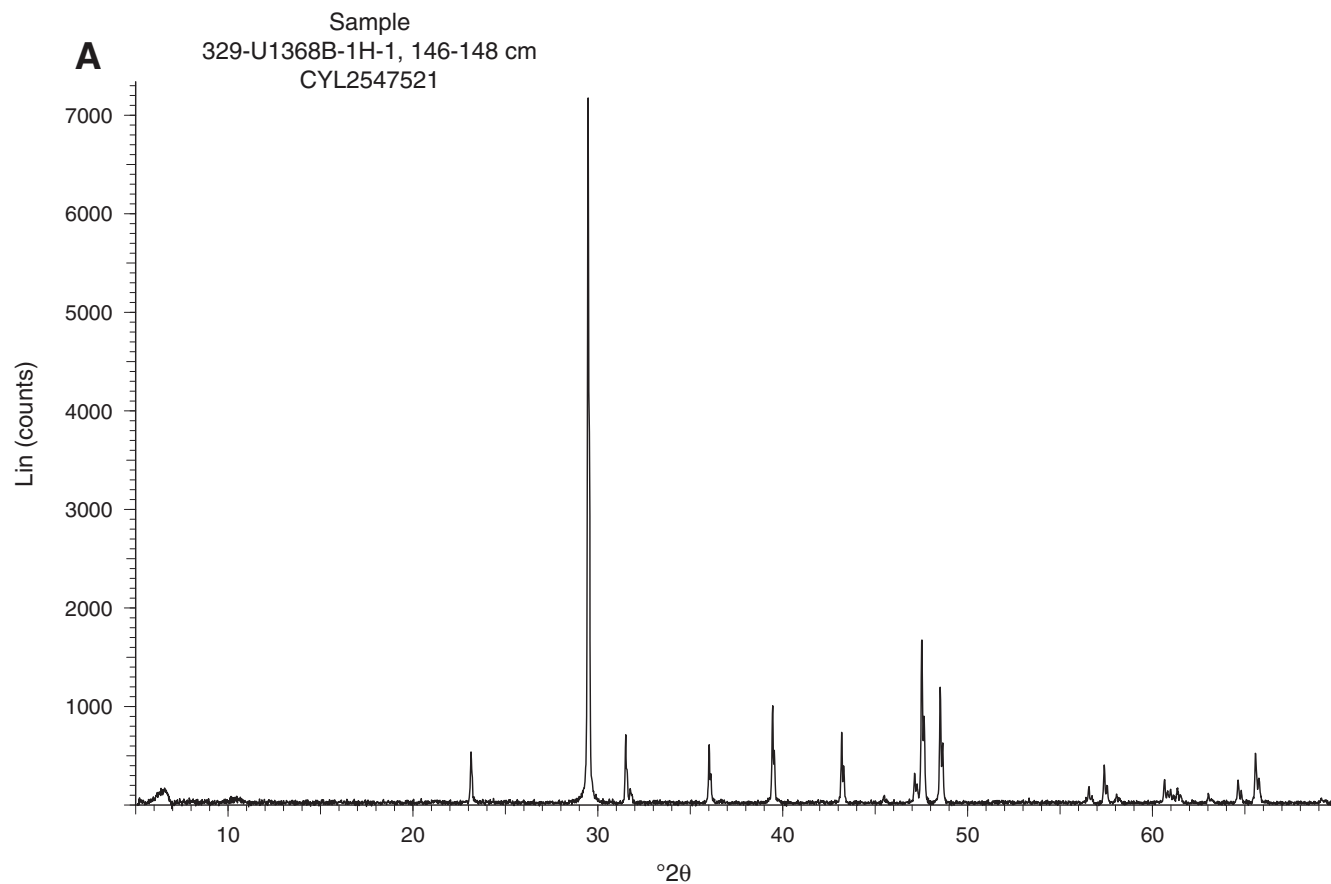


Figure F11 (continued). B. Two examples of XRD patterns from clay-rich sediment near the bottom of Hole U1368B. The pattern from the middle of Unit II (red) and upper part of Unit III (black) illustrate calcite (C), hematite (H), and montmorillonite and vermiculite (MV) content. The pattern from Unit III includes the annotated peak of a mineral identified as calciohelairite (Ch) by XRD pattern matching software. (Continued on next page.)

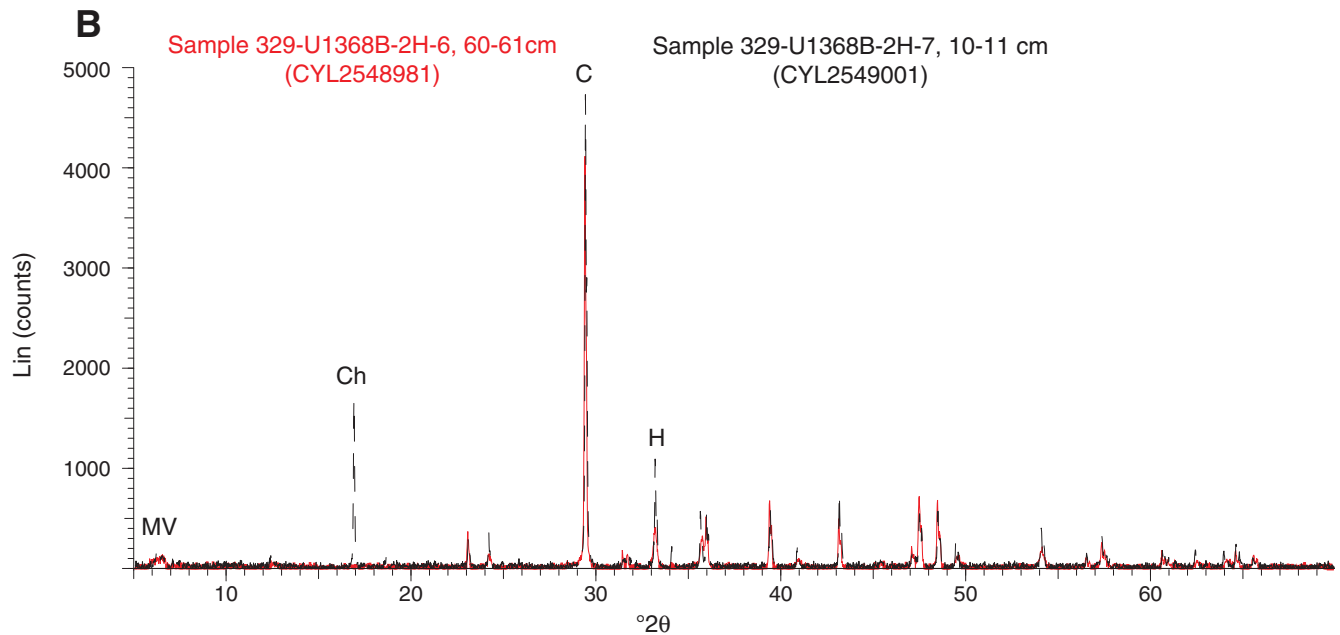


Figure F11 (continued). C. Differing coarse-sediment XRD mineralogy at Site U1368 from the upper (black) and middle (green) sand intervals of Unit III. Note especially the presence/absence of chlorite (Cl) in the two samples. Other labeled peaks represent albite-anorthite (Al/An), augite (Aug), and titanomagnetite (TM).

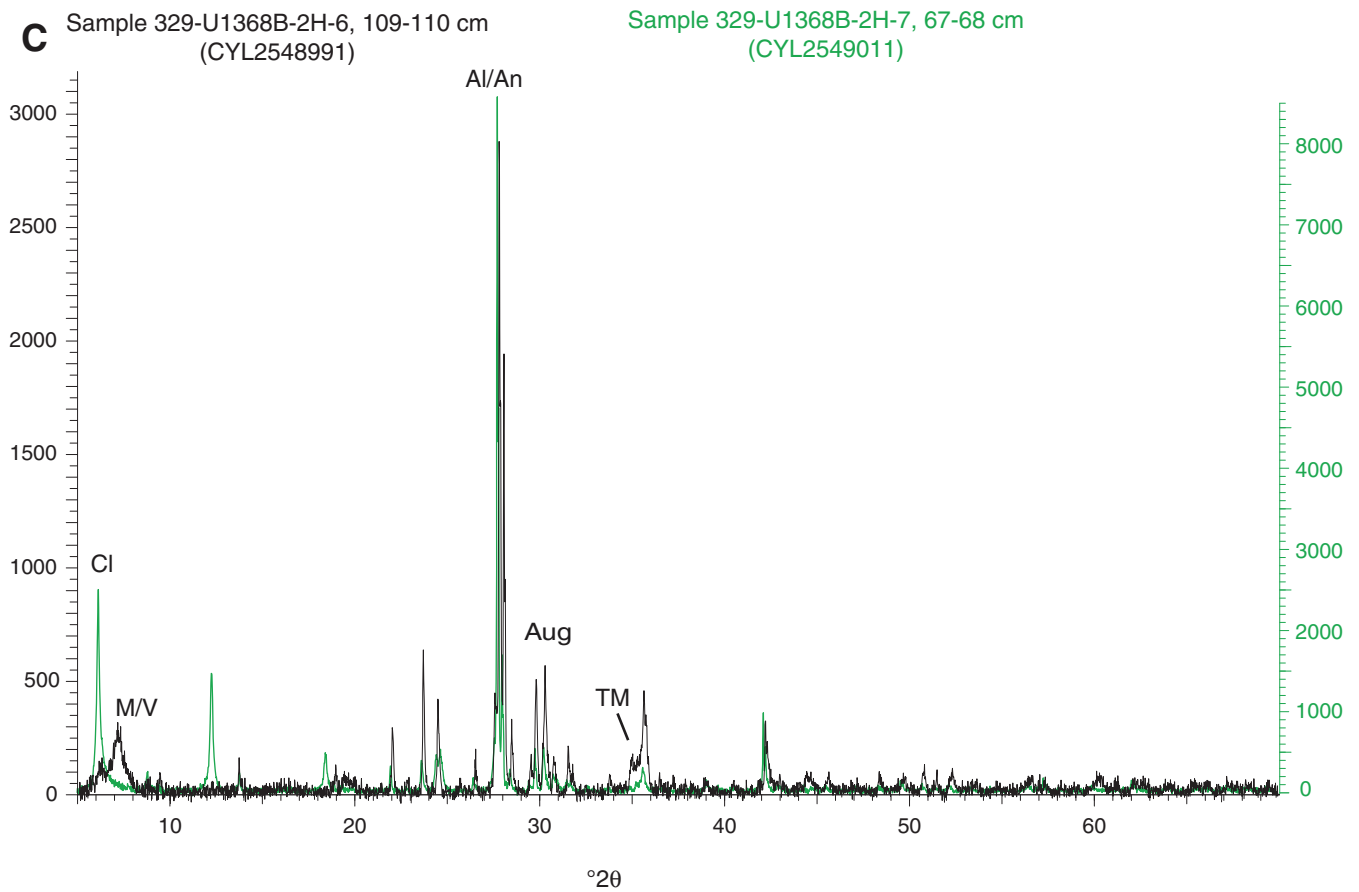


Figure F12. Core images of unit contacts, Site U1368. Images were digitally brightened by 50% to increase visibility of features. **A.** Inclined, pebble-clad, and RSO-enriched contact between Subunit IA (upper interval) and Subunit IB (lower interval). **B.** Contact of Units II and III.

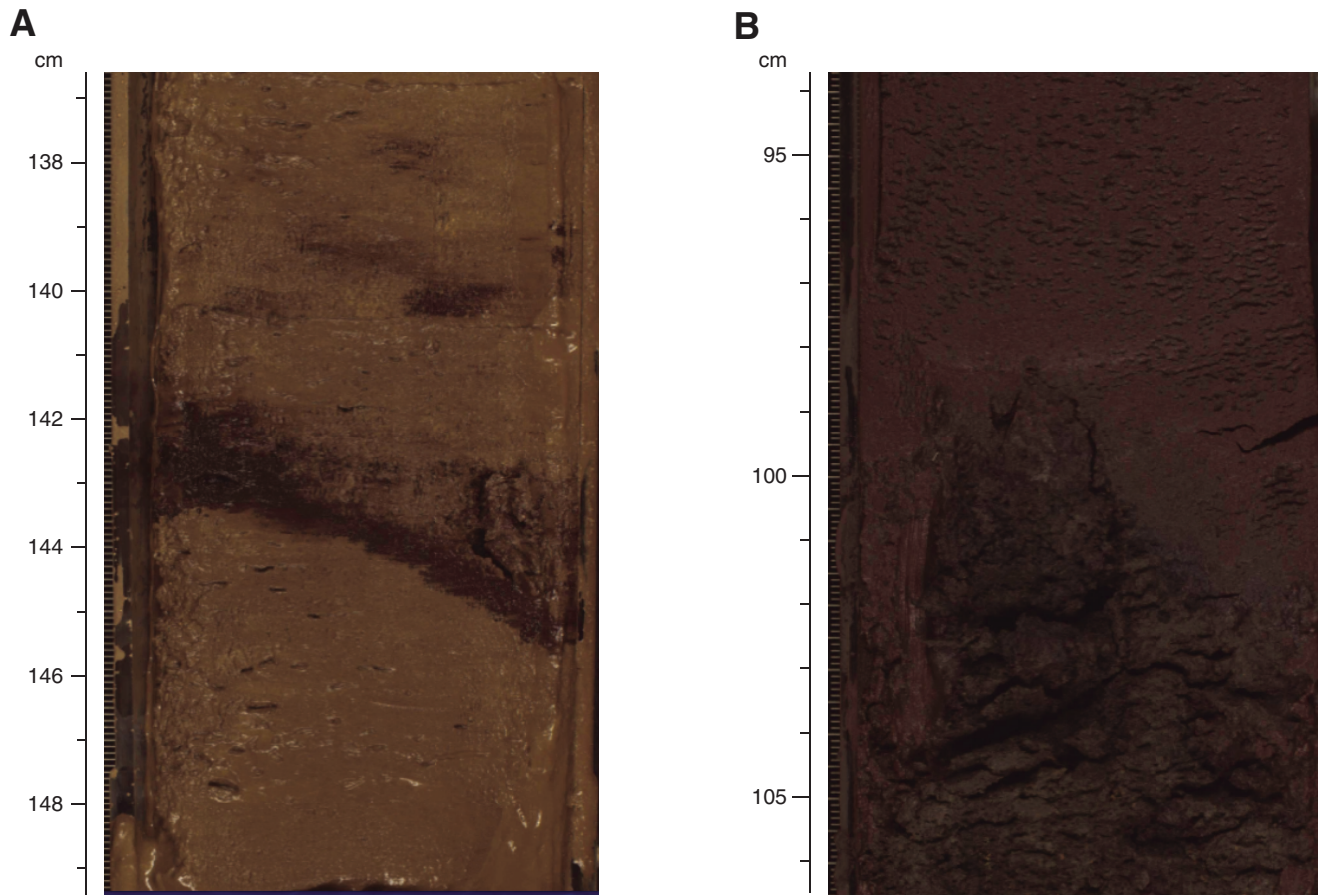
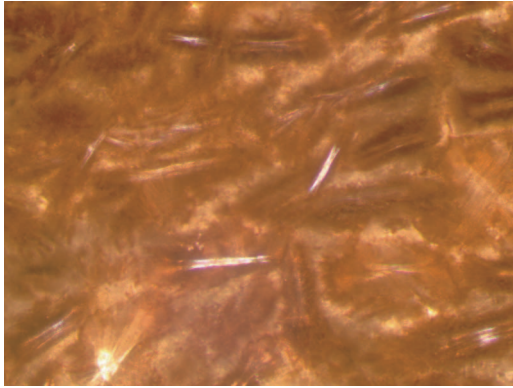
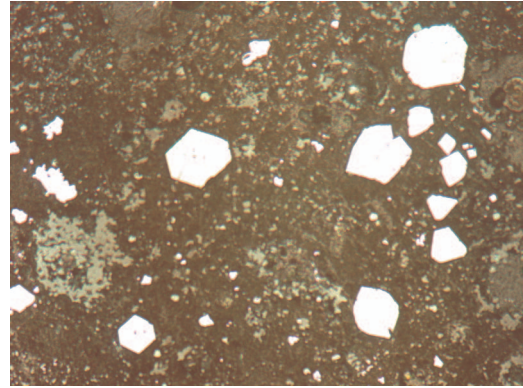


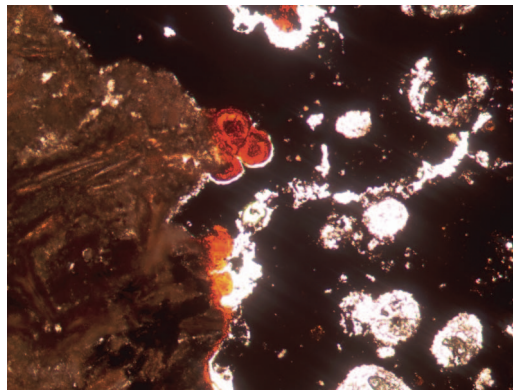
Figure F13. Thin section photomicrographs (Sample 329-U1368B-2H-6, 116–118 cm). **A.** Numerous plagioclase laths (bright rectangular bars) altering to clay (dark radiating fibers adjacent to each plagioclase) (transmitted light). **B.** Hexagon and triangular cross-sections of titanomagnetite octahedrons (reflected light). **C.** Botryoidal apatite (orange) and recrystallized microfossil shells in clay-rich matrix (black) filling a burrow.

A

0.5 mm

B

0.1 mm

C

0.5 mm

Figure F14. A. Image of planktonic foraminiferal ooze (Sample 329-U1368D-1H-CC). B. Image of black lithic sand sampled above the basement/sediment interface in Hole U1368D showing recrystallized planktonic foraminifers.

A**B**

Figure F15. Generalized stratigraphy for basement recovered at Site U1368.

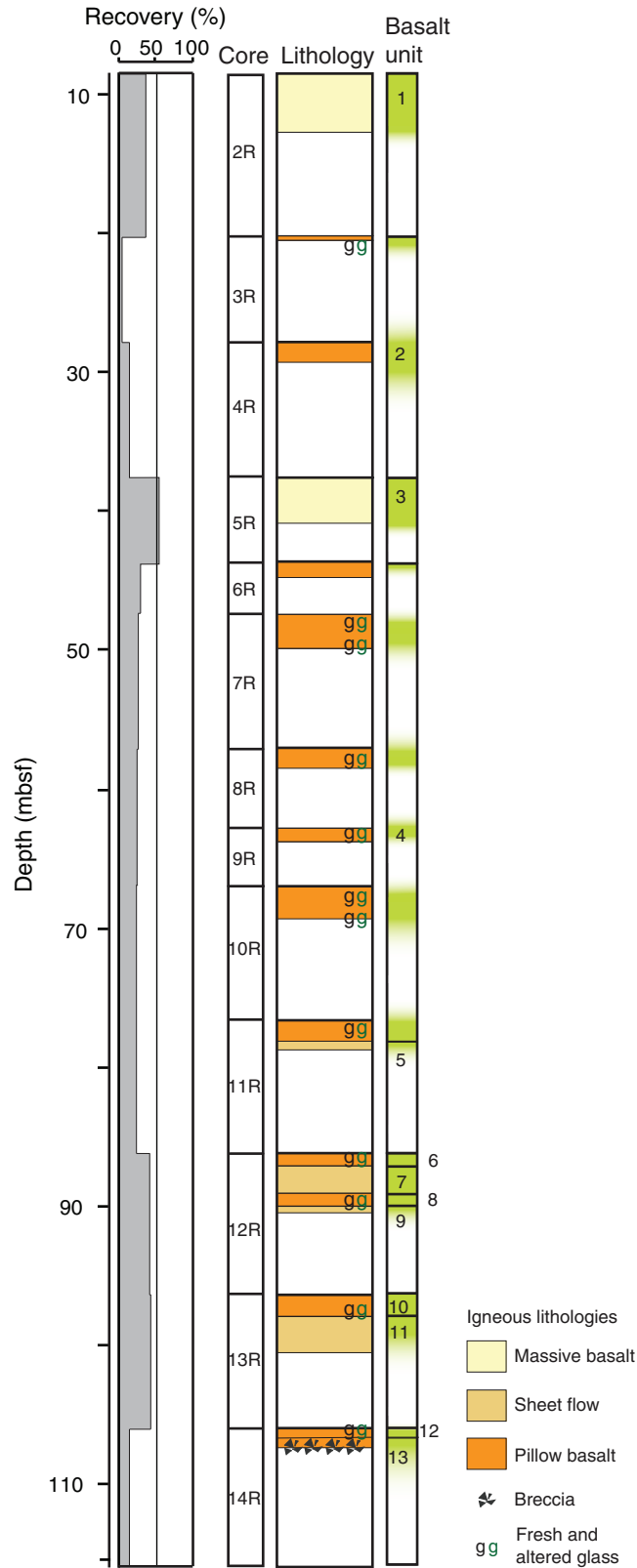


Figure F16. Core images of chilled margins and quenching structures (intervals 329-U1368F-6R-1, 112–118 cm, and 10R-1, 2–6 cm).

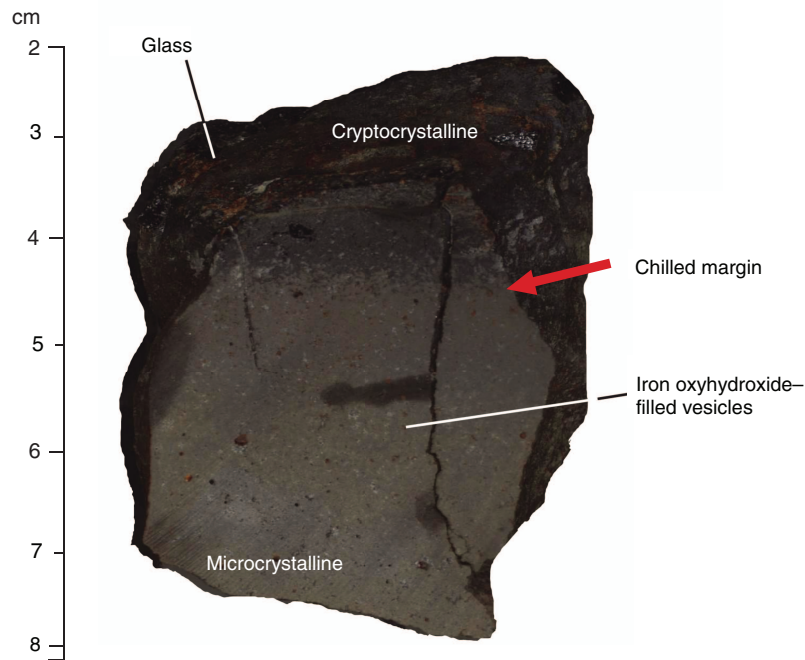
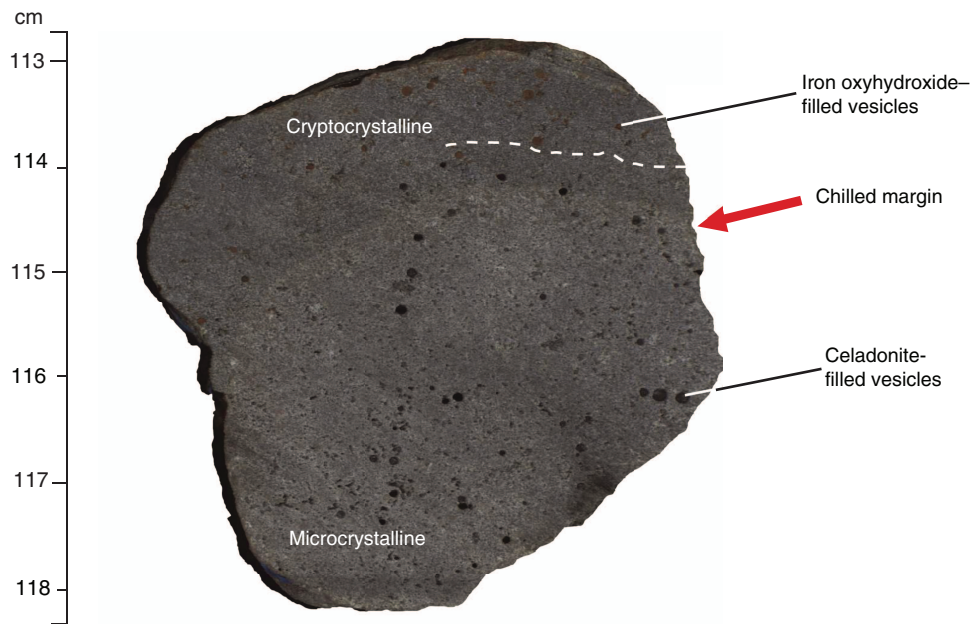


Figure F17. Core images and photomicrographs of concentric chilled margins within a pillow center exhibiting alteration, grain size variation, and vesicles and stages of lava cooling (interval 329-U1368F-10R-2, 1–17 cm). Fe-ox = iron oxyhydroxide. Core images are under plane-polarized light and photomicrographs are under cross-polarized light at 5× magnification. The large format whole section photo is in plane polarized light at 1× magnification.

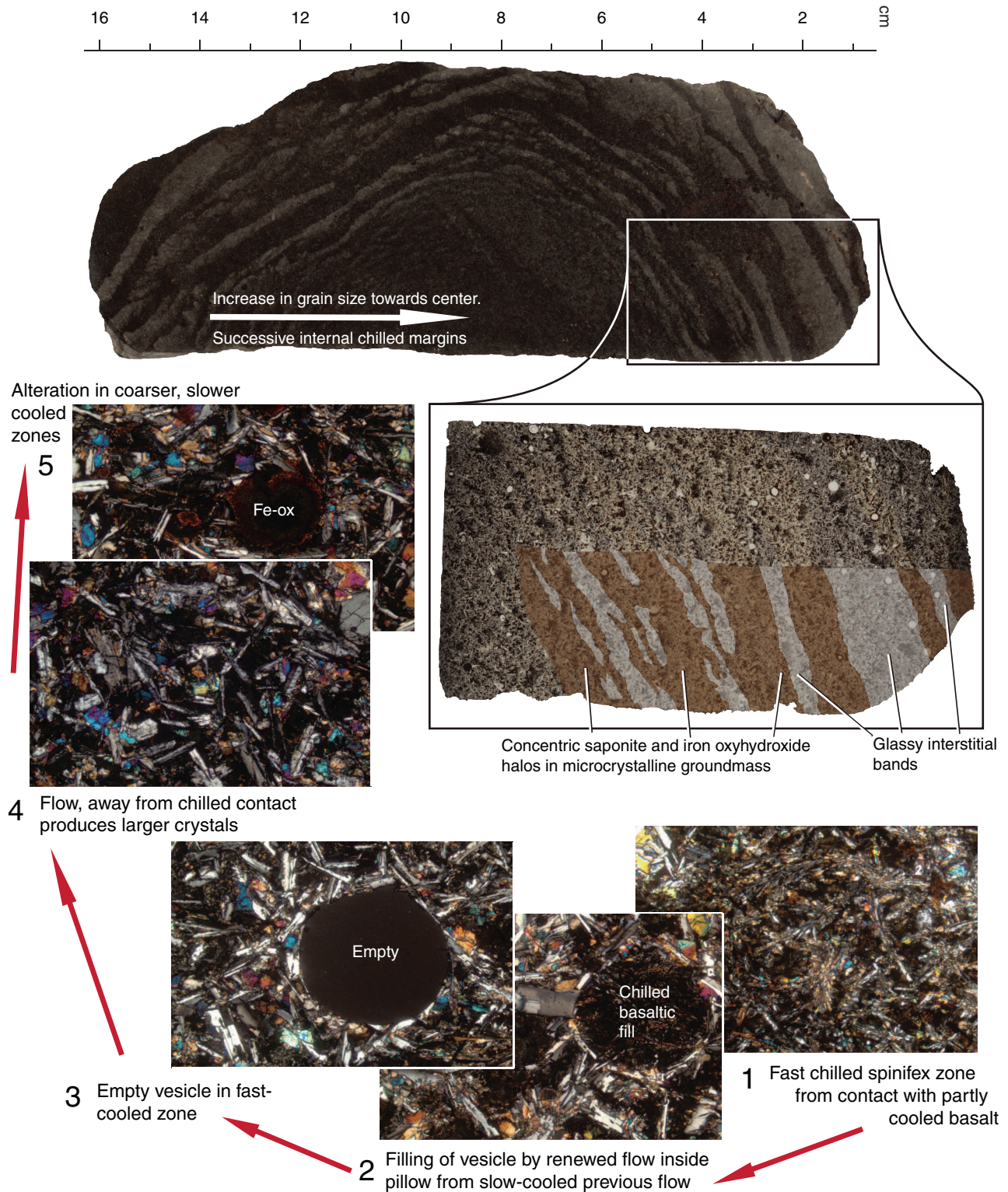


Figure F18. Core images of highly altered to completely altered clay and sand of basaltic origin in the sediment/basement interface, Site U1368.

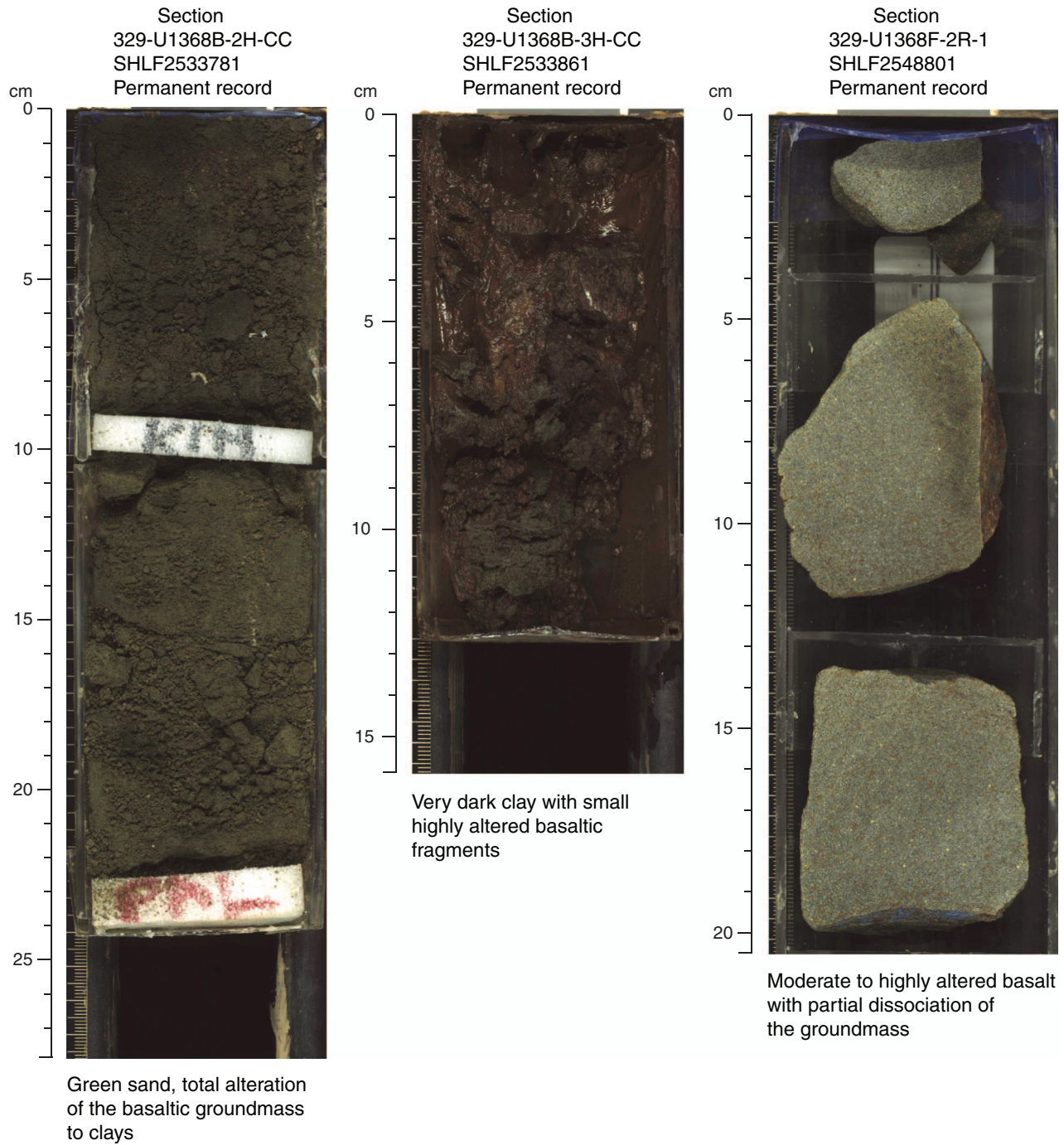


Figure F19. Photomicrographs of various plagioclase phenocryst styles. Pl = plagioclase, Cpx = clinopyroxene, Fe-Ti = Fe-Ti oxides. A. Sample 329-U1368F-4R-1, 51–53 cm. B. Sample 329-U1368F-6R-1, 21–25 cm. C. Sample 329-U1368F-4R-1, 118–121 cm. D. Sample 329-U1368F-12R-4, 53–54 cm. Cross-polarized light at 5× magnification.

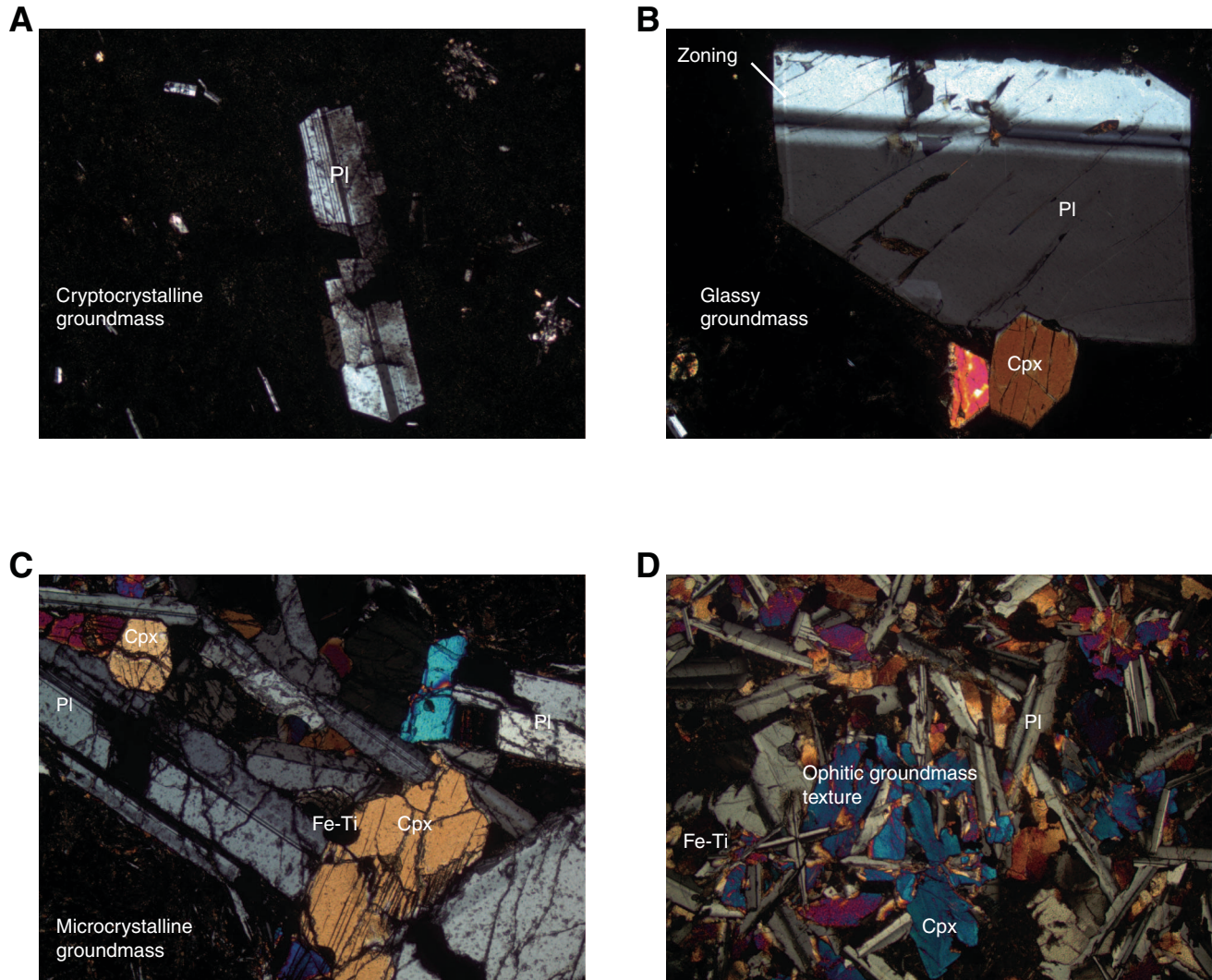


Figure F20. Photomicrographs of saponite pseudomorphs of olivine. **A.** Sample 329-U1368F-12R-1, 2–3 cm (plane-polarized light; 20× magnification). **B.** Sample 329-U1368F-6R-1, 21–25 cm (plane-polarized light; 10× magnification).

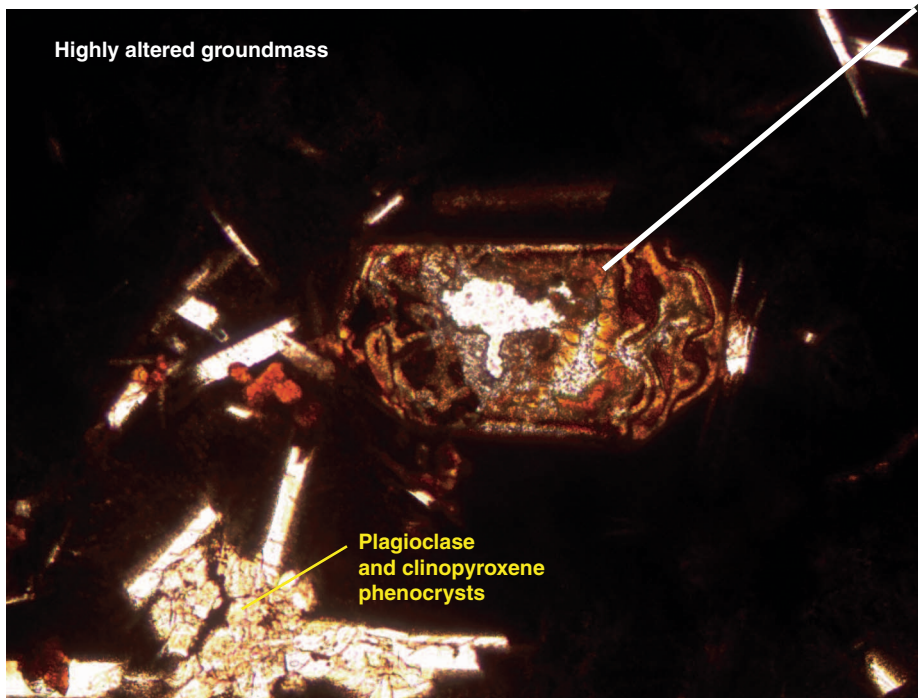
A**B**

Figure F21. Plots of selected ICP-AES analyses for least altered background rocks and altered sample pairs vs. depth. Pairings are based on alteration halos vs. background within the same sample piece. LOI = loss on ignition.

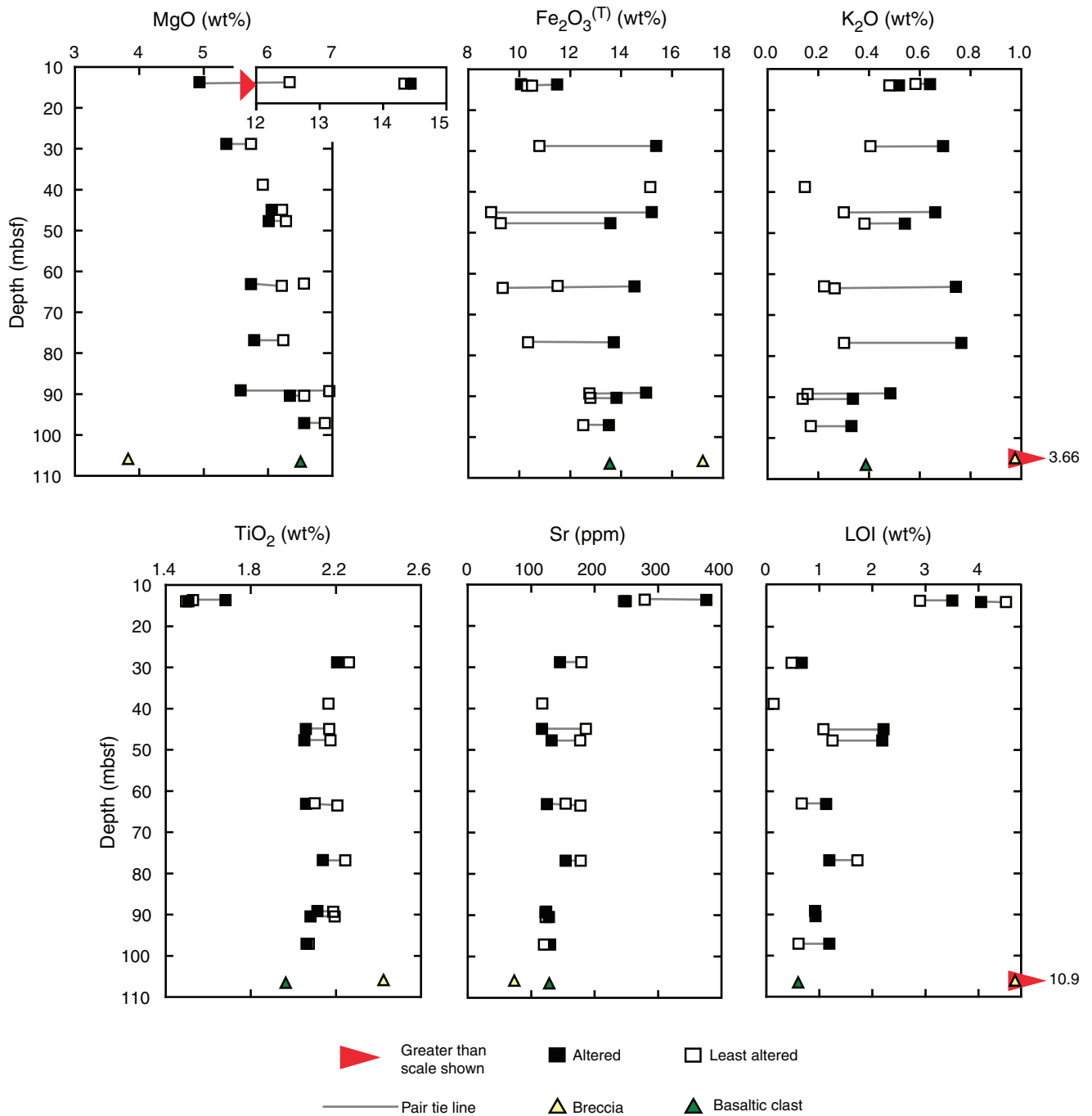


Figure F22. Fractionation trends for least altered background rocks, Site U1368. Gray arrows indicate potential fractionation trend. A. Na_2O vs. MgO . B. Fe_2O_3 vs. MgO . C. TiO_2 vs. MgO . D. K_2O vs. MgO .

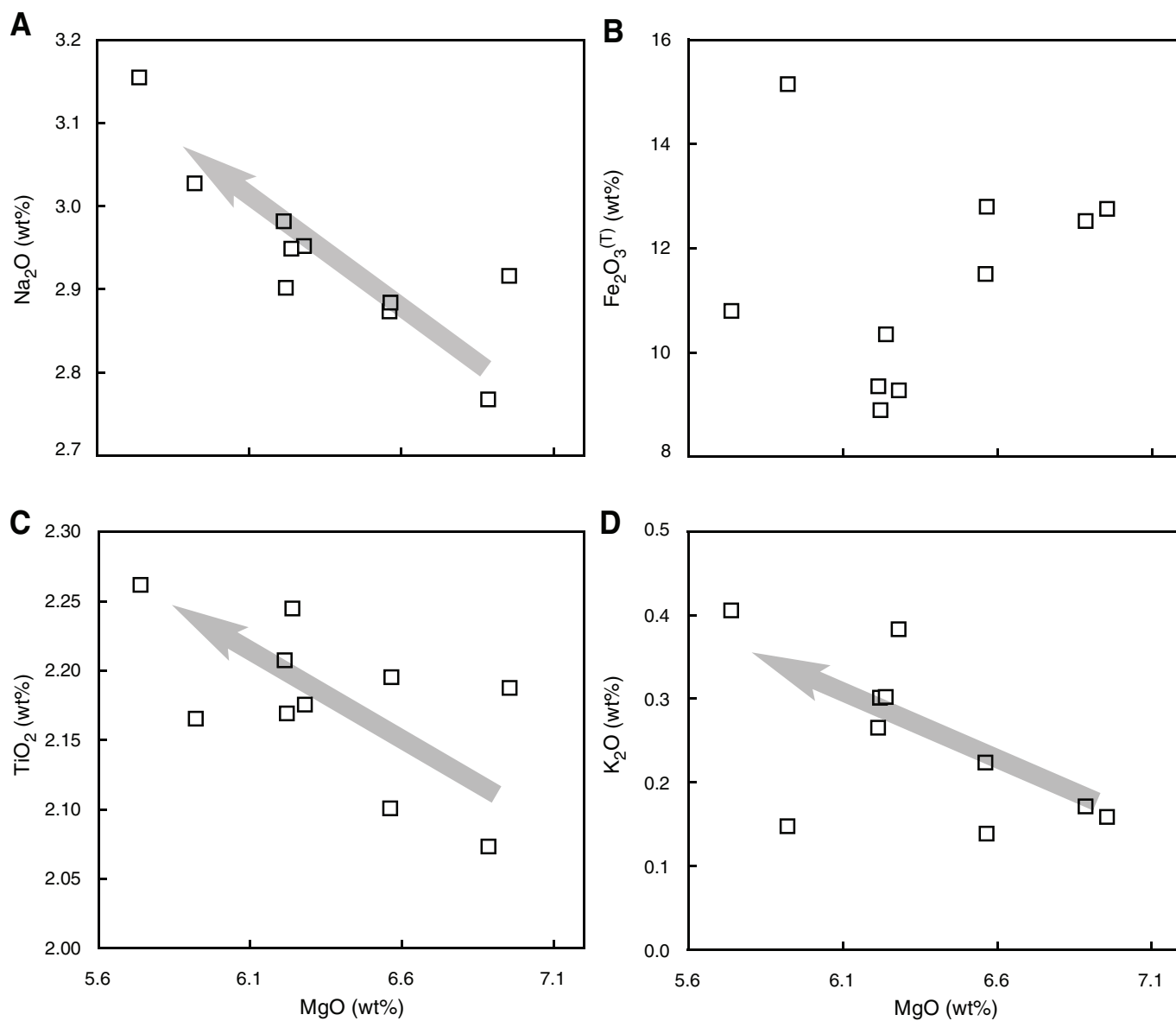


Figure F23. X-ray diffraction results, including interpretation of the major peaks for mineral separates in Hole U1368F.

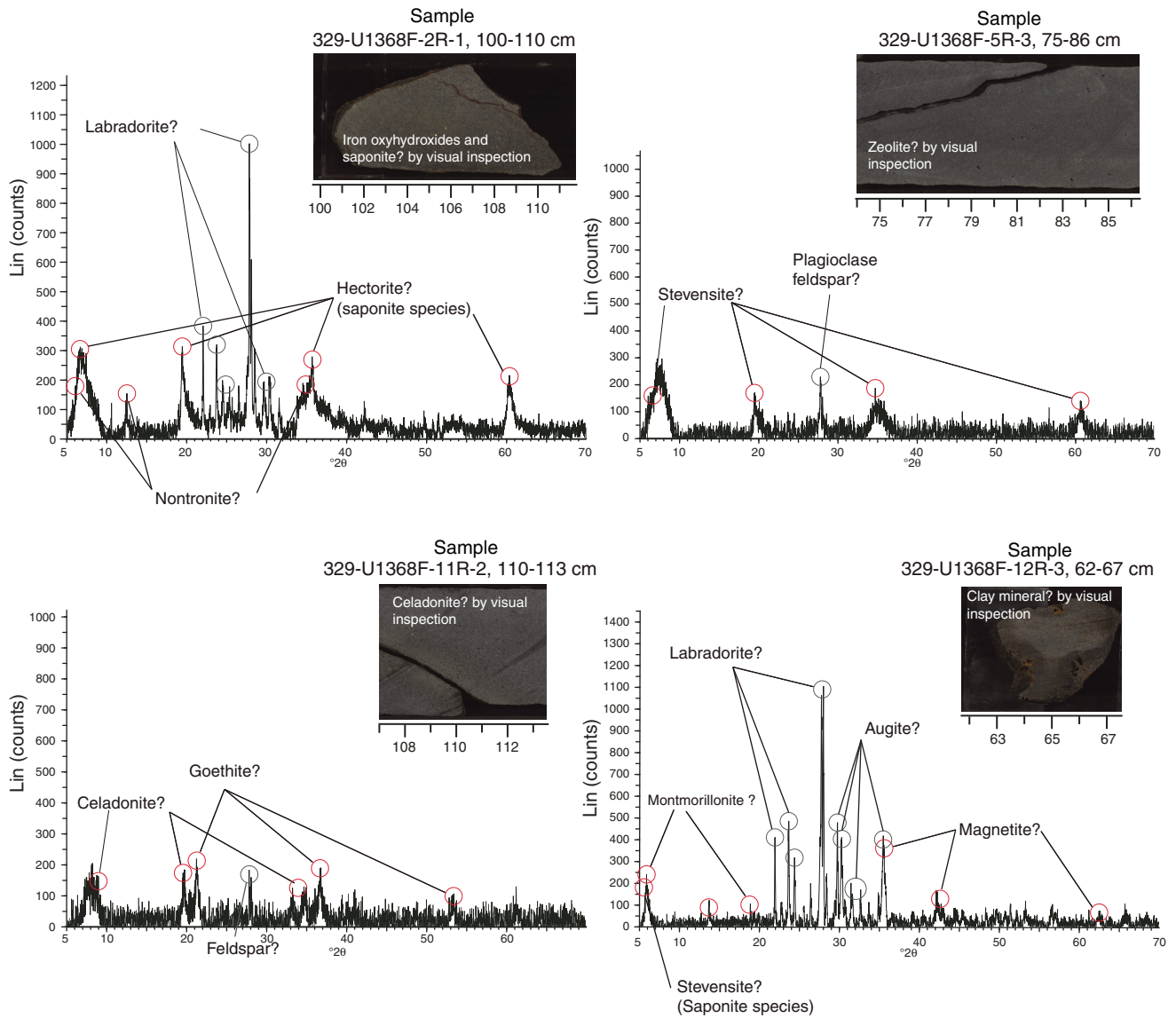


Figure F24. Core images and photomicrographs of volcanoclastic breccia (interval 329-U1368F-14R-1, 45–150 cm). Bottom photomicrograph is under plane-polarized light at 5× magnification.

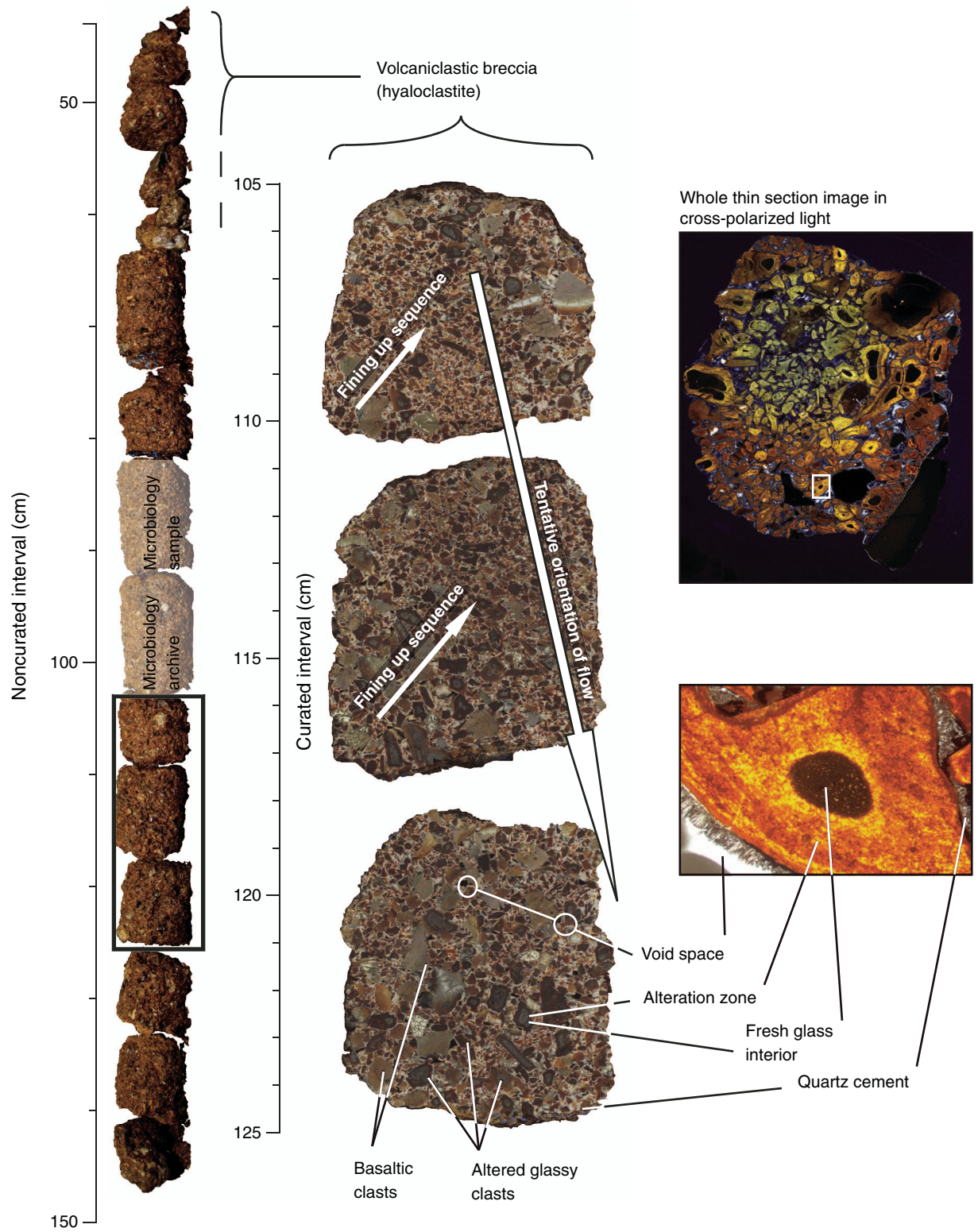


Figure F25. Core photos and a photomicrograph of halo types that occur in Hole U1368F. Photomicrograph is whole thin section in plane-polarized light at 1× magnification.

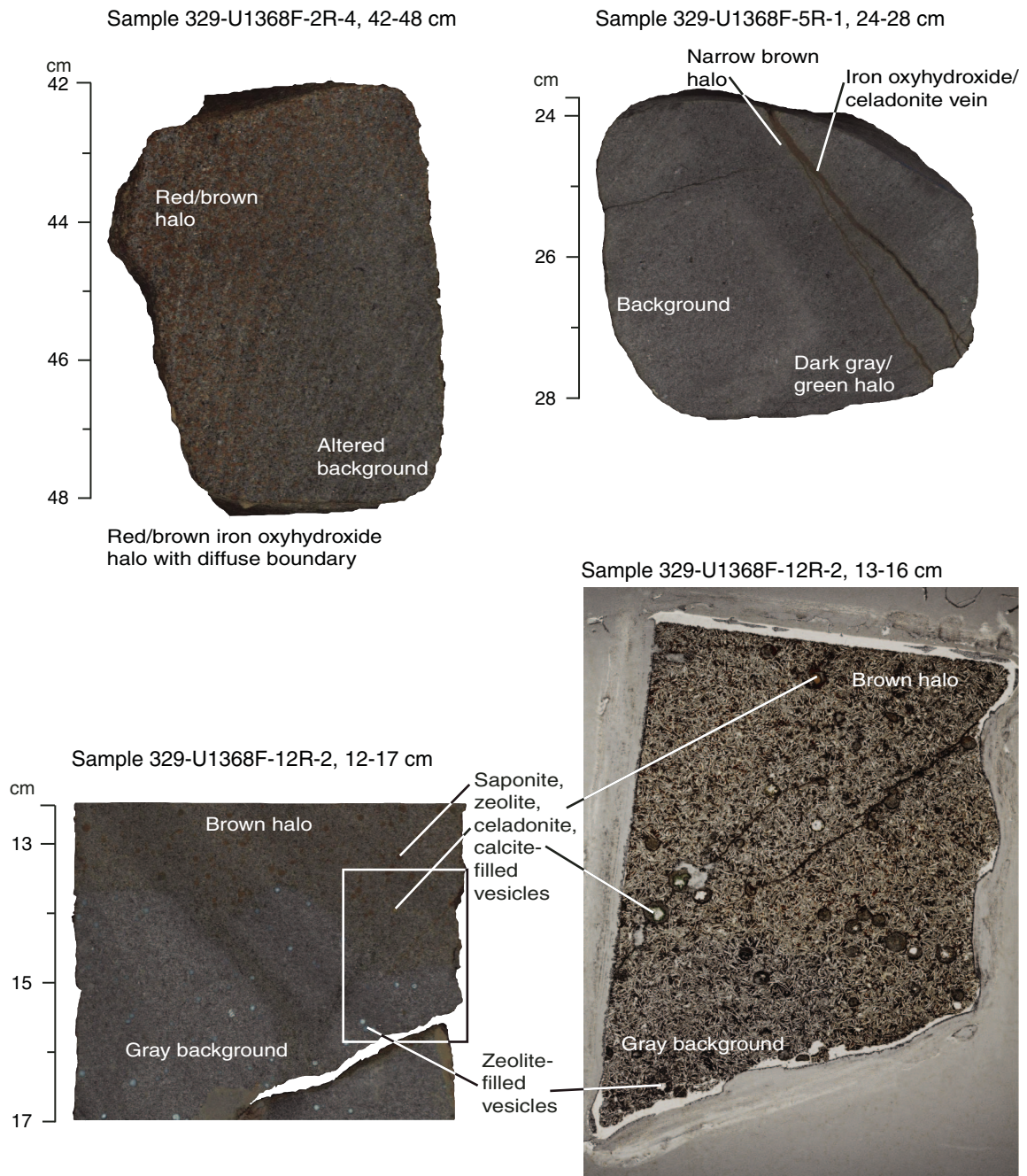


Figure F26. Photomicrographs of vein minerals. A. Iron oxyhydroxide (Sample 329-U1368F-9R-1, 52–55 cm). B. Saponite (Sample 329-U1368F-9R-1, 85–87 cm). Plane-polarized light at 5× magnification.

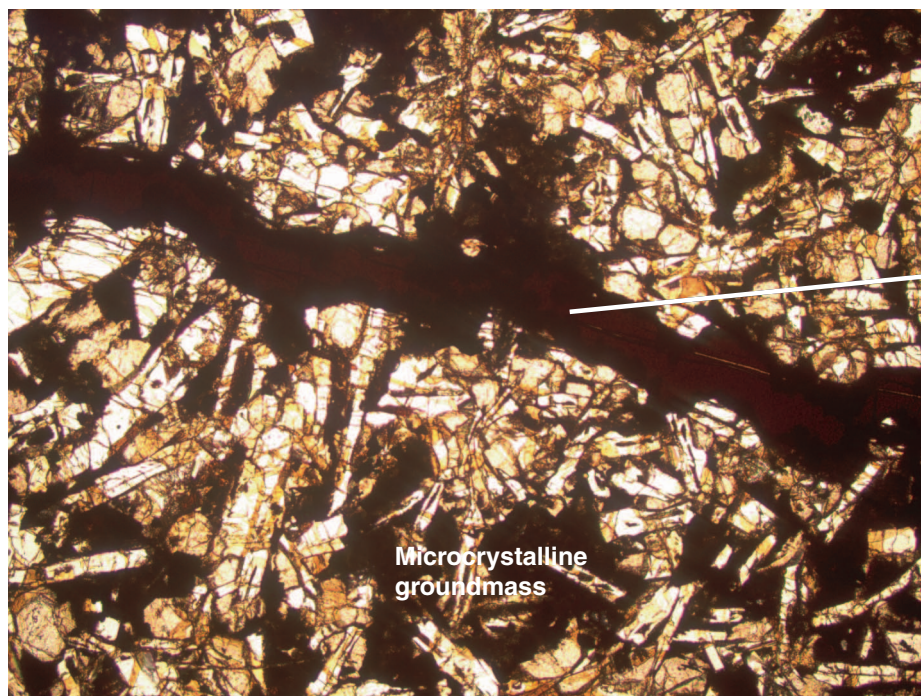
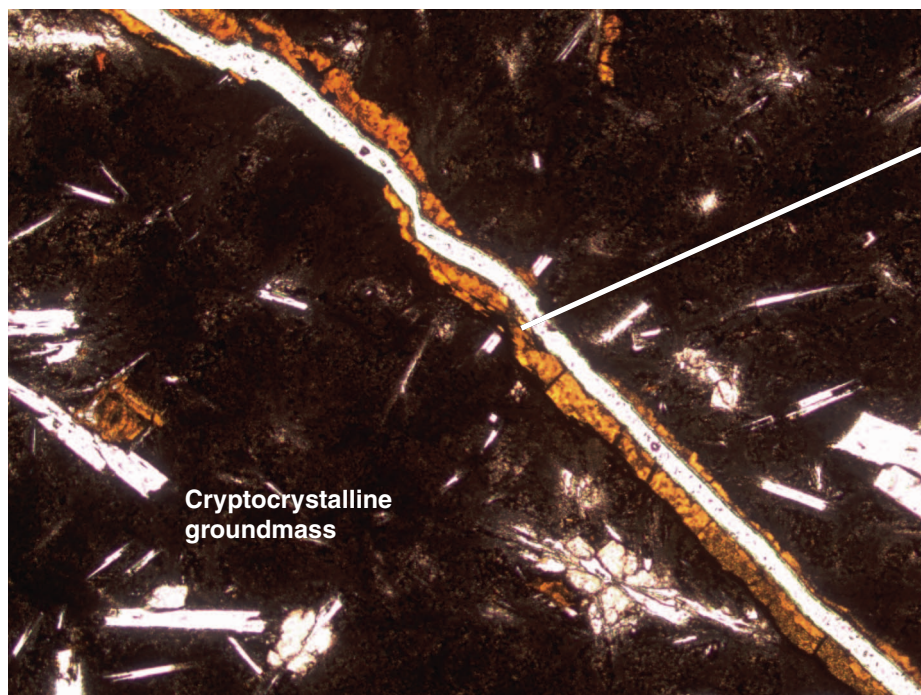
A**B**

Figure F27. Photomicrographs of vesicle fills. Cel = celadonite, Sap = saponite, Fe-ox = iron oxyhydroxide, Zeo = zeolite. **A.** Saponite-filled vesicle (Sample 329-U1368F-6R-1, 21–25 cm; cross-polarized light; 20× magnification). **B.** Iron oxyhydroxide-, zeolite-, celadonite-, and calcite-filled vesicles with crosscutting vein (Sample 329-U1368F-12R-2, 13–16 cm; cross-polarized light; 5× magnification). **C.** Saponite- and iron oxyhydroxide-filled vesicle (Sample 329-U1368F-12R-1, 2–3 cm; plane-polarized light; 10× magnification). **D.** Saponite partly filling vesicles (Sample 329-U1368F-9R-1, 85–87 cm; plane-polarized light; 5× magnification).

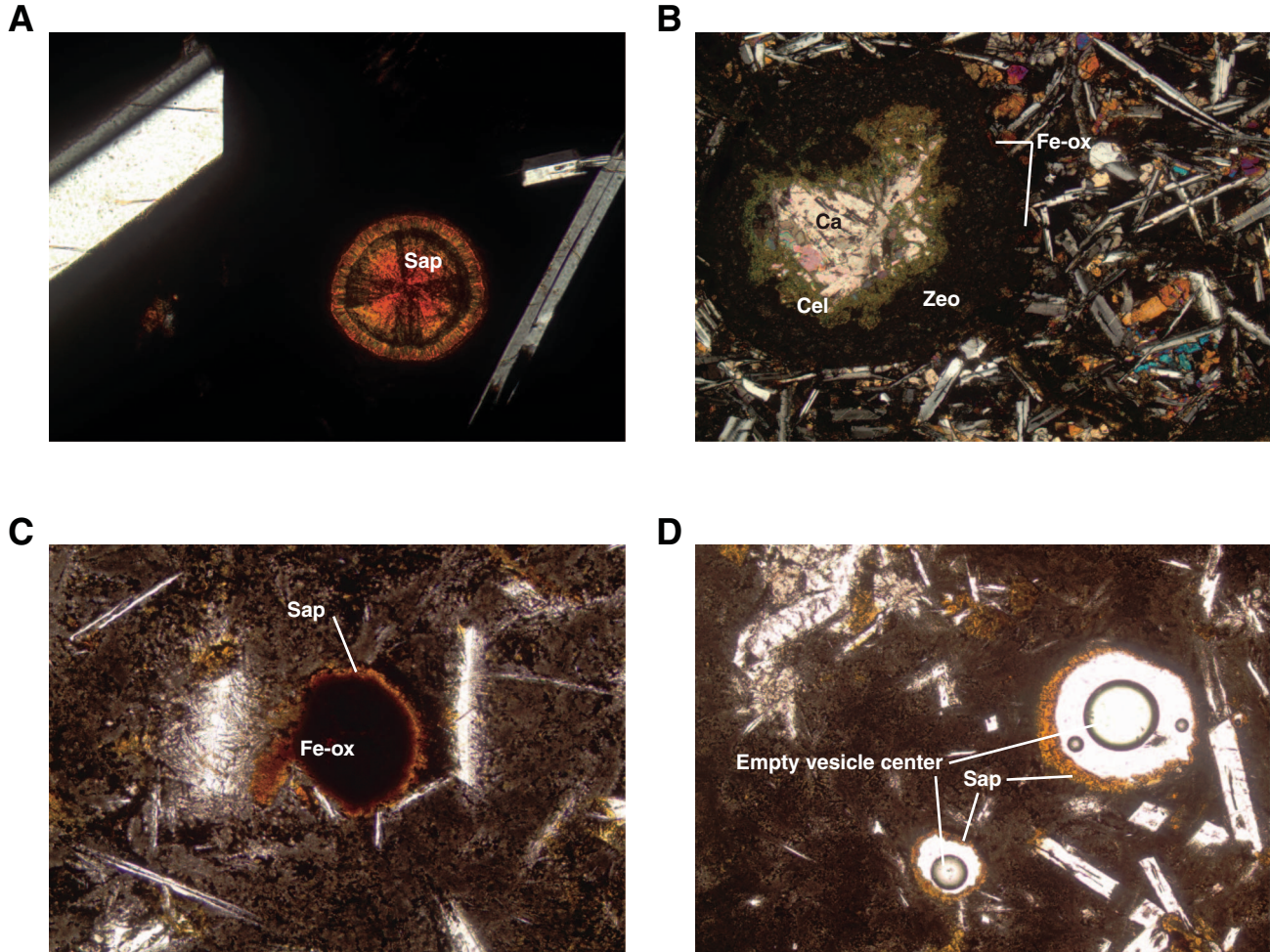


Figure F28. Chemical comparison of “fresh” background vs. altered for (A) in situ sample pairs and (B) selected sample pairings. LOI = loss on ignition.

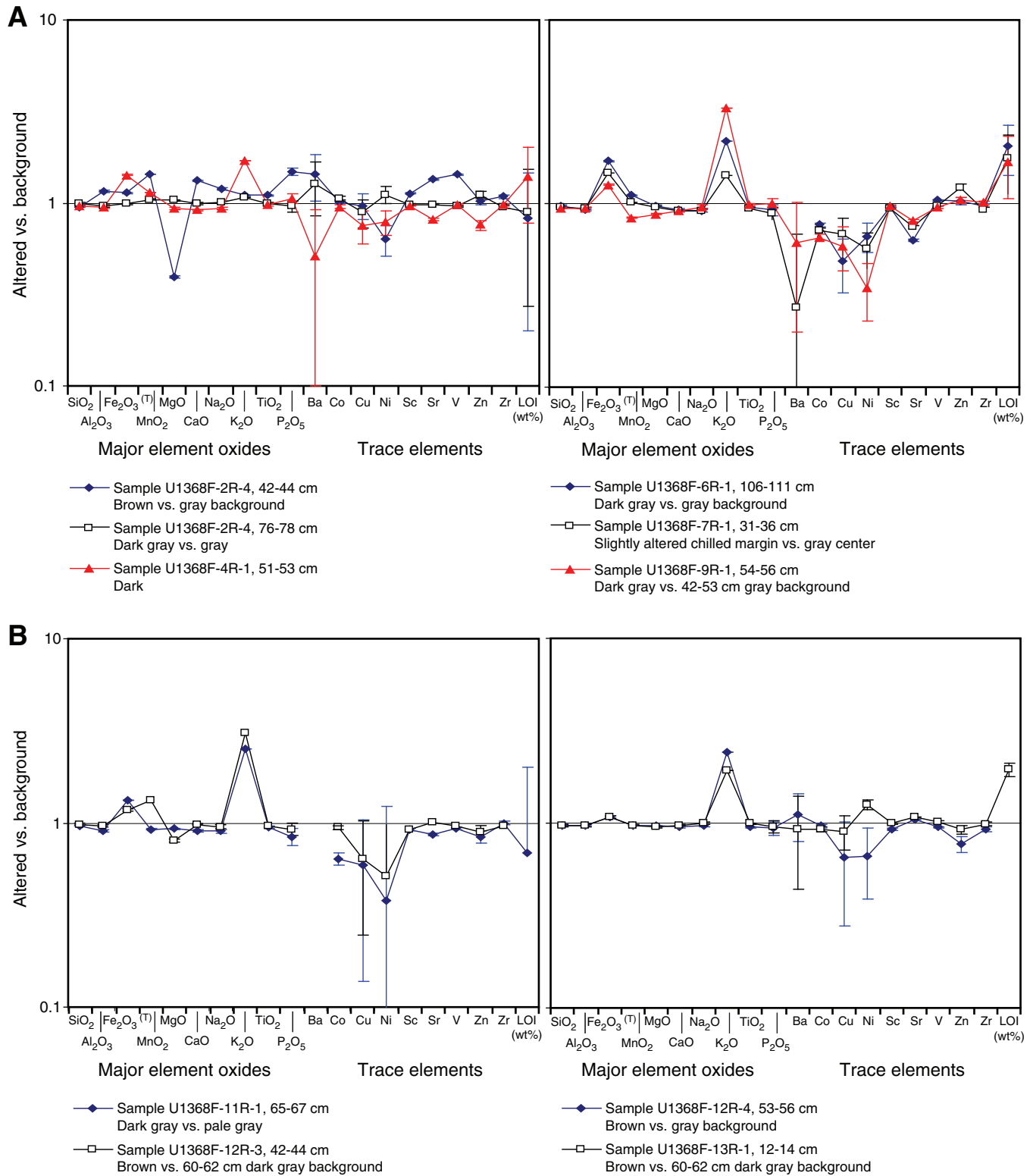


Figure F29. Reoriented true-dip and apparent-dip directions for (A) veins and (B) fractures, Site U1368.

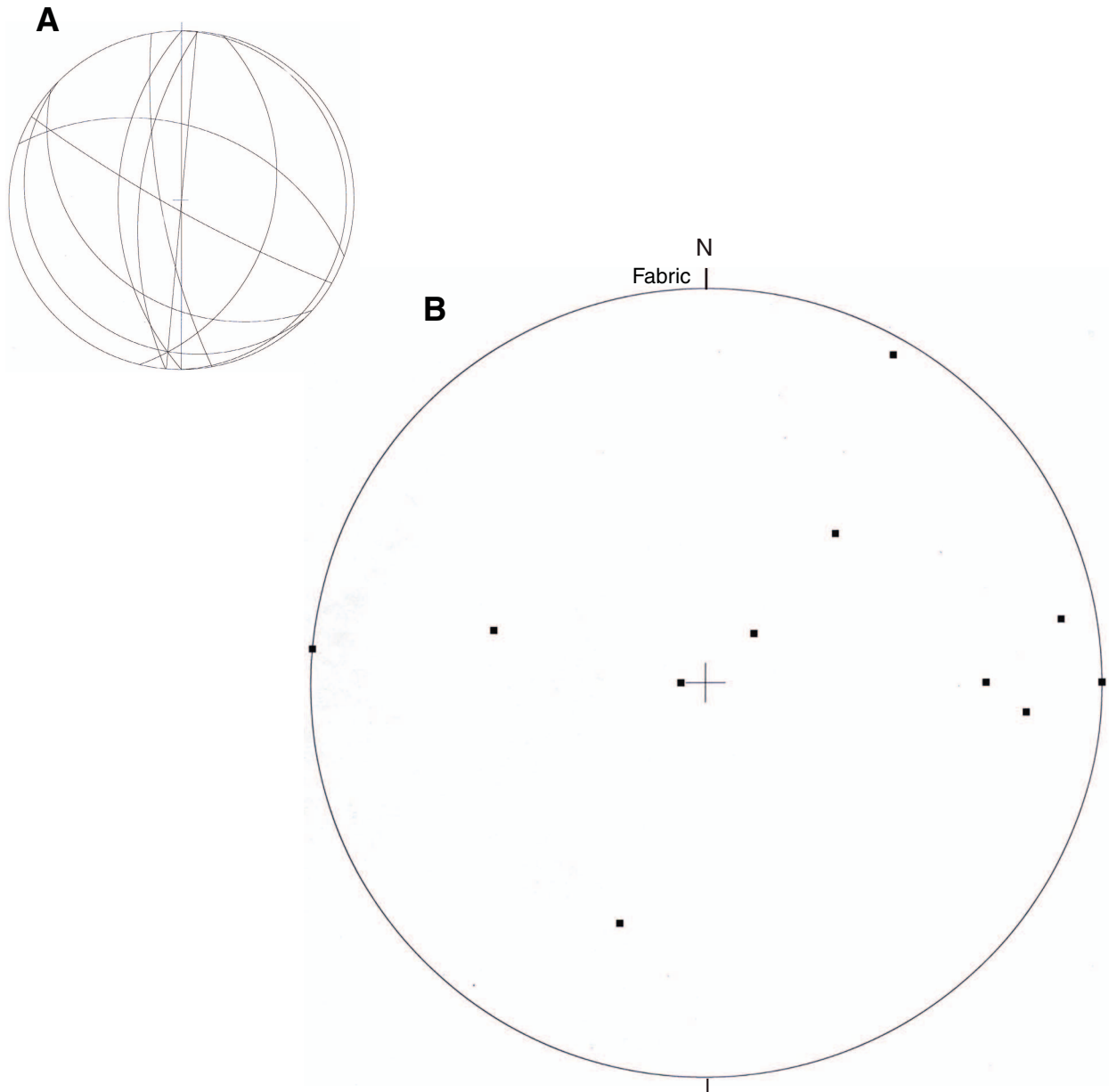


Figure F30. Lithology summary and preliminary biostratigraphy, Site U1368. Sample locations are indicated by arrows. Ages of the foraminiferal zones are based on Berggren et al. (1995), Pearson and Chaisson (1997), and Wade et al. (2011). * = samples taken from holes other than Hole U1367B, FO = first occurrence, LO = last occurrence.

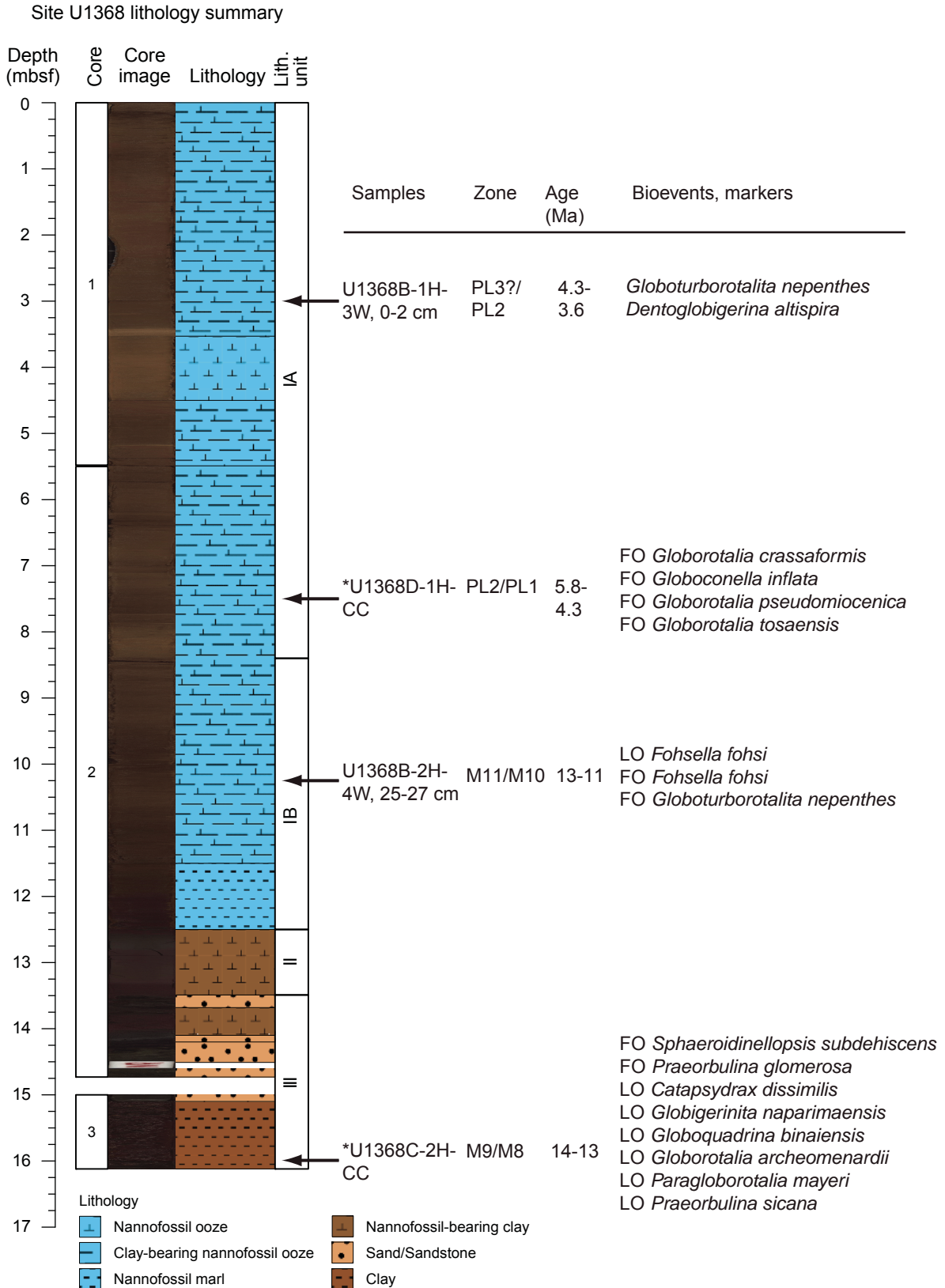


Figure F31. Bulk density plots, Hole U1368B. Black lines indicate section breaks, and green circles indicate bulk density derived from MAD measurements. **A.** Raw density. **B.** Raw density (blue circles) and linear trends (red lines) used to adjust data. Red circles show adjusted bulk density data. **C.** Adjusted bulk density data.

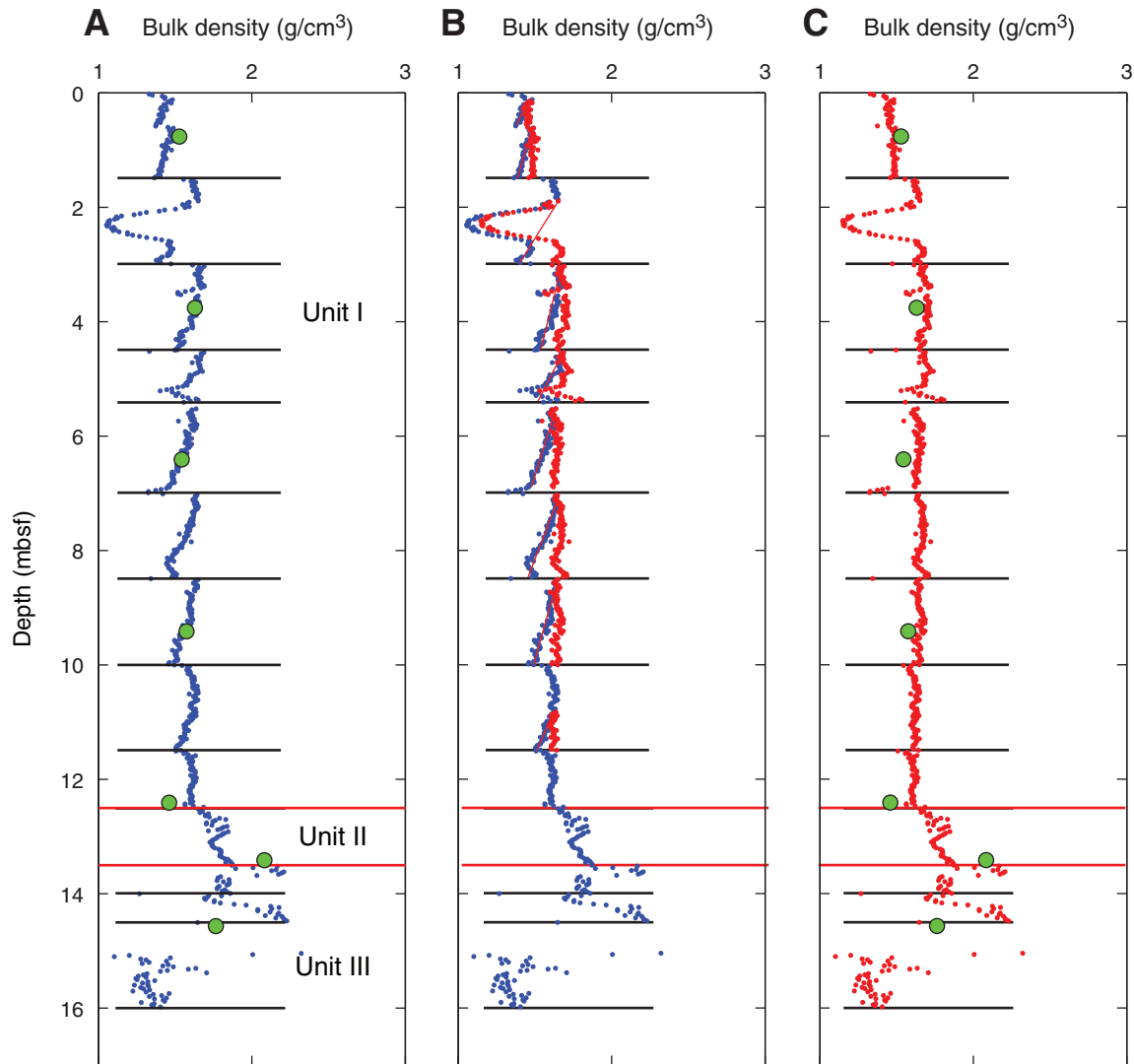


Figure F32. Plots of bulk density data, Site U1368. Red lines indicate lithologic unit boundaries, black lines indicate section breaks, red circles show bulk density derived from MAD measurements.

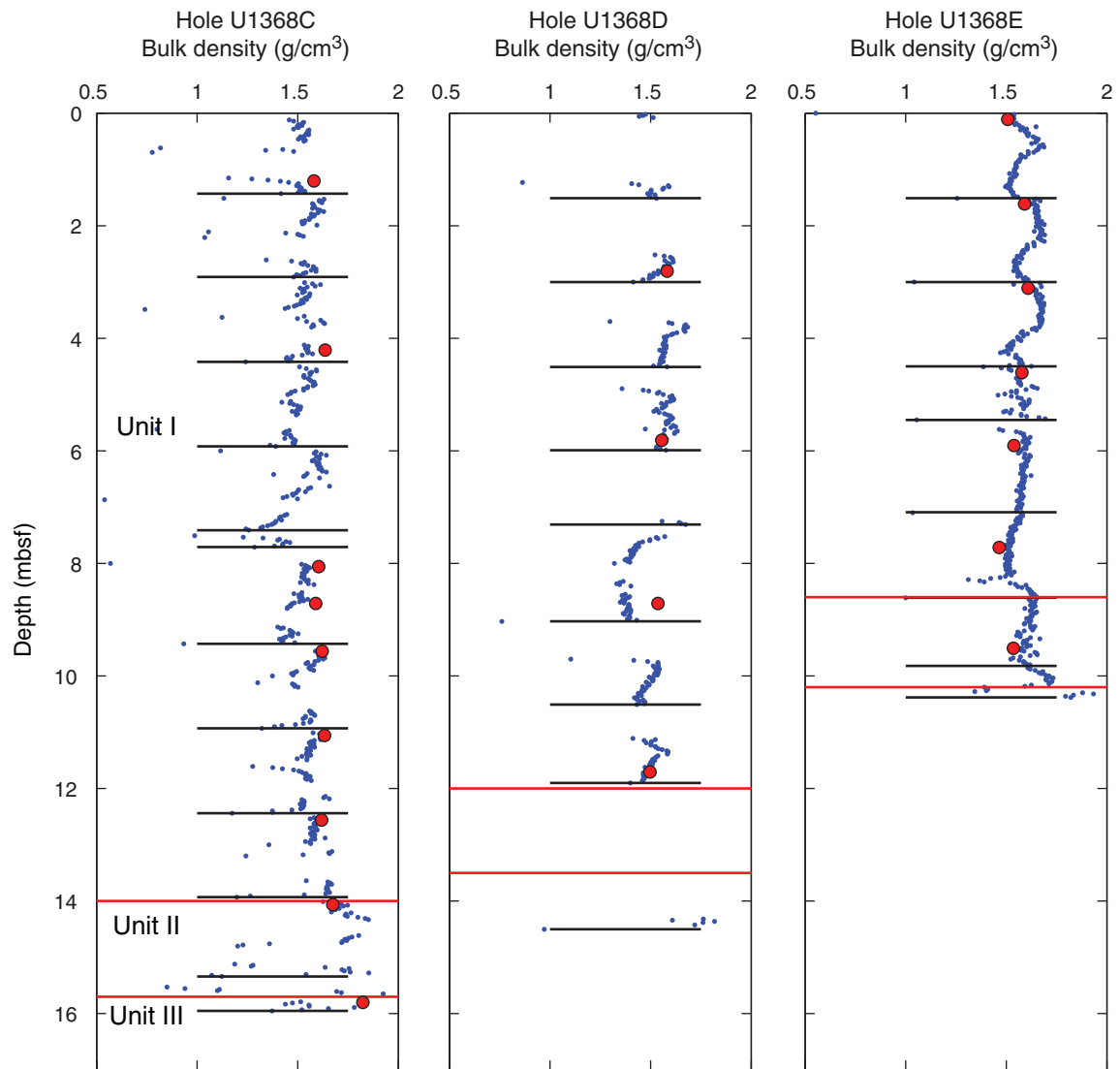


Figure F33. Plots of moisture and density measurements, Site U1368. Circles = measurements made in lithologic Unit I, triangles = measurements made in Unit II, diamonds = measurements made in Unit III.

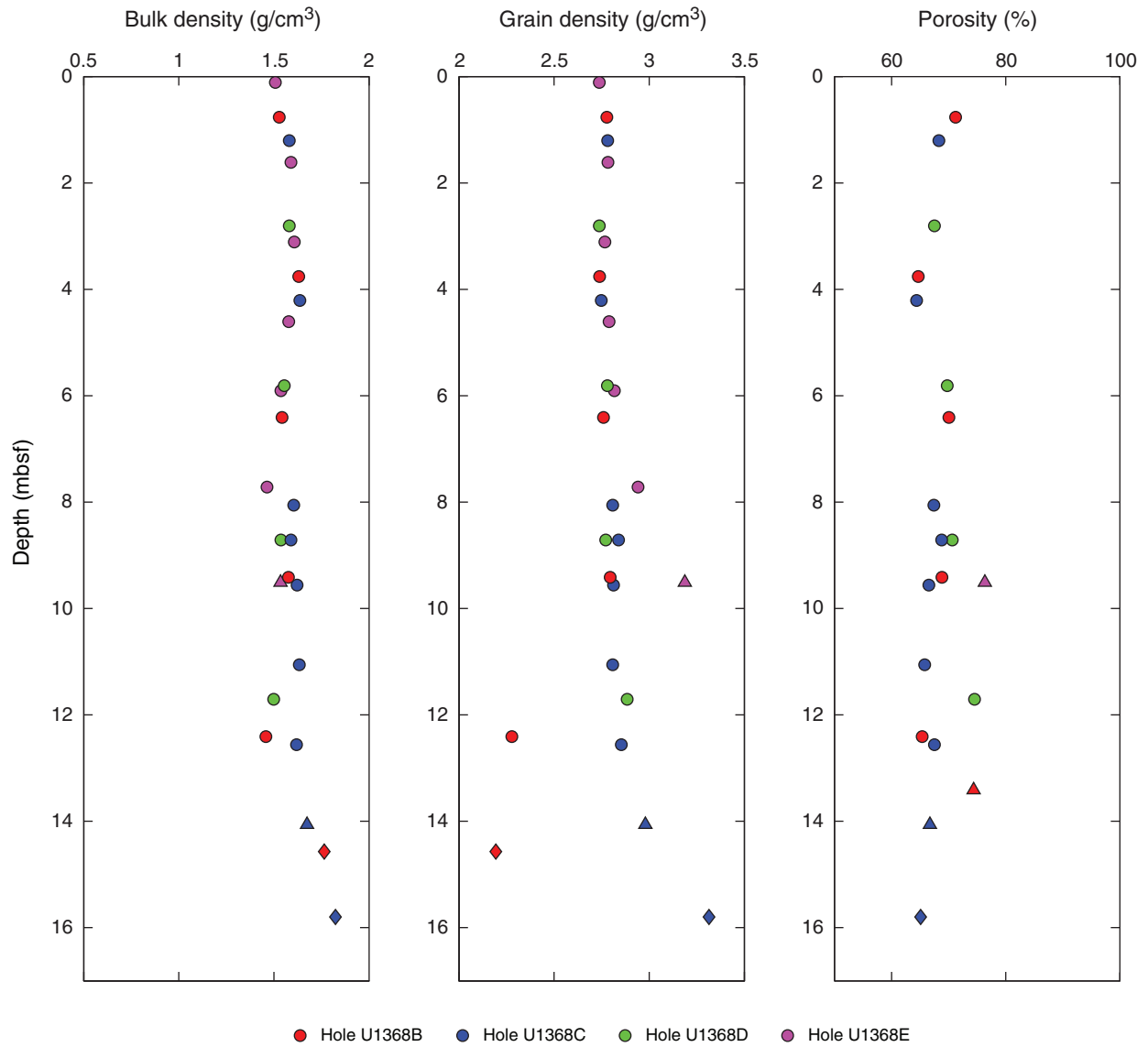


Figure F34. Plots of moisture and density measurements, Hole U1368F. **A.** Gamma ray attenuation (GRA) density measured with the Whole-Round Multisensor Logger on whole-round core sections (blue) and wet bulk density measured on discrete samples using the mass/volume method (red). **B.** Grain density measured on discrete samples using moisture and density (MAD) mass/volume methods. **C.** Porosity determined using MAD Method C.

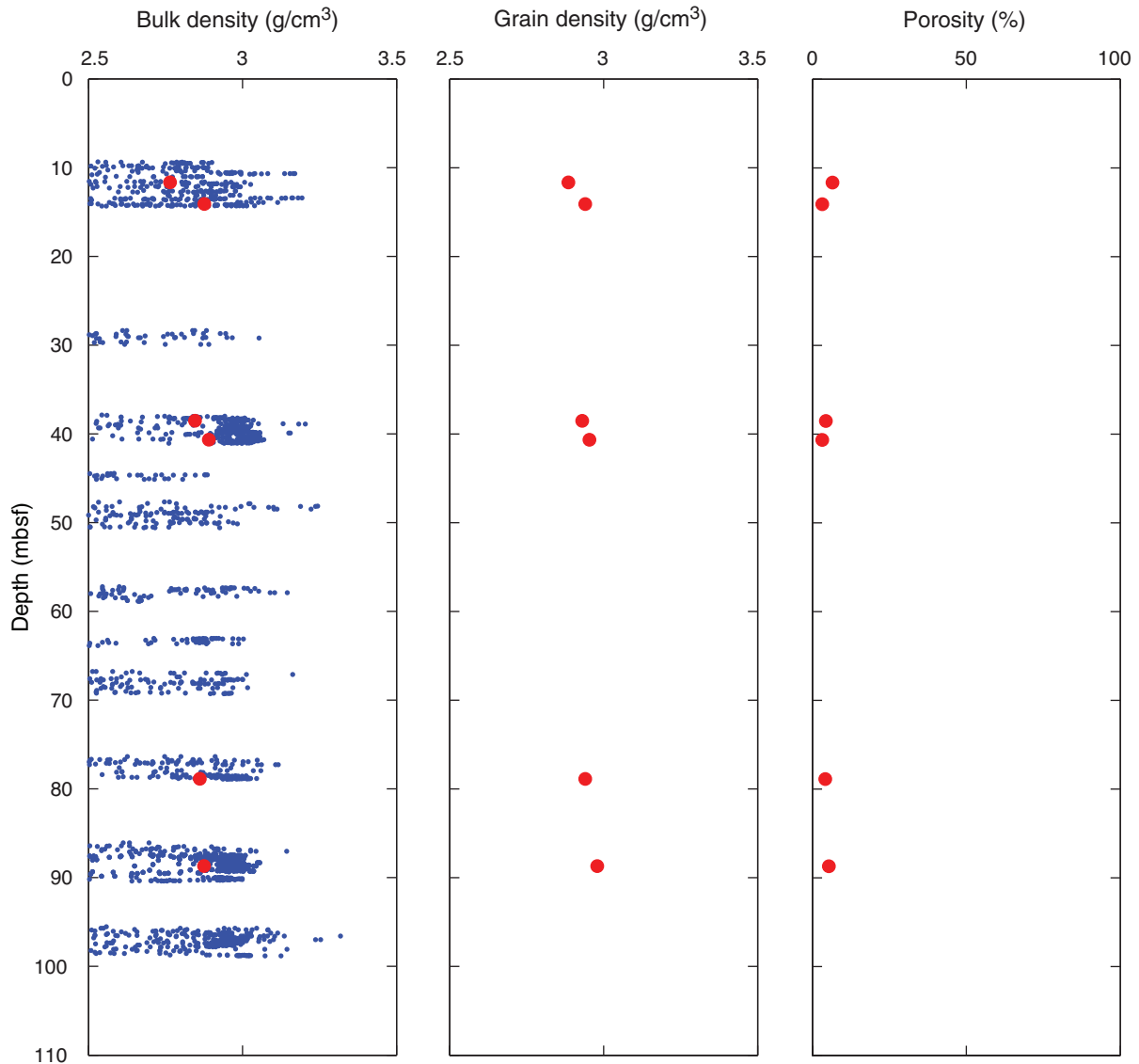


Figure F35. Plots of (A–D) magnetic susceptibility measurements made on the Whole-Core Multisensor Logger and (E–H) point magnetic susceptibility measurements made on the Section Half Multisensor Logger, Site U1368.

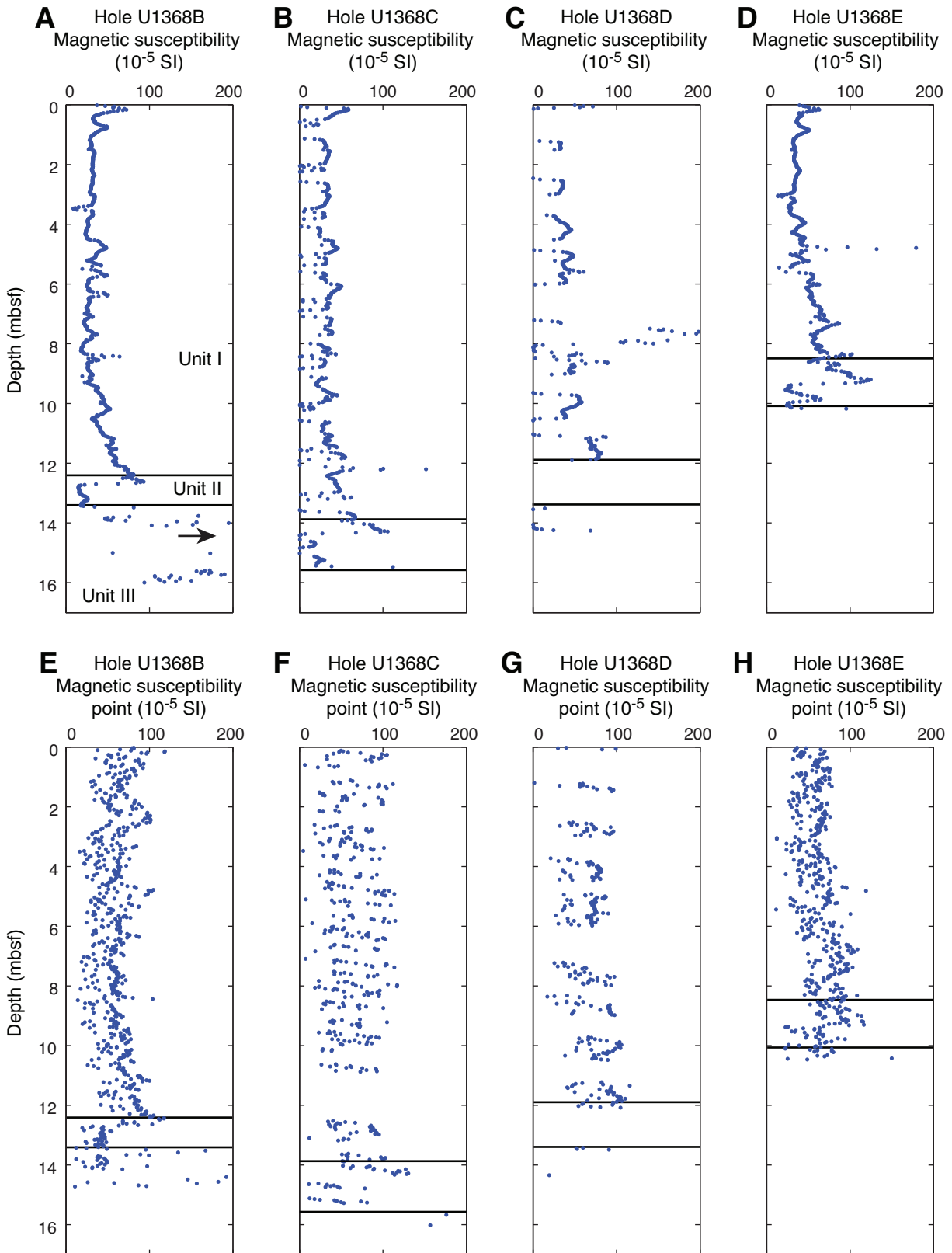


Figure F36. Plot of magnetic susceptibility as a function of depth, Hole U1368F.

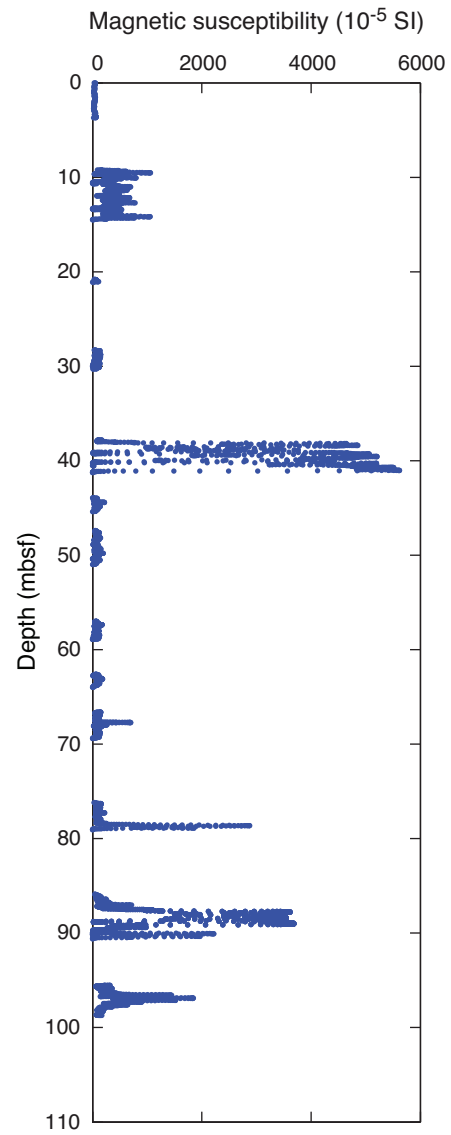


Figure F37. A. Plots of natural gamma radiation (NGR) as a function of depth, Site U1368. B. Same data as A at an expanded scale.

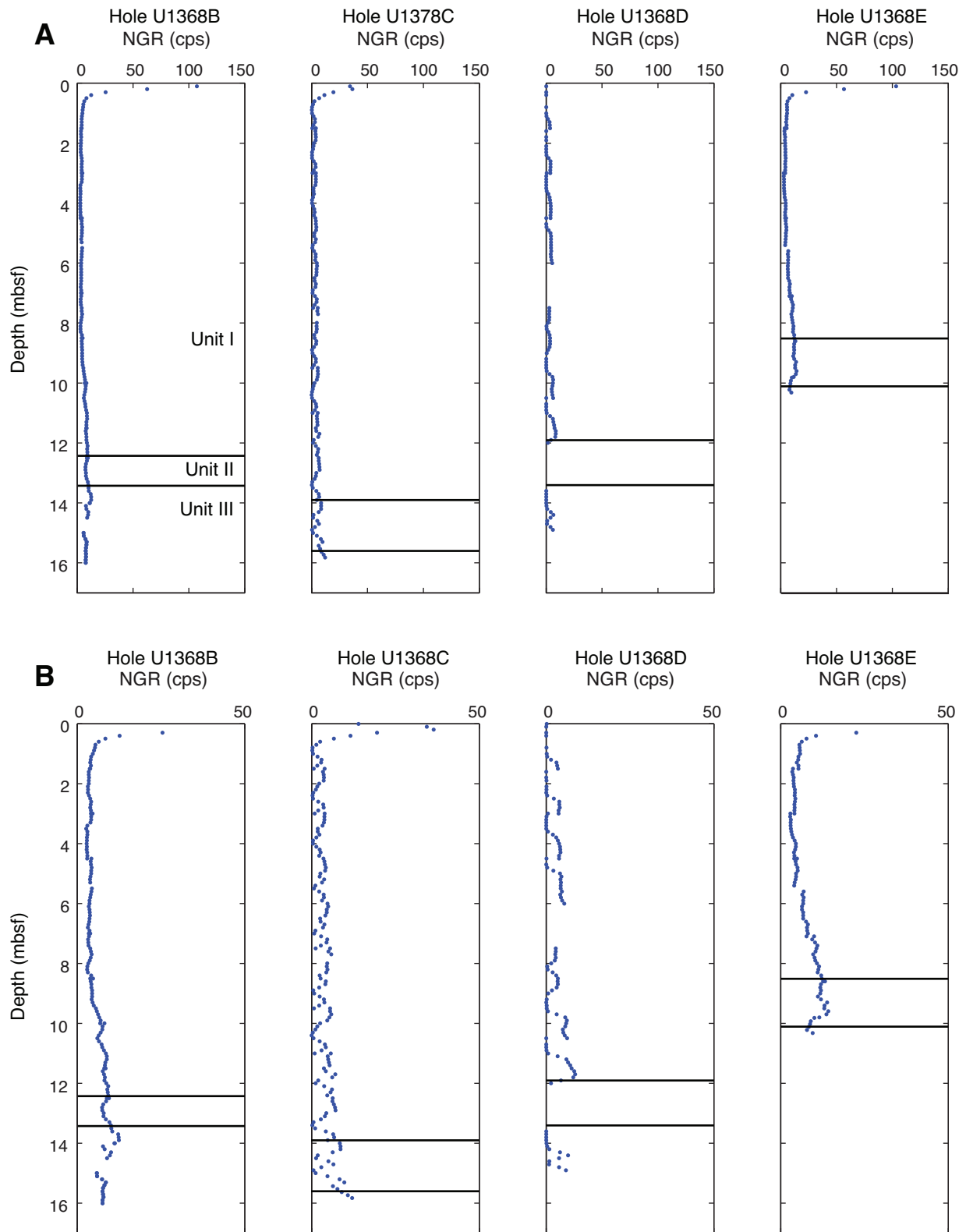


Figure F38. Plot of natural gamma radiation (NGR) as a function of depth, Hole U1368F.

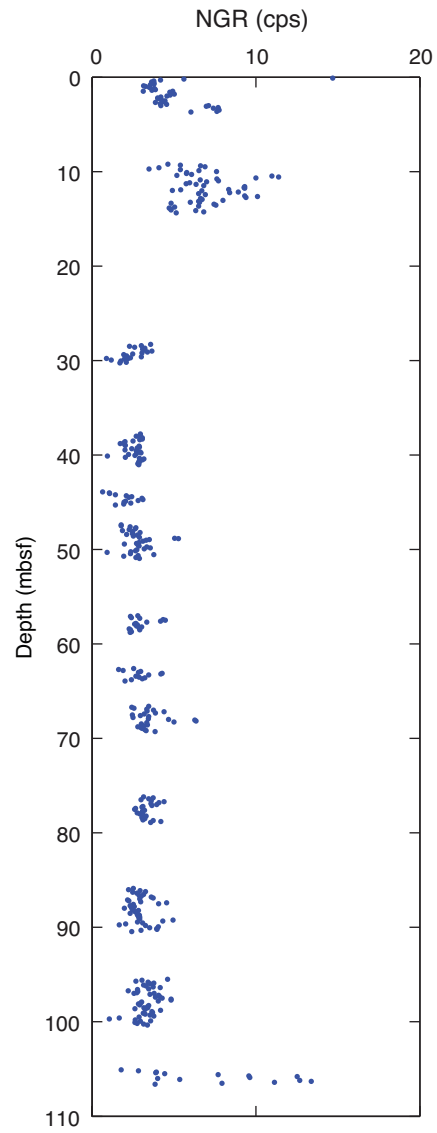


Figure F39. A. Plots of compressional wave velocity measured with the Whole-Round Multisensor Logger, Site U1368. Red circles indicate discrete measurements of *P*-wave velocity along *x*-axis. **B.** Histogram of sediment *P*-wave velocity from all holes.

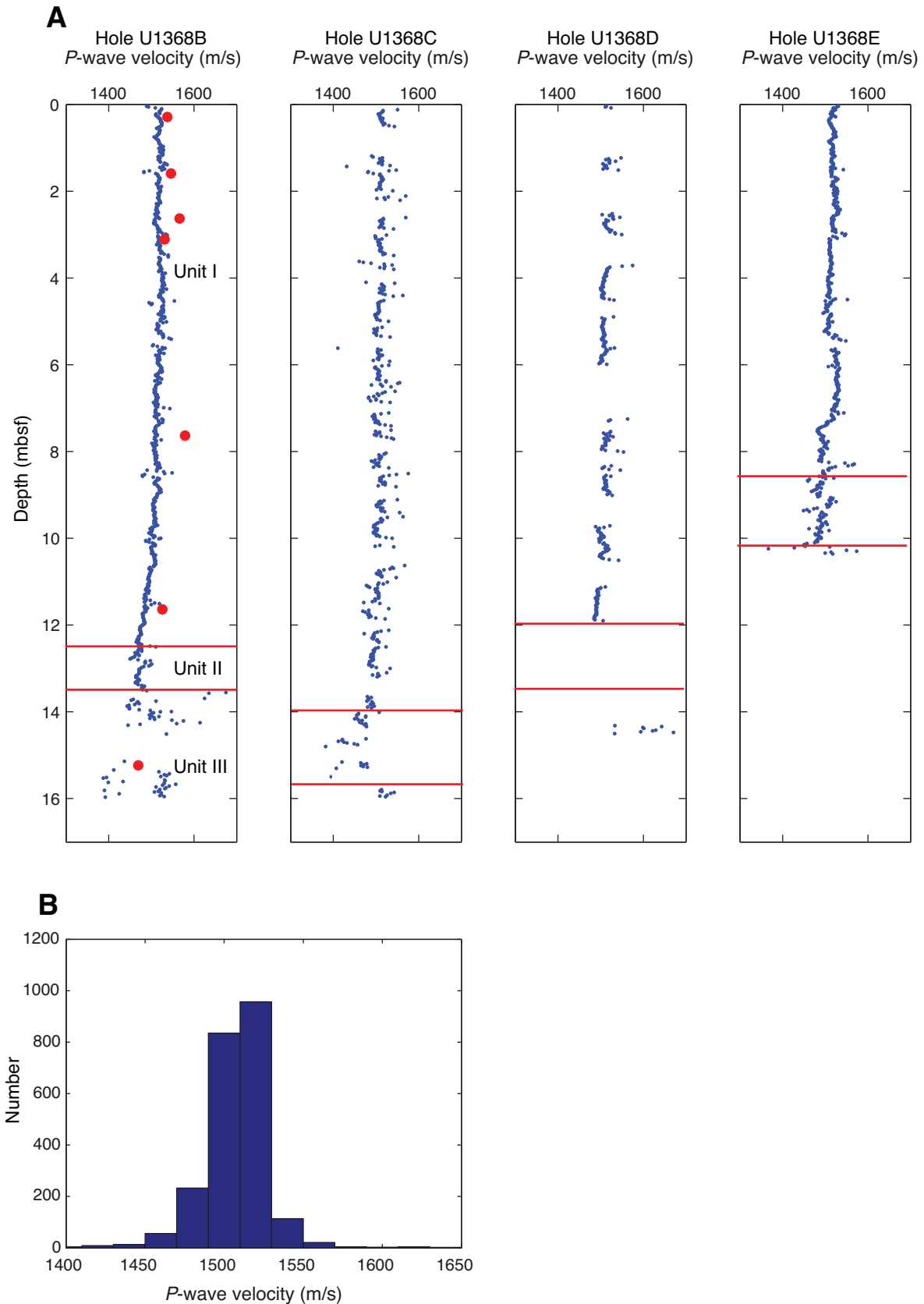


Figure F40. Plot of compressional wave velocity, Hole U1368F. Values from basalt were taken on cubes cut from the core.

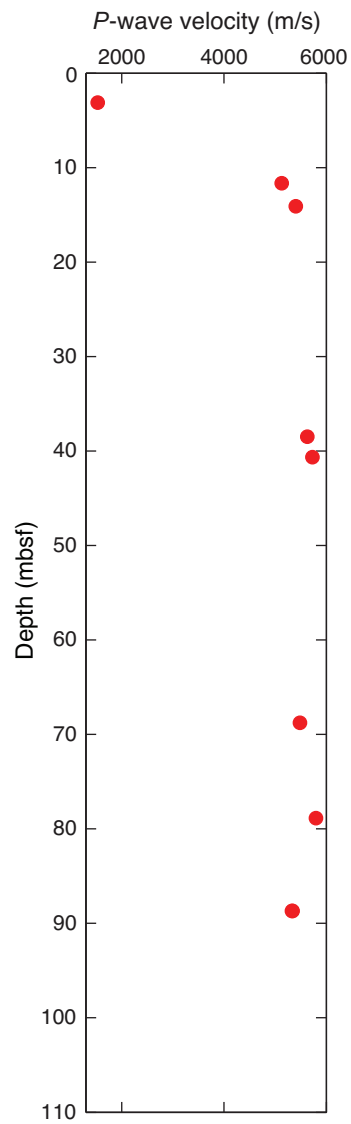


Figure F41. Plot of electrical conductivity measured on surface seawater standard, Site U1368. Line shows best linear fit to data. The best fitting slope and γ -intercept are -7×10^{-4} mS/m/measurement number and 49.67 mS/m, respectively.

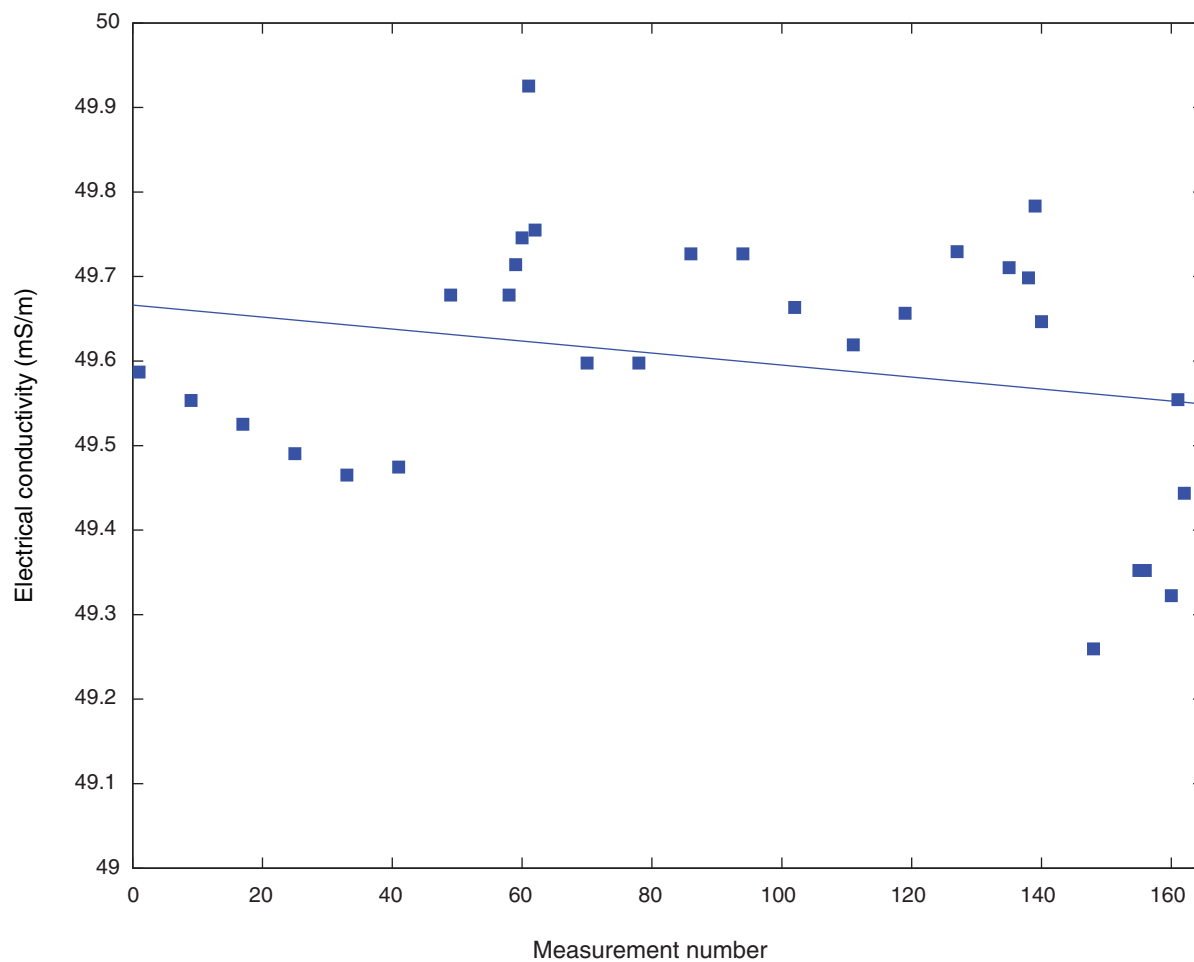


Figure F42. Plot of formation factor as a function of depth, Hole U1368B.

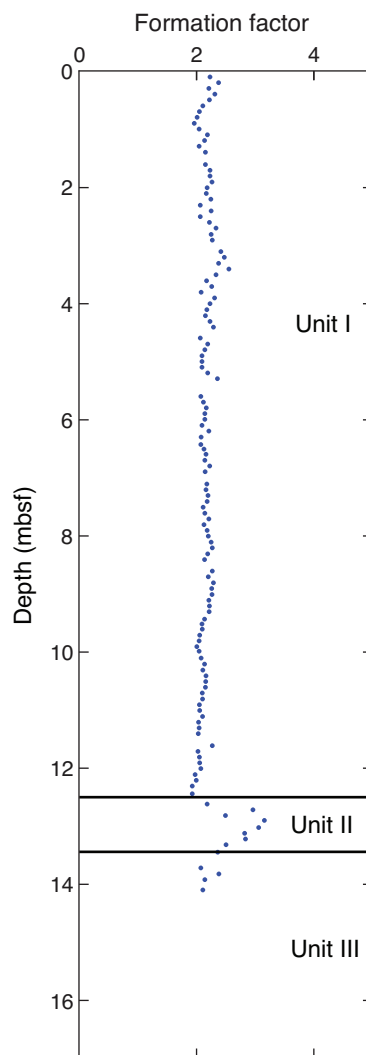


Figure F43. Plots of thermal data, Site U1368. **A.** Thermal conductivity values on sediments as a function of depth. Black triangles indicate values collected during KNOX-02RR site survey cruise. **B.** Hole U1368F thermal conductivity values.

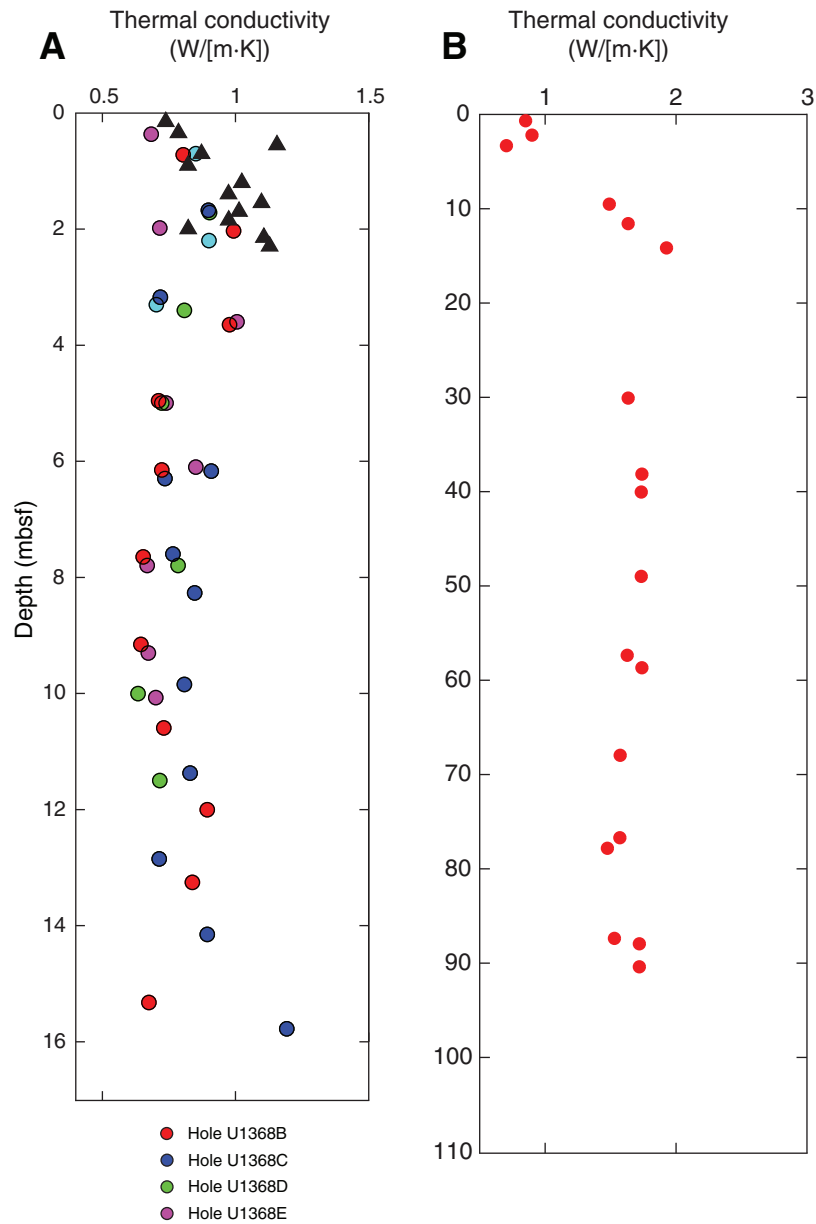


Figure F44. Plots of color spectrometry L* values, Site U1368.

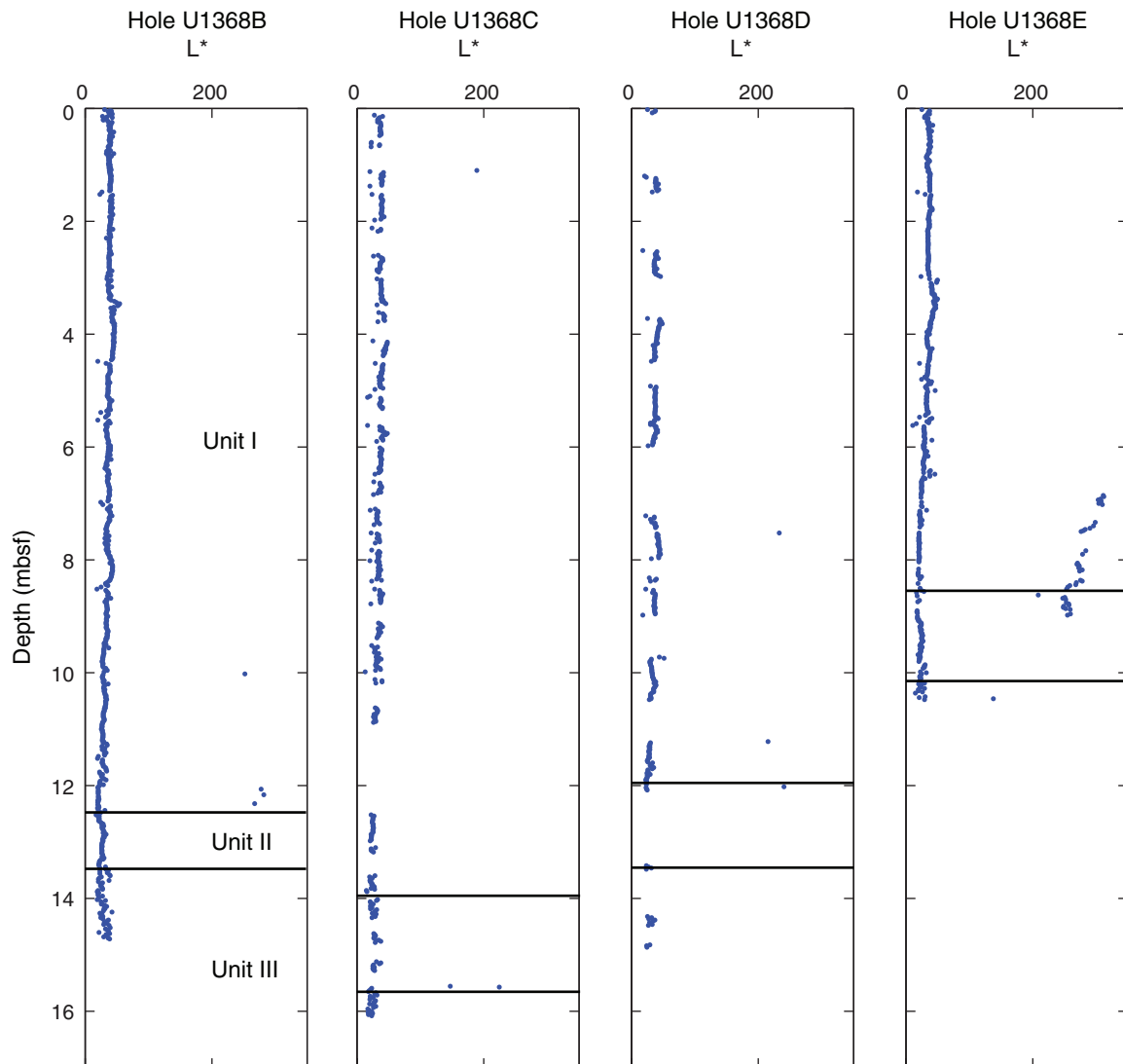


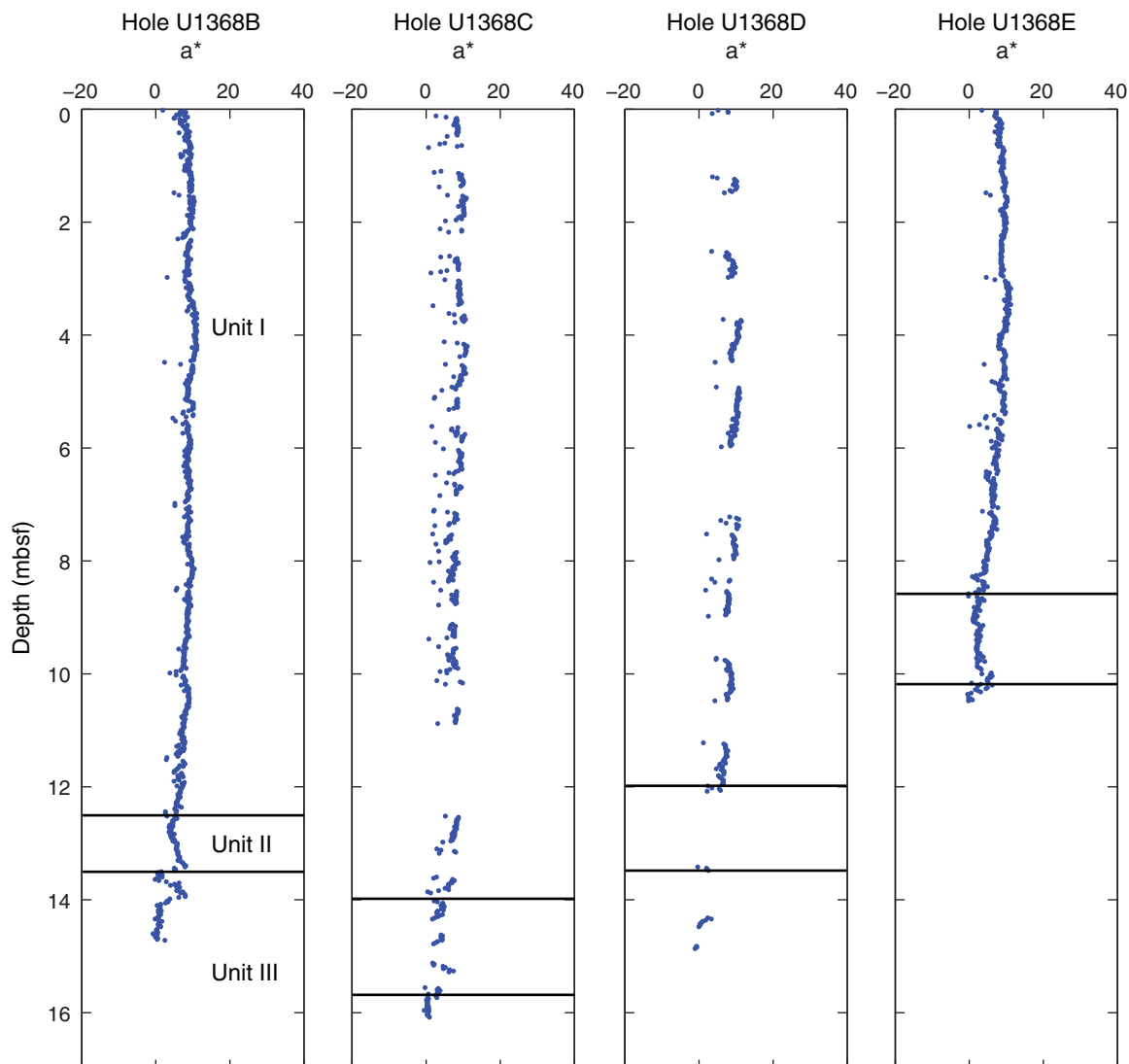
Figure F45. Plots of color spectrometry a^* values, Site U1368.

Figure F46. Plots of color spectrometry b^* values, Site U1368.

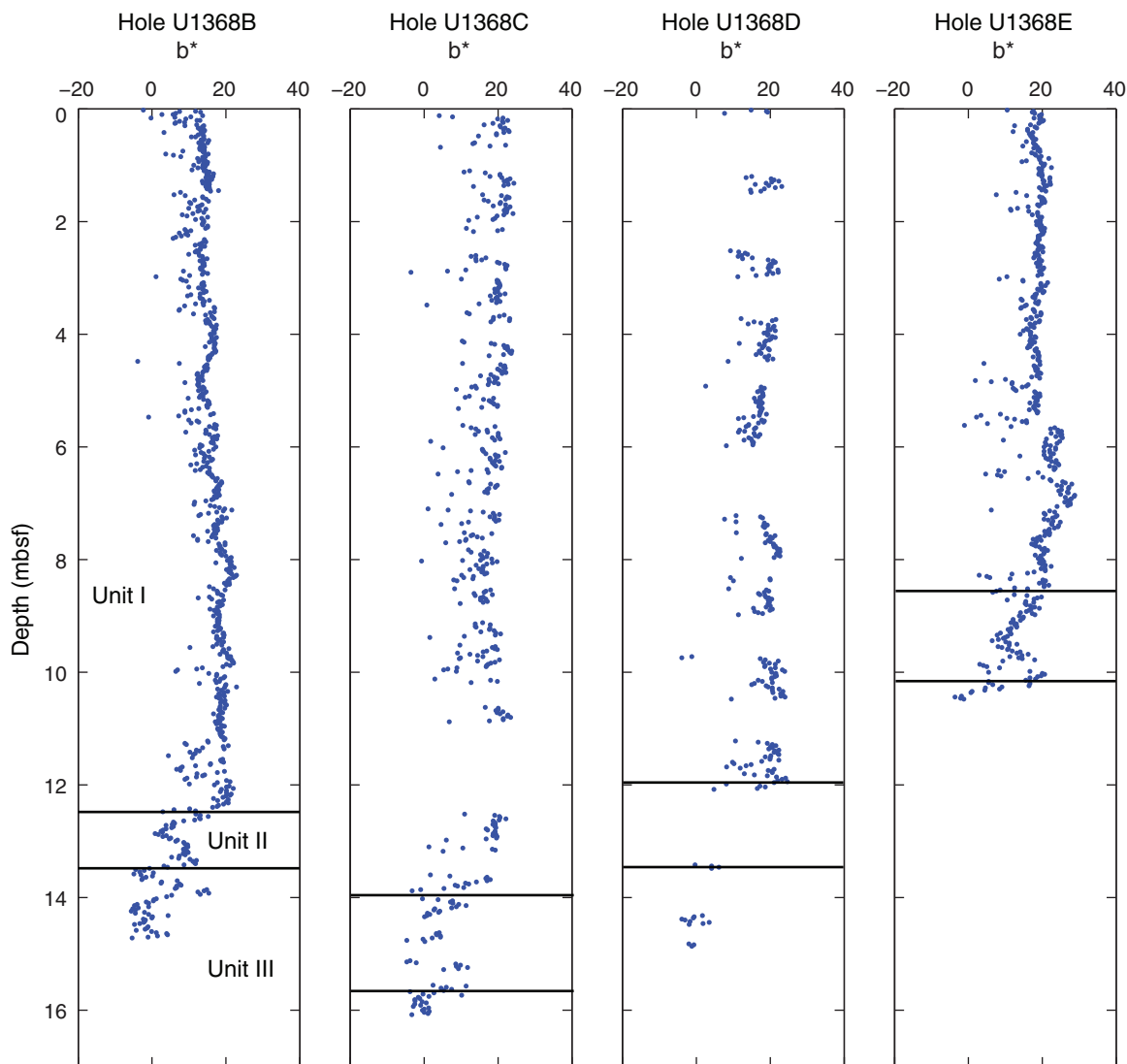


Figure F47. Plots of color spectrometry values, Hole U1368F.

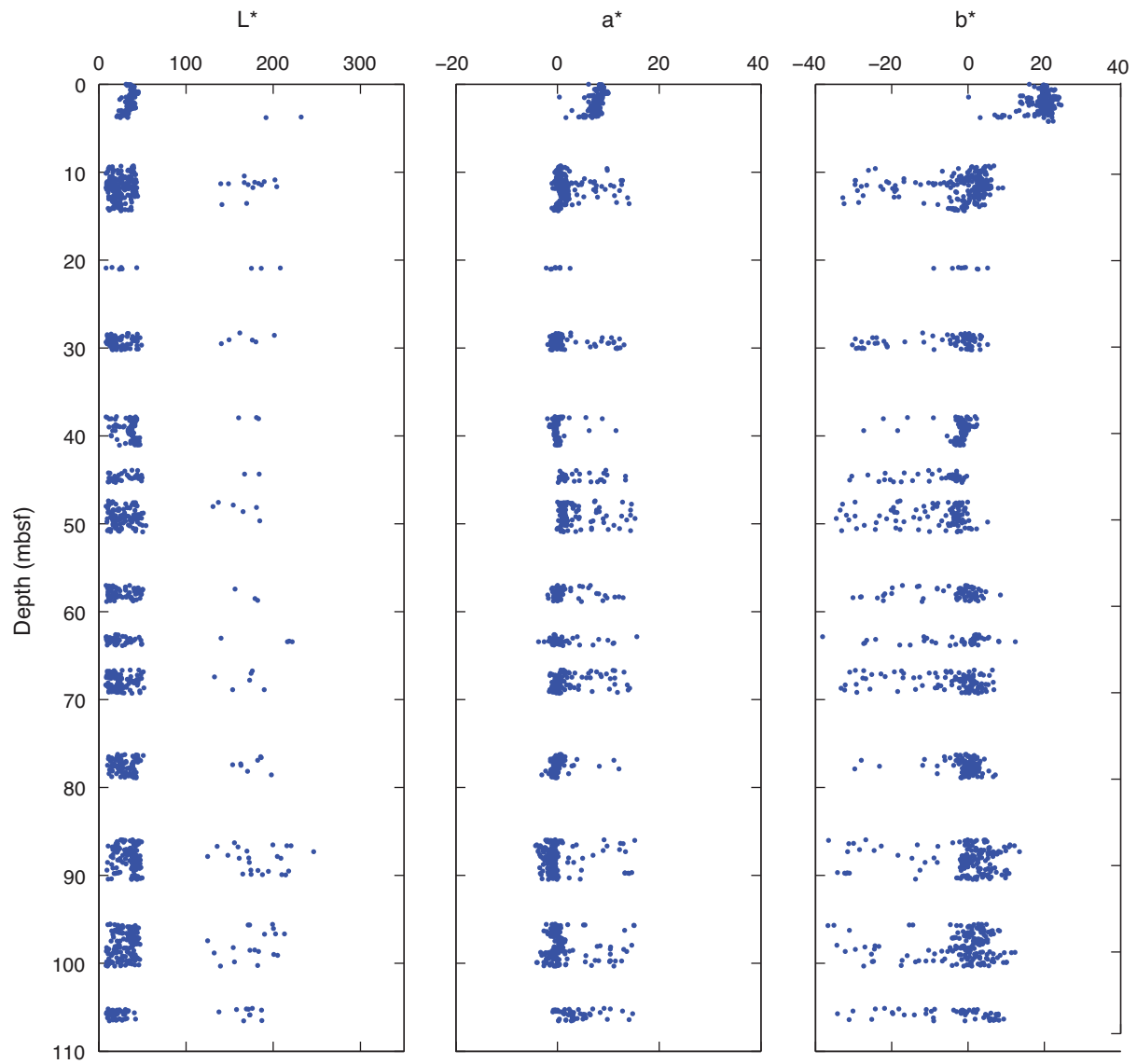




Figure F48. Plots of downhole caliper (blue = Pass 1, red = Pass 2) and electrical resistivity at three depths of investigation, Hole U1368F. IDPH = deep induction phasor-processed resistivity, IMPH = medium induction phasor-processed resistivity, SFLU = spherically focused resistivity. SFLU, IMPH, and IDPH resistivity profiles represent different depths of investigation into the formation (64, 76, and 152 cm, respectively) and different vertical resolutions (76, 152, and 213 cm, respectively).

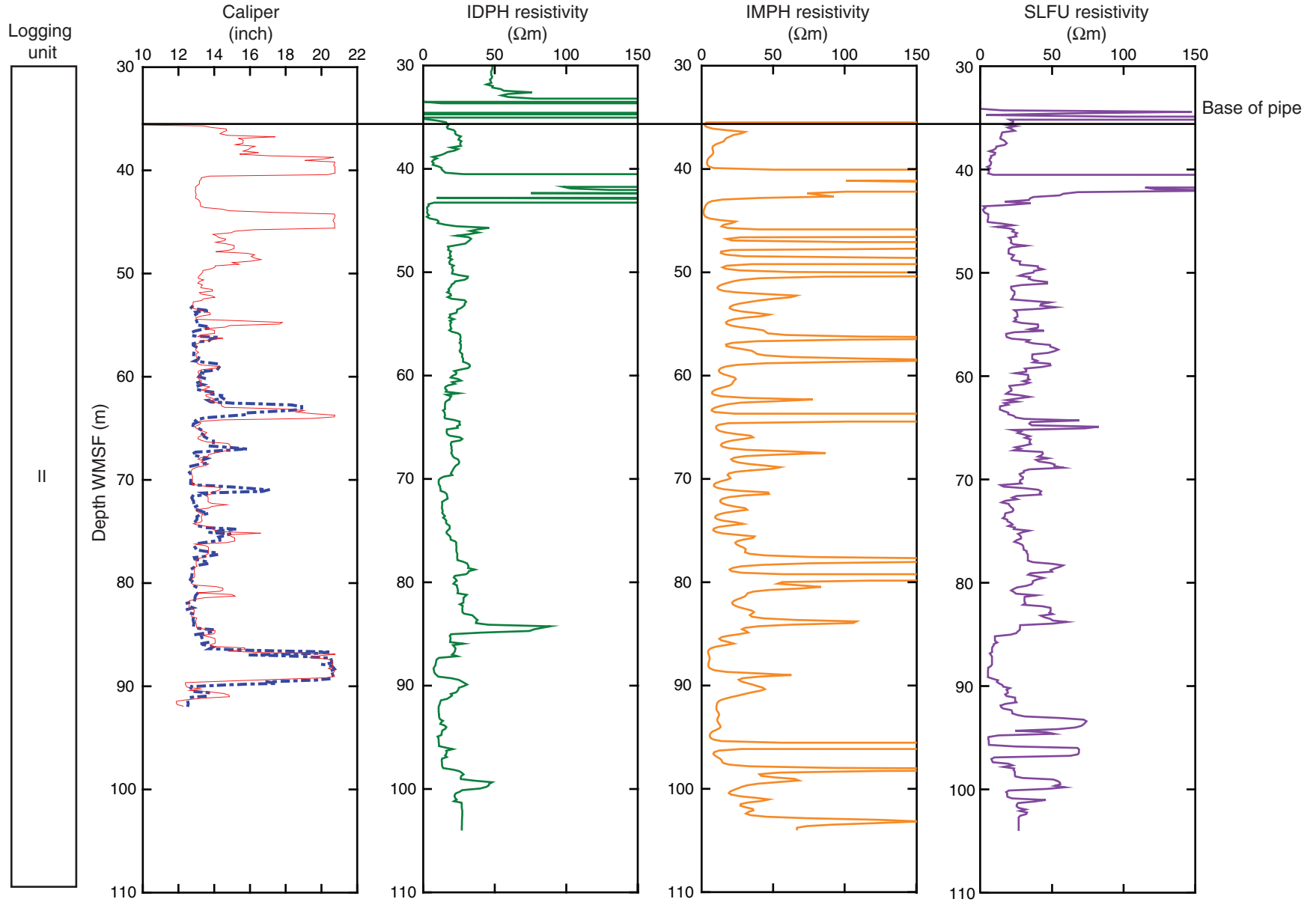




Figure F49. Downhole plots of total and spectral gamma ray measurements with the individual contributions of ^{238}U , ^{232}Th , and ^{40}K , Hole U1368F. Orange = total NGR, green = total NGR minus uranium.

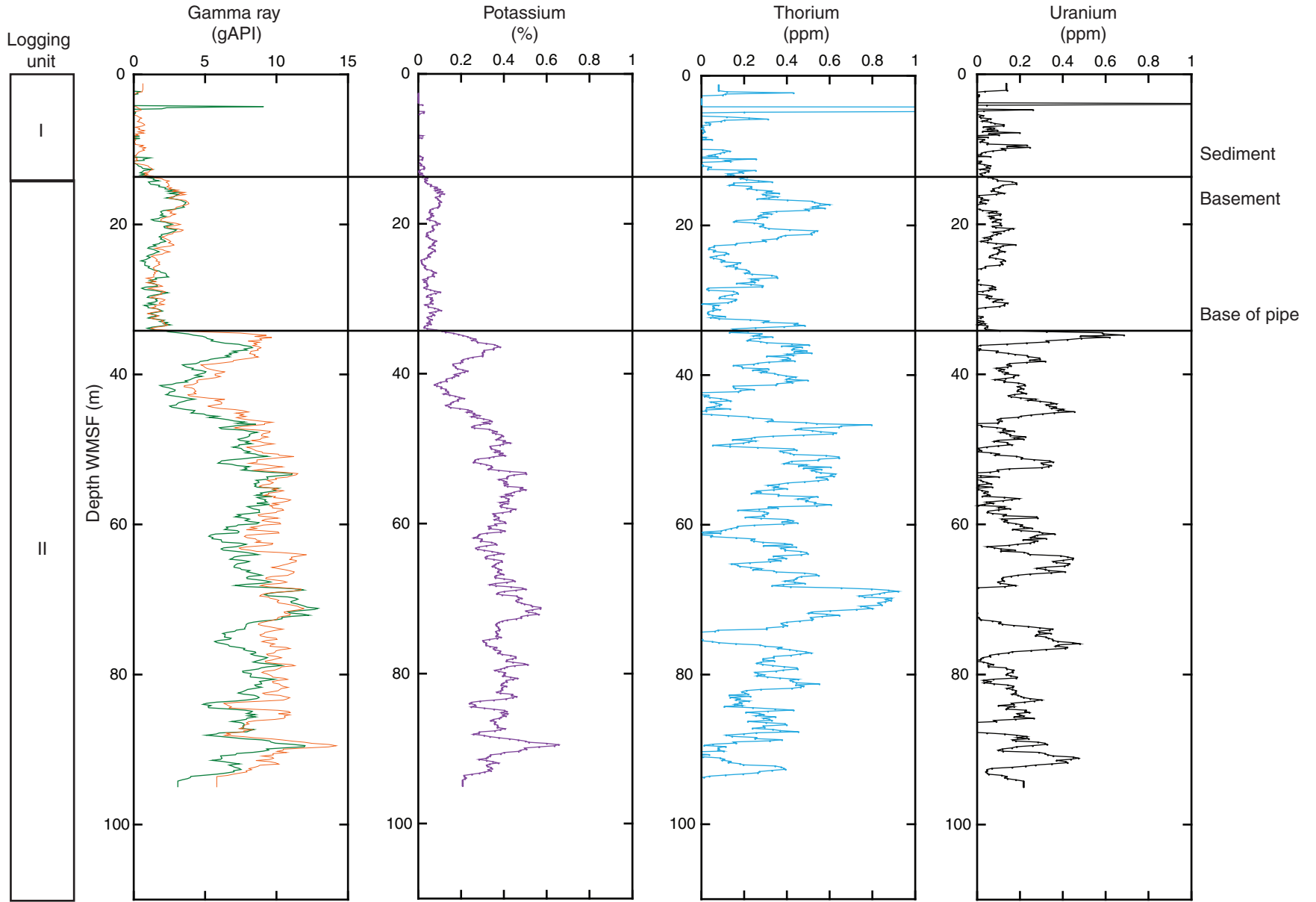


Figure F50. Plots comparing downhole total natural gamma radiation (NGR; red and blue), sediment (green) and basement (black) NGR, and total (purple) and whole-core section (green) potassium measurements, Hole U1368F. Total gamma ray data are corrected by a factor 3.5 to compensate for attenuation of the signal by the bottom-hole assembly.

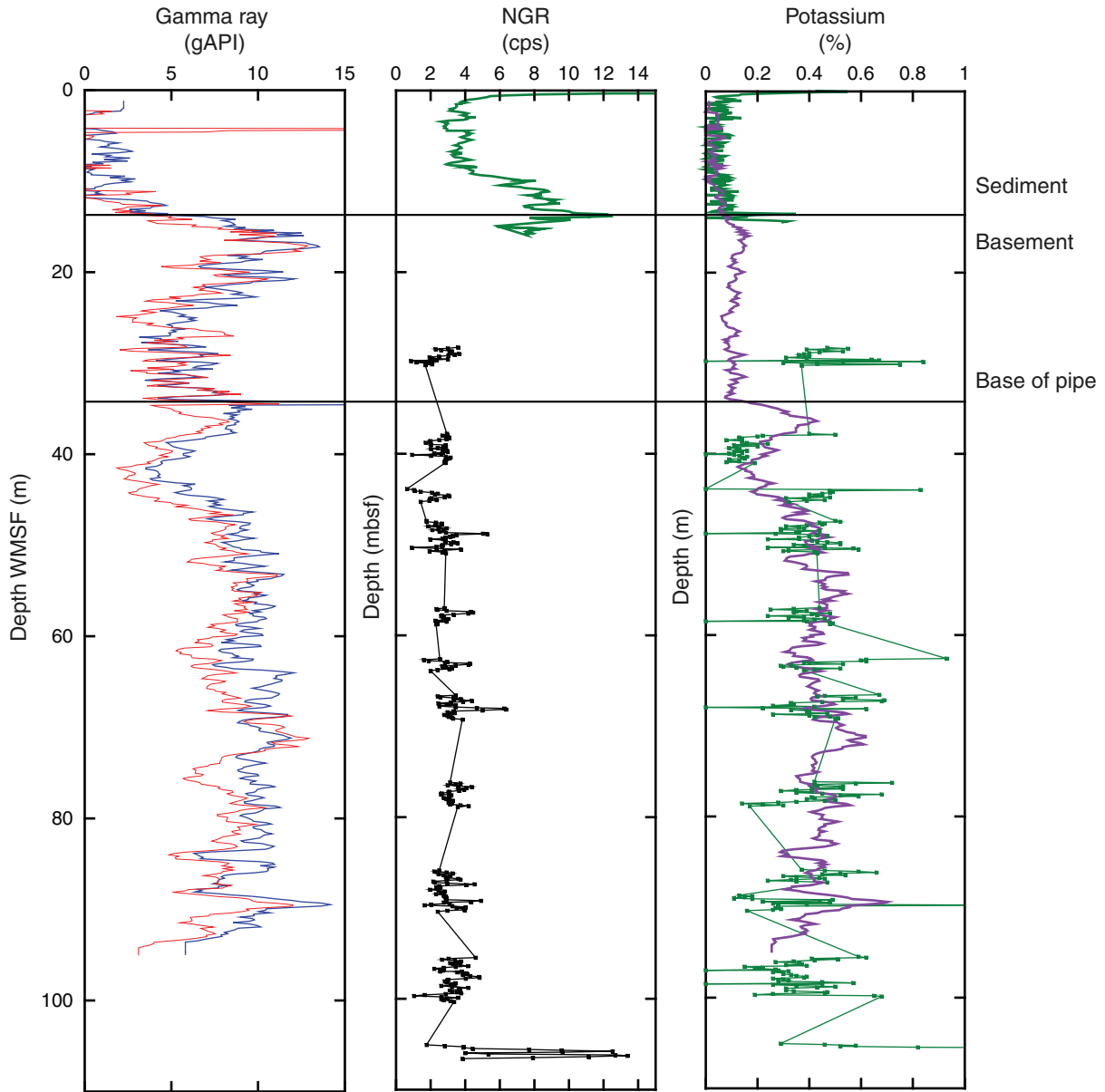


Figure F51. Plot of downhole caliper and density data, Hole U1368F. Blue = Pass 1, red = Pass 2.

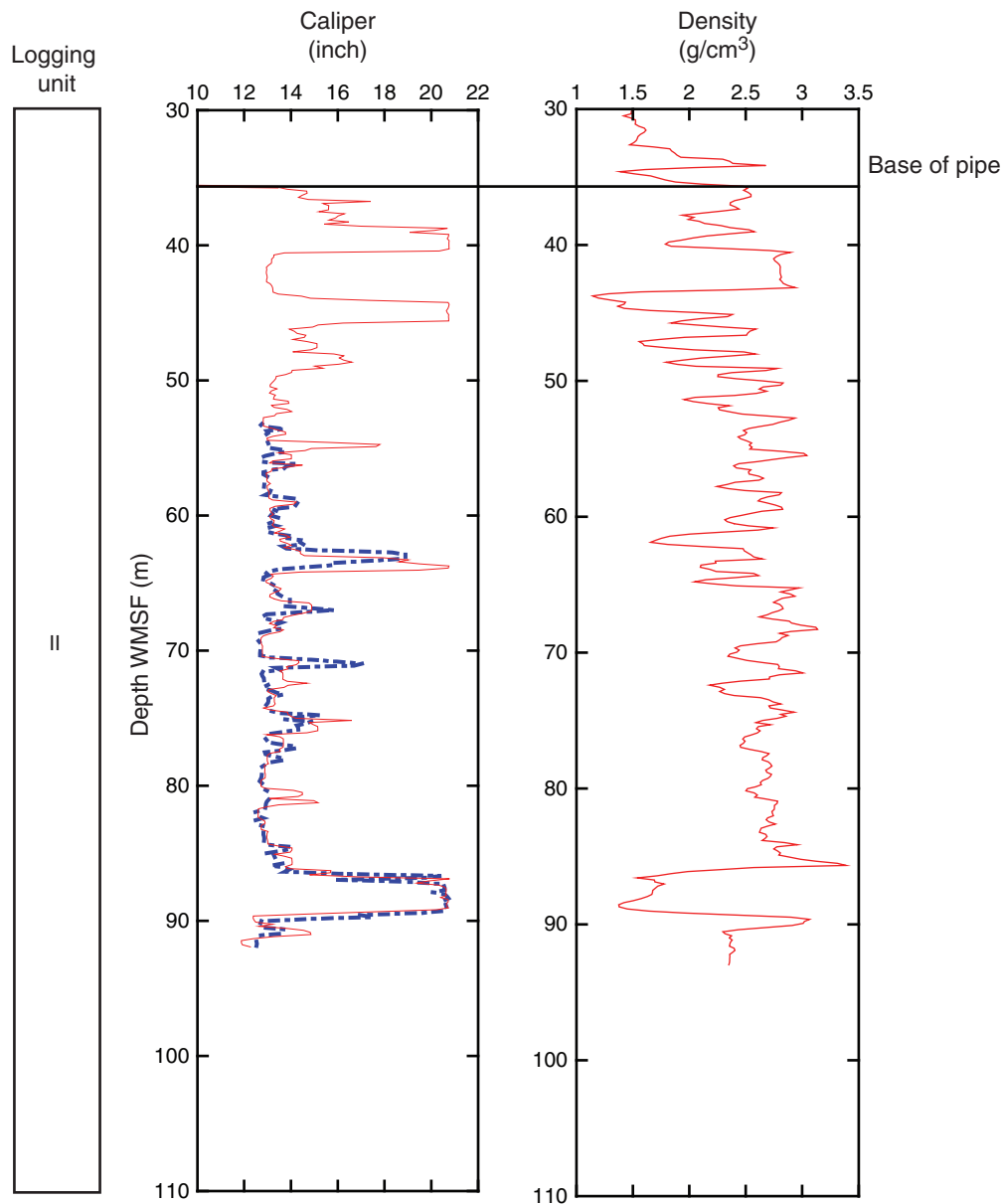


Figure F52. Formation MicroScanner images of pillow lavas and massive pillows, Hole U1368F.

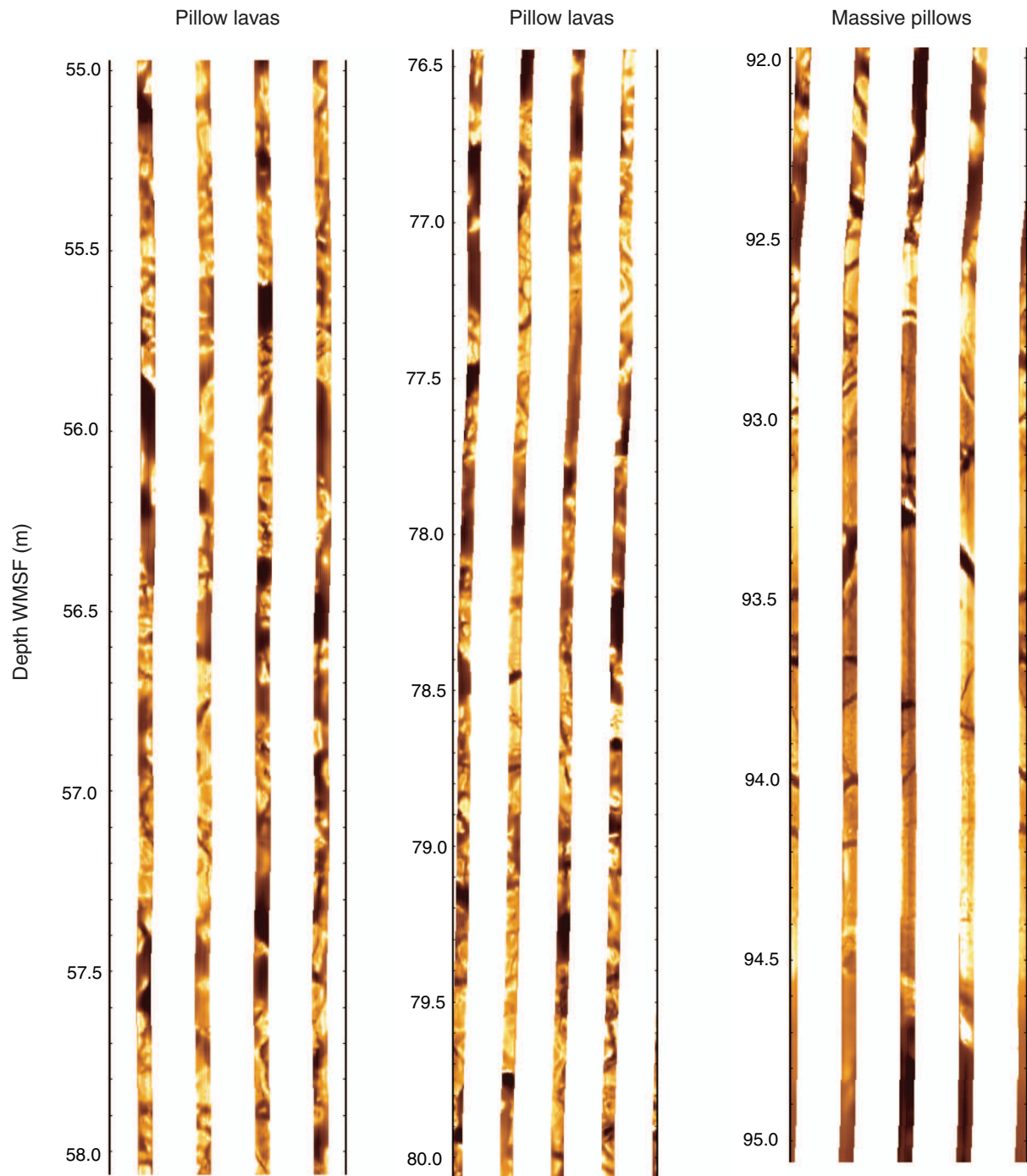


Figure F53. Formation MicroScanner images compared to images of Core 329-U1368F-5R showing massive pillow structures.

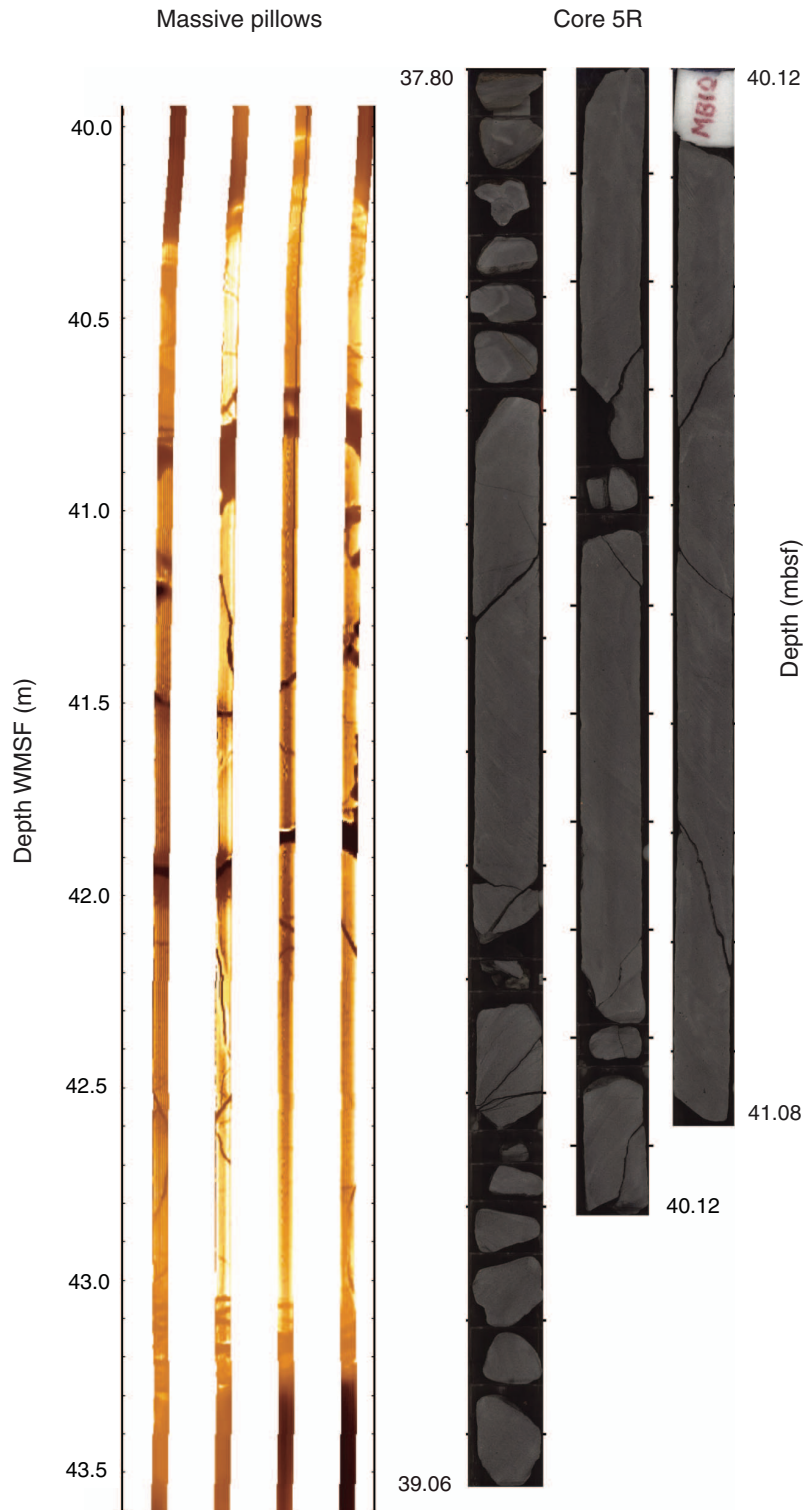


Figure F54. Summary of magnetic susceptibility and paleomagnetic intensity, Hole U1368B. Gray = measurement before demagnetization, red = measurement after 20 mT AF demagnetization step (inclination and intensity), blue = declination measurements, green = magnetic susceptibility data. Black squares = magnetic directions of discrete cube samples from the working-half cores.

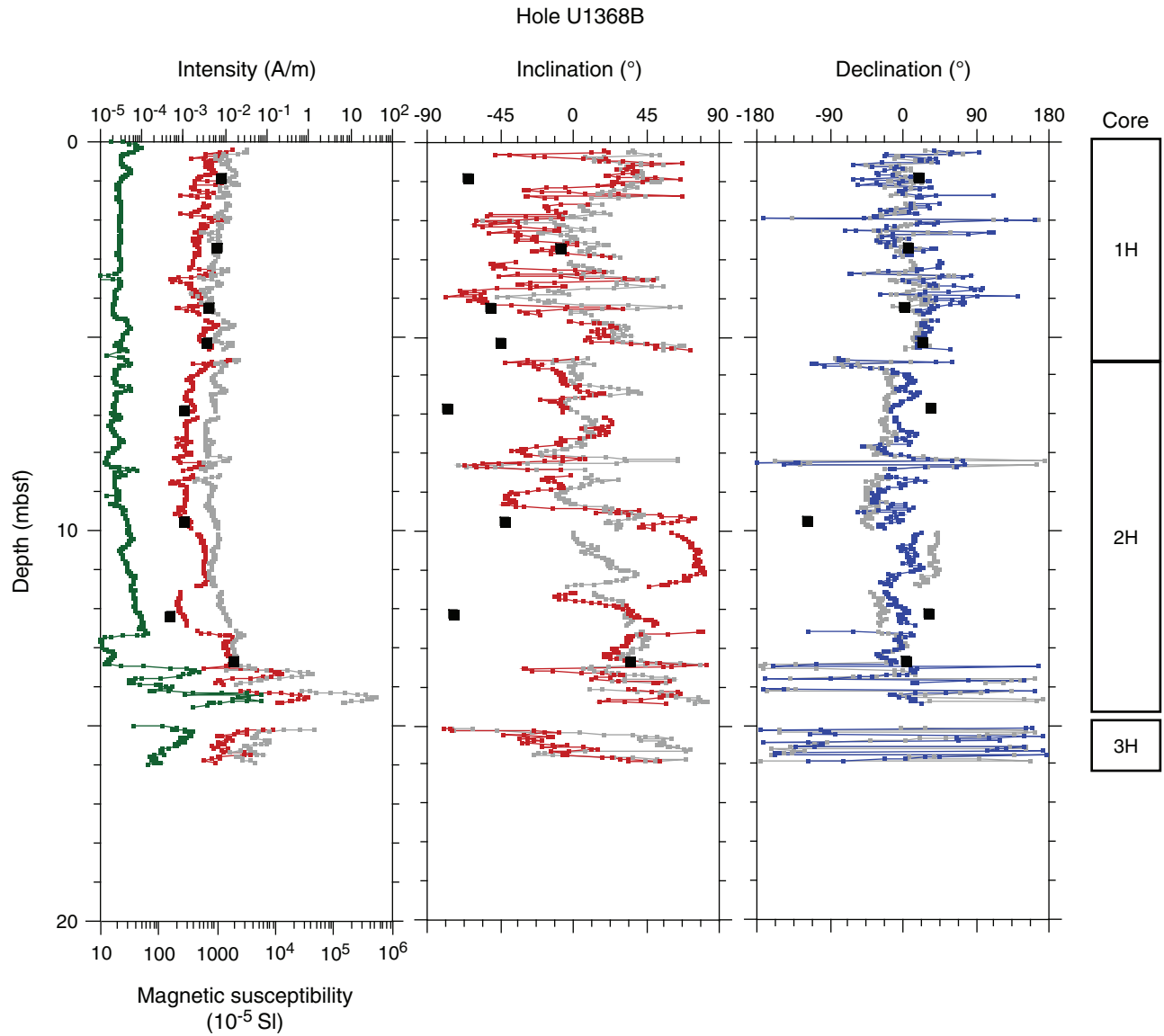


Figure F55. Summary of magnetic susceptibility and paleomagnetic results, Hole U1368C. Gray = measurement before demagnetization, red = measurement after 20 mT AF demagnetization step (inclination and intensity), blue = declination measurements, green = magnetic susceptibility data.

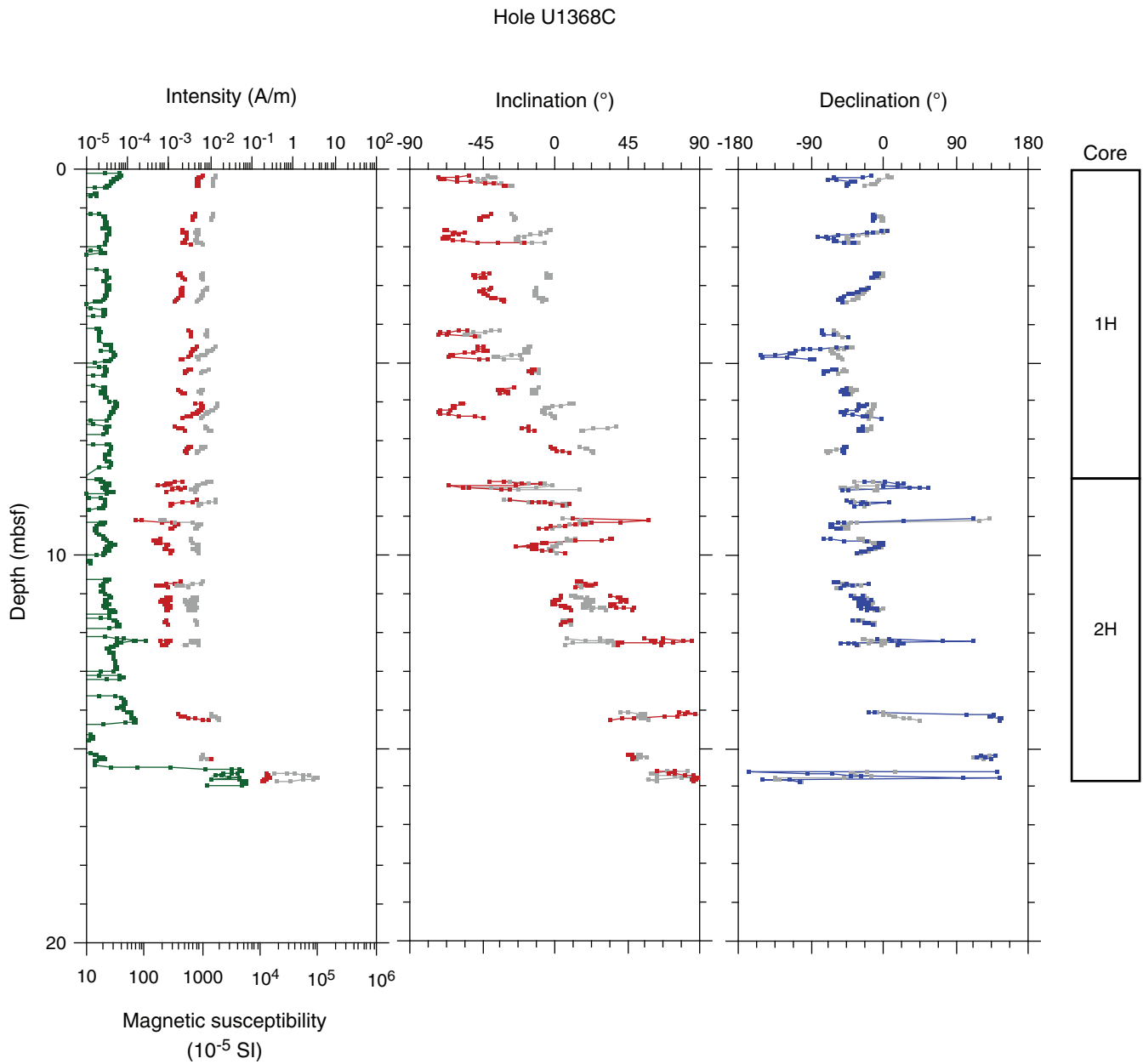


Figure F56. Summary of magnetic susceptibility and paleomagnetic results, Hole U1368D. Gray = measurement before demagnetization, red = measurement after 20 mT AF demagnetization step (inclination and intensity), blue = declination measurements, green = magnetic susceptibility data.

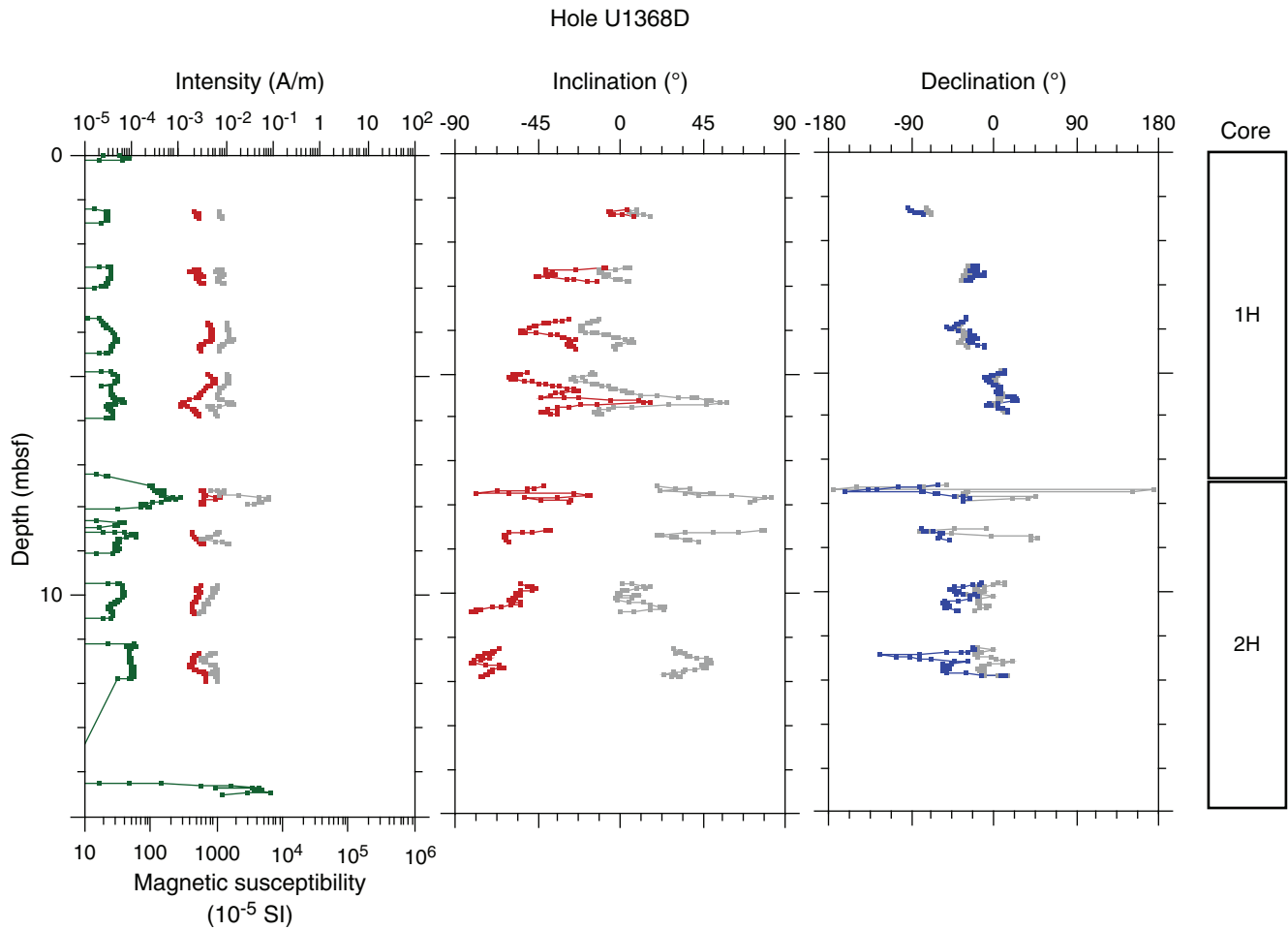


Figure F57. Summary of magnetic susceptibility and paleomagnetic results, Hole U1368E. Gray = measurement before demagnetization, red = measurement after 20 mT AF demagnetization step (inclination and intensity), blue = declination measurements, green = magnetic susceptibility data.

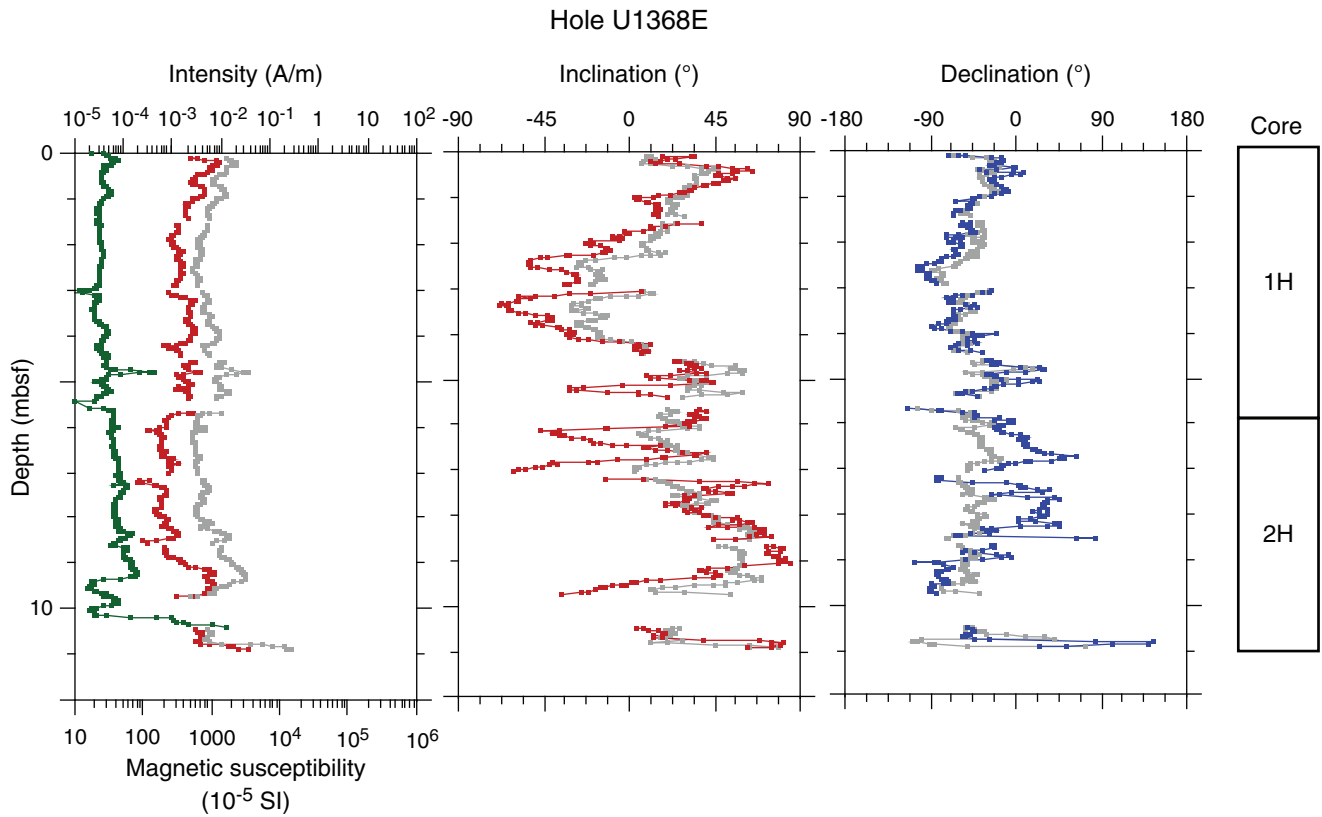


Figure F58. Summary of magnetic susceptibility and paleomagnetic results, Hole U1368F. Gray = measurement before demagnetization, red = measurement after 20 mT AF demagnetization step (inclination and intensity), blue = declination measurements, green = magnetic susceptibility data. Black squares = magnetic directions of discrete cube samples from the working-half cores.

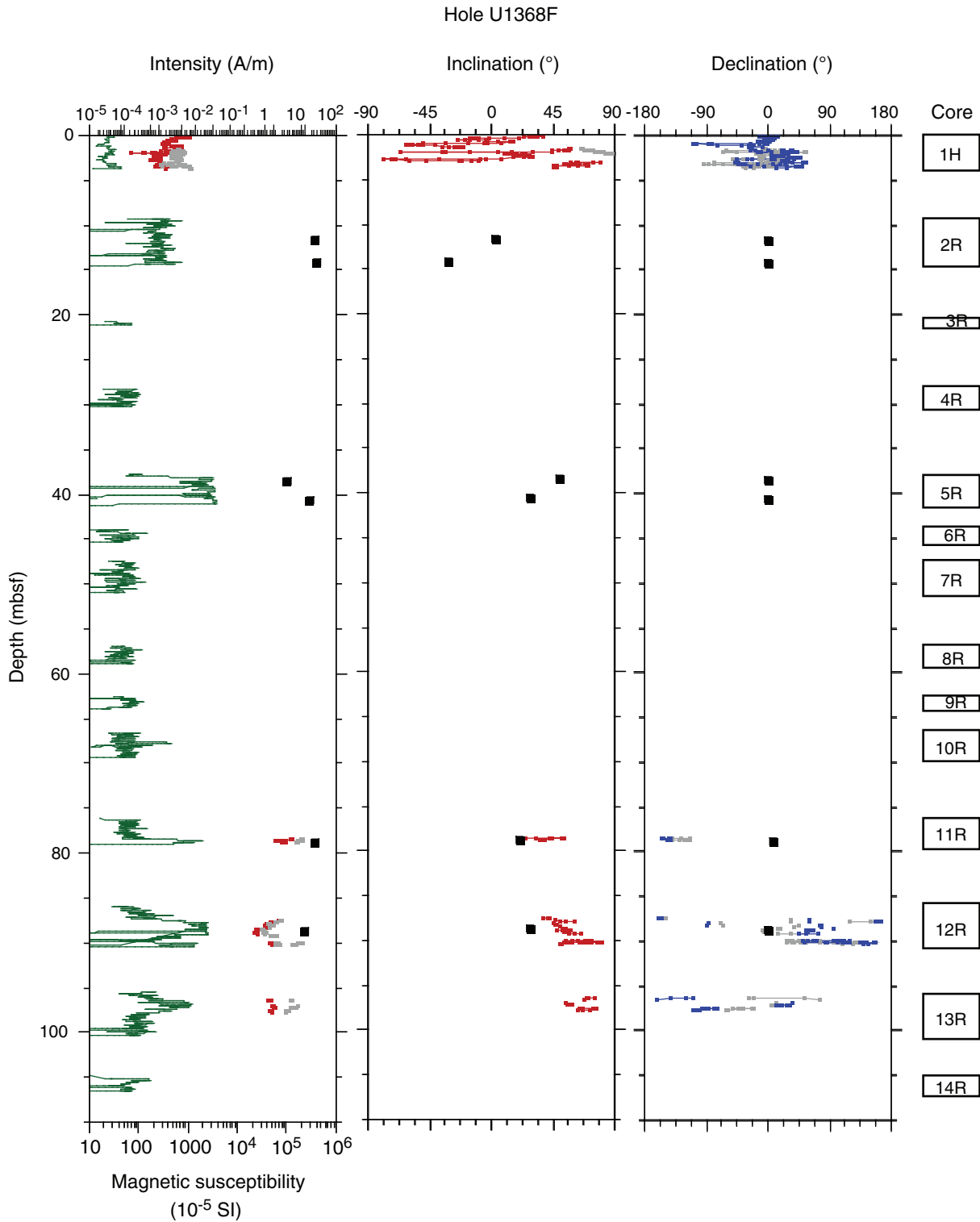


Figure F59. Results of hole-to-hole correlation using magnetic susceptibility from Holes U1368B and U1368E. Black lines indicate correlation points between holes.

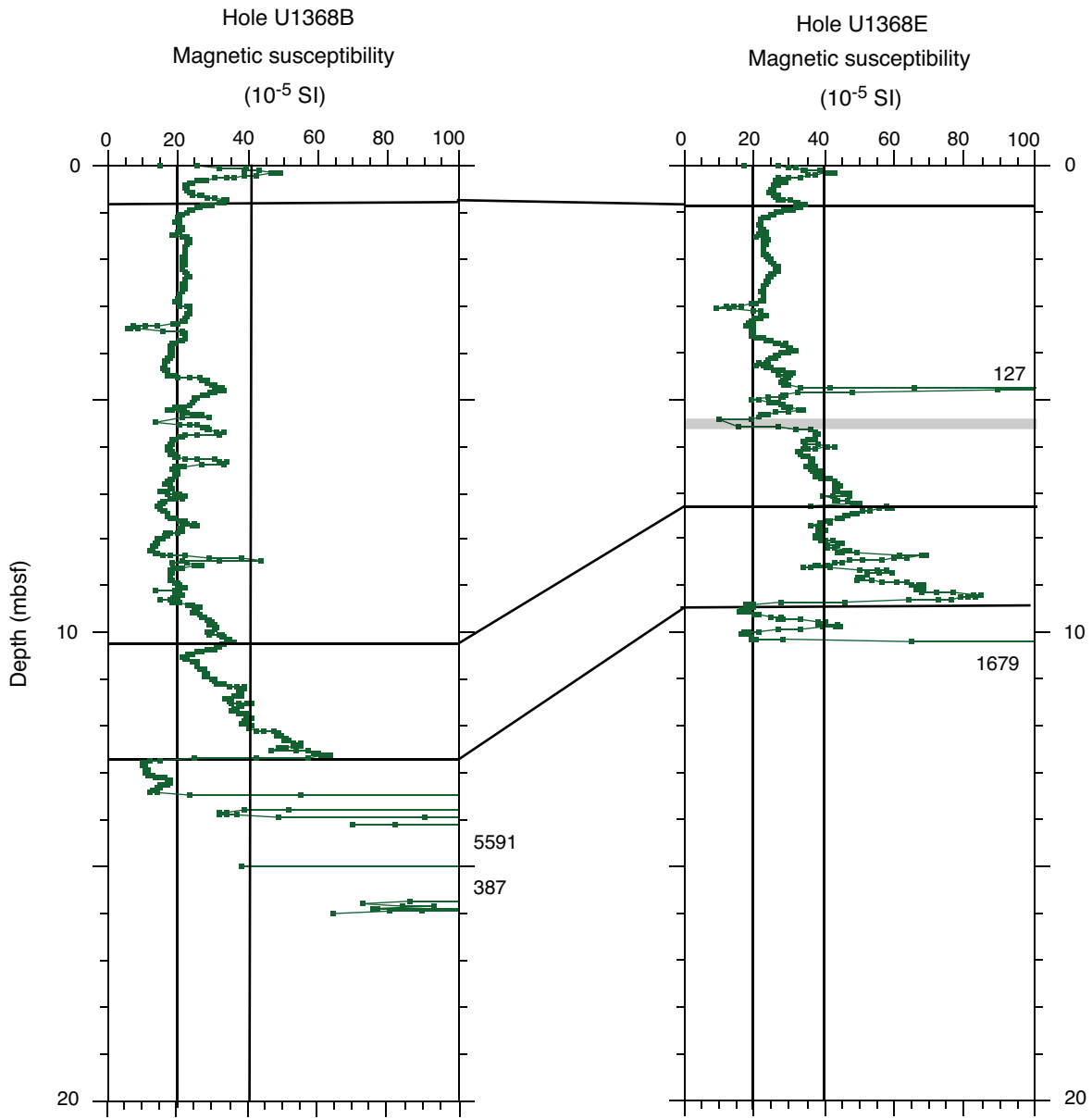


Figure F60. Correlation of polarity records between Holes U1368B and U1368E. Inclination (red) and declination (blue) data are after the 20 mT AF demagnetization step. Black lines indicate correlation points between holes. Gray = measurement before demagnetization. Black squares = magnetic directions of discrete cube samples from the working-half cores.

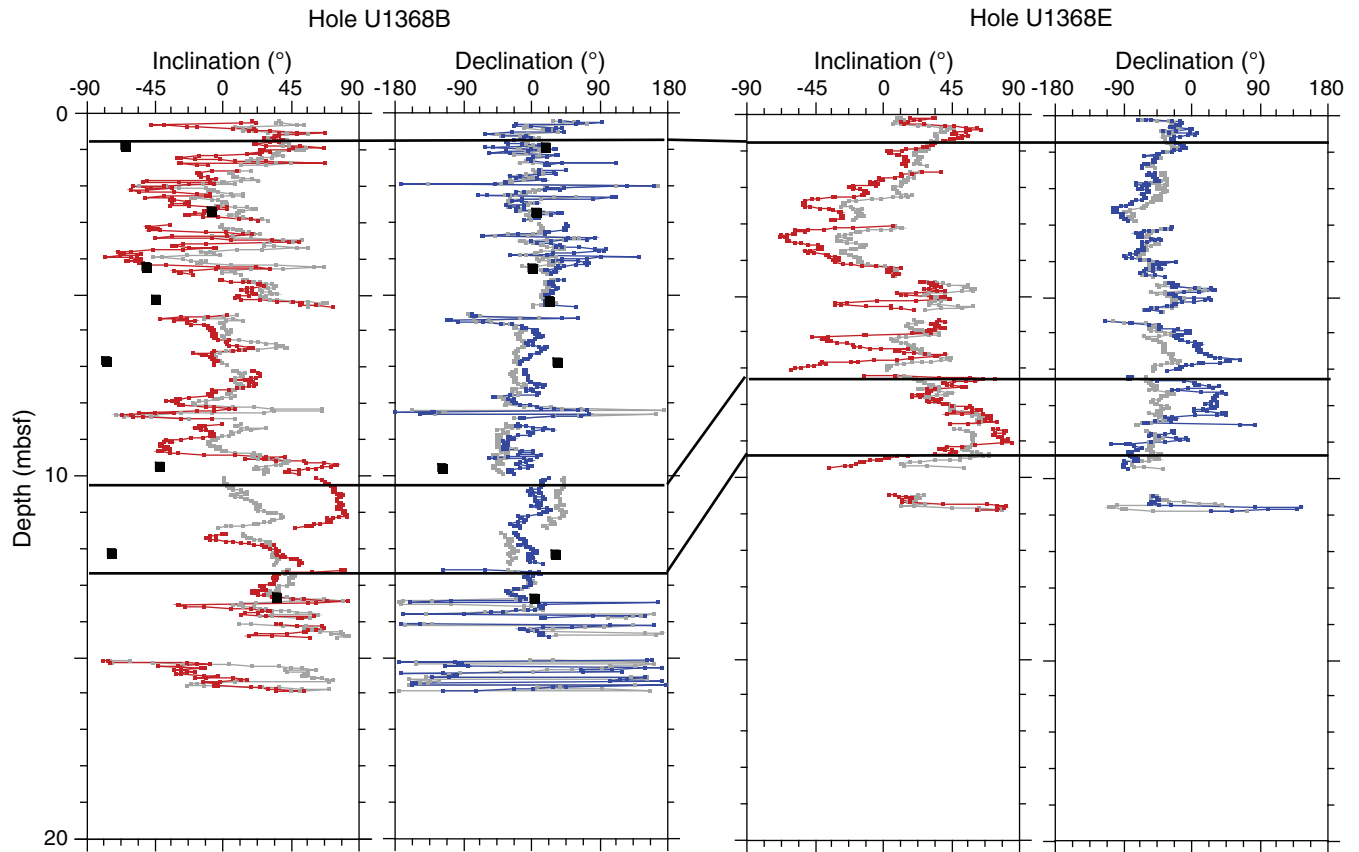


Figure F61. A. Plot of combined dissolved oxygen concentrations measured with optodes (Hole U1368B) and electrodes (Holes U1368B, U1368C, U1368E and U1368F). B. Combined dissolved oxygen concentrations in the uppermost 5.5 m of sediment, Hole U1368B.

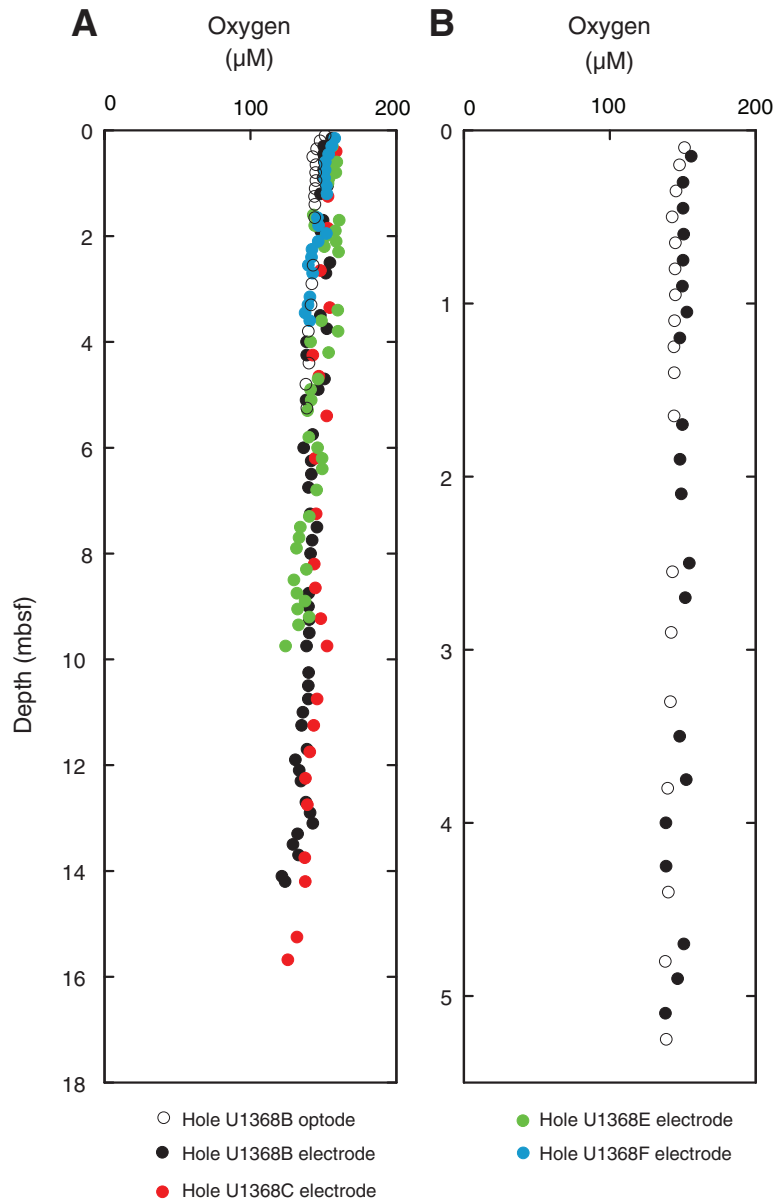


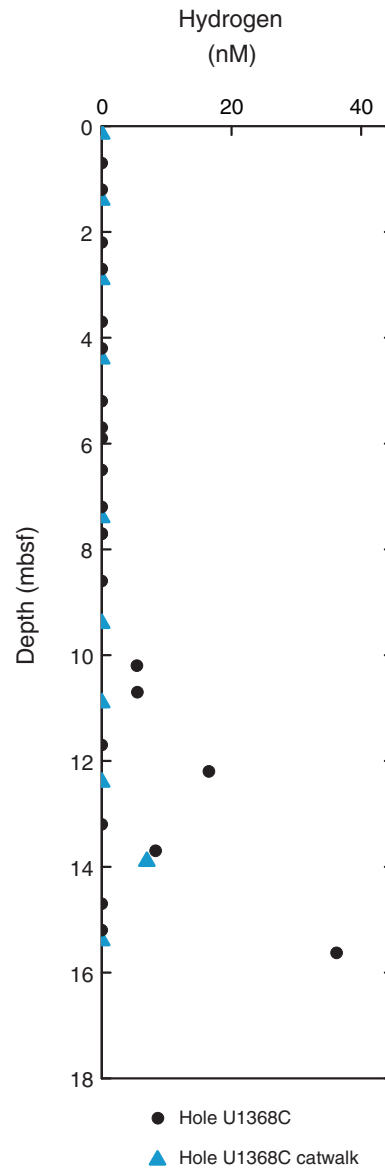
Figure F62. Plot of dissolved hydrogen, Hole U1368C.



Figure F63. Plot of dissolved interstitial water constituents, Hole U1368C. IC = ion chromatography, ICP = inductively coupled plasma-atomic emission spectroscopy. **A.** Nitrate. **B.** Phosphate. **C.** Silicate. **D.** Alkalinity. **E.** Dissolved inorganic carbon (DIC). (Continued on next two pages.)

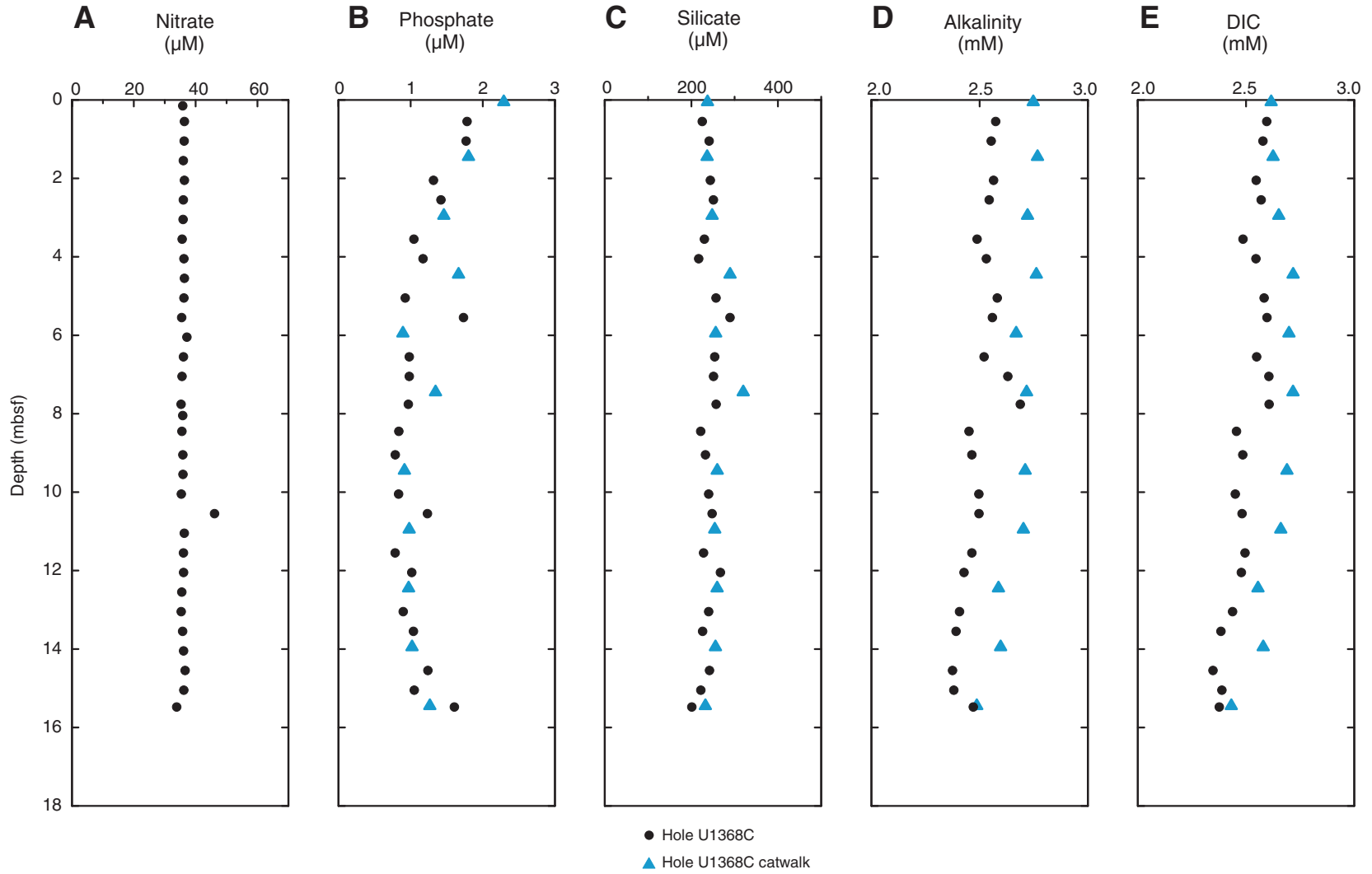




Figure F63 (continued). F. Sulfate. G. Sulfate anomaly. Dissolved sulfate concentrations normalized to chloride (see “Biogeochemistry” in the “Methods” chapter [Expedition 329 Scientists, 2011a]), Hole U1368C. H. Chloride. I. Calcium. J. Magnesium. (Continued on next page.)

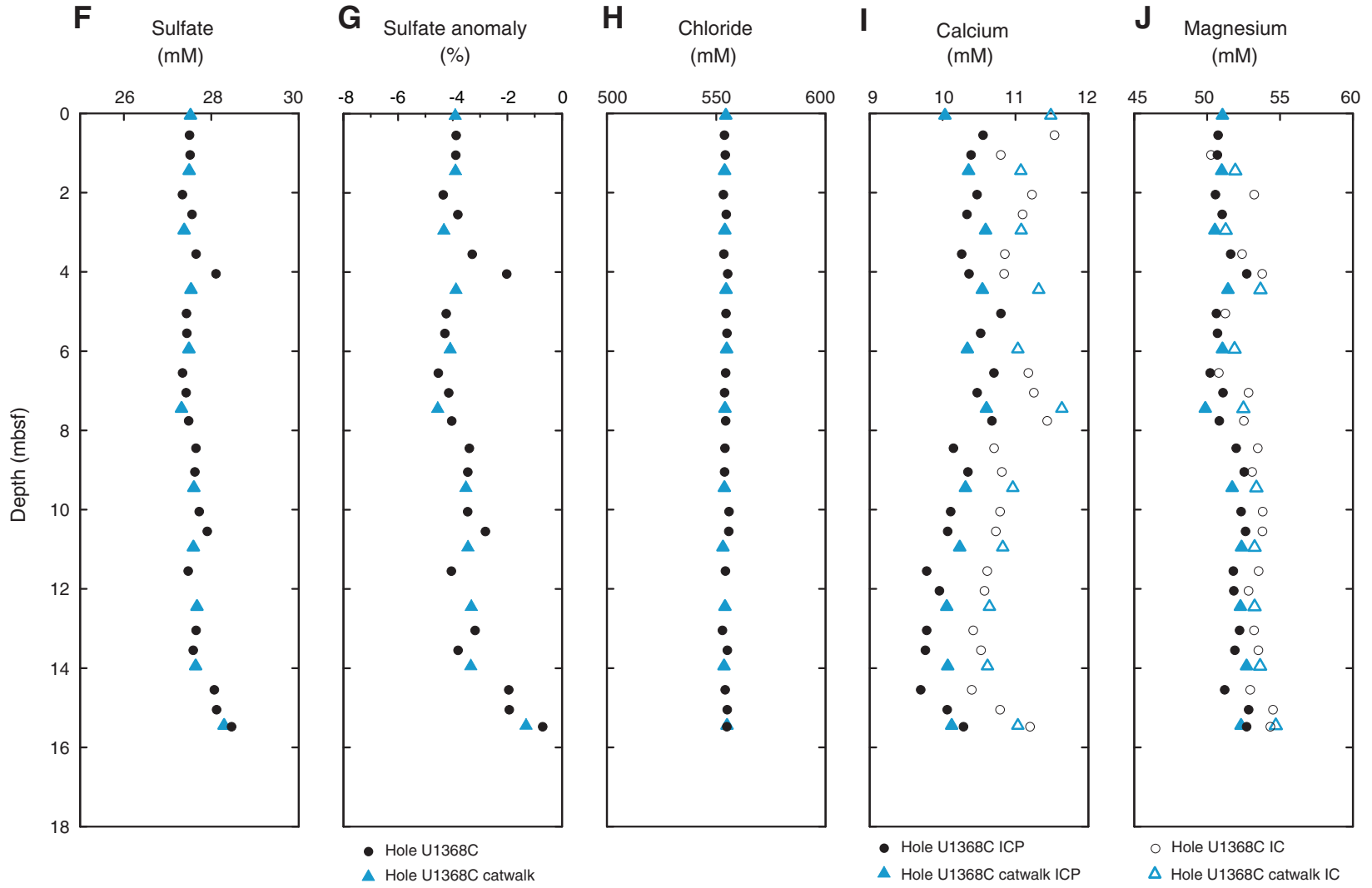




Figure F63 (continued). K. Sodium. L. Potassium.

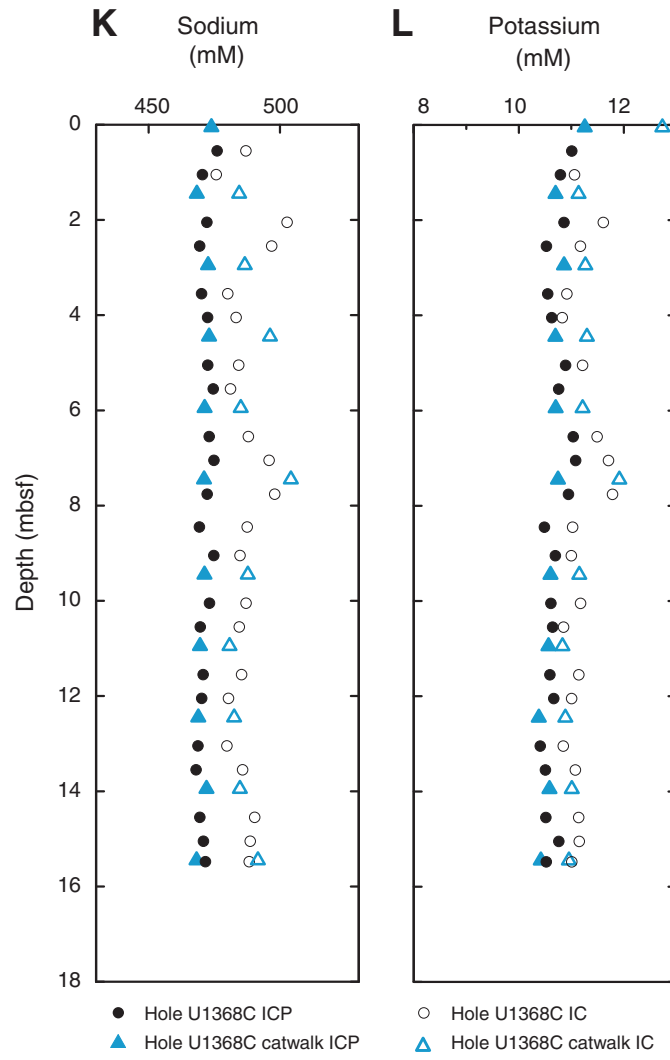


Figure F64. Plots of solid-phase nitrogen and carbon, Hole U1368B. **A.** Total nitrogen (TN). **B.** Total organic carbon (TOC). **C.** Calcium carbonate (CaCO₃).

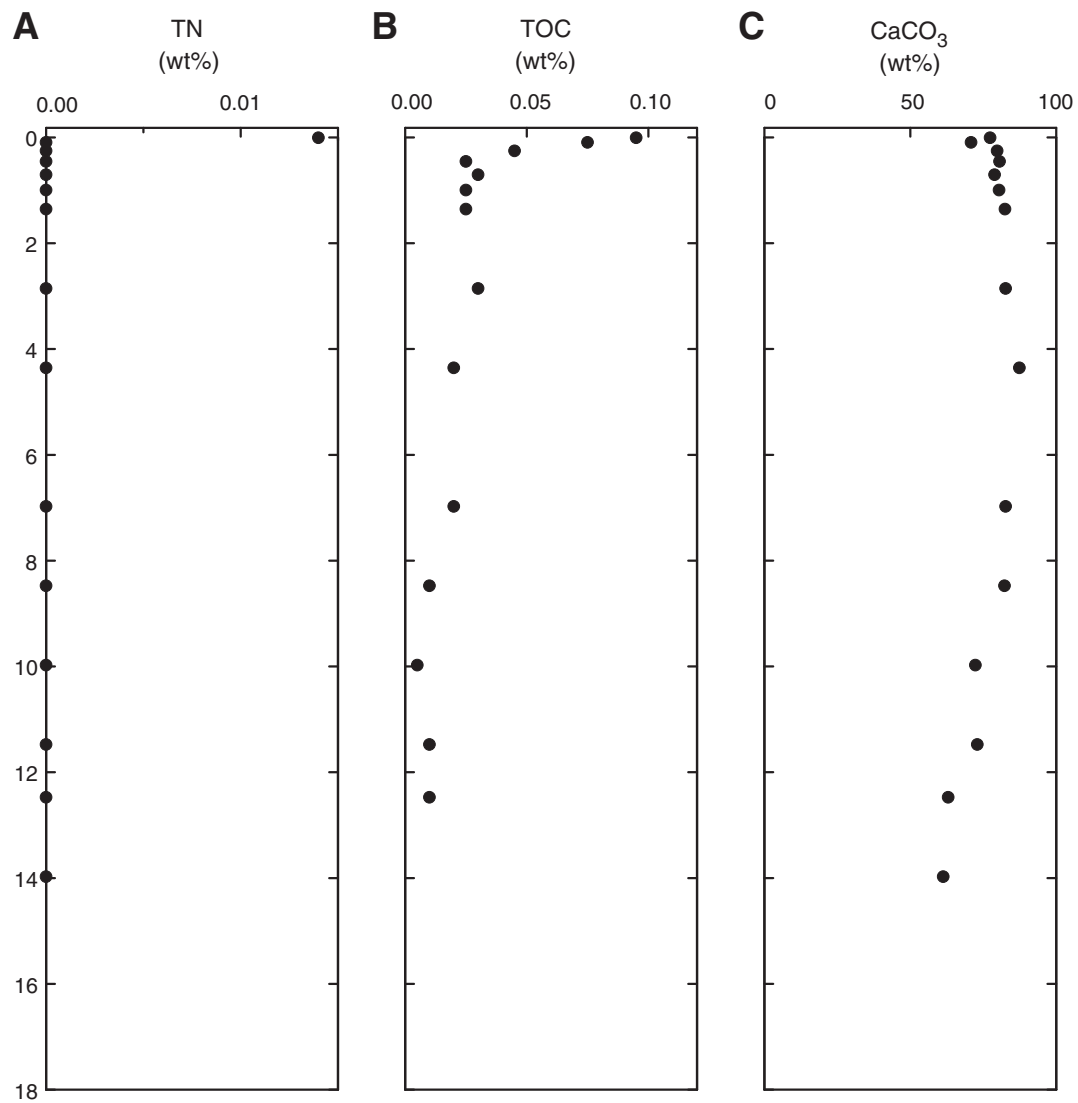


Figure F65. Plot of abundance of microbial cells and virus-like particles in Site U1368 sediment as determined by epifluorescence microscopy. Counts below the blank are shown as 10^2 cells/cm³ in order to present them in the graph. See “Microbiology” in the “Methods” chapter (Expedition 329 Scientists, 2011a) for a detailed description of the blank and minimum detection limit (MDL) calculation. Red line = MDL for cell counts from extracts, blue line = MDL for nonextracted samples, solid red circles = abundances above MDL, open red circles = direct counts below MDL, solid black squares = VLP counts, solid blue diamonds = nonextracted direct counts above MDL, open blue diamonds = nonextracted direct counts below MDL.

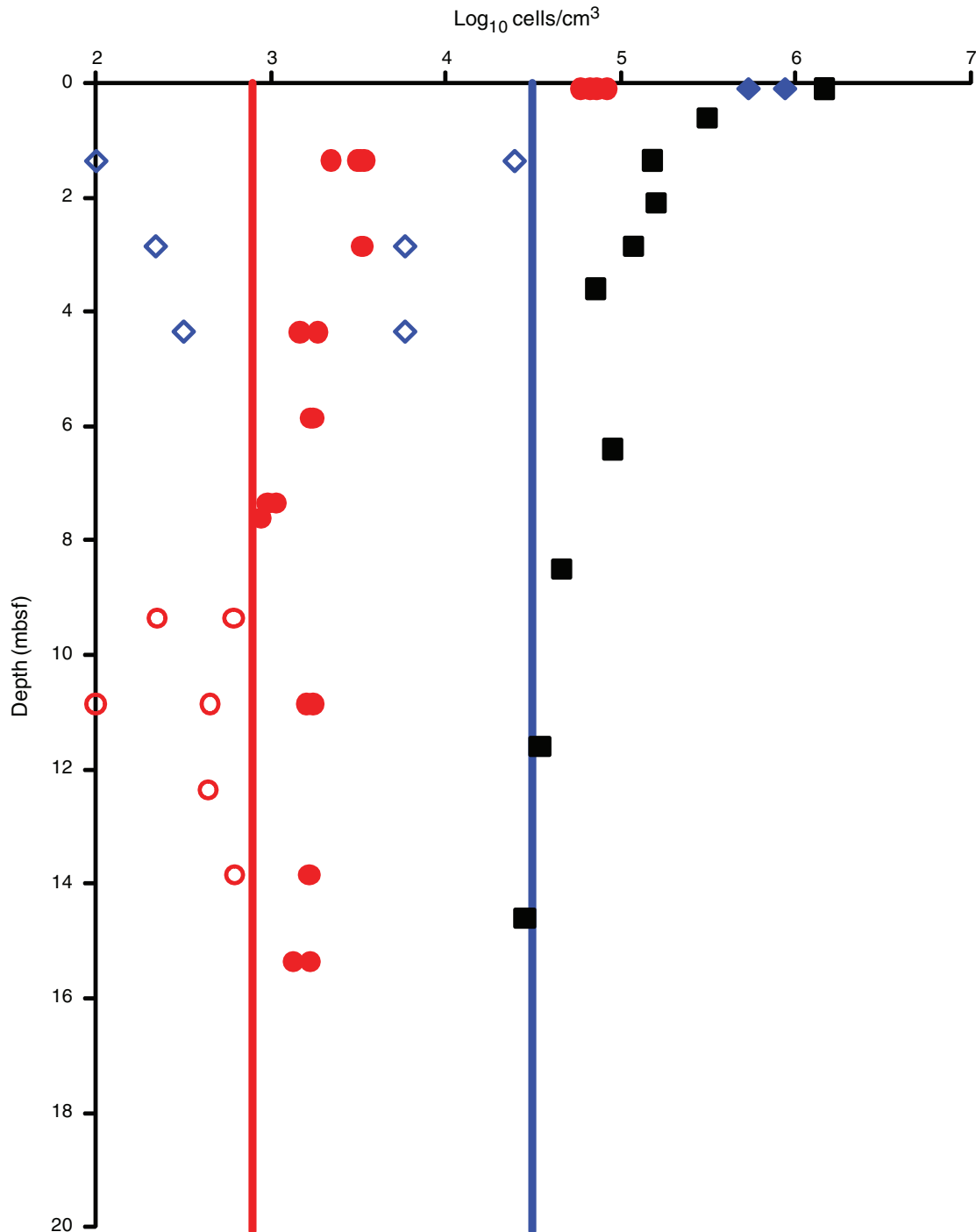


Figure F66. Plot of concentrations of microsphere fluorescent beads detected from basaltic samples, Hole U1368F.

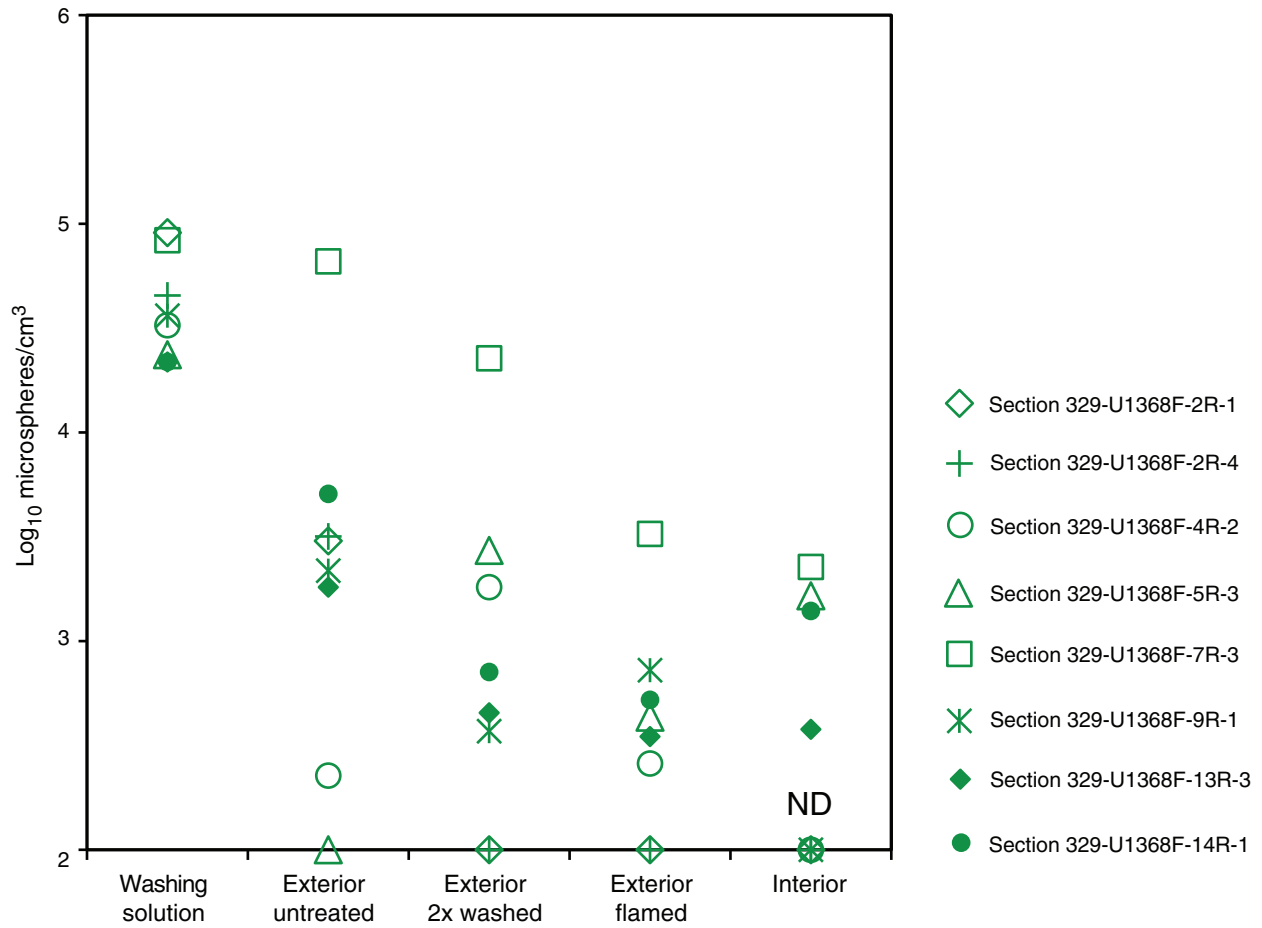


Table T1. Operations summary, Site U1368. (Continued on next page.)

Hole U1368A

Latitude: 27°55.0017'S
 Longitude: 123°9.6562'W
 Time on hole (h): 10.25
 Seafloor (drill pipe measurement below rig floor, m DRF): 3750.9
 Distance between rig floor and sea level (m): 11.2
 Water depth (drill pipe measurement from sea level, mbsl): 3740.0
 Total penetration (drilling depth below seafloor, m DSF): 13.6
 Total length of cored section (m): washdown to basement; basement contact established at 13.6 mbsf
 Total core recovered (m): NA
 Core recovery (%): NA
 Total number of cores: NA

Hole U1368B

Latitude: 27°55.0024'S
 Longitude: 123°9.6679'W (20 m west of Hole U1368A)
 Time on hole (h): 5
 Seafloor (drill pipe measurement below rig floor, m DRF): 3750.0
 Distance between rig floor and sea level (m): 11.2
 Water depth (drill pipe measurement from sea level, mbsl): 3739.1
 Total penetration (drilling depth below seafloor, m DSF): 16.0
 Total length of cored section (m): 16.0
 Total core recovered (m): 15.84
 Core recovery (%): 99
 Total number of cores: 3

Hole U1368C

Latitude: 27°54.9916'S
 Longitude: 123°9.6681'W (20 m north of Hole U1368B)
 Time on hole (h): 2.25
 Seafloor (drill pipe measurement below rig floor, m DRF): 3749.5
 Distance between rig floor and sea level (m): 11.2
 Water depth (drill pipe measurement from sea level, mbsl): 3738.5
 Total penetration (drilling depth below seafloor, m DSF): 16.3
 Total length of cored section (m): 16.3
 Total core recovered (m): 16.34
 Core recovery (%): 100.2
 Total number of cores: 2

Hole U1368D

Latitude: 27°54.9920'S
 Longitude: 123°9.6561'W (20 m east of Hole U1368C)
 Time on hole (h): 2.25
 Seafloor (drill pipe measurement below rig floor, m DRF): 3750.0
 Distance between rig floor and sea level (m): 11.2
 Water depth (drill pipe measurement from sea level, mbsl): 3739.1
 Total penetration (drilling depth below seafloor, m DSF): 15
 Total length of cored section (m): 15
 Total core recovered (m): 15.04
 Core recovery (%): 100.3
 Total number of cores: 2

Hole U1368E

Latitude: 27°54.9918'S
 Longitude: 123°9.6442'W (20 m west of Hole U1368D)
 Time on hole (h): 8.5
 Seafloor (drill pipe measurement below rig floor, m DRF): 3750.9
 Distance between rig floor and sea level (m): 11.2
 Water depth (drill pipe measurement from sea level, mbsl): 3740.9
 Total penetration (drilling depth below seafloor, m DSF): 10.6
 Total length of cored section (m): 10.6
 Total core recovered (m): 10.58
 Core recovery (%): 99.8
 Total number of cores: 2

Table T1 (continued).

Hole U1368F

Latitude: 27°55.0021'S

Longitude: 123°9.6433'W (20 m south of Hole U1368E)

Time on hole (h): 100.25

Seafloor (drill pipe measurement below rig floor, m DRF): 3752.2 (offset from Hole U1367E)

Distance between rig floor and sea level (m): 11.2

Water depth (drill pipe measurement from sea level, mbsl): 3741 (offset from Hole U1367E)

Total penetration (drilling depth below seafloor, m DSF): 115.1

Total length of cored section (m): 115.1

Total core recovered (m): 31.74

Core recovery (%): 27.6

Total number of cores: 14

Core	Date (2010)	Time (h)	Depth DSF (m)		Interval advanced (m)	Depth CSF (m)		Length of core recovered (m)	Recovery (%)	Sections (N)	Coring shoe type
			Top of cored interval	Bottom of cored interval		Top of cored interval	Bottom of cored interval				
329-U1368A-11	13 Nov	1216									
*****Drilled from 0.0 to 13.6 m DSF*****											
329-U1368B-1H	13 Nov	1355	0.0	5.5	5.5	0.0	5.48	5.48	100	5	STD
2H	13 Nov	1507	5.5	15.0	9.5	5.5	14.73	9.23	97	8	STD
3H	13 Nov	1635	15.0	16.0	1.0	15.0	16.13	1.13	113	2	STD
329-U1368C-1H	13 Nov	1750	0.0	8.0	8.0	0.0	8.05	8.05	101	7	STD
2H	13 Nov	1900	8.0	16.3	8.3	8.0	16.09	8.29	100	7	STD
329-U1368D-1H	13 Nov	2020	0.0	7.5	7.5	0.0	7.50	7.50	100	6	STD
2H	13 Nov	2125	7.5	15.0	7.5	7.5	15.04	7.54	101	6	STD
329-U1368E-1H	13 Nov	2230	0.0	5.6	5.6	0.0	5.61	5.61	100	5	STD
2H	14 Nov	2340	5.6	10.6	5.0	5.6	10.50	4.97	99	5	STD
329-U1368F-1R	14 Nov	1550	0.0	9.2	9.2	0.0	3.83	3.83	42	4	
2R	15 Nov	0014	9.2	20.8	11.6	9.2	14.43	4.01	35	4	
3R	15 Nov	0735	20.8	28.3	7.5	20.8	21.05	0.18	2	1	
4R	15 Nov	1425	28.3	37.8	9.5	28.3	30.25	1.35	14	2	
5R	15 Nov	2145	37.8	43.9	6.1	37.8	41.08	3.22	53	3	
6R	16 Nov	0240	43.9	47.4	3.5	43.9	45.35	0.97	28	1	
7R	16 Nov	0640	47.4	57.0	9.6	47.4	50.95	2.44	25	3	
8R	16 Nov	1120	57.0	62.6	5.6	57.0	58.84	1.32	24	2	
9R	16 Nov	1410	62.6	66.6	4.0	62.6	63.91	0.95	24	1	
10R	16 Nov	1800	66.6	76.2	9.6	66.6	69.34	2.07	22	2	
11R	16 Nov	2330	76.2	85.9	9.7	76.2	78.96	2.18	22	2	
12R	17 Nov	0630	85.9	95.5	9.6	85.9	90.47	3.92	41	4	
13R	17 Nov	1135	95.5	105.1	9.6	95.5	100.36	4.03	42	4	
14R	17 Nov	1705	105.1	115.1	10.0	105.1	106.60	1.27	13	1	
Advanced total:					186.6			89.54	52	85	
Total interval cored:					173.0						

NA = not applicable. DSF = drilling depth below seafloor, CSF = core depth below seafloor. H = APC core, R = RCB core, 1 = drilled interval. STD = standard. Time is UTC.

Table T2. ICP-AES analyses, Hole U1368F. (Continued on next page.)

Hole:	329-U1368F-								
Core:	2R	2R	2R	2R	2R	4R	4R	4R	5R
Section:	4	4	4	4	4	H 1	1	1	1
Interval:	42–44	47–49	76–78	76–78	76–78	21–31	51–53	51–53	101–105
Depth (mbsf):	13.68	13.73	14.02	14.02	14.02	22.21	28.81	28.81	38.81
Geological context:	Gray background	Brown	Dark gray	Dark gray	Gray	Gray	Dark gray	Gray background	Gray background
Major element oxide (wt%):									
SiO ₂	48.02	45.65	46.68	47.25	47.57	46.81	50.11	52.17	49.57
Al ₂ O ₃	14.88	17.16	13.92	13.97	14.44	12.51	13.32	14.09	13.07
Fe ₂ O ₃ ^(T)	10.16	11.50	10.31	10.37	10.51	17.60	15.38	10.80	15.15
MnO ₂	0.15	0.21	0.16	0.16	0.16	0.25	0.24	0.21	0.20
MgO	12.53	4.94	14.44	14.83	14.34	6.16	5.36	5.74	5.92
CaO	9.06	11.98	7.99	8.14	8.19	9.94	10.08	11.03	9.90
Na ₂ O	2.70	3.21	2.42	2.47	2.44	2.34	2.95	3.15	3.03
K ₂ O	0.58	0.64	0.52	0.52	0.48	0.92	0.69	0.41	0.15
TiO ₂	1.53	1.68	1.47	1.51	1.51	2.58	2.21	2.26	2.17
P ₂ O ₅	0.26	0.39	0.26	0.27	0.29	0.23	0.25	0.23	0.25
Total:	99.86	97.37	98.16	99.48	99.91	99.33	100.58	100.09	99.40
Trace element (ppm):									
Ba	64	93	86	82	65	36	20	40	—
Co	62	63	64	67	63	63	66	69	62
Cu	44	43	39	45	51	4	42	57	40
Ni	400	254	464	465	420	34	31	39	30
Sc	30	34	29	29	30	49	46	48	47
Sr	279	376	247	245	250	115	146	180	118
V	214	308	208	210	219	472	471	479	467
Zn	71	73	77	78	70	141	108	142	117
Zr	124	134	113	117	123	182	152	156	147
LOI (wt%)	3.51	2.9	4.05	4.05	4.52	1.59	0.67	0.48	0.14

LOI = loss on ignition, — = no data.

Hole:	329-U1368F-								
Core:	6R	6R	7R	7R	9R	9R	9R	11R	11R
Section:	1	1	1	1	1	1	1	1	1
Interval:	106–111	106–111	31–36	31–36	42–43	54–56	93–95	62–64	65–67
Depth (mbsf):	44.96	44.96	47.71	47.71	63.02	63.14	63.53	76.82	76.85
Geological context:	Dark gray	Gray background	Chilled margin	Center	Background	Dark gray	Pale gray	Dark gray	Pale gray
Major element oxide (wt%):									
SiO ₂	50.03	51.25	49.88	52.57	50.64	47.97	51.74	48.93	50.45
Al ₂ O ₃	13.64	14.67	13.71	14.65	14.12	13.35	14.86	13.34	14.69
Fe ₂ O ₃ ^(T)	15.21	8.89	13.58	9.27	11.51	14.53	9.35	13.72	10.35
MnO ₂	0.21	0.19	0.20	0.19	0.20	0.17	0.19	0.19	0.21
MgO	6.06	6.22	6.01	6.28	6.56	5.74	6.21	5.78	6.24
CaO	10.90	11.72	10.88	11.89	11.46	10.37	11.91	10.57	11.66
Na ₂ O	2.66	2.90	2.71	2.95	2.87	2.76	2.98	2.67	2.95
K ₂ O	0.66	0.30	0.54	0.38	0.22	0.74	0.27	0.76	0.30
TiO ₂	2.06	2.17	2.05	2.18	2.10	2.06	2.21	2.14	2.24
P ₂ O ₅	0.26	0.28	0.23	0.27	0.25	0.25	0.26	0.23	0.28
Total:	101.68	98.60	99.79	100.63	99.94	97.94	99.98	98.33	99.38
Trace element (ppm):									
Ba	—	43	14	50	38	23	53	25	—
Co	53	69	51	72	78	51	76	52	81
Cu	34	70	40	60	58	34	77	33	57
Ni	36	55	43	76	92	32	61	38	101
Sc	45	47	44	47	46	44	47	44	48
Sr	117	186	132	177	155	125	178	155	178
V	404	389	397	411	416	397	403	408	437
Zn	117	113	165	134	105	109	121	102	122
Zr	159	162	155	167	153	155	172	164	165
LOI (wt%)	2.21	1.08	2.19	1.25	0.67	1.13	—	1.19	1.72

Table T2 (continued).

Hole:	329-U1368F-							
Core:	12R	12R	12R	12R	13R	13R	14R	14R
Section:	3	3	4	4	2	2	1	1
Interval:	42–44	60–62	53–56	53–56	12–14	12–14	76–79	141–142
Depth (mbsf):	89.15	89.33	90.46	90.46	97.12	97.12	105.86	106.51
Geological context:	Brown	Dark gray	Brown	Gray	Brown	Gray background	Breccia	Basaltic clast
Major element oxide (wt%):								
SiO ₂	48.39	49.70	48.54	49.93	48.57	50.10	50.61	49.37
Al ₂ O ₃	13.37	13.96	13.49	14.02	13.36	13.77	13.88	13.75
Fe ₂ O ₃ ^(T)	14.98	12.75	13.83	12.80	13.52	12.52	17.21	13.55
MnO ₂	0.23	0.17	0.17	0.17	0.17	0.18	0.26	0.20
MgO	5.58	6.96	6.34	6.57	6.56	6.89	3.83	6.51
CaO	10.77	10.93	10.51	11.04	10.39	10.66	2.74	10.86
Na ₂ O	2.78	2.92	2.80	2.88	2.77	2.77	3.37	2.67
K ₂ O	0.48	0.16	0.34	0.14	0.33	0.17	3.65	0.39
TiO ₂	2.11	2.19	2.08	2.20	2.06	2.07	2.42	1.96
P ₂ O ₅	0.24	0.26	0.25	0.26	0.24	0.25	0.12	0.22
Total:	98.92	99.99	98.35	100.00	97.98	99.36	98.08	99.49
Trace element (ppm):								
Ba	—	—	18	16	20	22	69	14
Co	61	65	59	61	60	64	70	59
Cu	28	44	33	51	38	42	143	42
Ni	47	91	58	87	139	111	136	55
Sc	42	46	42	45	42	43	48	45
Sr	124	123	128	123	130	121	73	128
V	411	428	402	423	400	395	150	400
Zn	93	103	91	117	101	110	133	104
Zr	156	162	152	164	149	151	176	131
LOI (wt%)	0.92	—	0.93	—	1.19	0.61	10.9	0.6

Table T3. Distribution and overall and relative abundance of benthic foraminifers, Site U1368.

Hole, core, section, interval (cm)	Depth (mbsf)	Preservation	Overall abundance	<i>Anomalinooides globosus</i>	<i>Buliminella parvula</i>	<i>Globocassidulina subglobosa</i>	<i>Cibicides mundulus</i>	<i>Cibicides wuellerstorfi</i>	<i>Epistominella</i> sp.	<i>Gyroidina</i> sp.	<i>Gyroidinoides lamarkiana</i>	<i>Gyroidinoides soldanii</i>	<i>Karreriella chapapotensis</i>	<i>Lagena</i> spp	<i>Nodosaria</i> sp. A	<i>Nodosaria</i> sp. B	<i>Nuttallides umbonifer</i>	<i>Oridorsalis umbonatus</i>	<i>Polymorphina</i> spp.	<i>Siphonodosaria spinata</i>	Number of taxa
329-U1368B-1H-3, 0–2	3	M	Low						P												1
U1368D-1H-CC	7.47	G	Low	F	F	F	F		F	F	F	F	F	A	F			A	A	F	13
U1368B-2H-4, 25–27	10.25	M	Low			F	F	F			F			A	F		F		A	A	8
U1368C-2H-CC	16.08																				

Preservation: M = moderate, G = good. Abundance: A = abundant, F = few, P = present. For more specific preservation and abundance definitions, refer to "[Paleontology and biostratigraphy](#)" in the "Methods" chapter (Expedition 329 Scientists, 2011a).

Table T4. Distribution and overall and relative abundance of ostracods, Site U1368.

Hole, core, section, interval (cm)	Depth (mbsf)	Preservation	Overall abundance	<i>Bradleya</i>	<i>Eucythere</i>	<i>Heimia</i>	<i>Henryhowella</i>	<i>Kirithe</i>	<i>Pelecocythere</i>	<i>Poseidonamicus</i>	Number of genera	Comments	
329- U1368B-1H-3, 0-2	3.00		Barren									No ostracods found	
U1368D-1H-CC	7.47	G	Low		F	F	A	D		A	5		
U1368B-2H-4, 25-27	10.25	M-G	Low	F					D	R	A		4
U1368C-2H-CC	16.08												

Preservation: G = good, M = moderate. Abundance: D = dominant, A = abundant, F = few, R = rare. For more specific preservation and abundance definitions, refer to "[Paleontology and biostratigraphy](#)" in the "Methods" chapter (Expedition 329 Scientists, 2011a).

Table T6. Electrical conductivity measurements of surface seawater, Site U1368.

Measurement number	Electrical conductivity (mS/cm)	Temperature (°C)	Correction factor at 20°C (mS/cm)	Seawater electrical conductivity at 20°C (mS/cm)
1	53.00	23.2	51.20	49.60
9	52.70	23.0	51.00	49.60
17	52.70	23.0	51.00	49.50
25	52.80	23.1	51.10	49.50
33	52.90	23.2	51.20	49.50
41	52.90	23.2	51.20	49.50
49	53.00	23.1	51.10	49.70
58	53.00	23.1	51.10	49.70
59	51.80	22.0	49.90	49.70
60	52.70	22.8	50.80	49.70
61	52.50	22.4	50.40	49.90
62	52.70	22.8	50.80	49.80
70	52.70	22.9	50.90	49.60
78	52.70	22.9	50.90	49.60
86	52.70	22.8	50.80	49.70
94	52.70	22.8	50.80	49.70
102	52.80	22.9	50.90	49.70
111	52.80	23.0	51.00	49.60
119	52.90	23.0	51.00	49.70
127	52.80	22.9	50.90	49.70
135	52.80	22.9	50.90	49.70
138	52.70	22.8	50.80	49.70
139	52.80	22.8	50.80	49.80
140	52.10	22.3	50.30	49.60
148	51.80	22.4	50.40	49.30
155	52.10	22.6	50.60	49.40
156	52.10	22.6	50.60	49.40
160	51.80	22.3	50.30	49.30
161	52.10	22.4	50.40	49.60
162	52.10	22.5	50.50	49.40

Table T7. Formation factor measurements, Site U1368. (Continued on next page.)

Core, section, interval (cm)	Depth (mbsf)	Measurement number	Temperature-corrected seawater conductivity (mS/cm)	Sediment temperature (°C)	Sediment electrical conductivity (mS/cm)	Correction factor at 20°C (mS/cm)	Sediment electrical conductivity at 20°C (mS/cm)	Drift-corrected sediment electrical conductivity at 20°C (mS/cm)	Formation factor
329-U1368B-									
1H-1, 10	0.10	2	49.66	21.80	23.13	49.74	22.27	22.27	2.23
1H-1, 20	0.20	3	49.66	21.70	21.65	49.63	20.89	20.89	2.38
1H-1, 30	0.30	4	49.66	21.70	23.32	49.63	22.50	22.50	2.21
1H-1, 40	0.40	5	49.66	21.70	22.23	49.63	21.45	21.45	2.32
1H-1, 50	0.50	6	49.66	21.60	23.11	49.53	22.35	22.35	2.22
1H-1, 60	0.60	7	49.66	21.60	24.33	49.53	23.53	23.53	2.11
1H-1, 70	0.70	8	49.66	21.60	25.05	49.53	24.22	24.22	2.05
1H-1, 80	0.80	10	49.66	21.50	25.45	49.43	24.66	24.66	2.01
1H-1, 90	0.90	11	49.66	21.50	26.12	49.43	25.31	25.31	1.96
1H-1, 100	1.00	12	49.66	21.50	25.04	49.43	24.26	24.27	2.05
1H-1, 110	1.10	13	49.66	21.50	23.40	49.43	22.67	22.68	2.19
1H-1, 120	1.20	14	49.66	21.50	23.99	49.43	23.25	23.25	2.14
1H-1, 130	1.30	15	49.66	21.50	25.05	49.43	24.27	24.28	2.05
1H-1, 140	1.40	16	49.65	21.50	23.79	49.43	23.05	23.06	2.15
1H-2, 10	1.61	18	49.65	21.60	23.88	49.53	23.09	23.10	2.15
1H-2, 20	1.71	19	49.65	21.60	23.00	49.53	22.24	22.25	2.23
1H-2, 30	1.81	20	49.65	21.60	23.04	49.53	22.28	22.28	2.23
1H-2, 40	1.91	21	49.65	21.60	22.66	49.53	21.91	21.92	2.27
1H-2, 50	2.01	22	49.65	21.60	23.52	49.53	22.74	22.75	2.18
1H-2, 60	2.11	23	49.65	21.60	23.67	49.53	22.89	22.90	2.17
1H-2, 70	2.21	24	49.65	21.60	22.87	49.53	22.11	22.12	2.24
1H-2, 80	2.31	26	49.65	21.80	24.95	49.74	24.03	24.03	2.07
1H-2, 90	2.41	27	49.65	21.80	22.90	49.74	22.05	22.06	2.25
1H-2, 100	2.51	28	49.65	21.80	24.94	49.74	24.02	24.03	2.07
1H-2, 110	2.61	29	49.65	21.70	23.13	49.63	22.32	22.33	2.22
1H-2, 120	2.71	30	49.64	21.80	22.07	49.74	21.25	21.26	2.33
1H-2, 130	2.81	31	49.64	21.80	22.87	49.74	22.02	22.03	2.25
1H-2, 140	2.91	32	49.64	21.60	22.59	49.53	21.84	21.85	2.27
1H-3, 10	3.11	34	49.64	22.20	21.50	50.15	20.53	20.54	2.42
1H-3, 20	3.21	35	49.64	21.80	20.84	49.74	20.07	20.08	2.47
1H-3, 30	3.31	36	49.64	21.70	21.62	49.63	20.86	20.87	2.38
1H-3, 40	3.41	37	49.64	21.70	20.16	49.63	19.45	19.46	2.55
1H-3, 50	3.51	38	49.64	21.70	22.04	49.63	21.27	21.28	2.33
1H-3, 60	3.61	39	49.64	21.70	23.68	49.63	22.85	22.86	2.17
1H-3, 70	3.71	40	49.64	21.70	22.73	49.63	21.93	21.95	2.26
1H-3, 80	3.81	42	49.64	21.70	24.70	49.63	23.83	23.85	2.08
1H-3, 90	3.91	43	49.64	21.60	22.24	49.53	21.51	21.52	2.31
1H-3, 100	4.01	44	49.64	21.50	22.94	49.43	22.23	22.24	2.23
1H-3, 110	4.11	45	49.63	21.50	23.50	49.43	22.77	22.79	2.18
1H-3, 120	4.21	46	49.63	21.50	23.78	49.43	23.04	23.06	2.15
1H-3, 130	4.31	47	49.63	21.50	22.93	49.43	22.22	22.23	2.23
1H-3, 140	4.41	48	49.63	21.50	22.40	49.43	21.70	21.72	2.29
1H-4, 10	4.60	50	49.63	21.70	24.87	49.63	24.00	24.02	2.07
1H-4, 20	4.70	51	49.63	21.60	23.41	49.53	22.64	22.65	2.19
1H-4, 30	4.80	52	49.63	21.60	23.92	49.53	23.13	23.15	2.14
1H-4, 40	4.90	53	49.63	21.60	24.50	49.53	23.69	23.71	2.09
1H-4, 50	5.00	54	49.63	21.60	24.52	49.53	23.71	23.73	2.09
1H-4, 60	5.10	55	49.63	21.60	24.46	49.53	23.65	23.67	2.10
1H-4, 70	5.20	56	49.63	21.70	23.40	49.63	22.58	22.60	2.20
1H-4, 80	5.30	57	49.63	21.70	21.78	49.63	21.02	21.03	2.36
2H-1, 10	5.60	63	49.62	21.30	24.57	49.22	23.91	23.93	2.07
2H-1, 20	5.70	64	49.62	21.40	24.09	49.32	23.39	23.41	2.12
2H-1, 30	5.80	65	49.62	21.40	23.55	49.32	22.87	22.89	2.17
2H-1, 40	5.90	66	49.62	21.40	23.86	49.32	23.17	23.19	2.14
2H-1, 50	6.00	67	49.62	21.40	23.81	49.32	23.12	23.14	2.14
2H-1, 60	6.10	68	49.62	21.40	24.33	49.32	23.62	23.65	2.10
2H-1, 70	6.20	69	49.62	21.40	23.13	49.32	22.46	22.48	2.21
2H-1, 80	6.30	71	49.62	21.30	24.49	49.22	23.83	23.85	2.08
2H-1, 93	6.43	72	49.62	21.30	24.57	49.22	23.91	23.93	2.07
2H-1, 101	6.51	73	49.61	21.40	23.99	49.32	23.29	23.32	2.13
2H-1, 110	6.60	74	49.61	21.40	23.59	49.32	22.91	22.93	2.16
2H-1, 120	6.70	75	49.61	21.40	23.82	49.32	23.13	23.15	2.14
2H-1, 130	6.80	76	49.61	21.40	22.94	49.32	22.27	22.30	2.22
2H-1, 140	6.90	77	49.61	21.40	23.78	49.32	23.09	23.12	2.15
2H-2, 10	7.11	79	49.61	21.30	23.37	49.22	22.74	22.76	2.18
2H-2, 20	7.21	80	49.61	21.30	23.56	49.22	22.92	22.95	2.16

Table T7 (continued).

Core, section, interval (cm)	Depth (mbsf)	Measurement number	Temperature-corrected seawater conductivity (mS/cm)	Sediment temperature (°C)	Sediment electrical conductivity (mS/cm)	Correction factor at 20°C (mS/cm)	Sediment electrical conductivity at 20°C (mS/cm)	Drift-corrected sediment electrical conductivity at 20°C (mS/cm)	Formation factor
2H-2, 30	7.31	81	49.61	21.30	23.15	49.22	22.53	22.55	2.20
2H-2, 40	7.41	82	49.61	21.30	23.31	49.22	22.68	22.71	2.18
2H-2, 50	7.51	83	49.61	21.30	24.04	49.22	23.39	23.42	2.12
2H-2, 60	7.61	84	49.61	21.30	23.79	49.22	23.15	23.18	2.14
2H-2, 70	7.71	85	49.61	21.30	23.01	49.22	22.39	22.42	2.21
2H-2, 80	7.81	87	49.60	21.40	23.99	49.32	23.29	23.32	2.13
2H-2, 90	7.91	88	49.60	21.40	23.36	49.32	22.68	22.71	2.18
2H-2, 100	8.01	89	49.60	21.40	23.16	49.32	22.49	22.52	2.20
2H-2, 110	8.11	90	49.60	21.40	22.69	49.32	22.03	22.06	2.25
2H-2, 120	8.21	91	49.60	21.40	22.49	49.32	21.84	21.87	2.27
2H-2, 130	8.31	92	49.60	21.40	23.29	49.32	22.61	22.64	2.19
2H-2, 140	8.41	93	49.60	21.40	23.87	49.32	23.18	23.21	2.14
2H-3, 10	8.61	95	49.60	21.30	22.41	49.22	21.81	21.83	2.27
2H-3, 20	8.71	96	49.60	21.30	23.11	49.22	22.49	22.52	2.20
2H-3, 30	8.81	97	49.60	21.30	22.25	49.22	21.65	21.68	2.29
2H-3, 40	8.91	98	49.60	21.30	22.49	49.22	21.88	21.91	2.26
2H-3, 50	9.01	99	49.60	21.30	22.45	49.22	21.84	21.87	2.27
2H-3, 60	9.11	100	49.60	21.30	23.03	49.22	22.41	22.44	2.21
2H-3, 70	9.21	101	49.59	21.30	22.92	49.22	22.30	22.33	2.22
2H-3, 80	9.31	103	49.59	21.40	23.03	49.32	22.36	22.39	2.21
2H-3, 93	9.44	104	49.59	21.40	23.86	49.32	23.17	23.20	2.14
2H-3, 101	9.52	105	49.59	21.40	24.38	49.32	23.67	23.71	2.09
2H-3, 110	9.61	106	49.59	21.40	24.28	49.32	23.58	23.61	2.10
2H-3, 120	9.71	107	49.59	21.40	24.83	49.32	24.11	24.15	2.05
2H-3, 130	9.81	108	49.59	21.40	24.93	49.32	24.21	24.24	2.05
2H-3, 140	9.91	109	49.59	21.40	25.45	49.32	24.71	24.75	2.00
2H-3, 148	9.99	110	49.59	21.40	24.98	49.32	24.26	24.29	2.04
2H-4, 10	10.11	112	49.59	21.30	24.45	49.22	23.79	23.83	2.08
2H-4, 20	10.21	113	49.59	21.30	23.79	49.22	23.15	23.19	2.14
2H-4, 30	10.31	114	49.59	21.30	24.12	49.22	23.47	23.51	2.11
2H-4, 40	10.41	115	49.58	21.30	23.49	49.22	22.86	22.89	2.17
2H-4, 50	10.51	116	49.58	21.30	23.57	49.22	22.93	22.97	2.16
2H-4, 60	10.61	117	49.58	21.30	23.62	49.22	22.98	23.02	2.15
2H-4, 70	10.71	118	49.58	21.30	24.23	49.22	23.58	23.62	2.10
2H-4, 80	10.81	120	49.58	21.30	24.18	49.22	23.53	23.57	2.10
2H-4, 90	10.91	121	49.58	21.30	24.81	49.22	24.14	24.18	2.05
2H-4, 100	11.01	122	49.58	21.30	24.75	49.22	24.08	24.12	2.06
2H-4, 110	11.11	123	49.58	21.30	24.13	49.22	23.48	23.52	2.11
2H-4, 120	11.21	124	49.58	21.30	24.98	49.22	24.31	24.35	2.04
2H-4, 130	11.31	125	49.58	21.30	24.87	49.22	24.20	24.24	2.05
2H-4, 140	11.41	126	49.58	21.30	25.03	49.22	24.35	24.40	2.03
2H-5, 10	11.61	128	49.58	21.40	22.42	49.32	21.77	21.81	2.27
2H-5, 20	11.71	129	49.57	21.40	25.15	49.32	24.42	24.47	2.03
2H-5, 30	11.81	130	49.57	21.40	24.88	49.32	24.16	24.20	2.05
2H-5, 40	11.91	131	49.57	21.40	24.81	49.32	24.09	24.14	2.05
2H-5, 50	12.01	132	49.57	21.40	24.56	49.32	23.85	23.89	2.07
2H-5, 60	12.11	133	49.57	21.40	25.81	49.32	25.06	25.11	1.97
2H-5, 70	12.21	134	49.57	21.40	25.51	49.32	24.77	24.82	2.00
2H-5, 80	12.31	136	49.57	21.10	26.21	49.02	25.61	25.66	1.93
2H-5, 93	12.44	137	49.57	21.10	26.27	49.02	25.67	25.72	1.93
2H-6, 10	12.62	141	49.57	21.20	23.26	49.12	22.68	22.72	2.18
2H-6, 20	12.72	142	49.57	21.30	17.14	49.22	16.68	16.71	2.97
2H-6, 30	12.82	143	49.56	21.30	20.39	49.22	19.84	19.88	2.49
2H-6, 38	12.90	144	49.56	21.30	16.08	49.22	15.65	15.68	3.16
2H-6, 50	13.02	145	49.56	21.30	16.61	49.22	16.16	16.20	3.06
2H-6, 60	13.12	146	49.56	21.30	18.01	49.22	17.52	17.56	2.82
2H-6, 70	13.22	147	49.56	21.30	17.93	49.22	17.45	17.48	2.83
2H-6, 80	13.32	149	49.56	21.00	20.16	48.91	19.74	19.78	2.51
2H-6, 93	13.45	150	49.56	21.00	21.37	48.91	20.92	20.97	2.36
2H-6, 110	13.62	151	49.56	21.00	7.23	48.91	7.08	7.09	6.99
2H-6, 120	13.72	152	49.56	21.10	24.39	49.02	23.83	23.88	2.08
2H-6, 130	13.82	153	49.56	21.10	21.26	49.02	20.77	20.82	2.38
2H-6, 140	13.92	154	49.56	21.10	23.65	49.02	23.11	23.16	2.14
2H-7, 10	14.10	157	49.55	21.30	24.10	49.22	23.45	23.50	2.11
2H-7, 30	14.30	158	49.55	21.30	10.10	49.22	9.83	9.85	5.03
2H-7, 38	14.38	159	49.55	21.30	8.02	49.22	7.80	7.82	6.34

Table T8. Dissolved oxygen concentrations determined using electrodes, Holes U1368B, U1368C, U1368E, and U1368F.

Core, section, interval (cm)	Depth (mbsf)	O ₂ (μM)	Core, section, interval (cm)	Depth (mbsf)	O ₂ (μM)	Core, section, interval (cm)	Depth (mbsf)	O ₂ (μM)
329-U1368B-			2H-6, 80	13.30	132.4	1H-3, 80	3.80	160.1
1H-1, 15	0.15	155.8	2H-6, 100	13.50	129.2	1H-3, 100	4.00	141.3
1H-1, 30	0.30	150.2	2H-6, 120	13.70	133.0	1H-3, 120	4.20	153.6
1H-1, 45	0.45	150.2	2H-7, 10	14.10	121.6	1H-4, 20	4.70	146.4
1H-1, 60	0.60	150.7	2H-7, 20	14.20	123.8	1H-4, 40	4.90	141.3
1H-1, 75	0.75	150.3	329-U1368C-			1H-4, 60	5.10	141.7
1H-1, 90	0.90	149.8	1H-1, 30	0.40	158.8	1H-4, 80	5.30	139.1
1H-1, 105	1.05	152.9	1H-1, 125	1.25	153.1	2H-1, 20	5.80	140.0
1H-1, 120	1.20	148.0	1H-2, 35	1.85	153.1	2H-1, 40	6.00	146.1
1H-2, 20	1.70	149.8	1H-2, 125	2.65	148.0	2H-1, 60	6.20	149.1
1H-2, 40	1.90	148.2	1H-3, 35	3.35	154.3	2H-1, 80	6.40	149.2
1H-2, 60	2.10	149.0	1H-3, 125	4.25	142.7	2H-1, 120	6.80	145.4
1H-2, 100	2.50	154.5	1H-4, 15	4.65	146.9	2H-2, 20	7.30	140.4
1H-2, 120	2.70	151.8	1H-4, 90	5.40	152.3	2H-2, 40	7.50	134.2
1H-3, 50	3.50	147.9	1H-5, 20	6.20	144.4	2H-2, 60	7.70	133.4
1H-3, 75	3.75	152.4	1H-5, 125	7.25	145.1	2H-2, 80	7.90	131.6
1H-3, 100	4.00	138.5	1H-1, 20	8.20	143.8	2H-2, 120	8.30	138.4
1H-3, 125	4.25	138.6	2H-1, 65	8.65	144.5	2H-2, 140	8.50	129.9
1H-4, 20	4.70	150.8	2H-1, 123	9.23	148.2	2H-3, 15	8.75	131.9
1H-4, 40	4.90	146.5	2H-2, 25	9.75	152.6	2H-3, 30	8.90	137.5
2H-4, 60	5.10	138.2	2H-2, 125	10.75	145.7	2H-3, 45	9.05	132.3
2H-1, 25	5.75	142.7	2H-3, 25	11.25	143.5	2H-3, 60	9.20	140.2
2H-1, 50	6.00	136.5	2H-3, 75	11.75	140.7	2H-3, 75	9.35	133.1
2H-1, 75	6.25	141.7	2H-3, 125	12.25	137.7	2H-3, 115	9.75	124.1
2H-1, 100	6.50	141.8	2H-4, 25	12.75	139.1	329-U1368F-		
2H-1, 125	6.75	139.8	2H-4, 125	13.75	137.3	1R-1, 15	0.15	157.8
2H-2, 25	7.25	141.0	2H-5, 20	14.20	137.6	1R-1, 30	0.30	155.7
2H-2, 50	7.50	145.6	2H-5, 125	15.25	131.9	1R-1, 45	0.45	153.6
2H-2, 75	7.75	142.3	2H-6, 35	15.68	125.7	1R-1, 60	0.60	151.3
2H-2, 100	8.00	141.2	329-U1368E-			1R-1, 75	0.75	151.2
2H-3, 25	8.75	140.0	1H-1, 30	0.30	156.1	1R-1, 90	0.90	150.9
2H-3, 50	9.00	139.8	1H-1, 60	0.60	159.2	1R-1, 105	1.05	152.1
2H-3, 75	9.25	140.4	1H-1, 70	0.70	155.9	1R-1, 120	1.20	152.4
2H-3, 100	9.50	140.4	1H-1, 80	0.80	158.6	1R-2, 15	1.65	145.9
2H-3, 125	9.75	138.5	1H-1, 90	0.90	153.9	1R-2, 30	1.80	146.7
2H-4, 25	10.25	139.9	1H-1, 100	1.00	153.2	1R-2, 45	1.95	152.1
2H-4, 50	10.50	139.7	1H-2, 10	1.60	143.1	1R-2, 60	2.10	146.4
2H-4, 75	10.75	139.7	1H-2, 20	1.70	160.8	1R-2, 75	2.25	142.3
2H-4, 100	11.00	136.0	1H-2, 30	1.80	144.1	1R-2, 90	2.40	141.9
2H-4, 125	11.25	135.0	1H-2, 40	1.90	158.2	1R-2, 105	2.55	139.7
2H-5, 20	11.70	138.9	1H-2, 50	2.00	151.8	1R-2, 120	2.70	142.6
2H-5, 40	11.90	130.8	1H-2, 60	2.10	158.8	1R-3, 15	3.15	140.8
2H-5, 60	12.10	133.4	1H-2, 70	2.20	150.7	1R-3, 30	3.30	139.5
2H-5, 80	12.30	134.6	1H-3, 80	2.30	160.5	1R-3, 45	3.45	137.5
2H-6, 20	12.70	138.0	1H-3, 40	3.40	159.8	1R-3, 60	3.60	140.7
2H-6, 40	12.90	140.9	1H-3, 60	3.60	148.7			
2H-6, 60	13.10	142.7						

Table T9. Dissolved oxygen concentrations determined using optodes, Hole U1368B.

Core, section, interval (cm)	Depth (mbsf)	O ₂ (μM)
329-U1368B-		
1H-1, 10	0.10	151.2
1H-1, 20	0.20	147.8
1H-1, 35	0.35	145.4
1H-1, 50	0.50	142.8
1H-1, 65	0.65	144.9
1H-1, 80	0.80	144.7
1H-1, 95	0.95	145.0
1H-1, 110	1.10	144.4
1H-1, 125	1.25	143.9
1H-1, 140	1.40	144.2
1H-2, 15	1.65	144.1
1H-2, 105	2.55	143.0
1H-2, 140	2.90	142.1
1H-3, 30	3.30	141.5
1H-3, 80	3.80	139.6
1H-3, 140	4.40	140.1
1H-4, 30	4.80	138.1
1H-4, 75	5.25	138.7

Table T10. Dissolved hydrogen measured headspace gas method, Site U1368.

Core, section	Depth (mbsf)	H ₂ (nM)	Catwalk sampling
329-U1368C-			
1H-1	0.20	BD	Yes
1H-1	0.70	BD	No
1H-1	1.20	BD	No
1H-1	1.40	BD	Yes
1H-2	2.20	BD	No
1H-2	2.70	BD	No
1H-2	2.90	BD	Yes
1H-3	3.70	BD	No
1H-3	4.20	BD	No
1H-3	4.40	BD	Yes
1H-4	5.20	BD	No
1H-4	5.70	BD	No
1H-4	5.90	BD	No
1H-5	6.50	BD	No
1H-5	7.20	BD	No
1H-5	7.40	BD	Yes
1H-6	7.70	BD	No
1H-6	7.70	BD	No
2H-1	8.60	BD	No
2H-1	9.40	BD	Yes
2H-2	10.20	5.4	No
2H-2	10.70	5.5	No
2H-2	10.90	BD	Yes
2H-3	11.70	BD	No
2H-3	12.20	16.5	No
2H-3	12.40	BD	Yes
2H-4	13.20	BD	No
2H-4	13.70	8.3	No
2H-4	13.90	7.0	Yes
2H-5	14.70	BD	No
2H-5	15.20	BD	No
2H-5	15.40	BD	Yes
2H-6	15.60	36.2	No

BD = below detection.

Table T11. Interstitial fluid chemistry, Site U1368.

Core, section, interval (cm)	Depth (mbsf)	pH ISE	Alkalinity (mM) TITRAUTO	DIC (mM) OI-IC	Cl (mM) M-IC	SO ₄ (mM) M-IC	S/Cl (%) Calc. anom.	P (μM) Spec.	Si (μM) Spec.	Ca (mM) ICPAES	Mg (mM) ICPAES	Na (mM) ICPAES	K (mM) ICPAES
329-U1368C-													
1H-1	0.05	7.67	2.75	2.62	554.41	27.52	-3.91	2.29	237.42	10.03	51.05	473.93	11.26
1H-1, 50-60	0.55	7.76	2.57	2.60	553.78	27.50	-3.87	1.78	225.21	10.56	50.76	476.09	11.01
1H-1, 100-110	1.05	7.77	2.55	2.58	554.15	27.52	-3.88	1.77	241.14	10.39	50.70	470.52	10.79
1H-1, 140-150	1.45	7.61	2.77	2.62	553.82	27.50	-3.90	1.80	236.64	10.36	51.01	468.39	10.70
1H-2, 50-60	2.05	7.75	2.56	2.55	554.62	27.56	-3.81	1.42	251.07	10.34	51.04	469.47	10.53
1H-2, 100-110	2.55	7.77	2.54	2.57	553.27	27.34	-4.35	1.32	243.94	10.47	50.57	472.23	10.86
1H-2, 140-150	2.95	7.69	2.72	2.65	553.93	27.38	-4.33	1.46	248.06	10.59	50.54	472.63	10.86
1H-3, 50-60	3.55	7.95	2.49	2.49	555.29	28.11	-2.02	1.17	217.01	10.36	52.73	472.57	10.63
1H-3, 100-110	4.05	7.75	2.53	2.55	553.49	27.65	-3.29	1.05	230.32	10.26	51.62	470.19	10.55
1H-3, 140-150	4.45	7.67	2.76	2.72	554.49	27.54	-3.88	1.66	289.47	10.55	51.43	473.04	10.70
1H-4, 50-60	5.05	7.76	2.58	2.58	554.95	27.44	-4.28	1.73	289.53	10.52	50.72	474.60	10.76
1H-4, 100-110	5.55	7.76	2.56	2.60	554.49	27.43	-4.24	0.93	257.11	10.80	50.64	472.57	10.89
1H-4, 140-150	5.95	7.74	2.67	2.70	554.80	27.49	-4.09	0.89	256.24	10.34	51.06	471.34	10.70
1H-5, 50-60	6.55	7.78	2.52	2.55	553.85	27.43	-4.15	0.98	251.36	10.47	51.09	474.88	11.08
1H-5, 100-110	7.05	7.75	2.63	2.61	554.35	27.34	-4.53	0.98	253.99	10.71	50.22	473.07	11.04
1H-5, 140-150	7.45	7.77	2.72	2.72	554.01	27.32	-4.55	1.35	319.78	10.60	49.88	471.12	10.75
1H-6, 21-31	7.76	7.74	2.69	2.61	554.34	27.48	-4.03	0.97	257.41	10.68	50.84	472.30	10.95
2H-1, 40-50	8.45	7.76	2.45	2.46	553.85	27.63	-3.45	0.79	232.76	10.35	52.55	474.82	10.70
2H-1, 100-110	9.05	7.74	2.46	2.49	553.98	27.65	-3.39	0.84	221.78	10.15	52.00	469.39	10.49
2H-1, 140-150	9.45	7.73	2.71	2.69	553.75	27.60	-3.52	0.92	259.82	10.31	51.72	471.30	10.60
2H-2, 50-60	10.05	7.76	2.50	2.45	555.76	27.91	-2.80	1.23	247.99	10.07	52.64	469.71	10.64
2H-2, 100-110	10.55	7.77	2.50	2.48	555.85	27.72	-3.45	0.83	240.09	10.11	52.33	473.22	10.61
2H-2, 140-150	10.95	7.71	2.70	2.66	553.07	27.59	-3.44	0.98	254.13	10.24	52.36	469.61	10.57
2H-3, 50-60	11.55	7.72	2.46	2.50	—	—	—	1.02	267.36	9.96	51.84	470.25	10.67
2H-3, 100-110	12.05	7.80	2.43	2.48	554.20	27.47	-4.05	0.79	228.40	9.78	51.80	470.80	10.59
2H-3, 140-150	12.45	7.76	2.59	2.56	554.01	27.67	-3.32	0.97	259.54	10.06	52.28	468.91	10.38
2H-4, 50-60	13.05	7.77	2.41	2.44	555.11	27.59	-3.80	1.04	226.29	9.76	51.91	468.13	10.51
2H-4, 100-110	13.55	7.78	2.39	2.38	552.87	27.65	-3.18	0.90	240.19	9.78	52.23	468.80	10.41
2H-4, 140-150	13.95	7.74	2.60	2.58	553.55	27.64	-3.34	1.02	255.82	10.07	52.71	472.03	10.58
2H-5, 50-60	14.55	7.80	2.37	2.35	555.03	28.12	-1.93	1.05	222.17	10.06	52.86	470.90	10.76
2H-5, 100-110	15.05	7.81	2.38	2.39	554.11	28.07	-1.95	1.24	242.14	9.70	51.21	469.50	10.52
2H-5, 140-150	15.45	7.82	2.49	2.43	554.93	28.29	-1.32	1.27	232.59	10.13	52.32	468.26	10.42
2H-6, 0-10	15.48	7.92	2.47	2.38	554.88	28.46	-0.70	1.61	201.24	10.29	52.71	471.66	10.52

ISE = ion-selective electrode, TITRAUTO = automated titration, IC = ion chromatography, OI-IC = OI analytical IC, M-IC = Metrohm IC, Calc. anom. = calculated anomaly, Spec. = spectrophotometry, Dx-IC = Dionex IC, ICPAES = inductively coupled plasma-atomic emission spectroscopy. — = no data.

Table T12. Interstitial fluid nitrate concentration in Rhizon samples, Site U1368.

Core, section, interval (cm)	Depth (mbsf)	NO ₃ (μM)
329-U1368B-		
1H-1, 1-50	0.15	35.84
1H-1, 50-60	0.55	36.39
1H-1, 100-110	1.05	36.31
1H-2, 1-50	1.55	36.05
1H-2, 50-60	2.05	36.38
1H-2, 100-110	2.55	36.04
1H-3, 1-50	3.05	35.95
1H-3, 50-60	3.55	35.66
1H-3, 100-110	4.05	36.24
1H-4, 1-50	4.55	36.37
1H-4, 50-60	5.05	36.21
1H-4, 100-110	5.55	35.52
1H-5, 1-50	6.05	37.20
1H-5, 50-60	6.55	36.08
1H-5, 100-110	7.05	35.61
1H-6, 21-31	7.76	35.30
2H-1, 1-40	8.05	35.83
2H-1, 40-50	8.45	35.56
2H-1, 100-110	9.05	35.90
2H-2, 1-50	9.55	35.92
2H-2, 50-60	10.05	35.39
2H-2, 100-110	10.55	46.14
2H-3, 1-50	11.05	36.36
2H-3, 50-60	11.55	36.07
2H-3, 100-110	12.05	36.10
2H-4, 1-50	12.55	35.54
2H-4, 50-60	13.05	35.33
2H-4, 100-110	13.55	35.82
2H-5, 1-50	14.05	36.13
2H-5, 50-60	14.55	36.60
2H-5, 100-110	15.05	36.20
2H-6, 0-10	15.48	33.87

Table T13. Solid-phase carbon and nitrogen, Site U1368.

Core, section, interval (cm)	Depth (mbsf)	TC (wt%)	TN (wt%)	TOC (wt%)	TIC (wt%)	CaCO ₃ (wt%)
329-U1368B-						
1H-1, 0-1	0.01	9.31	0.014	0.085	9.28	77.3
1H-1, 9-10	0.10	8.55	BD	0.063	8.50	70.8
1H-1, 25-26	0.26	9.52	BD	0.037	9.57	79.8
1H-1, 45-46	0.46	9.64	BD	0.016	9.67	80.6
1H-1, 70-71	0.71	9.56	BD	0.021	9.47	78.9
1H-1, 99-100	1.00	9.80	BD	0.013	9.66	80.4
1H-1, 135-136	1.36	9.77	BD	0.014	9.90	82.5
1H-2, 135-136	2.86	9.96	BD	0.017	9.92	82.7
1H-3, 135-136	4.36	10.51	BD	0.012	10.49	87.4
2H-1, 147-148	6.98	9.90	BD	0.012	9.92	82.7
2H-2, 147-148	8.48	9.84	BD	0.010	9.88	82.3
2H-3, 147-148	9.98	8.70	BD	BD	8.68	72.3
2H-4, 147-148	11.48	8.75	BD	BD	8.76	73.0
2H-5, 97-98	12.48	7.66	BD	BD	7.56	63.0
2H-6, 147-148	13.98	7.33	BD	BD	7.36	61.3

TC = total carbon, TN = total nitrogen, TOC = total organic carbon, TIC = total inorganic carbon. BD = below detection (TN < 0.001%; TOC < 0.002%).

Table T14. Epifluorescence microscopy cell counts in sediment samples, Site U1368.

Core, section, interval (cm)	Depth (mbsf)	Cell count (\log_{10} cells/cm ³)					
		Extracted				Nonextracted	
		Count 1	Count 2	Count 3	Count 4	Count 1	Count 2
329-U1368C-							
1H-1, 10–15	0.10	4.8	4.9	4.9	4.8	5.9	5.7
1H-1, 60–70	0.60						
1H-1, 110–120	1.10						
1H-1, 135–140	1.35	3.5	3.3	3.5	3.5	4.4	BD
1H-2, 60–70	2.10						
1H-2, 110–120	2.60						
1H-2, 135–140	2.85	3.5	3.5			3.8	2.3
1H-3, 60–70	3.60						
1H-3, 110–120	4.10						
1H-3, 135–140	4.35	3.2	3.3			3.8	2.5
1H-4, 60–70	5.10						
1H-4, 110–120	5.60						
1H-4, 135–140	5.85	3.2	3.2				
1H-5, 40–50	6.40						
1H-5, 110–120	7.10						
1H-5, 135–140	7.35	3.0	3.0				
1H-6, 10–20	7.60	2.9	2.9				
1H-6, 16–21	7.66						
2H-1, 50–60	8.50						
2H-1, 135–140	9.35	2.8	2.3				
2H-2, 60–70	10.10						
2H-2, 110–120	10.60						
2H-2, 135–140	10.85	3.2	2.7	3.2	BD		
2H-3, 60–70	11.60						
2H-3, 110–120	12.10						
2H-3, 135–140	12.35	2.6					
2H-4, 60–70	13.10						
2H-4, 110–120	13.60						
2H-4, 135–140	13.85	2.8	3.2				
2H-5, 60–70	14.60						
2H-5, 110–120	15.10						
2H-5, 135–140	15.35	3.2	3.1				
2H-6, 10–20	15.53						

BD = below detection. Blank cells = no counts (will be counted postexpedition).

Table T15. Abundance of virus-like particles in sediment samples determined by epifluorescence microscopy, Site U1368.

Core, section	Depth (mbsf)	VLP/cm ³	STD
329-U1368C-			
1H-1	0.10	1.47E+06	6.81E+04
1H-1	0.60	3.11E+05	1.98E+04
1H-1	1.10		
1H-1	1.35	1.53E+05	1.13E+04
1H-2	2.10	1.61E+05	1.16E+04
1H-2	2.60		
1H-2	2.85	1.20E+05	7.76E+03
1H-3	3.60	7.23E+04	5.51E+03
1H-3	4.10		
1H-3	4.35		
1H-4	5.10		
1H-4	5.60		
1H-4	5.85		
1H-5	6.40	9.08E+04	7.57E+03
1H-5	7.10		
1H-5	7.35		
1H-6	7.60		
1H-6	7.66		
2H-1	8.50	4.60E+04	3.81E+03
2H-1	9.35		
2H-2	10.10		
2H-2	10.60		
2H-2	10.85		
2H-3	11.60	3.47E+04	2.70E+03
2H-3	12.35		
2H-4	13.10		
2H-4	13.85		
2H-5	14.60	2.83E+04	2.57E+03
2H-5	15.35		
2H-6	15.53		
329-U1368D-			
1H-1	1.20		
1H-2	2.60		
1H-3	3.70		
1H-4	4.90		
1H-5	7.20		
2H-1	8.40		
2H-2	9.70		
2H-3	11.10		
2H-4	13.40		
2H-5	14.80		

VLP = virus-like particles. STD = standard deviation. Blank cells = no counts (samples will be analyzed postexpedition).

Table T16. List of samples and culture media used for onboard cultivation experiments, Site U1368.

Core, section	Media used for cultivation
329-U1368D-	
1H-1	Mmm1, Mmm2, SPG-ASW, SPG-JL, MA, MB, MR2A, SLURRY
1H-2	SPG-JL, MA, MB, MR2A
1H-3	Mmm1, Mmm2, SPG-ASW, MA, MB, MR2A, SLURRY
1H-4	MA, MB, MR2A
1H-5	Mmm1, Mmm2, SPG-ASW, SPG-JL, SLURRY
2H-2	SLURRY
2H-4	Mmm1, Mmm2, SPG-ASW, SPG-JL, MA, MB, MR2A
2H-5	Mmm1, Mmm2, SPG-ASW, SPG-JL, MA, MB, MR2A, SLURRY
329-U1368E-	
14R-1	Mmm1, Mmm2, SPG-ASW

SLURRY = slurry in artificial seawater. For more detailed information on the media, see “**Microbiology**” in the “Methods” chapter (Expedition 329 Scientists, 2011a).

Table T17. Epifluorescence microscopy microsphere counts in basement basalt samples, Site U1368.

Core, section	Depth (mbsf)	Microsphere count (\log_{10} microspheres/cm ³)				
		Washing solution	Exterior untreated	Exterior washed 2x	Exterior flamed	Interior
329-U1368F-						
2R-1	9.7	5.0	3.5	ND	ND	ND
2R-4	13.4	4.7	3.5	ND	ND	ND
4R-2	30.0	4.5	2.4	3.3	2.4	ND
5R-3	40.2	4.4	ND	3.4	2.6	3.2
7R-3	50.4	4.9	4.8	4.4	3.5	3.4
9R-1	62.8	4.6	3.3	2.6	2.9	ND
13R-3	99.7	4.3	3.3	2.7	2.5	2.6
14R-1	106.1	4.3	3.7	2.9	2.7	3.1

ND = no microspheres observed by microscopic observations.

Appendix

Foraminifer and ostracod taxa

Benthic foraminifers

Anomalinoidea globosus (Chapman and Parr) 1937
Buliminella parvula Brotzen, 1948
Cibicidoides mundulus Brady, Parker, and Jones, 1888
Cibicidoides wuellerstorfi (Schwager) 1866
Epistominella sp.
Globocassidulina subglobosa (Brady) 1881
Gyroidina sp.
Gyroidinoides soldanii (d'Orbigny) 1826
Gyroidinoides orbicularis (sensu Parker, Jones, and Brady) 1865
Karrerella chapotensis (Cushman) 1911
Lagena spp.
Nodosaria sp. A
Nodosaria sp. B
Nuttallides umbonifer (Cushman) 1933
Oridorsalis umbonatus (Reuss) 1851
Polymorphina spp.
Siphonodosaria spinata Deshayes, 1832

Planktonic foraminifers

Catapsydrax dissimilis (Cushman and Bermudez, 1937) Bolli, Loeblich, and Tappan, 1957
Dentoglobigerina altispira (Cushman and Jarvis, 1936) Blow, 1979
Globorotalia (Fohsella) fohsi s.l. Cushman and Ellisor, 1939; Kennett and Srinivasan, 1983
Globanomalina pseudomenardii (Bolli, 1957) Beggren and Norris, 1997
Globoturbotalita woodi (Jenkins, 1960) Hofker, 1977
Globigerinita uvula Ehrenberg, 1862
Globigerinatella insueta Cushman and Stainforth, 1945
Globigerinella praesiphonifera Blow, 1969
Globigerinita naparimaensis Bronnimann, 1951
Globigerinoides ruber (white) d'Orbigny, 1839
Globigerinoides trilobus Reuss, 1850

Globoconella inflata d'Orbigny, 1839
Globoquadrina binaiensis (Koch, 1935) Kennett and Srinivasan, 1983
Globoquadrina dehiscens (Chapman, Parr, and Collins, 1934) Finlay, 1947
Globorotalia archaeomenardii Bolli, 1957
Globorotalia crassaformis Galloway and Wissler, 1927
Globorotalia pseudomiocenica Bolli and Bermudez, 1965
Globorotalia tosaensis Takayanagi and Saito, 1962
Globoturbotalita decoraperta (Takayangi and Saito, 1962) Chaisson and Pearson, 1997
Globoturbotalita nepenthes (Todd, 1957) Hofker, 1977
Neogloboquadrina dutertrei d'Orbigny, 1839
Neogloboquadrina dutertrei blowi Rogl and Bolli, 1973
Orbulina biloba d'Orbigny, 1839
Orbulina suturalis Brönnimann, 1951
Orbulina universa d'Orbigny, 1839
Paragloborotalia mayeri (Cushman and Ellisor, 1939) Spezzaferri, 1991
Praeorbulina glomerata (Blow, 1956) Olsson, 1964
Praeorbulina sicana (de Stefani, 1952) Jenkins, 1981
Praeorbulina transitoria Blow, 1956
Sphaeroidinellopsis disjuncta Finlay, 1940
Sphaeroidinellopsis kochi Caudri, 1934
Sphaeroidinellopsis seminulina (Schwager, 1866) Banner and Blow, 1970
Sphaeroidinellopsis dehiscens Blow, 1970

Ostracods

Bradleya sp.
Eucythere sp.
Heinia sp.
Henryhowella sp.
Krithe spp.
Pelecocythere sp.
Poseidonamicus sp.